Physik - Department

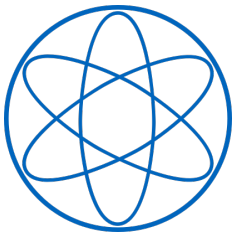

Enhancing the Dark Matter Sensitivity of CRESST: Purification, Stress Reduction and ^{17}O Enrichment of $CaWO_4$ Target Crystals

Dissertation
von

Angelina Carina Kinast

Technische Universität München

Technische Universität München
TUM School of Natural Sciences

Enhancing the Dark Matter Sensitivity of CRESST: Purification, Stress Reduction and ^{17}O Enrichment of $CaWO_4$ Target Crystals

Angelina Carina Kinast

Vollständiger Abdruck der von der TUM School of Natural Sciences der Technischen Universität München zur Erlangung des akademischen Grades einer

Doktorin der Naturwissenschaften (Dr. rer. nat.)

genehmigten Dissertation.

Vorsitz:	apl. Prof. Dr. Norbert Kaiser
Prüfer*innen der Dissertation:	1. Prof. Dr. Stefan Schönert
	2. Prof. Dr. Bastian Märkisch

Die Dissertation wurde am 08.11.2023 bei der Technischen Universität München eingereicht und durch die TUM School of Natural Sciences am 14.12.2023 angenommen.

Abstract

The nature of dark matter (DM) is one of the greatest mysteries in cosmology, astro- and particle physics. Despite its observation via the gravitational force on all scales, a particle nature could not be verified yet. The CRESST (Cryogenic Rare Event Search with Superconducting Thermometers) experiment, located at the Laboratori Nazionali del Gran Sasso, aims to detect light DM particles directly via their elastic scattering off nuclei in scintillating $CaWO_4$ target crystals operated at cryogenic temperatures. The search for light DM requires a low detector threshold in combination with a low background. Currently, the challenge lies in understanding a low-energy excess rate (LEE) observed below 200 eV and radioactive backgrounds. The research carried out during this thesis project aims to increase the sensitivity of CRESST to spin-independent and spin-dependent DM searches by: (i) reducing radioactive backgrounds in the $CaWO_4$ target crystals, (ii) improving intrinsic crystal properties and (iii) enriching the $CaWO_4$ crystals with ^{17}O (only relevant for spin-dependent searches).

To reduce crystal-intrinsic backgrounds, chemical purification was applied to the raw materials $CaCO_3$ and WO_3, and the synthesized $CaWO_4$ powder. The purified material was used to grow the crystal TUM93, from which three CRESST modules were produced. The radio-impurities are traced by measuring α-decays using a novel energy reconstruction method. TUM93A shows the lowest intrinsic α-activity of $(369 \pm 19)\mu$Bq/kg, a factor of 8.3 lower than previously produced $CaWO_4$ crystals at TUM. With this purity, a background-free measurement could be performed up to 50 kgd, in the absence of external backgrounds. For CRESST-III phase 2, with a planned exposure of 1000 kgd and detector thresholds of 10 eV, the use of these crystals would push the sensitivity close to the neutrino floor (achievable cross sections of $4.56 \cdot 10^{-7}$ pb at 0.8 GeV/c^2).

An essential contribution of this work towards understanding the LEE involves investigating the impact of intrinsic crystal stress on the LEE rate. This stress might be an origin of the LEE via relaxation processes. Intrinsic stress is caused by temperature gradients during crystal growth. Following temperature gradient simulations, optimisations of the Czochralski furnace and the growth process were conducted prior to the growth of TUM93. A DM analysis of the TUM93A module was performed, and the LEEs of both the crystal TUM93 and its light detector were investigated. The LEE of TUM93 is higher compared to the LEE of another module with crystal TUM73, grown in the previous configuration. The latter exhibits higher intrinsic stress. This excludes intrinsic stress as a primary source of LEE. In addition, the shape, rate and time evolution of the LEE were investigated. Due to a temperature and time dependence of the LEE observed in all detectors, radiation was also excluded as a source, pointing to external stress as the main source.

To boost CRESST's sensitivity to spin-dependent DM, a method for enriching $CaWO_4$ crystals with the ^{17}O isotope was developed through annealing in ^{17}O gas. Two crystals were enriched to 0.124 % and 0.276 % of ^{17}O, extending the achievable DM sensitivities by factors of 3.26 and 7.26, respectively. This is a milestone for the ^{17}O enrichment project.

Zusammenfassung

Die Natur dunkler Materie (DM) ist eines der größten Rätsel der Kosmologie, Astro- und Teilchenphysik. Trotz ihrer gravitativen Beobachtung konnte ihre Teilcheneigenschaft bisher nicht nachgewiesen werden. Das in Italien angesiedelte CRESST-Experiment zielt darauf ab, leichte DM-Teilchen direkt über ihre elastische Streuung an Kernen in szintillierenden $CaWO_4$-Kristallen bei kryogenen Temperaturen nachzuweisen. Die Suche nach leichten DM-Teilchen erfordert eine niedrige Detektorschwelle in Kombination mit einem niedrigen Untergrund. Derzeit besteht die Herausforderung darin, einen Überschuss an niederenergetischen Ereignissen (NEE) unterhalb von 200 eV zu verstehen und den radioaktiven Untergrund zu reduzieren. Die im Rahmen dieses Dissertationsprojektes durchgeführten Forschungsarbeiten zielen darauf ab, die Empfindlichkeit von CRESST für die Suche nach spinunabhängiger und spinabhängiger DM zu erhöhen, durch: (i) Verringerung des radioaktiven Untergrunds in den $CaWO_4$-Kristallen, (ii) Verbesserung der intrinsischen Kristalleigenschaften und (iii) Anreicherung der $CaWO_4$-Kristalle mit ^{17}O (nur relevant für spinabhängige Suche).
Zur Reduzierung der intrinsischen Radioaktivität im Kristall wurden die Rohmaterialien $CaCO_3$ und WO_3 sowie das synthetisierte $CaWO_4$-Pulver chemisch gereinigt. Aus diesem Material wurde der Kristall TUM93 gezüchtet, aus dem drei CRESST-Module hergestellt wurden. Die Reinheit wurde durch Messung der α-Zerfälle mit einer neuartigen Energierekonstruktionsmethode bestimmt. TUM93A weist die niedrigste intrinsische α-Aktivität von $(369 \pm 19)\mu$Bq/kg auf, was um einen Faktor 8,3 niedriger ist als bei zuvor an der TUM hergestellten $CaWO_4$-Kristallen. Mit dieser Reinheit könnte, in Abwesenheit von externen Untergründen, eine untergrundfreie Messung bis zu 50 kgd durchgeführt werden. Für CRESST-III Phase 2 mit einer geplanten Exposition von 1000 kgd und Detektorschwellen von 10 eV könnte die Empfindlichkeit fast bis zur Neutrinoschwelle verbessert werden.
Zusätzlich wurde der Einfluss der intrinsischen Kristallspannung auf die NEE-Rate untersucht. Die Relaxation dieser Spannung könnte eine Ursache des NEE sein. Diese Spannungen entstehen durch Temperaturgradienten während des Kristallwachstums. Nach Simulationen des Temperaturgradienten wurden Optimierungen des Czochralski-Ofens und des Wachstumsprozesses vor der Züchtung von TUM93 durchgeführt. Eine DM-Analyse von TUM93A wurde durchgeführt und die NEEs des Kristalls und des Lichtdetektors untersucht. Der NEE von TUM93 ist höher als der NEE eines anderen Moduls mit dem Kristall TUM73, der in der vorherigen Konfiguration gezüchtet wurde. Letzterer hat eine höhere intrinsische Spannung. Dies schließt intrinsische Spannungen als Hauptursache für den NEE aus. Zusätzlich wurden die Form, die Rate und die zeitliche Entwicklung des NEE untersucht. Da der NEE in allen Detektoren temperatur- und zeitabhängig ist, konnte Strahlung als Quelle ausgeschlossen werden, was auf externe Spannungen hindeutet.
Um die Empfindlichkeit von CRESST für spinabhängige DM zu erhöhen, wurde eine Methode zur Anreicherung von $CaWO_4$-Kristallen mit dem ^{17}O-Isotop durch Glühen in ^{17}O-Gas entwickelt. Zwei Kristalle wurden auf 0,124 % und 0,276 % ^{17}O angereichert, was die erreichbaren DM-Empfindlichkeiten um den Faktor 3,26 bzw. 7,26 erhöht. Dies ist ein Meilenstein für das ^{17}O-Anreicherungsprojekt.

Contents

List of Figures

List of Tables

Acronyms

Awu After Warmup Data Set

Bck Background Data Set

CAT Cryogenic Analysis Tools - CRESST Analysis Software

CEvNS Coherent Elastic neutrino-Nucleus Scattering

CMB Cosmic Microwave Background

CP Control Pulse

CPE Convert Pulseheight to Energy factor

CRESST Cryogenic Rare Event Search with Superconducting Thermometers

DAQ Data ACquisition

DM Dark Matter

FQLs Flux-Quantum-Losses

HF High-Frequency

HPGe High Purity Germanium

ICP-MS Inductively Coupled Plasma Mass Spectrometry

LD Light Detector

LEE Low-Energy Excess

LLE Liquid Liquid Extraction

LNGS Laboratori Nazionali del Gran Sasso

LY Light Yield

MPP Max Plank Institute for Physics

Ncal Neutron Calibration Data Set

NMR Nuclear Magnetic Resonance

NPS Noise Power Spectrum

OFilter Optimum Filter

PD Phonon Detector

PDF Probability Density Function

PostCal Post Neutron Calibration Data Set

RF Radio-Frequency

ROI region of interest

SM Standard Model

SOS Silicon On Sapphire

SQUID Superconducting QUantum Interference Device

TES Transition Edge Sensor

TP Test Pulse

TPE Test Pulse Equivalent

TPR Test Pulse Response

TUM Technische Universität München

UGL shallow UnderGround Laboratory

WIMPs Weakly Interacting Massive Particles

WP Working Point

Chapter 1

Introduction to Dark Matter

The nature of Dark Matter (DM) might be the biggest mystery in nowadays cosmology, astro- and particle physics. Proof of the existence of DM can be derived from observations on all cosmic scales (see section 1.1), but it has yet to be measured in laboratories. Several observations hint at the nature of DM, and various DM candidates were derived from them (see section 1.2). Hence, a great effort is taken within the community to detect these particles in various ways, described in section 1.3.

1.1 Evidence for Dark Matter

The term Dark Matter was first proposed by Fritz Zwicky in 1933 when he published a paper named "Die Rotverschiebung von extragalaktischen Nebeln" [1]. He calculated the motion of galaxies and their masses in the Coma cluster, based on their luminosity, concluding that the viral mass of the cluster is 400 times the visible mass and that this big dispersion of velocities "bears an unsolved problem" [1]. As most of the mass was invisible, he named it Dark Matter.

1.1.1 Galaxy Rotation Curves

A similar observation was reported in the 1970s by Vera Rubin et al. [2], who studied the rotation curves of galaxies by measuring the red- and blueshifts of the 21 cm line of hydrogen in the galaxies. They found that the rotation velocities as a function of the distance from the centre of the galaxies do not follow their calculated behaviour. Following the Birkhoff theorem, the rotational curve for a point-like mass, assuming that most of the mass is located in the bulge, is

$$v(r) = \sqrt{\frac{GM}{r}} \propto \frac{1}{\sqrt{r}} \tag{1.1}$$

This means that the velocity should drop with a $1/\sqrt{r}$ dependency for stars outside the bulge. However, the galaxies' rotation curves studied by Rubin et al. did not show this dependency. The velocity stayed flat or even rose with the distance to the

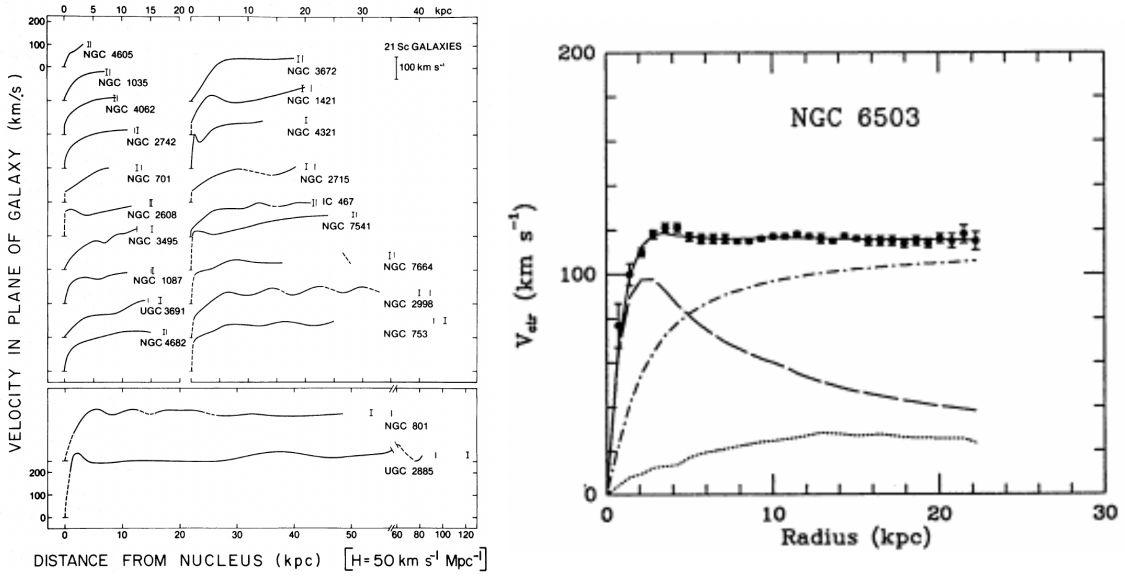

Figure 1.1: Left: Mean velocities in the plane of the galaxy as a function of linear distance to the nucleus for 21 galaxies. Contrary to the theoretical predictions, the velocities do not decrease with $1/\sqrt{r}$ dependency. Picture taken from [2]. Right: Fit of the rotation curve of galaxy NGC 6503. The dashed curve represents the visible mass component, the dotted line the gas component and the dashed-dotted line the DM component needed to describe the rotation curve observed for the galaxy. Figure taken from [3].

centre of the galaxy, as shown in figure 1.1 on the left. A fit to one of the galaxies by Bergeman et al. [3] showed that the galaxies have to be surrounded by extended spherical DM halos to explain this behaviour as shown in figure 1.1 (right) by the point-dashed line.

1.1.2 Galaxy Cluster Mergers

The characteristics of galaxy cluster mergers are another strong hint for the existence of DM. For its observation, a method called gravitational lensing is used. It is based on the theory of general relativity by A. Einstein, which states that massive gravitational objects bend light. When light sent out by stars in the background passes massive gravitational objects, their light is bent, and the stars appear distorted [4]. This effect can be used to determine the mass between the observed distorted light sources and the observer on Earth. Hence it is a powerful method to determine the mass of an object or a region. This mass distribution can then be compared to visible matter distributions. The optical picture of the galaxy cluster merger of the so-called bullet cluster by the Hubble Space Telescope is shown in figure 1.2 (NASA/STScI; Magellan/U.Arizona/D.Clowe et al.). Two areas are highlighted. The main mass contribution in a galaxy cluster is interstellar gas which, after the collision, cumulates in the middle of the clusters as the collision slows it down. This

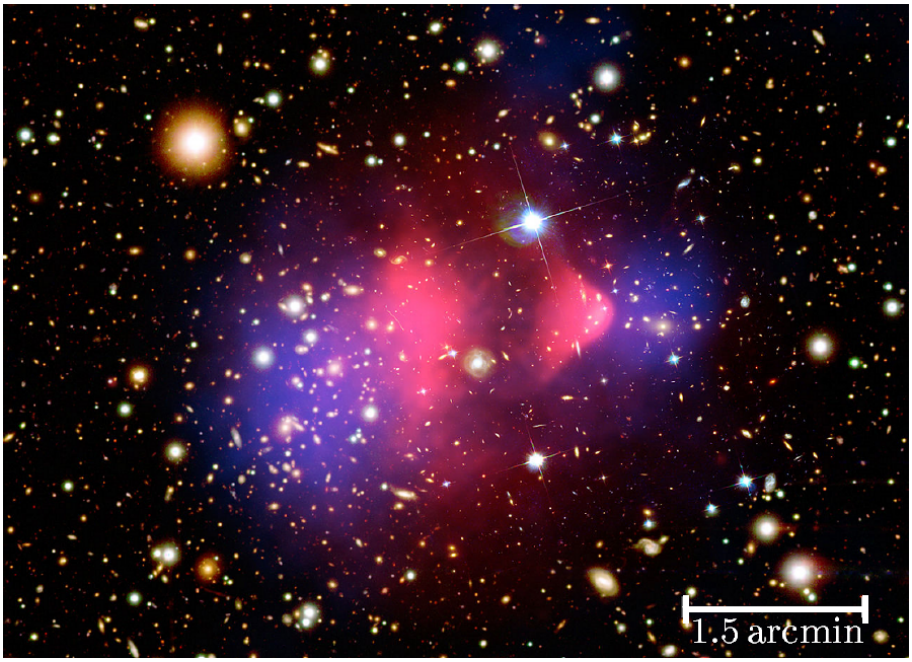

Figure 1.2: Picture of the Bullet cluster taken by the Hubble space telescope (credit: NASA/STScI; Magellan/ U.Arizona/D. Clowe et al.). The main amount of visible mass in galaxy clusters is made from clouds that emit X-rays. They were recorded by the Chandra Telescope and are overlaid in pink (credit: NASA/CXC/CfA/ M.Markevitch et al.). The cluster's centre of mass was determined via gravitational lensing and is overlaid in blue (credit: NASA/STScI; ESO WFI; Magellan/U.Arizona/D. Clowe et al.). The centre of baryonic mass and gravitational mass do not coincide.

gas was measured using the Chandra Telescope (NASA/CXC/CfA/ M.Markevitch et al.) and is highlighted in pink. The overall centre of mass was determined by gravitational lensing (NASA/STScI; ESO WFI; Magellan/U.Arizona/D. Clowe et al.) and is highlighted in blue. The absolute centre of mass does not coincide with the baryonic centre of mass, another evidence that a large amount of matter is not visible in galaxy clusters [5]. This observation also excludes theories that describe the discrepancy between the expected and observed velocity distribution in galaxies by modified Newton dynamics laws on large scales.

1.1.3 Cosmic Microwave Background

In the early universe, when the temperature T was larger than two times the mass of the electron, the reaction

$$\gamma \rightarrow e^+ + e^- \tag{1.2}$$

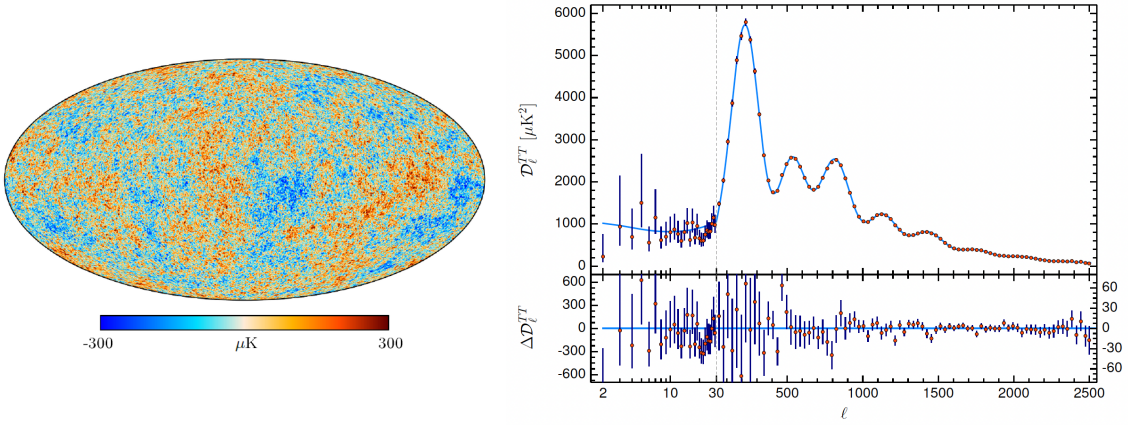

Figure 1.3: Left: Cosmic microwave radiation detected by the Planck satellite. The temperature fluctuations are colour coded from -300 μK (dark blue) to +300 μK (dark red). Figure from [6]. Right: Power spectrum of the temperature anisotropies detected by Planck. Several acoustic peaks are visible, fitted by the Planck collaboration's six-parameter λCDM model. The universe's total matter density and the relative density between baryonic matter and DM can be derived from the peak's relative and absolute heights. Figure from [7].

was in thermal equilibrium with its reverse reaction, and photons had only a short mean free path. As the universe cooled down below this temperature, the reaction was "frozen out", and the photons reacted via Thomson scattering on electrons

$$e^- + \gamma \rightarrow e^- + \gamma \tag{1.3}$$

or ionised hydrogen via

$$\gamma + H \rightarrow p + e^- \tag{1.4}$$

While these reactions were in thermal equilibrium, no free propagation of the photons was possible. At $T \sim 0.3\,eV$ also these reactions froze out, and the photons started propagating freely through the universe, forming the so-called Cosmic Microwave Background (CMB) [8]. It represents a spectrum of perfect black body radiation with a temperature redshifted to $T_{CMB} = (2.72548 \pm 0.00057)\,K$ with fluctuations in the tens of μK range [9] (see figure 1.3 (left)). The spectrum of the CMB gives insight into structure formation in the early universe as the large structures we observe now condensed on the tiny fluctuations in the early universe. The temperature fluctuations originate from the differences in the gravitational potential from which the photons at their last scattering surface during the freeze-out had to escape. The CMB fluctuations can be translated into spherical harmonics with

$$\frac{\Delta T(\Theta,\phi)}{T} = \sum_{lm} a_{lm} Y_{lm}(\Theta,\phi) \tag{1.5}$$

with the average

$$C_l = \langle a_{lm} a_{lm}^* \rangle \tag{1.6}$$

containing information on the average temperature fluctuation at an angle corresponding to multipole l or the angular frequency. The Planck satellite measured this power spectrum and is shown in figure 1.3 (right). The frequency and amplitude of the peaks depend strongly on the universe's geometry and content. They are fitted with a six-parameter λCDM model. The first peak is sensitive to the curvature of the universe Ω and the baryon-to-photon ratio. The relative height of the first and second peaks depends on the ratio of Ω_B and Ω_{DM}, the baryonic matter density and the dark matter density in our universe. In this way, the existence of DM can be observed, and the ratio of DM to baryonic matter can be calculated. The PLANCK collaboration determined the baryonic matter density to be $\Omega_B = 0.0486$ and the DM density to be $\Omega_{DM} = 0.2589$ [10]. These results show that only 5 % of the total energy density of the universe is composed of baryonic dark matter, and 26 % can be assigned to DM. The main part $\Omega_\Lambda = 0.685$ is due to the so-called dark energy which drives the expansion of our universe.

1.1.4 Structure Formation

The small temperature fluctuations in the CMB were the seeds for forming the large-scale structures observed in the universe today. An interplay of gravitation and expansion in the universe can qualitatively explain the growth of density fluctuations. In regions where the gravitational field is stronger than average, the expansion rate is slower, and the density decrease due to expansion is suppressed. In an area with a weaker gravitational field than average, the opposite is the case, the density decreases. This causes growth of the density contrast between the two regions [11]. The solutions for the differential equations describing the growth in density contrast are not analytically calculable and must be derived through numerical simulations [12]. Several simulations, including different percentages of baryonic mass and DM mass, have been performed, and the results compared to the output of sky surveys, e.g. the Sloan Digital Sky Survey [13]. The Millennium simulation by the Virgo consortium, e.g., used more than 10 billion particles to trace the evolution of the dark and baryonic matter distribution in a cubic region of the universe, spanning 2 billion light years on each side. By this, the evolutionary history of more than 220 million galaxies and supermassive black holes could be recreated [14].

The simulations confirmed that baryonic matter is not alone able to create the observed large-scale structures from the fluctuations in the CMB temperature. The simulation only converges towards the structures we observe today when a certain amount of DM is included [12].

The structure formation process is derived from these observations in the following way. It is believed to have started well before the baryons decoupled from photons. The DM components started forming structures while baryons were still distributed smoothly until they decoupled. When decoupling, they fell into the potential wells formed by the DM components.

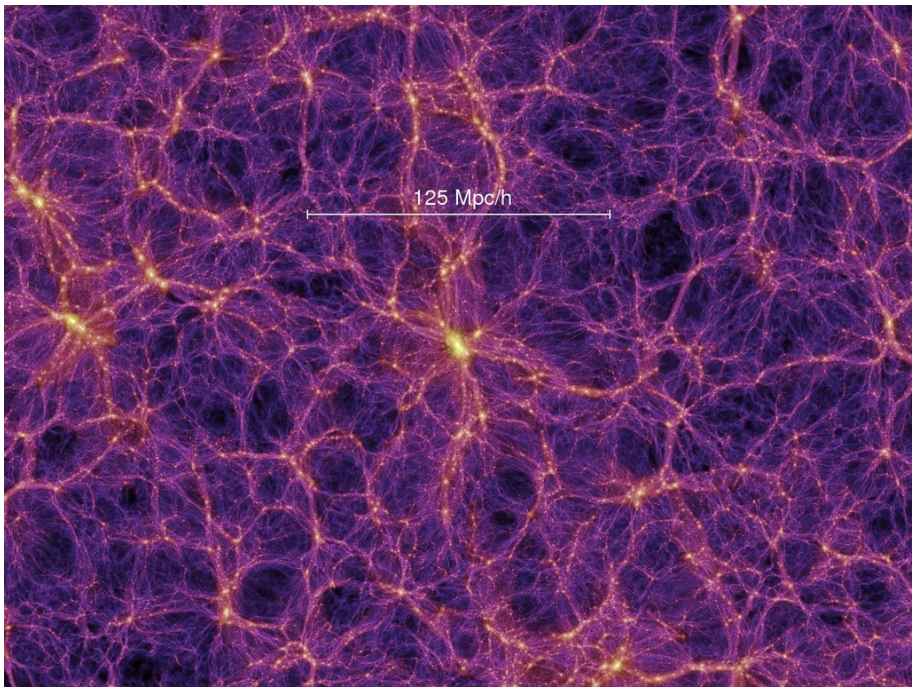

Figure 1.4: The image shows the projected DM density field colour-coded by density and local dark matter velocity dispersion from the Millennium simulation. Figure taken from [14].

1.2 Dark Matter Candidates

As the reported observations show, the existence of DM is evident on all scales of the universe, starting from galaxies and their rotation curves up to the structure formation of our universe. Despite numerous experiments searching for DM, it has yet to be detected. Several theoretical predictions evolved from the observations predicting particles which have to fulfil the following criteria:

- DM particles are not visible in any optical channels. Hence, they cannot interact electromagnetically and must be neutral.
- The self-interaction cross-section has to be very small due to, e.g. the observations of the Bullet Cluster, where the DM particles seem to be passing through each other during the collision without scattering on each other.
- The abundance of the DM has to fit the CMB observations and the structure formations. This leads to the requirement of DM being non-relativistic (so-called cold DM), as relativistic DM could not explain the structure formation.
- As the effect of DM is visible today, the particles have to be stable or at least have a lifetime in the order of the universe's age.

Several theories predict DM particles by considering other inconsistencies and possible solutions in particle physics like the Axion for the strong CP-Problem, the

Kaluza-Klein particle for the unification of forces, Neutralinos for the hierarchy problem and asymmetric DM for the baryon matter-antimatter asymmetry. These theories are discussed in the following. They are, however, only a small selection. Others, like e.g. a sterile neutrino or primordial black holes, are discussed in [15].

1.2.1 Axions

Several experiments proved that CP conservation is violated in e.g. the decay of the neutral kaon [16] or the B meson decay [17]. In quantum chromodynamics (QCD), however, no CP-symmetry violation could be experimentally determined. There is no known reason why it should be conserved in QCD, specifically, introducing the strong CP problem. An additional dynamic field is introduced to avoid the need for so-called fine-tuning, which has a minimal potential for the parameter describing the CP violation Θ to be zero. Introducing a field with a new degree of freedom with quantised states introduces a new particle called Axion. Relic oscillations around the minimum potential could carry the energy or mass, explaining the dark matter problem.

1.2.2 Kaluza-Klein-Particles

Comparing the relative strength of the fundamental forces, the strong, weak, and electromagnetic forces to the gravitational force shows that gravity is much weaker than the three other forces. To unify the forces, the four-dimensional space-time introduced by Einstein can be expanded with an additional dimension. Gravity propagates on this dimension. Again, adding extra dimensions adds degrees of freedom. These can be excited, and these excitations' propagations can be interpreted as a particle, the Kaluza-Klein-Particle. If this particle is stable, it would be a viable DM candidate [18, 19].

1.2.3 Neutralino - WIMPs

The so-called gauge hierarchy problem deals with the question of why the mass of the Higgs boson is much smaller than the Planck mass. This problem can be solved by supersymmetry which proposes new particles that couple to the Higgs and can change its mass. In a minimal supersymmetric model, each boson gets a fermionic partner assigned and each fermion a bosonic partner. The particles from the standard model of particle physics with an R-parity P_R = -1 are assigned to a new partner with R-parity P_R = +1. As R-parity is conserved, the lightest supersymmetric particle must be stable, creating a candidate for DM. This particle, named neutralino, is a superposition of the supersymmetric partners of gauge bosons and Higgs particle [20].
The neutralino is a candidate for the group of Weakly Interacting Massive Particles (WIMPs) with predicted masses $\mathcal{O}(10\,\mathrm{GeV/c^2}$ - $\mathrm{TeV/c^2})$ and a cross-section in the scale of the electroweak interaction. Due to their high mass, they were produced through thermal freeze-out in the early universe. Creation was suppressed when the

universe's temperature dropped below the WIMPs' mass. However, annihilation was still possible until the universe's density was so small that the WIMPs could no longer find partners to annihilate. From this point, their density stayed constant. For the mass predicted for WIMPs, this density is consistent with the density observed by Planck and the sky surveys. This fact is often referred to as the WIMP miracle [21].

1.2.4 Asymmetric Dark Matter

Asymmetric dark matter (ADM) models are based on the assumption that the observed abundance of DM has the same origin as the observed abundance of visible matter, i.e. the asymmetry in the abundance of particles and their antiparticles. The asymmetry of visible matter is due to a slight excess of baryons over anti-baryons in the early universe. In asymmetric DM models, the current density is also based on a DM particle-antiparticle asymmetry due to processes occurring during the early time of our universe. The density of ADM would not only depend on the freeze-out principle, and the proposed DM particle mass is lower than the WIMP mass. Most ADM models require the DM particles to have masses between 1-15 $\mathrm{GeV/c^2}$ [15]. For a list of candidates derived from this theory, the reader is referred to [22].

1.3 Detection Methods

Weak interactions with Standard Model (SM) particles are possible for all DM candidates described in the non-complete list above. Figure 1.5 shows a Feynman diagram of the interaction of a DM particle with a SM particle. Three different detection modes of this interaction are possible. The production of DM particles with colliders, the indirect detection of the annihilation of DM particles to SM particles and the direct detection measuring the recoil of a DM particle scattering on SM particles.

1.3.1 Production at Colliders

High energetic collisions of SM particles at colliders could produce a pair of DM particles. The sensitive detectors would not detect the energy used to create these DM particles due to the small cross-section of DM. Hence, colliders search for missing momenta in their collisions. If the missing energy events can be distinguished from, e.g., neutrinos carrying away energy from the reaction, the existence of DM with an energy of half the missing energy could be reported. However, collider experiments could not state whether the produced particles are short or long-lived as they only report the lost energy from the collision. With the last LHC upgrade, the detectors ATLAS [24] and CMS [25] now operate at high centre of mass energies of $\sqrt{s}$=13 TeV and could, in principle, be sensitive to a DM mass in this energy region.

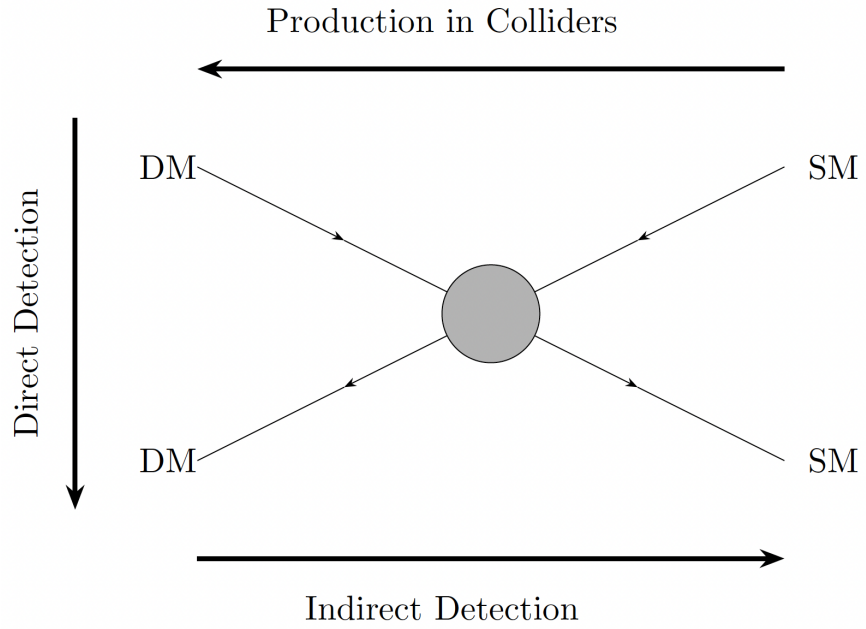

Figure 1.5: Detection and production channels for DM illustrated with a Feynman diagram. Three detection processes are possible. The production at colliders, the indirect detection and the direct detection. The figure is taken from [23].

1.3.2 Indirect Detection

Indirect detection experiments aim to detect secondary particles produced through the annihilation of DM particles like proton-antiproton and electron-positron pairs, γ-radiation or neutrinos [26]. The annihilation can only occur in dense environments like the centre of the milky way or our sun. Experiments looking for γ-radiation and neutrinos are mainly located on Earth. Experiments looking for positrons and antiprotons are usually situated in satellites as these particles would be shielded by the Earth's magnetic field. An example of an experiment looking for γ-radiation is the Fermi large area telescope (Fermi-LAT) [27, 28] and for neutrinos the Ice Cube experiment [29]. The alpha magnetic spectrometer 2 (AMS-02) is located on the international space station facing away from Earth and is looking for an excess of charged particles.

1.3.3 Direct Detection

Direct detection experiments aim to detect a nuclear recoil by DM nucleon scattering in detectors located on Earth. For this detection channel, DM has to interact also via the weak force. The signal seen by a detector depends on the detector material, the cross-section of the process and the number of DM particles passing through the detector. The expected signal rate for standard assumptions is less than 0.1 events/kg/day [30]. Due to this low signal rate, cosmic radiation and radioactivity can represent a significant background contribution. To reduce these

background components, detectors are usually located deep underground and surrounded by multiple shielding layers to minimise any remaining radiation.
Typical direct DM search detectors read out the nuclear recoil by one or two of the following detection channels in their target material:

- Phonons (heat)
- Scintillation (light)
- Ionisation (charge)

Usually, the percentage of energy distributed to the different channels depends on the type of interaction. A nuclear recoil deposits a different ratio of energies in the three channels compared to electron recoils. In this way, the readout of two channels provides a strong tool to distinguish between the expected signal and the electromagnetic backgrounds. The following sections give examples of experiments that combine the three channels.

Scintillation-Ionisation

Examples of experiments using the two-channel scintillation-ionisation readout are the liquid noble gas experiments LUX (large underground xenon experiment)[31], PandaX (particle and astrophysical xenon detector)[32] and XENON [33, 34] which all use xenon as target material operated in dual-phase time projection chambers. An interaction in the liquid xenon produces prompt scintillation light (prompt signal)and ionises electrons that drift towards the gaseous xenon, producing electroluminescence (delayed signal). Combining both signals allows a position reconstruction for defining a fiducial volume and particle discrimination due to the two-channel readout. These experiments are usually sensitive to higher mass dark matter as they can scale their detector mass relatively easily but have thresholds $\mathcal{O}(1\,\mathrm{keV})$.

Phonon-Ionsiation

Two examples for the phonon-ionisation readout are the EDELWEISS (expérience pour detecter les WIMPs en site souterrain)[35] experiment and SuperCDMS (Super Cryogenic Dark Matter Search)[36]. Both are operating semiconductor crystals made from germanium or silicon. An interaction in the crystal creates phonons which are detected by a sensitive thermometer. In addition, the reaction creates electron-hole pairs, which are collected by electrodes covering the crystal surface. This way, electron recoils can be distinguished from nuclear recoils and surface backgrounds can be discriminated.

Phonon-Scintillation

Another possibility is the readout of phonons and scintillation. This method is used by CRESST (cryogenic rare event searches with superconducting thermometers) [37] and COSINUS (cryogenic observatory for signals seen in next-generation

underground searches)[38]. They are operating scintillating target crystals made from $CaWO_4$ and NaI as cryogenic calorimeters. An interaction in the crystal creates phonons which are detected by sensitive thermometers and scintillation light detected by cryogenic light detectors. This two-channel readout also allows for distinguishing nuclear recoils from electron recoils.
Phonon-ionisation and phonon-scintillation techniques cannot be scaled up easily in mass like the liquid noble gas experiments. However, they reach thresholds $\mathcal{O}$(10-100 eV), making them sensitive to direct DM searches down to masses of 0.1 $\mathrm{GeV/c^2}$. This work focuses on the CRESST experiment described in more detail in chapter 2.

Chapter 2

The CRESST Experiment

This chapter introduces the CRESST (Cryogenic Rare Event Search with Superconducting Thermometers) experiment [37], located at the Laboratori Nazionali del Gran Sasso (LNGS) in Italy. It is shielded by a water-equivalent overburden of 3600 m [39]. CRESST aims to directly detect DM particles via their elastic scattering off target nuclei in scintillating $CaWO_4$ crystals. The experimental setup is described in section 2.1, followed by a description of the working principle of the detectors in section 2.2. The results of CRESST-III phase one, published in 2019, are presented in section 2.3. A study of the sensitivity limiting factors, performed in the scope of this thesis, is discussed in section 2.4. Afterwards, the current status of CRESST is discussed, and an overview of the detector modules, assembled in the context of this work, is given in section 2.5. A novel idea for the sensitivity enhancement of $CaWO_4$ crystals for the search for spin-dependent DM is explained in section 2.6.

2.1 Experimental Setup

The experimental setup of CRESST consists of the detector modules, surrounded by several active and passive shielding layers to reduce background. A cryostat cools down the modules. A sketch of the different parts of the setup is shown in figure 2.1.

The expected count rate for DM particles is less than 0.1 counts per kg and day [30]. Hence, it is crucial to reduce the background seen by the detectors as much as possible. The underground location of LNGS with its 3600 m. w. e. shields the experiment from most components of the cosmic radiation and reduces the muon flux to roughly $3 \cdot 10^{-4}/\mathrm{m}^2/\mathrm{s}$ [40]. To veto the remaining muons passing the experimental setup, a muon veto consisting of plastic scintillator panels is installed (indicated in dark blue in figure 2.1).

These muons can also produce fast neutrons (energies $\mathcal{O}(\mathrm{GeV})$) when interacting in the surrounding rock and other materials. Neutrons with energies $\mathcal{O}(\mathrm{MeV})$ can be produced in nuclear reactions. Both types of neutrons represent a dangerous background source as interactions with the detector modules show the same experimental

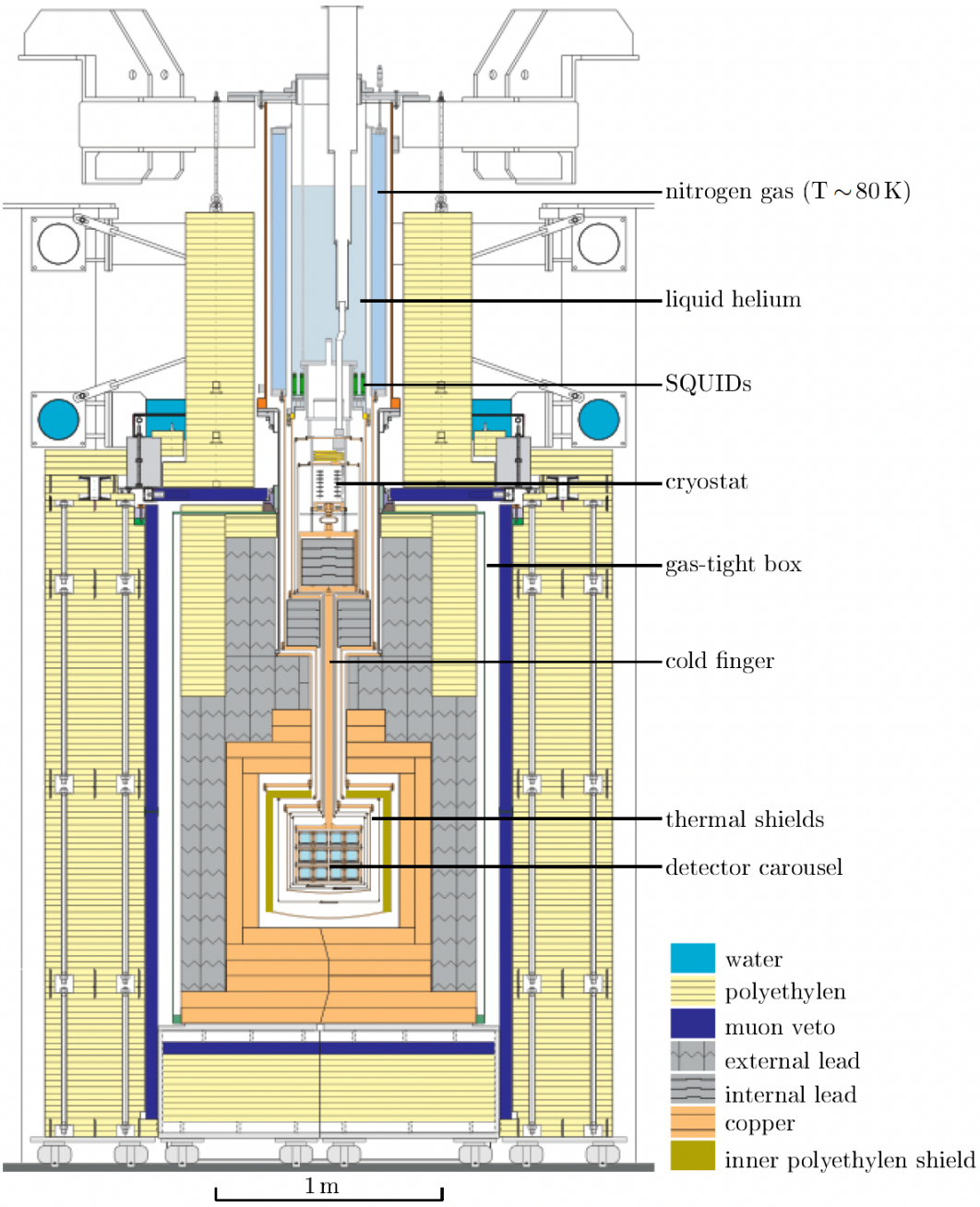

Figure 2.1: Schematic drawing of the CRESST setup located deep underground at LNGS. The heart of the experiment is the detector carousel hosting the DM detectors. It is connected to the cryostat, supplying a base temperature of <10 mK via a cold finger made from copper. To shield the carousel from external radiation, it is surrounded by an inner polyethylene shield (green), radiopure copper (orange), lead (grey), a muon veto (blue) and an outer polyethylene shield (yellow). In addition, it is surrounded by a radon box which is constantly flushed with nitrogen gas to avoid radon contact with any part of the experiment.

signature as expected from the interactions of DM particles with the detectors. A neutron flux of $10^{-6}/\mathrm{cm}^2/\mathrm{s}$ near the CRESST experiment was measured in [41]. To shield from these muons, two polyethylen shieldings were added around the setup (yellow) and in the inner detector box (green) to moderate muons produced outside of the experiment and in the inner shieldings to energies $\mathcal{O}(\mathrm{meV})$. To avoid radon from adsorbing to materials in the vicinity of the detectors, a gas-tight box is flushed with nitrogen gas. To shield the detectors from remaining electrons and γ-radiation, a layer of lead (grey) and radiopure copper (orange), which shields against the decay from ^{210}Pb, surrounds the detectors. The detectors are situated in the carousel located in the heart of the experiment. The whole lower part of the setup is located in a clean room.

The detector modules are operated at cryogenic temperatures of $\mathcal{O}(10\,\mathrm{mK})$. To reach this temperature, they are cooled down by a commercial ^{3}He/^{4}He dilution refrigerator or cryostat. The working principle of such a cryostat is described in section 9.1. As the cryostat is not made from radiopure materials, it would introduce unwanted backgrounds and has to be shielded from the detectors. This is achieved by installing lead bricks below the cryostat but well above the detectors. In this way, no line of sight is present between the cryostat and the detectors. A thermal link from the coldest part of the cryostat to the detectors is provided by a radiopure copper cold finger of 1.5 m in length. To reduce the impact of heat radiation, the detector carousel is enclosed by several heat shields of different temperature stages, which are coupled thermally to different temperature stages of the cryostat.

To reduce mechanical vibrations that would warm up the detectors, the cryostat rests on an air-damped construction, and the detector carousel is mounted on a spring-loaded support. Each detector is connected to the cold finger by dedicated thermal links. Electromagnetic interference is reduced by a Faraday cage enclosing the whole setup. Magnetic coils are mounted around the radon box to compensate for magnetic field changes influencing the detector operation.

2.2 Cryogenic Detector Principle

This section gives a short introduction to the cryogenic detection principle exploited by CRESST, followed by an overview of the signal readout in 2.2.1, the detector stabilisation in 2.2.2 and the data acquisition in 2.2.3. The standard CRESST-III module is described in section 2.2.4 followed by a description of the background discrimination of the two-channel readout in CRESST 2.2.5.

A cryogenic detector consists of an absorber cooled to temperatures $\mathcal{O}(10\,\mathrm{mK})$. At these temperatures, the crystal lattice vibrations are strongly reduced. Interactions of particles inside the crystal produce phonons that propagate through the crystal and induce a temperature rise read out by a sensitive thermometer. A dedicated heat link connects the detector to a thermal bath to cool it down again.

In a first approximation the temperature change ΔT can be described by the deposited energy ΔE and the heat capacity C of the detector [42]:

$$\Delta T = \frac{\Delta E}{C} \tag{2.1}$$

A small heat capacity is needed to increase the signal ΔT. As the heat capacity of a material is proportional to T^3 the lowest heat capacity is achieved at low temperatures, which is why the detectors are operated at $\mathcal{O}(10\,\mathrm{mK})$ [42].

2.2.1 Signal Readout

A very sensitive thermometer is needed to read out the absorber's temperature change ΔT. In the case of CRESST, so-called Transition-Edge-Sensors (TES) based on thin tungsten films are used. For its operation, the detector is heated to the temperature in which the tungsten film is just between its normal conducting phase and its superconducting phase, called the Working Point (WP) or operation point (see figure 2.2, left). In this transition region, a slight temperature increase (ΔT) results in a resistance change (ΔR) proportional to the energy deposition. This response becomes non-linear in the region where the curve approaches the normal conducting phase. Hence, only a defined energy region has a linear ΔT to ΔR relation. For energy depositions exceeding a specific temperature increase, the TES becomes completely normal conducting and no resistance change above the maximal resistance ΔR_{max}=R_{normal}-R_{WP} is measured.
The change in the TES resistance is read out by a Superconducting QUantum Interference Device (SQUID) as shown in figure 2.2 (right). A constant bias current is split between two branches, one containing the TES and the other containing the SQUID input coil and two shunt resistances. A variation in the TES resistance changes the ratio of the bias currents flowing through both branches. This causes a change in the magnetic field created by the SQUID input coil and hence a variation of the magnetic flux in the SQUID.
A SQUID comprises a superconducting loop broken by two insulating Josephson tunnel junctions. The magnetic flux through a superconducting ring has to be an integer multiple of the magnetic flux quantum $\Phi_0 = h/(2e)$. Without an external magnetic field, an input current sent through the SQUID splits equally through the two branches. The presence of an external magnetic field causes a ring current in the loop creating a voltage across the junctions. The voltage drop across the SQUID is periodic in magnetic flux with a period of one magnetic flux quantum.
A feedback coil is used to cancel the flux signal in the SQUID, keeping the voltage constant and linearising the output of the SQUID. It holds the SQUID at a fixed working point, so the magnetic flux through the SQUID is kept constant. The output signal of the SQUID is proportional to the feedback current necessary to keep the SQUID at its working point and is hence proportional to the magnetic change. If the magnetic field rises faster than the feedback loop can follow, the number of magnetic flux quanta can change in the SQUID (the system "loses some flux quanta"). After the input coil current returns to the original value, this results in a step change in the output voltage. This effect usually happens when highly energetic particles react within the target crystal.

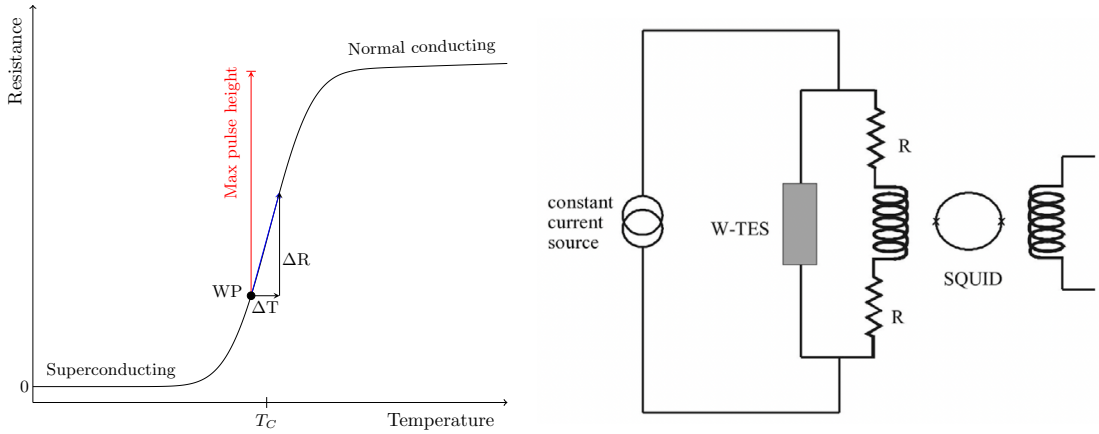

Figure 2.2: Left: schematic drawing of a TES transition from its superconducting to normal conducting phase in dependence of its temperature. The TES is stabilised near the critical temperature of the TES T_C. A small increase in temperature ΔT in the order of μK leads to a resistance change $\mathcal{O}(\,\mathrm{m}\Omega)$. The maximum resistance change that can be measured by it, is the difference in the resistance to the completely normal conducting phase. This also defines the maximum measurable pulse height of an event. The picture was taken from [23]. Right: A simplified sketch of the SQUID readout circuit used in CRESST. A current is split between two branches, one containing the TES, the other containing two shunt resistances and the SQUID input coil. A change in resistance in the TES changes the current flowing through the SQUID input coil. This changes the magnetic flux in the SQUID actively reverted by the feedback coil on the right. The feedback coil's reaction produces a measurable signal (see text for details). Schematic drawing taken from [39].

For a standard particle event with energies $\mathcal{O}(1\,\mathrm{keV})$, the output produced by the SQUID is a pulse similar to the one shown in figure 2.3. The interaction with the target materials produces phonons which heat the detector. The TES has a relatively fast resistance change which is visible by the sharp voltage increase in the SQUID. Afterwards, the detector slowly cools down again, which reduces the resistance of the TES and is represented by the decrease in the SQUID output voltage.

2.2.2 Detector Stabilisation

A constant heater current is applied to a dedicated heater produced next to the TES on the crystal to keep the detector in its WP. As operation conditions change over time, this heater current has to be adjusted regularly. Artificial heat pulses with a pulse shape similar to particle interactions are routinely injected via the same heater. Two classes of these pulses are sent, control pulses and test pulses. The control pulses are designed to have enough energy to drive the TES into its normal conducting phase. As the maximum resistance change measurable with the TES depends on the resistance difference between the normal conducting resistance

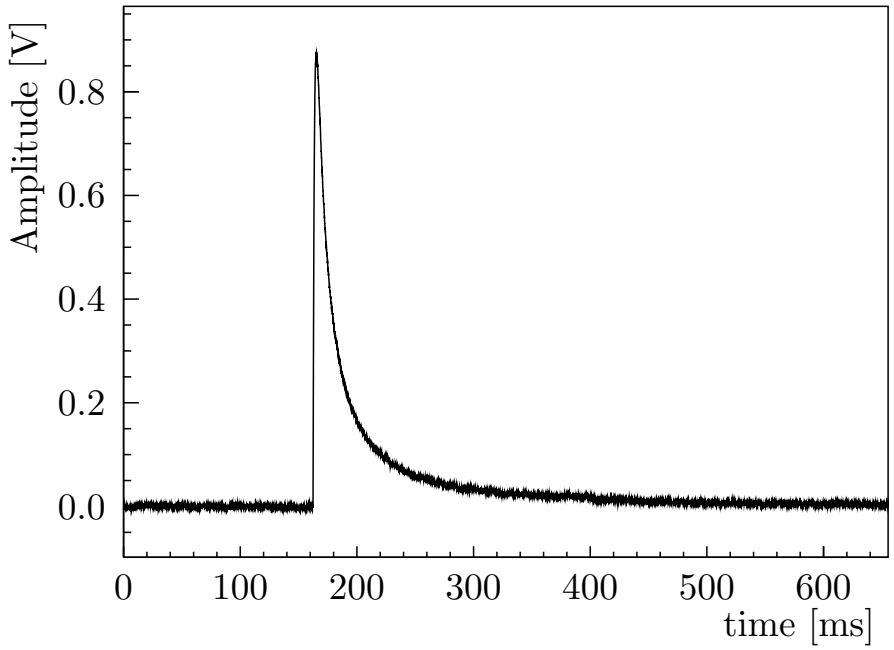

Figure 2.3: Typical SQUID response for a particle event in the absorber crystal. The event happens at t =160 ms.

and the WP resistance, the measured pulse height of the control pulses can be used to check if the TES is in its WP. If the TES is not at its WP, a PID controller adjusts the flat heater value accordingly, stabilising the TES WP. The test pulses are heater pulses of several defined voltages which do not drive the TES into its normal conducting range. They are designed to map the response of the TES in its linear range and, more importantly, in the non-linear range in the top part of the transition. They are later used in the analysis to correct for time-dependent changes in the response of the TES to defined energy injections. They can be used to linearise the spectrum due to the non-linear behaviour of $\Delta R(\Delta T)$ in the higher part of the transition.

2.2.3 Data Acquisition

For the data taking, three primary circuits are used in CRESST. They are indicated in three different colours in figure 2.4.
The purple circuit supplies the TES and the SQUID input coil with a constant bias current which is split between the SQUID input coil and the TES branch depending on their current resistance ratio. A low-pass filter at 4K is used to reduce electrical noise.
On the left, in blue, the heater circuit is shown. It consists of two inputs which are summed up. The inputs are a digital-to-analogue converter (DAC) that provides

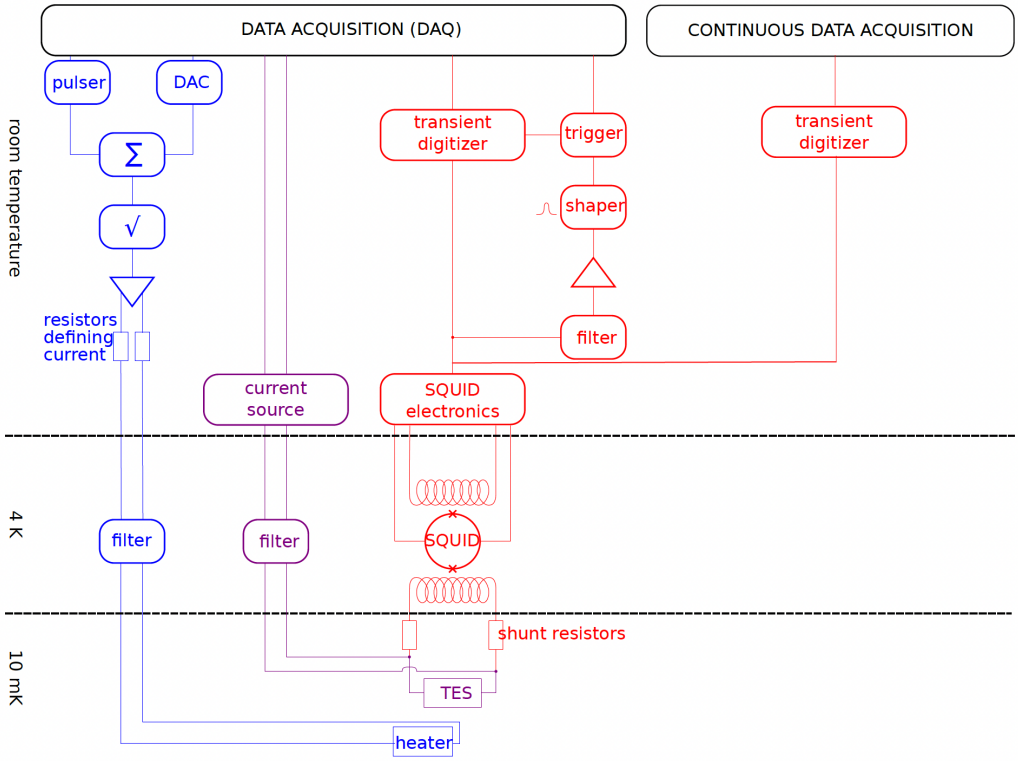

Figure 2.4: Schematic drawing of the electronics required to operate and read out a detector in CRESST. The three colours denote the three different circuits. The bias line is shown in purple, the heater system in blue and the SQUID readout and data acquisition in red. For details, see the text. Figure taken from [43]

the constant heater current for stabilising the TES at its WP and a pulser which is an arbitrary waveform generator responsible for sending test and control pulses of various heights to the detector heaters. Both signals are summed up and sent through a square rooter due to the quadratic dependence of the total heating powder from the voltage U. This helps to linearise the power input so that test pulses sent to the detector do not depend on the DAC.

$$P = (\sqrt{U_{DAC} + U_{pulser}}^{2} \cdot R^{-1}) = P_{DAC} + P_{pulser}. \tag{2.2}$$

The readout circuit is shown in red. It consists of the SQUID electronics located at a temperature of 4 K at which the SQUID coil is superconducting. The signal is then split into three branches. Two are connected to the conventional Data ACquisition (DAQ), and the other to the continuous DAQ. In the conventional DAQ, the first branch is connected to the digitiser. The second branch passes a filter, amplifier, shaper and trigger module. Only if the signal is above a certain threshold the trigger unit sends a signal to the digitiser, which saves the pulse together with a pre-defined pre-trigger range giving information about, e.g. the baseline level before a signal was detected. Afterwards, the trigger is blocked for a certain period.
Since 2016 the data is additionally read out with a continuous DAQ meaning the

whole measurement time is digitised and saved to disc. For this, two digitisers are operated in parallel in a switching mode. One is recording while the other one is read out. By this, dead times are avoided, and the thresholds and window lengths can be chosen during the analysis and adapted to the specific needs. For details concerning the continuous DAQ, the reader is referred to [44]. Recording a continuous data stream allows applying optimised filter algorithms before triggering the data. This method is described in detail in section 5.1.

2.2.4 Detector Module

CRESST modules typically consist of two cryogenic detectors, the primary Phonon Detector (PD) made from scintillating 24 g $CaWO_4$ single crystals and a dedicated Light Detector (LD) made from Silicon On Sapphire (SOS). In this way, the phonon signal created by a particle interaction in the $CaWO_4$ crystal is read out, and additionally the scintillation light produced by the $CaWO_4$ crystal is detected by the LD. The detectors are held by three sticks each, usually made from $CaWO_4$ and are enclosed by a copper housing. Each detector is equipped with a TES and stabilised and read out by the electronics described above. Both detectors are surrounded by a scintillating and reflecting foil to enhance the light collection and veto surface events. The TES is connected to the read-out through wire bonding. A schematic drawing of the standard CRESST detector is shown in figure 2.5 (left), and a picture of one of the modules (TUM93A) currently being operated in the ongoing CRESST data-taking campaign is shown on the right. More details on the TUM93A module are given in chapter 4.

2.2.5 Background Discrimination

The simultaneous readout of the phonon and the light channel enables event discrimination on an event-by-event basis. This is due to the scintillation light produced by the $CaWO_4$ crystals. Roughly 2%-3% of the total energy is converted to scintillation light, whereas the rest of the energy is measured by the main absorber, the PD. The fraction of the energy converted into scintillation light strongly depends on the type of interaction. Events which react via the electromagnetic force and hence with the electron shell of the atoms produce more light compared to interactions of particles which perform recoils on the nuclei of the target, like neutrons or DM particles. Figure 2.6 (left) shows this behaviour for the detected light vs phonon energy on the left. The detected energy by the LD is denoted with "ee" for electron-equivalent, which means the energy is calibrated using the detected energy for an electron event in the PD. The electromagnetic events are located in the e^-/γ-band shown in red, α-decays are situated in a band shown in orange and nuclear recoils on Oxygen (O), Calcium (Ca) and Tungsten (W) are shown in green bands.
Usually, this band behaviour is described using the parameter light yield (LY)

$$LY = \frac{E_{LD}}{E_{PD}} \tag{2.3}$$

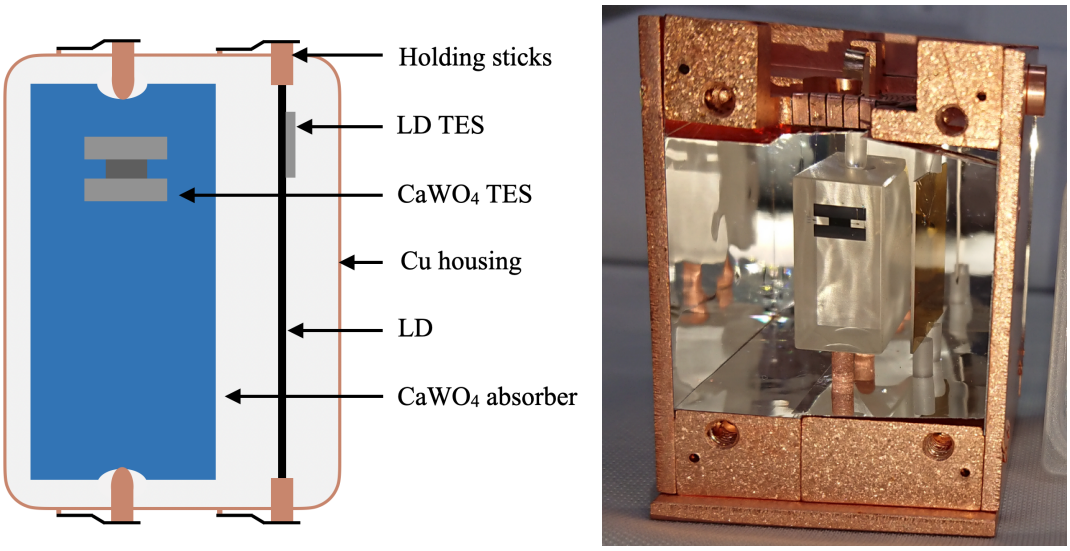

Figure 2.5: Left: Schematic drawing of the main components of the standard CRESST-III module (not to scale). The $CaWO_4$ absorber (blue) is equipped with a TES and held by three holding sticks. The light detector (black) is facing the main detector and is also held by three sticks. Right: Picture of one of the CRESST modules (TUM93A) currently operated in the ongoing CRESST data-taking campaign with the translucent $CaWO_4$ crystal in the middle and the orange-coloured light detector on the right.

Which is normalised to one for the light created by an ^{55}Fe event in the $CaWO_4$ crystal. The LY is plotted against the energy detected in the PD as shown in figure 2.6 (right). In this way, a region of interest (ROI) for the search for DM can be defined. An example of an ROI is shown in light green. Depending on the performance of the PD and the LD, this ROI can be adapted accordingly.

The background discrimination power becomes weaker for lower energies as the light produced by the $CaWO_4$ crystal becomes less. Hence, leakage from the e^-/γ-band to the nuclear recoil band is expected. Reducing the e^-/γ-background is crucial to minimise this as much as possible. Therefore, CRESST focuses on only using the cleanest available materials near the detector and reducing the intrinsic contaminations in the $CaWO_4$ crystals as much as possible. For this reason, the $CaWO_4$ crystals have been grown in-house at Technische Universität München (TUM) for many years. This improved the background introduced by intrinsic contamination compared to commercially purchased $CaWO_4$ crystals [45, 46]. CRESST wants to improve the radiopurity further to reduce the e^-/γ background. The radiopurity improvement of the $CaWO_4$ crystals is a major topic in this work and is discussed in chapters 3, 4, 6 and 9.

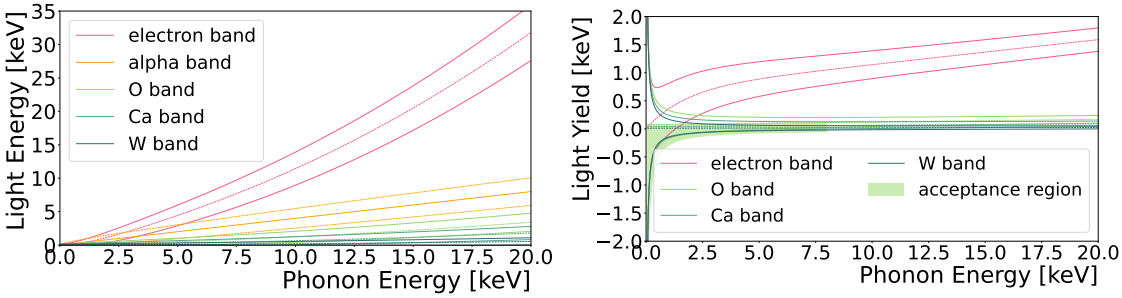

Figure 2.6: Left: Schematic drawing of the energy-dependent different relative light outputs for electromagnetic interactions (red, e^-/γ-band), α-decays (orange, α-band) and nuclear recoils on Oxygen, Calcium and Tungsten (shades of green)as a function of the energy detected in the phonon detector. Right: Instead of the light energy, the LY is plotted as a function of the detected phonon energy for the e^-/γ-band and the nuclear recoil bands. The LY of the e^-/γ-band is normalised to one at 5.9 keV. At lower energies, the bands overlap due to the finite resolution of the LD. The green shaded area indicates a possible ROIor acceptance region for DM searches. This ROI depends on the energy resolution of both the PD and the LD.

2.3 Results of CRESST-III phase 1

In the first physics run of CRESST-III phase 1, ten detector modules were operated between October 2016 and January 2018. Eight out of ten $CaWO_4$ crystals were supplied by TUM, and the other two were cut from commercially purchased crystals. Of the ten detectors, five (all made from the crystals TUM56 and TUM73) reached the detector threshold design goal of 100 eV, four of them even exceeding it. The best detector, DetA (crystal TUM56), reached a threshold as low as 30.1 eV [37].
A DM analysis was performed for the detectors DetA (TUM56) [43, 48], DetB (TUM73) [43], DetE (TUM73) [43] and DetJ (TUM56) [43] and the results for DetA are published in [37].
For the DetA DM analysis, an exposure of 5.689 kg d was analysed. The resulting LY plot is shown in figure 2.7 (left) with the acceptance region highlighted in yellow. The resulting energy spectrum is shown in figure 2.7 (right), with all events in grey and the events in the acceptance region highlighted in red. In the previously inaccessible energy range below 200 eV an exponentially rising excess above the flat background level is observed. This excess was also observed in the modules DetB, DetE and DetJ; due to different shapes and rates, DM as origin could be excluded. Nonetheless, the presence of this background limits the sensitivity of CRESST.
From this spectrum shown in figure 2.7, DM exclusion limits are derived using the Yellin optimum interval algorithm described in section 7.2.4. For the calculations a standard halo model with density $\rho_{DM} = 0.3\,(\mathrm{GeV/c^2})/\mathrm{cm^3}$, an asymptotic velocity $v_a = 220\,\mathrm{km/s}$ and an escape velocity of $v_{esc} = 544\,\mathrm{km/s}$ is assumed. The resulting DM exclusion limits extracted from this measurement are shown in figure 2.8 for the case of elastic spin-independent DM nucleus scattering and in figure 2.9 for spin-

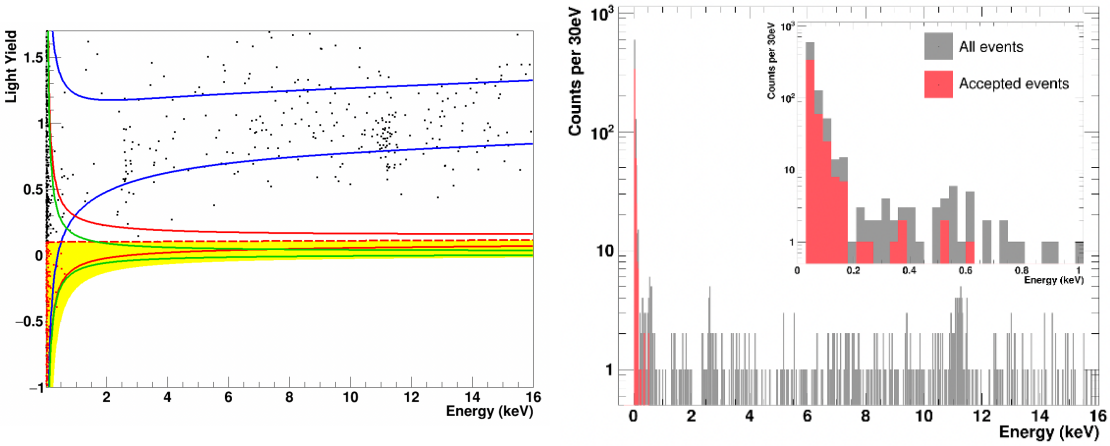

Figure 2.7: Left: Light yield versus energy plot for the analysed data set of DetA in CRESST-III phase 1. The coloured bands represent the 90 % upper and lower boundaries of the e^-/γ-band (blue) and nuclear recoil bands (red and green). The yellow region denotes the ROI, which spans the lower half of the oxygen band down to 99.5 % lower boundary of the oxygen band. Figure taken from [37]. Right: Energy spectrum of all events shown in the light yield plot on the left in grey. Events in the ROI are highlighted in red. Below 200 eV, a sharp rise in events towards the threshold is observed. Figure is taken from [47].

dependent neutron-only interactions with the isotope ^{17}O in $CaWO_4$. In both cases, the DM particle nucleon cross-section is plotted against the DM particle mass. The CRESST 2019 exclusion limit is shown in solid red compared to other measurements (for references, see figure captions). An exclusion line drawn by an experiment excludes all cross-section mass pairs above this line with a 90 % confidence level. The plots show the status of the DM search in 2019 when the CRESST-III DM exclusion limits were published. At this time, CRESST was able to improve the sensitivity to low mass DM by a factor of three down to 0.16 GeV/c^2 and improved existing exclusion limits at 0.5 GeV/c^2 by a factor of 6 compared to NEWS-G (dashed pink) the formerly most sensitive experiment in this mass region and by a factor of 30 compared to the CRESST-II exclusion limits (dashed red). In the case of spin-dependent DM searches, CRESST improved the exclusion limit with only 0.46 g d of exposure and started to explore a new parameter space for neutron-only interactions in the DM particle mass range of 0.16 GeV/c^2 to 1.5 GeV/c^2 [37].

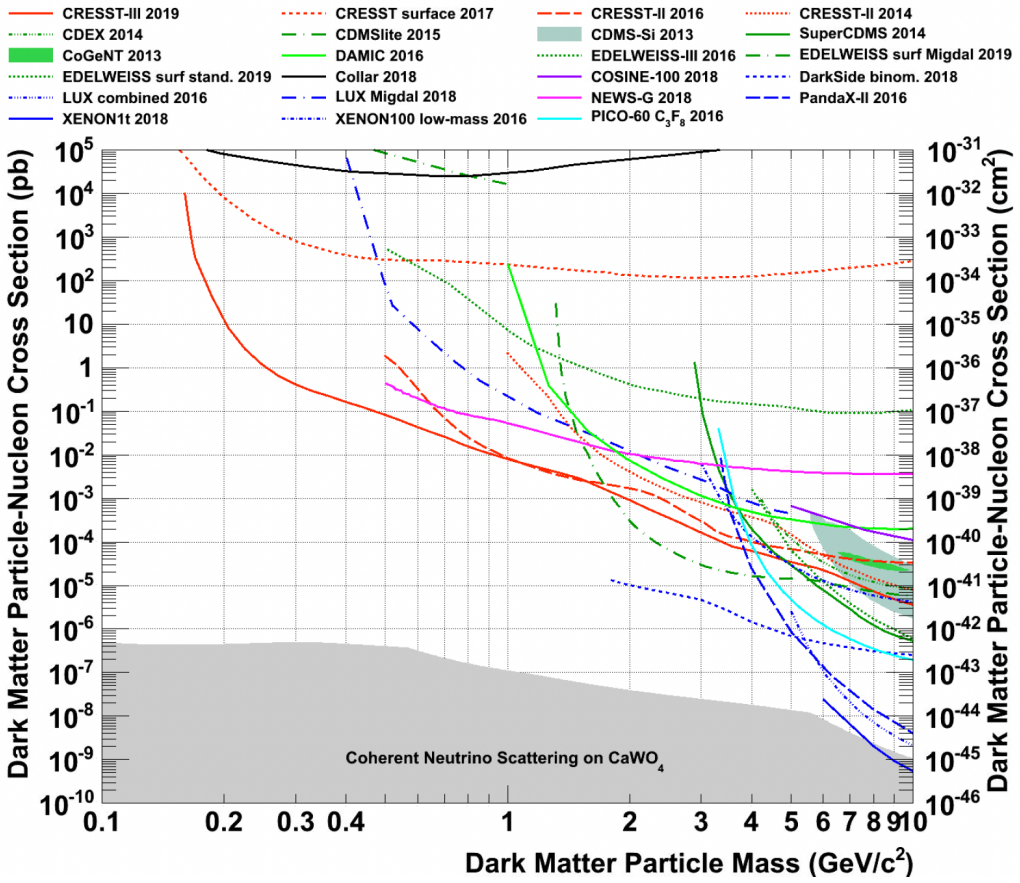

Figure 2.8: DM exclusion limit plot as published by CRESST in 2019 for the spin-independent direct search. The DM particle-nucleon cross-section is plotted against the DM particle mass. An exclusion limit excludes all cross-section mass pairs above this line with 90 % confidence level. The CRESST-III exclusion limit is shown in solid red, former CRESST-II exclusion limits and a CRESST surface run in dashed red [49, 50, 51]. Exclusion limits obtained by solid-state detectors are shown in green for CDEX [52], CDMSlite [53], DAMIC [54], EDELWEISS [35, 55], SuperCDMS [56] and positive evidence islands are shown for CDMS-Si [56] and CoGeNT [57]. The results from liquid noble gas experiments are shown in blue for DarkSide [58], LUX [31, 59], Panda-X [32], Xenon100 [33] and Xenon1t [34]. Other experiments with various target materials and detection techniques are COSINE-100 (NaI) [60], Collar (H) [61], NEWS-Ge (Ne + CH_4) [62] and PICO (C_3F_8) [63]. Figure is taken from [37].

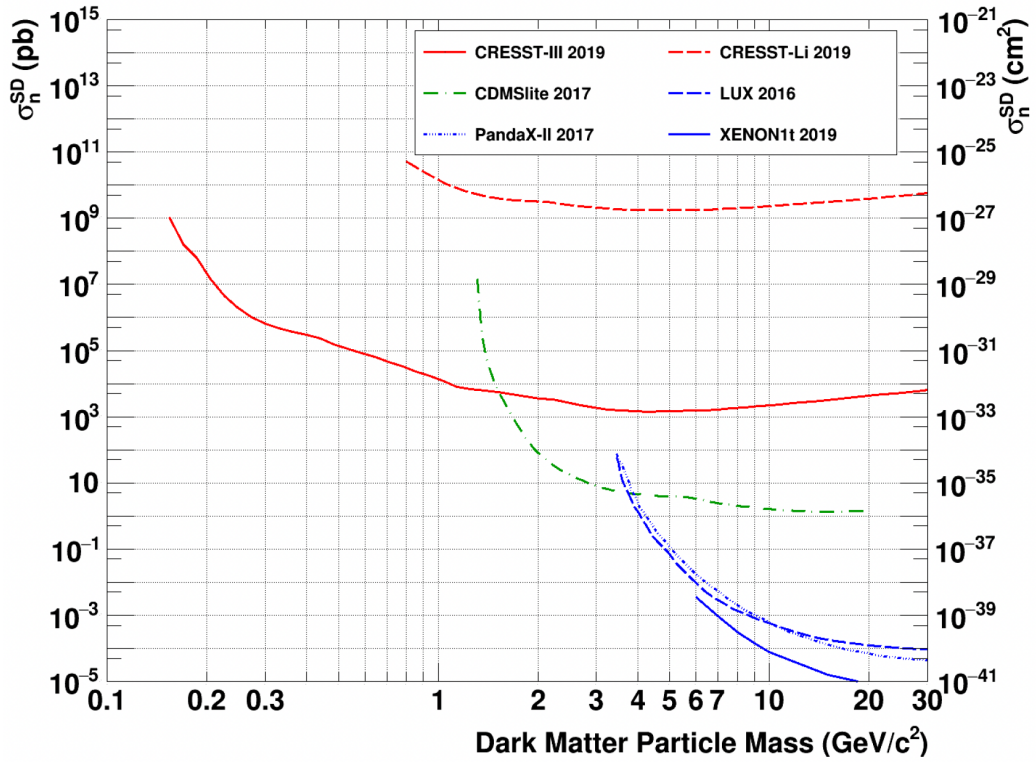

Figure 2.9: DM exclusion limit plot as published by CRESST in 2019 for the search of spin-dependent DM search. The CRESST-III limit is shown in solid red, an above-ground CRESST run with a crystal containing Li in dashed red [64]. In addition, exclusion limits from CDMSlite [65], LUX [66], PandaX-II. [67] and XENON1t. [68] are shown. Figure is taken from [37].

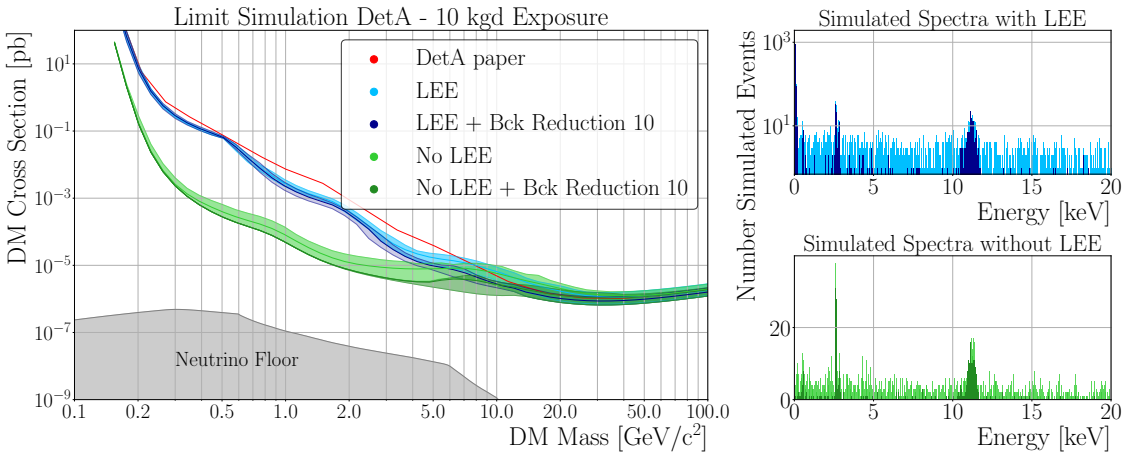

Figure 2.10: Limit projections (left) and simulated spectra (right) for an exposure of 10 kgd for DetA. The published DetA exclusion limit is plotted in red (5.7 kgd exposure). The projection for 10 kgd containing the LEE is shown in light blue and with a reduction of the background level by a factor of 10 in dark blue. The light green curve represents the DetA projection in case of no LEE, and the dark green curve with an additional background reduction by a factor of 10. The bands around the exclusion limit represent a 95% C.L..

2.4 Sensitivity Limiting Factors

CRESST-III explored a new parameter space in 2019 and set new exclusion limits on the DM particle-nucleon elastic scattering cross section below 0.5 GeV/c^2 by lowering the detector thresholds down to 30.1 eV and improving the quality of the target materials in terms of radiopurity by using $CaWO_4$ crystals produced at TUM instead of commercially available crystals. In the previously inaccessible energy range below 200 eV an unexpected excess of events was observed in all detectors. In addition, the discrimination power of the 2-channel readout is low at such low energies. Hence, background from the e^-/γ-band leaks into the ROI.

To further improve the sensitivity for the search of low mass DM, these two main limiting factors, the Low-Energy Excess (LEE) and the radioactive background, must be reduced. To investigate the influence of these two factors on CRESST's DM sensitivity, exclusion limit projections for modified energy spectra of DetA are calculated. Figure 2.10 shows an exclusion limit projection for DetA with an exposure of 10 kgd and the measured DetA spectrum (light blue), the same spectrum with a flat background reduced by a factor of 10 (dark blue), a projection with the measured background level in which the LEE was removed (light green) and a combination of both effects (dark green) [1]. The spectra used for the simulations are shown on the right side of figure 2.10. For the reduction of the flat background, the cosmic activation lines at ~0,5 keV, 2.8 keV and 11.2 keV were not reduced as they originate from, e.g. the transportation of the crystal to LNGS and can hardly

[1] The *limitless* software used for these projections is developed by L. Einfalt [69].

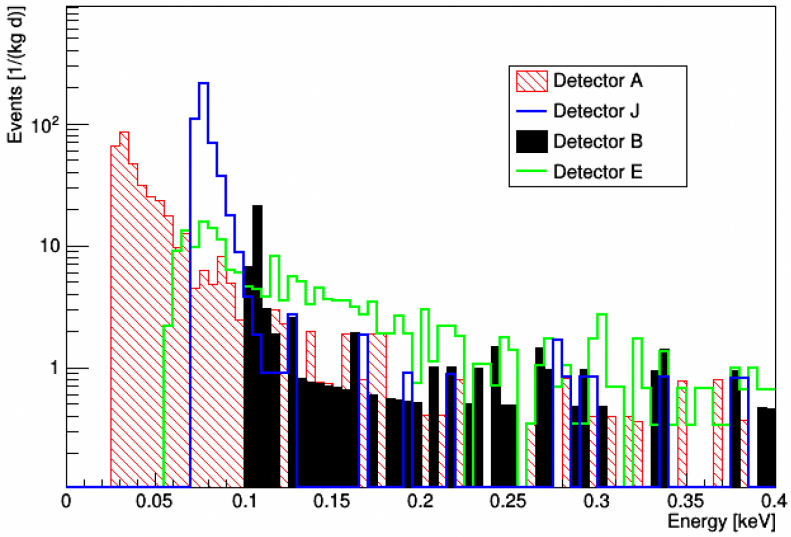

Figure 2.11: Comparison of the low energy excess observed in the detectors A, B, J and E in CRESST-III phase 1. The spectral shape and rate of the excess differ between different modules. Hence, a DM signal could be excluded. Figure and analysis from [43].

be reduced. The projections show that the LEE currently represents the main limiting factor. Reducing the flat background level in the presence of the LEE still improves the exclusion limit to a much smaller extent than eliminating the LEE. In the following, the source of the LEE and the impact of both the LEE and the flat background level on the CRESST sensitivity are investigated in more detail.

2.4.1 Low-Energy Excess

The LEE was observed for all four detectors reaching an energy threshold below 100 eV in the first physics run of CRESST-III phase one. A comparison of the spectra of the detectors A, J, B and E are shown in figure 2.11 for LY values of ± 15, i.e. including also the e^-/γ-band of the detectors. The LEE is different in all four detector modules concerning its starting energy, rate and shape. Hence, a common particle-like source like DM interactions could be excluded. Nonetheless, the background represents a major limiting factor on the CRESST sensitivity to DM interactions.

To quantify this impact of the LEE on the sensitivity of CRESST, simulations with several LEE levels were performed based on the DetA data for several exposures. An exclusion limit projection plot is exemplarily shown in figure 2.12 for an exposure of 10 kgd with the dark blue exclusion limit showing the projection for the full LEE, the medium blue for a reduction of the LEE by a factor of 10 and the light blue for a factor of 100. The exclusion limit with no LEE present is shown in green. The corresponding energy spectra created for the simulation are shown on the right. An

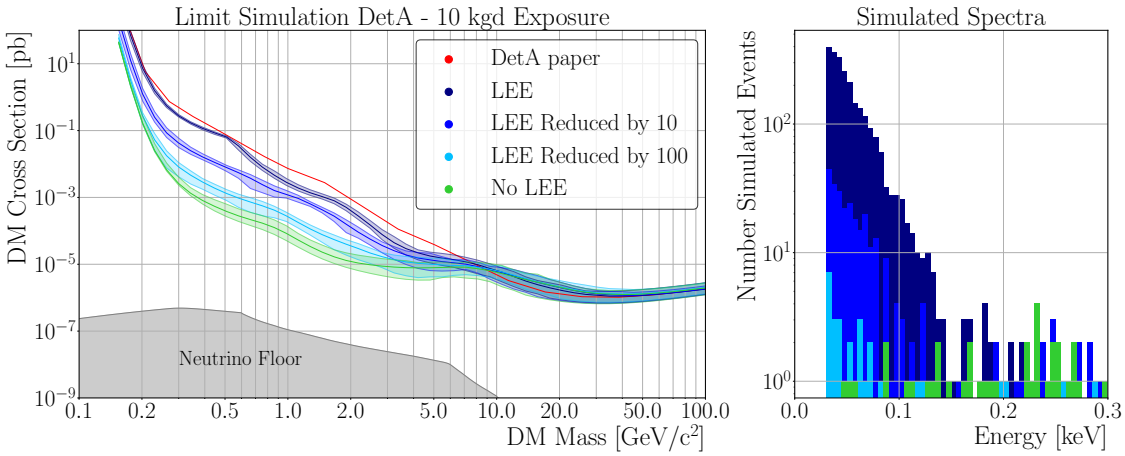

Figure 2.12: Exclusion limit projections for DetA with an exposure of 10 kgd and different LEE levels. The projection for the full background spectrum, as measured by DetA, is shown in dark blue. The LEE was reduced by a factor of 10 for the exclusion limit shown in medium blue, by a factor of 100 for light blue and completely removed for the exclusion limit shown in green. The bands correspond to a 95% C.L.. The simulated spectra are shown on the right, zoomed in to the low energy region.

apparent sensitivity increase with the reduction of the LEE is visible by up to two orders of magnitude.

To study this effect in more detail, an exposure-dependent sensitivity simulation was performed for these different LEE levels at a DM mass of ∼0.5 GeV, at which CRESST sets leading exclusion limits. Figure 2.13 shows the DM cross-section sensitivity as a function of exposure and LEE levels. The black dashed line represents the expected exclusion limit improvement in the case of background-free data taking. The green curve shows the case of no LEE. A near background-free measurement is possible with the DetA flat background level up to an exposure of 100 kgd, from there, the flat background limits it. In the case of the three different LEE fractions, the data in the ROI is not background free even for exposures $\mathcal{O}$(1 kgd). Reducing the LEE by one order of magnitude improves the exclusion limit by nearly an order of magnitude. All exclusion limits for the cases with the LEE present are background limited, as shown by the deviation of the curves from the black dashed line. Above 10 kgd exposure, no significant improvement in the sensitivity is expected even in the case of a LEE reduced by a factor of 100. This underlines the importance of understanding the source of the LEE to remove it and increase the sensitivity of CRESST towards smaller DM cross-sections.

Several other collaborations searching for DM and Coherent Elastic neutrino-Nucleus Scattering (CEvNS) reported a similar LEE feature detected in their latest data-taking campaigns reaching thresholds in the sub-keV energy range. Even though it is not clear that the origin of these excesses is the same, it is nonetheless the main sensitivity limiting factor for all these experiments. Hence, the whole field of

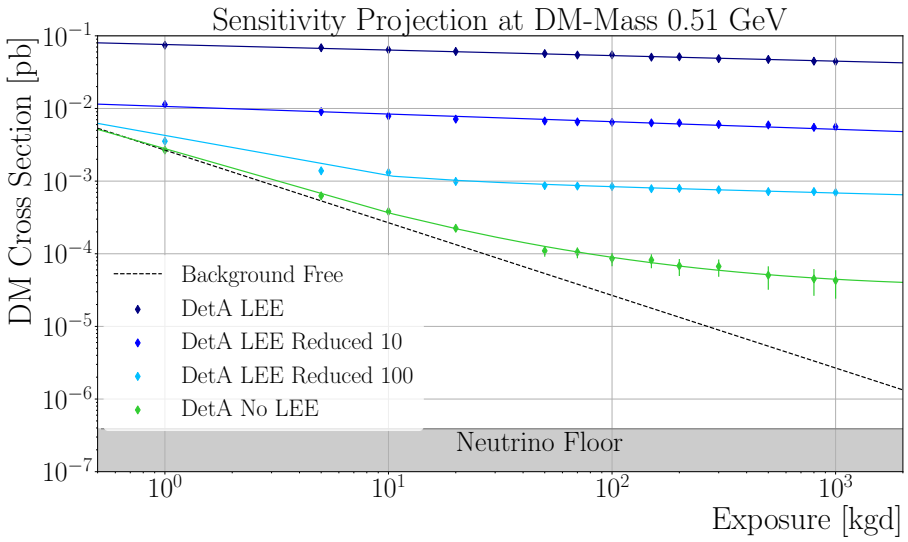

Figure 2.13: Sensitivity projections for a DM mass of 0.51 GeV showing the cross-section as a function of exposure and LEE fraction. The simulated sensitivity for the full LEE is shown in dark blue, reduced by a factor of 10 in medium blue and by a factor of 100 in light blue. In addition, the sensitivity for the case of a LEE-free measurement is shown in green. The black dashed line represents the sensitivity improvement with exposure in the case of a background-free measurement.

low mass DM search and CEvNS tries to understand its origin. In June 2021, the EXCESS workshop took place to discuss and compare the obtained spectra. In this way, a broad overview of also non-published R&D data was presented, providing insight into common observations. The participating collaborations were CONNIE [70], CRESST [37], DAMIC [71], EDELWEISS [72, 73], MINER [74], NEWS-G [62], NUCLEUS [75], RICOCHET[76], SENSEI [77] and SuperCDMS [36, 78]. The observations were summarised in a combined paper [47].

From the discussions in the workshop, several hypotheses for the origin of the LEE were concluded, which fall mainly into two groups: Group one includes sources related to particle interactions within the target or the surrounding materials like luminescence, scintillation, surface backgrounds, neutrons or Cherenkov interactions [47]. The other group includes stress induced by the detector holder, the TES-detector surface or intrinsic stress. To test these hypotheses and narrow down the number of possibilities, CRESST is currently carrying out dedicated R&D campaigns.

This includes a modification of several detector modules, which was carried out in the scope of this work and is described in 2.5. To test the hypothesis that the origin of the LEE is related to intrinsic stress, which relaxes at low operating temperatures, the growth process of the TUM $CaWO_4$ crystals is optimised in the scope of this work (described in section 3.3). Three detector crystals from the $CaWO_4$ ingot TUM93 grown with reduced intrinsic stress were mounted in CRESST, and a LEE analysis was performed on the module TUM93A presented in chapter 7. The results

are compared to the LEE measured in the module DetE from the first data-taking campaign of CRESST-III phase 1.

2.4.2 Radioactive Impurities in $CaWO_4$ Detector Crystals

As briefly mentioned in 2.2.5, the e^-/γ background can leak in the ROI at the lowest energies where the e^-/γ-band overlaps with the nuclear recoil bands. As part of the e^-/γ-background originates from intrinsic crystal impurities, these represent a limiting factor for the DM search, causing events in the ROI and lowering the sensitivity of the experiment. To reduce this background, the $CaWO_4$ crystals are grown in-house at TUM. The resulting crystals feature a factor 2-10 reduction of intrinsic crystal impurities when compared to commercially purchased $CaWO_4$ crystals which show a wide spread in impurities.
The module DetA consisted of the TUM-produced crystal TUM56. To study the impact of a reduction of the flat background on the sensitivity of CRESST, the sensitivity simulations as already performed to study the LEE were repeated for different background levels again for a DM mass of $0.5\,\mathrm{GeV/c^2}$ to investigate the region in which CRESST set leading exclusion limits in 2019. For this, the flat background level, as measured, reduced by a factor of 10 and by a factor of 100, was simulated for different LEE levels. The simulated exclusion limits are collected in appendix A. The expected sensitivity to a DM cross-section depending on the exposure and background level of the crystal is shown in four plots in figure 2.14. Pictured is the simulated sensitivity with the standard background level (always dark blue), the background reduced by a factor of 10 (always light blue) and the background reduced by a factor of 100 (always in green). A similar plot for a higher DM mass is shown in figure A.4. The top left plot shows the case with no LEE. From there on, the LEE is added to the data: The top right plot shows the sensitivity with 1% of the DetA LEE added to the spectra, the bottom left with 10%, and the bottom right with the full LEE.
The sensitivity simulations for the cases with any fraction of the LEE present show that different background levels do not have an impact on the sensitivity at $0.5\,\mathrm{GeV/c^2}$ as the LEE dominates it entirely. In the LEE-free case, a difference in sensitivity is visible for the three different background levels. For a background reduction by a factor of 100, a background-free measurement is possible up to an exposure of $\sim$300 kgd. In case of a reduction by a factor of 10, this is possible up to an exposure of $\sim$30 kgd. For higher DM masses, the sensitivity is less affected by the LEE as differences in the radiopurity impact the sensitivity even for the LEE fully present. This is visible in figure A.4, which shows the sensitivity gain in the different cases for a DM mass of $4.8\,\mathrm{GeV/c^2}$. At this mass, reducing the flat background level always improves the sensitivity, however, the presence of the LEE still affects it. In the case of a LEE-free measurement with a reduced background by a factor of 100, a background-free measurement up to an exposure of 100 kgd would be possible.
The results show the importance of background reduction for higher exposures with CRESST. As CRESST plans to upgrade to 288 readout channels to increase the ex-

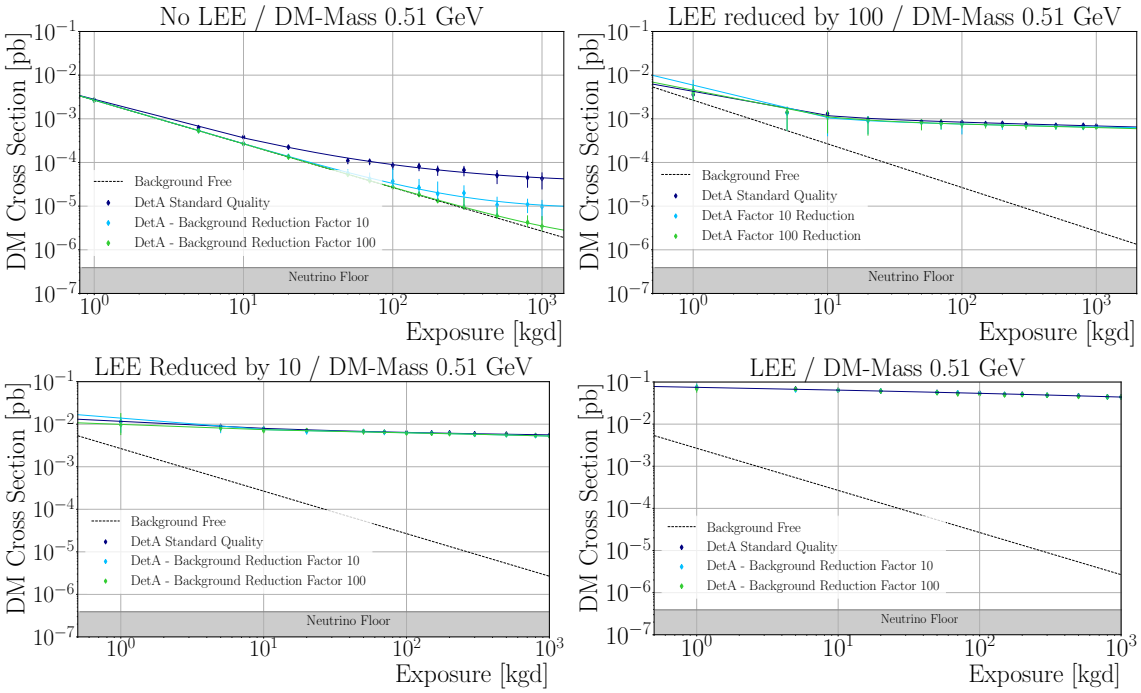

Figure 2.14: Sensitivity projections for a DM mass of 0.51 GeV showing the cross-section as a function of exposure and background level for different LEE fractions. The excluded cross-sections for the standard background level are shown in dark blue, reduced by a factor of 10 in light blue and by a factor of 100 in green. On the top left, the case with no LEE is shown, on the top right with 1% of the DetA LEE level, on the bottom left with 10% and on the bottom right with the full LEE. The black dashed line represents the sensitivity improvement in the case of a background-free measurement and is the same in all four plots.

posure to 1000 kgd, a background reduction is needed to provide a higher sensitivity towards lower DM cross-sections at all DM masses. The sensitivity can be increased at higher masses even with the LEE present. At lower DM masses only if the LEE can be eliminated. Hence, one goal of CRESST is to reduce the flat background level by at least a factor of 10.

This work focuses on reducing the intrinsic radiopurities in the TUM-produced $CaWO_4$ crystals via chemical purification to lower the overall background in the ROI.

The $CaWO_4$ crystal production, including the powder's chemical purification process, is described in chapter 3. The production of the crystal TUM93 grown from this purified powder, which features reduced intrinsic stress and enhanced radiopurity, is described in chapter 4. The results of the radiopurity analysis of the crystal TUM93 operated in CRESST are summarised in chapter 6. A new module developed to measure the radiopurity of TUM-grown crystals in the Munich shallow underground laboratory and an analysis of the radiopurity of a recrystallised crystal TUM81 with this module is presented in chapter 9.

2.5 Current Status of CRESST

The current data-taking campaign of CRESST-III targets both sensitivity-limiting backgrounds mentioned above. For an investigation of the LEE, the standard CRESST-III modules were modified as part of this dissertation. This includes a selection of different target materials, the modification of the detector holding and optical housing, and the introduction of a low-energy calibration source. To investigate the background reduction possible via chemical purification, three detector crystals cut from the crystal ingot TUM93, produced from chemically purified powder, are operated.

For the main detectors, $LiAlO_2$, Si, Al_2O_3, and $CaWO_4$ (TUM93 and commercially produced crystals) were selected. They have different hardness, mass, crystal lattices, intrinsic stress and surface area to give insight into the LEE dependence on these factors. TUM93 was produced with a focus on low intrinsic stress and high radiopurity to investigate the impact of these factors on the LEE and radioactive backgrounds. For some detectors, the standard $CaWO_4$ holding sticks of the main detectors were replaced mainly by softer, non-scintillating, Cu-sticks or bronze clamps to study effects from the point-like connections of the holding sticks. Additionally, the scintillating foil was removed in the Si, Al_2O_3 and commercial $CaWO_4$ modules. For the Si module, both the phonon and "light" detectors are made from

Module	PD	LD	Holding	Foil	Mass PD/LD (g)
Si-Double	Si	Si	Cu	No	9.3/0.35
	Si	Si	Cu	No	9.3/0.35
Sapp1	Al_2O_3	SOS	Cu	No	16/0.6
Sapp2	Al_2O_3	SOS	Cu	No	16/0.6
Sapp3	Al_2O_3	SOS	Cu	No	16/0.6
Li1	$LiAlO_2$	SOS	Cu	Yes	11/0.6
Li2	$LiAlO_2$	SOS	Cu	Yes	11/0.6
TUM93A	$CaWO_4$	SOS	2 Cu + 1 $CaWO_4$	Yes	24/0.6
TUM93B	$CaWO_4$	SOS	2 Cu + 1 $CaWO_4$	Yes	24/0.6
TUM93C	$CaWO_4$	SOS	Cu	Yes	24/0.6
Comm1	$CaWO_4$	SOS	Bronze Clamps	No	24/0.6
Comm2	$CaWO_4$	SOS	Bronze Clamps	No	24/0.6
Gode1	$CaWO_4$	Si	Glue	No	24
Gode2	$CaWO_4$	Si	Glue	No	24
Gode3	$CaWO_4$	Si	Glue	No	24

Table 2.1: Overview of different modules mounted for the current CRESST-III data-taking campaign. Summarised are the main materials used for each module, including the holding technique and the mass of the main detector crystal.

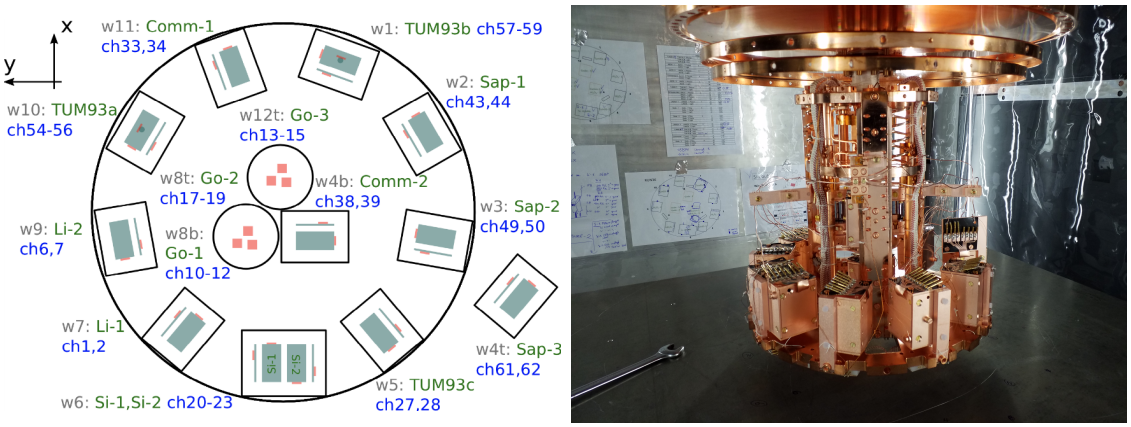

Figure 2.15: Left: Schematic drawing of the module setup in the CRESST detector carousel. The detectors are shown in green, and their TES in red. The assigned channel numbers are shown in blue. Right: Picture of the fully mounted carousel. All modules are connected to the read-out wires and thermal links. Figures by the LNGS mounting team.

silicon to construct a fully non-scintillating module. A low-activity ^{55}Fe source was introduced to all modules to allow for a fast and accurate energy calibration at low energies.

For redundancy, two or three modules of the same type were prepared whenever possible. In addition to these modules, three other modules with a beaker-like LD named Gode 1, Gode 2 and Gode 3 were produced. These modules aim to provide an active 4π-surface cover of the main detector by an additional $CaWO_4$ crystal on the top and a beaker made from silicon as enclosing LD. Further details on this module are described in [79, 80]. A list of all modules currently mounted in CRESST is shown in table 2.1.

All modules were mounted in the CRESST set-up according to the scheme shown in figure 2.15 (left). Indicated are the orientation of the modules with the detectors (green) and the TES (red), together with the channel numbers assigned to the modules. Figure 2.15 (right) shows a picture of the mounted detector carousel without temperature shields.

2.6 Sensitivity Enhancement for Spin-Dependent Dark Matter Search

In addition to increasing the sensitivity for spin-dependent and spin-independent DM searches via background reduction, the sensitivity for spin-dependent DM searches can be increased by isotopic enrichment of the $CaWO_4$ crystals with isotopes with unpaired spins. The CRESST exclusion limit for the spin-dependent DM search, shown in 2.9, is derived from the ^{17}O isotope in $CaWO_4$ and yields a competitive exclusion limit in the spin-dependent DM field. As the natural abundance of ^{17}O is

only 0.038 % a higher relative amount of ^{17}O in the total amount of oxygen could improve the exclusion limit for the spin-dependent case significantly. The exclusion limit improvement by enrichment of the target crystal with ^{17}O is studied in detail in the scope of this work (see section 8). In addition, a practical method to enrich $CaWO_4$ with ^{17}O is developed and applied to two crystals in this chapter, and the enrichment level is determined via Nuclear Magnetic Resonance (NMR) spectroscopy.

Chapter 3

Improving the Quality of $CaWO_4$ Crystals

The high quality and radiopurity of the $CaWO_4$ target crystals are key ingredients for the high sensitivity of CRESST-III in the low mass DM region. The $CaWO_4$ crystals have been produced at TUM for many years to achieve such quality.[1] This includes a selection of the cleanest commercially available raw materials $CaCO_3$ and WO_3, followed by the synthesis of $CaWO_4$, the crystal growth in a dedicated Czochralksi furnace and a careful post-growth treatment including cutting/polishing and underground storage. The first crystal produced with this procedure operated in CRESST was named TUM40 (produced 2012), which showed significantly lower radioactive impurities compared to commercially produced $CaWO_4$ crystals [45]. The main goal of this work is to further improve the quality of TUM-grown $CaWO_4$ crystals by reducing impurities and stress and enrichment of $CaWO_4$ with ^{17}O to enhance the sensitivity for spin-dependent DM searches. Section 3.1 gives an overview of the material $CaWO_4$ and its main characteristics, followed by section 3.2 containing the state-of-the-art crystal production as used for the production of TUM40 and DetA (TUM56)[2]. To reduce the intrinsic stress in $CaWO_4$, a possible origin for the LEE, simulations of the growth process were conducted within the framework of this thesis, and the Czochralski furnace was modified accordingly. The process and first results of reducing intrinsic stress in $CaWO_4$ crystals are described in section 3.3. As a central component of this dissertation, an extensive chemical purification of the raw materials and synthesised $CaWO_4$ powder to further reduce impurities was applied. The different steps of this purification and the first screening results are summarised in section 3.4.

[1] The growth process was developed and is performed by Prof. A. Erb (TUM)

[2] the detector which was analysed for the exclusion limit shown in 2.3

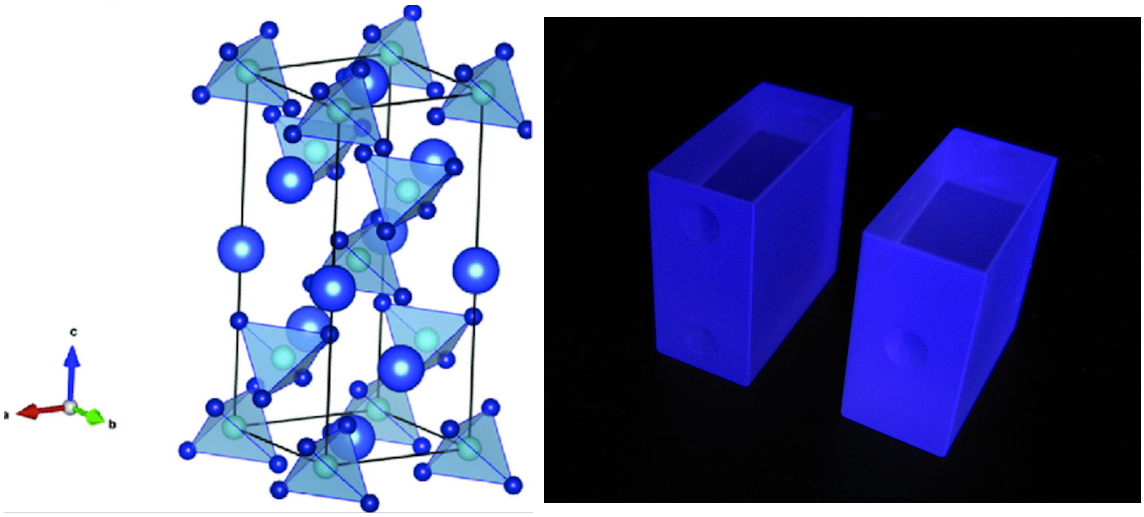

Figure 3.1: Left: Unit cell of $CaWO_4$. Ca^{2+} ions (blue dots) are surrounded by $(WO_4)^{2-}$ ions (pyramids), forming a tetragonal crystal structure. The figure is taken from [87]. Right: $CaWO_4$ CRESST-III shaped crystals under UV light. The crystals are scintillating with a wavelength of 420 nm. Picture by A. Münster (TUM).

3.1 $CaWO_4$ Crystal Properties

The name Calcium-Tungstate originated from the Swedish word tung sten (heavy stone) and was named after it due to its high density. Later, it was called scheelite after the Swedish chemist C. W. Scheele. It is a transparent mineral and consists of a tetragonal crystal structure [81] with $(WO_4)^{2-}$ ions surrounding Ca^{2+} ions forming a cuboid unit cell with $a = b = 5.24\,\text{Å}$ and $c = 11.37\,\text{Å}$ [82], shown in figure 3.1 (left). It has a density of $6.06\,\text{g/cm}^3$, a melting point of 1620 °C and a hardness of 4.5-5 Mohs [81, 83]. It is birefringent with an ordinary refractive index of 1.92 and an extraordinary refractive index of 1.94. Due to the tetragonal structure, the $CaWO_4$ crystal has a pronounced cleavage tendency within the 101 and 110 planes and is otherwise easily fracturable. Therefore, the crystals are grown along the c-axis [84, 85]. In addition, it is scintillating with a decay time of several μs and a wavelength peaked at 420 nm [86]. The scintillation of the crystal is shown in figure 3.1 (right).

3.2 Overview of the State-of-the-Art $CaWO_4$ Crystal Production at TUM

These $CaWO_4$ crystals are produced in-house at TUM to ensure their high quality. The following section covers the state-of-the-art crystal production procedure with which the crystals up to TUM72 have been produced at TUM, starting from the production of the $CaWO_4$ powder from the raw materials, the Czochralski growth process and the post-growth treatment of the crystal ingot.

3.2.1 Production of $CaWO_4$ via Solid State Reaction

$CaWO_4$, both as powder and crystal, cannot be treated chemically as it is only solvable in hot acid (e.g. hydrofluoric acid). Hence, the powder cannot be bought off the shelf and cleaned afterwards by chemical cleaning procedures. As $CaWO_4$ is not commercially available at the required radiopurity, the powder is produced from the raw materials calcium carbonate ($CaCO_3$) and tungsten oxide (WO_3), which are purchased from MV Laboratories with a purity of 99.999 % ($CaCO_3$) and 99.995 % (WO_3) [46]. Great care is taken to avoid cross-contamination with other impurities. The whole process is performed under a dedicated flow box. To achieve the proper stoichiometry, the powder is mixed with 2.316 g WO_3 per 1.000 g of $CaCO_3$. The powder is mixed in a rotating container with two grinding balls made from Teflon. The mixture is filled into an Al_2O_3 container and heated to 1100°C with a rate of 275°C/h. The temperature is kept for 10 h before the furnace is cooled down again. The solid-state reaction forming $CaWO_4$ powder in the crucible is [85]:

$$CaCO_3 + WO_3 \rightarrow CaWO_4 + CO_2 \uparrow \tag{3.1}$$

After the first cycle, the powder has not entirely reacted as the molecules usually are not mixed perfectly. The half-formed $CaWO_4$ powder has a slightly greenish colour. It is remixed using the grinding balls. Afterwards, it is baked again at 1100°C, followed by another mixing step. In the third baking step, the temperature is increased to 1200°C to complete the reaction. The whole process is monitored by weighing the powder after each step. As 13.25% of the initial mass is lost due to the release of the CO_2 gas, the mass of powder after a complete reaction can be calculated. The resulting powder has a white colour.

3.2.2 Czochralski Growth of $CaWO_4$

For the growth of a single crystal, the $CaWO_4$ powder has to be heated up to its melting point at 1620 °C. The crystal is transparent to visible and infrared radiation, so it cannot be grown in an optical furnace. Additionally, $CaWO_4$ is an insulator, so direct inductive heating is impossible as applied in floating zone furnaces. Therefore, $CaWO_4$ crystals are grown via the Czochralski principle, a widespread technique for single crystal growth. For this, a crucible containing the powder is heated until the powder is completely melted, and a homogeneous melt is formed. The temperature is kept around the melting point. A seed crystal made from $CaWO_4$ with a vertically aligned c-axis is lowered into the melt until it touches the surface. It is then under rotation, pulled out slowly from the melt. At the contact point, due to the colder temperature of the seed crystal, a crystal of the same crystallographic orientation is forming. Figure 3.2 shows a picture of a $CaWO_4$ crystal just after the growth. The crucible with the rest melt is the hottest point in the picture, glowing whiteish. It is heated inductively by High-Frequency (HF) water-cooled coils surrounding the crucible. The seed holder with the seed crystal is visible at the top of the picture, below the $CaWO_4$ single crystal formed during the growth. In the following, the different parts of the furnace and the growth process are described in more detail.

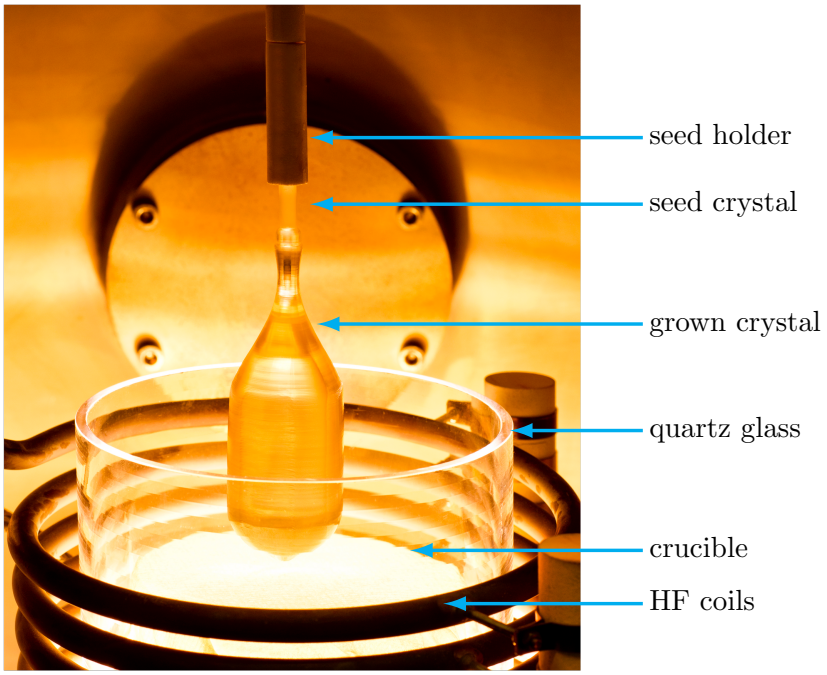

Figure 3.2: $CaWO_4$ crystal hanging in the Czochralski furnace just after the growth. The seed holder contains the seed crystal (dull part) to which the $CaWO_4$ crystal was grown (clear crystal). The crucible is the hottest part of the picture and is visible in a whiteish colour. It is heated by HF coils which are water-cooled. A quartz glass vessel insulates the coils to avoid any discharges. Picture by A. Erb.

Furnace

The Czochralski furnace used for $CaWO_4$ crystal growth at TUM is a Cyberstar oxypuller 20-04 [84] shown in figure 3.3. It is only used for the growth of $CaWO_4$ crystals for the CRESST experiment to avoid cross-contamination from other materials. The pulling head of the furnace is equipped with a precision balance which measures the crystal mass with a resolution of 1 mg. Water-cooled coils heat the crucible inductively with a frequency of ∼7 kHz. Between the crucible and the HF coil, several layers of insulation made from porous ZrO_2 stabilised by Y_2O_3 and Al_2O_3 minimise heat losses during growth. A quartz cylinder is added between the crucible and the coils to avoid electrical discharges. An additional after-heater is installed above the crucible to reduce spontaneous cleavage along the 101 and 110 planes during the cooling process. It is switched on during the whole growth process and keeps the temperature after the growth process at ∼1200 °C for 24 h before slowly cooling down the crystal ingot.

Crucible Selection

The crucible material must be selected carefully depending on the crystal material. First, its melting point has to be higher than the $CaWO_4$ melting temperature. Second, for the growth of an oxide crystal, the material should have a high chemical inertness against oxygen. This excludes standard crucibles like iridium or tungsten [88]. A crucible made from rhodium was selected at TUM as it has the highest resistance against oxygenation. It has an inner diameter of 80 mm, a wall thickness of 2 mm and mass of ∼ 700g. It can hold about 1.6 kg of molten $CaWO_4$ [84].

Growth Atmosphere

Even though the rhodium crucible has the highest chemical inertness, an oxygen-rich growth atmosphere would still lead to the formation of rhodium oxide falling out and causing black flakes, which are built into the crystal lattice [84]. Hence, the amount of oxygen has to be reduced as much as possible in the growth atmosphere. On the other hand, an atmosphere containing no oxygen would cause oxygen to evaporate from the $CaWO_4$ melt resulting in oxygen vacancies in the crystal. These vacancies have a negative influence on the optical quality of the crystal and can cause stress. A balance between these two effects is obtained using the noble gas argon (99 %) mixed with oxygen (1 %). The gas mixture is guided through the oven during growth with a rate of ∼ 10 l/h.

Seed Holder and Crystal

The correct orientation of the seed crystal along the c-axis is mandatory to avoid asymmetric crystal growth or cleavage due to intrinsic stress. A method to align the crystal is the Laue method based on X-ray diffractometry [84]. The seed crystal is usually cut from the top part of an existing $CaWO_4$ crystal in a conical way and

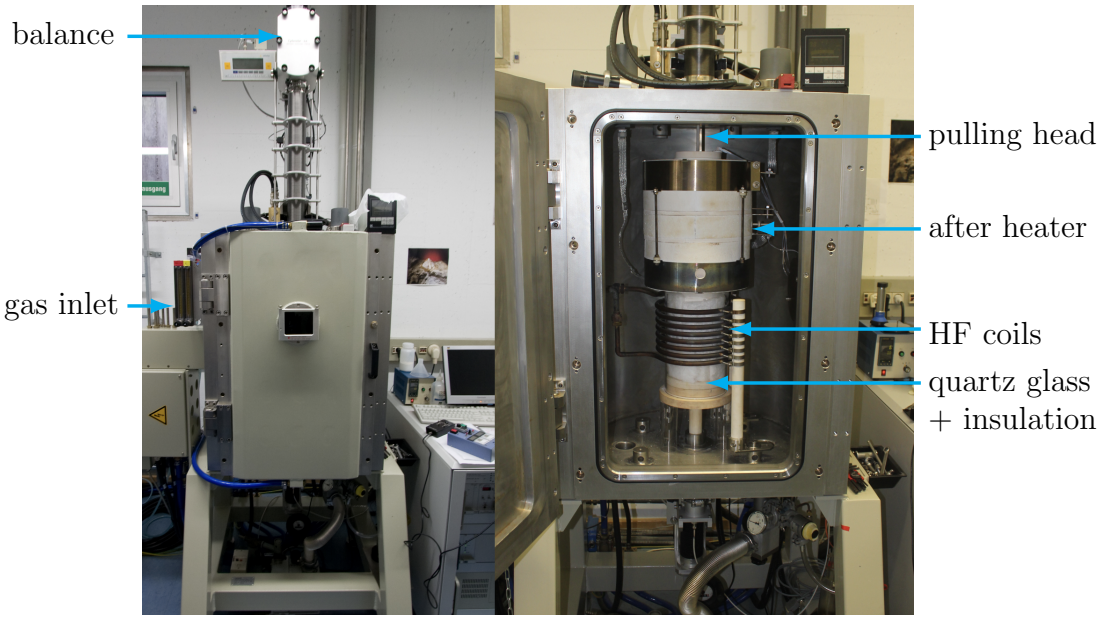

Figure 3.3: Closed (left) and opened (right) Czochralski furnace used for the growth of $CaWO_4$ at TUM. The crystal pulling head is connected to the seed holder (not shown), and the precision balance is included in the pulling head on the top of the furnace. The gas inlet regulates the flow of the growth atmosphere. The crucible is inside the oven, surrounded by several insulation layers, quartz glass and water-cooled HF coils. The after heater ensures the crystal's slow and controlled cooling when the growth is finished.

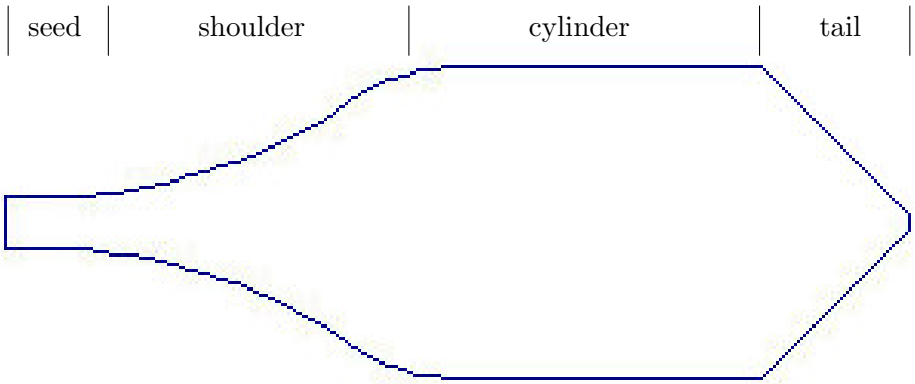

Figure 3.4: Schematic drawing of the crystal shape of the $CaWO_4$ crystals grown at TUM. First, the seed is grown, followed by the shoulder part, in which the diameter of the crystal is increased until it reaches the desired diameter. The cylindric part of the cylinder is later used to cut detector crystals. At the end of the growth process, the diameter is reduced, and the tail is produced.

fixed in a conical Al_2O_3 holder, the seed holder. The seed can be used multiple times, as the final crystal is cut from the seed crystal after the growth.

Crystal Shape

To further reduce the stress in the crystal and avoid cleavage during or after the growth, the crystal shape is optimised as shown in figure 3.4. The typical crystal geometry consists of the seed part with a diameter of ∼7 mm, followed by the shoulder, in which the diameter grows until it reaches the maximum diameter of around ∼44 mm. The next part is the cylindrical part of the crystal, where the diameter is kept constant. It is later used to cut detector crystals. In the end, a tail is grown, and the diameter is reduced to 0 mm, which ends the growth. The typical crystal geometry is shown in figure 3.2. In the shoulder part of the crystal, radial mechanical forces due to the weight of the crystal can appear if the diameter is changed too fast. These forces can cause cleavage of the crystal. To overcome this problem, the shoulder part of the crystals is elongated, minimising the radial forces [84].

Growth Process

Before starting the growth process, it has to be guaranteed that all the $CaWO_4$ material has melted. For this, the melt is overheated, i.e. heated to ∼100°C above the melting point. Afterwards, the temperature is lowered again to a few degrees above the melting point. At this temperature, a first seeding attempt is performed with the rotating seed crystal. The temperature window for a successful seeding is only a few degrees. If the temperature in the melt is too high, the tip of the seed is melted away. Conversely, a too-cold melt would cause an uncontrolled crystallisation. In most cases, several seeding attempts have to be performed, adjusting the temperature of the melt for each shot. When the seeding is successful, a computer

program takes over the growth. The desired shape, mass, growth rate and rotation speed of the crystal are given to the program before the growth is started. The software reads the current mass from the precision scale and calculates the crystal's present diameter and growth rate. A PI controller then compares the current and calculated parameters and adjusts the HF generator's power accordingly. The temperature in the melt is not constant but a gradient from hot (at the wall of the crucible) to colder areas in the middle of the crucible. The gradient is, therefore, a radial gradient. The crystal is growing in the areas where the Isotherms are colder than the melting temperature. Hence, by increasing or reducing the generator's power, the isotherms in the melt are shifted, and the diameter of the crystal which is forming can be controlled. At the end of the growth, the crystal is pulled up in the after-heater. The rotation is slowly reduced until the crystal rests in the after-heater. An abrupt rotation stop could, again, lead to cleavage of the crystal and has to be avoided. The generator is ramped down for several hours to prevent too large temperature gradients. The after-heater is kept at a constant temperature of 1200°C for 24 hours before the crystal is slowly cooled down with a rate of 50°C/h to avoid cleavage due to a too-high temperature gradient.

3.2.3 Post-Growth Treatment

The resulting crystal shows a grey colouration. This is due to oxygen vacancies in the crystal, as the growth atmosphere contains only 1% oxygen to avoid the oxidation of the crucible. Still, some of the oxygen evaporates from the melt during the growth. These oxygen vacancies can be filled by annealing the crystal ingot in a 100% oxygen atmosphere in a dedicated furnace at high temperatures. During this process, oxygen diffuses into the $CaWO_4$ crystal. The diffusion follows Fick's second law and is also called the diffusion equation:

$$\frac{\partial C}{\partial t} = \nabla(D\nabla C) \tag{3.2}$$

With the oxygen concentration C and diffusion coefficient D [89]. The second-order partial differential equation describes the concentration change with respect to time caused by diffusion. To solve this equation, some assumptions have to be made. As $CaWO_4$ is an unisotropic material, the diffusion coefficient is different in all directions. For tetragonal crystals in the 100 crystal orientation, the diffusion coefficient along the different axes are $D_1 = D_2 \neq D_3$ [89]. This means the diffusion in the a-b plane is independent of the direction as the crystals are grown along the c-axis. Most of the diffusion happens in the a-b plane [90]. For the annealing procedure, the diffusion coefficient D is not constant as a chemical gradient drives the diffusion due to the oxygen vacancies in the crystal lattice.
In addition to the dependence on the chemical gradient, the diffusion coefficient D is temperature dependent, following the Arrhenius formula [89]

$$D = D_0 \cdot exp\big(-\frac{\Delta H}{k_B T}\big) \tag{3.3}$$

with ΔH the activation enthalpy and D_0 the so-called frequency factor. Both are also called activation parameters for diffusion, k_B is the Boltzmann constant and T the absolute temperature [89].
The formula shows that the diffusion coefficient D increases with increasing temperature T. For the annealing process, the temperature should be chosen in a way that the temperature is still below the melting point but above the activation enthalpy [88]. As many variables are unknown for $CaWO_4$, the time needed to fill all oxygen vacancies cannot be calculated. The procedure applied at TUM was developed by A. Erb, testing different combinations of temperature and time and optimising the process iteratively [88]. The following procedure is applied: The annealing furnace is flushed with 10 l/h of pure oxygen gas. The crystal is heated up to a temperature of 1400 °C over a time of 7 h. The temperature is kept for 20 h before the crystal is cooled down with a rate of 5 °C/h to 1200 °C. Diffusion is happening between 1400 °C and 1200 °C. At 1400 °C, oxygen mobility is high, meaning the diffusion coefficient is large, and the oxygen is also diffusing to the inner parts of the crystal. However, due to the high mobility, vacancies can still be produced. Via the slow cool down towards the equilibrium condition at 1200 °C (below 1200 °C, nearly no diffusion is happening in $CaWO_4$), most vacancies can be filled in the crystal [88]. Below 1200 °C the crystal is cooled with 50 °C/h down to room temperature. After the annealing procedure, the crystal is further processed by the crystal laboratory at TUM. The cylindrical part is cut into CRESST crystals of the desired size. For CERSST-III, the crystals are cut into (20x20x10) mm^3 cuboids and polished afterwards. To avoid cosmic activation and contamination from, e.g. radon, the raw materials, $CaWO_4$ powders, crystal ingots and CRESST detector crystals are stored in a nitrogen locker in the shallow underground laboratory (UGL) at TUM.

3.3 Reduction of the Intrinsic Stress in $CaWO_4$ Crystals

As described in detail in section 3.2.2, great care is taken to reduce intrinsic stress in the crystals by orienting the seed crystal in c-direction, growing a long shoulder to reduce radial forces and keeping the crystal in an After-Heater after the growth to avoid cleavage during the growth. However, there is still a certain amount of intrinsic stress in the crystal lattice originating from thermal gradients during growth. One theory for the origin of the low energy excess seen in CRESST (see section 2.4.1) and many other experiments is the relaxation of intrinsic stress present in the crystal lattice at the low detector operation temperatures. To study this theory, two approaches are followed. On the one hand, the operation of a detector crystal made from a material with nearly no intrinsic stress like Silicon and, on the other hand, the production of a $CaWO_4$ crystal with a reduced amount of intrinsic stress.

Intrinsic stress in oxide crystals mainly depends on the temperature field in the crucible and the shape of the crystal-melt interface [91]. Figure 3.5 shows a sketch of the crystal during the growth. The coils (blue) heat the crucible (black) by inducing a strong magnetic field in the walls of the crucible and a weaker field at the bottom of the crucible due to the finite penetration depth of the magnetic field in rhodium of $\sim$1.25 mm [92]. Hence, the walls are hotter than the bottom. The insulation material (grey) decreases the heat losses of the crucible to the sides and the bottom. This causes vertical temperature gradients in the melt (yellow) and convection of the melt, leading to the growth of a cone below the melt level. Many parameters influence the cone's exact shape, the melt's temperature gradient influenced by convection and the gradient in the crucible walls, the latent heat caused by the crystallisation (depending on the growth rate), and the heat conductivity of the crystal and heat radiation of the melt.

Thermal stress is caused by the thermal gradients inside the melt and, most important, at the interface of the melt and the crystal. In case of a cone growth below the melt surface, this interface is the cone's surface. Due to the high temperature in the interface region, the stress is relaxed by plastic deformations. During the growth, the formerly newly grown area is moving away from the hot region and is cooling down. Towards lower temperatures, the critical shear stress for plastic deformation strongly increases and exceeds the local thermal stress. This causes freezing of the before-formed dislocation structures. These structures cause an uneven thermal expansion and so-called internal thermal stress in the final crystal [93]. One common way to reduce thermal stresses in oxides is to flatten the growth interface (i.e. the cone) by increasing the rotation speed and the growth rate as this increases the latent heat [91]. However, an increased growth speed also causes stress in the crystal as the formerly newly grown regions are cooled down faster. Another way to reduce thermal stress is the overall reduction of vertical thermal gradients in the melt, decreasing the cone growth and a slower growth rate. To investigate these effects in detail for the growth setup at TUM, a dedicated numerical growth simulation was performed.

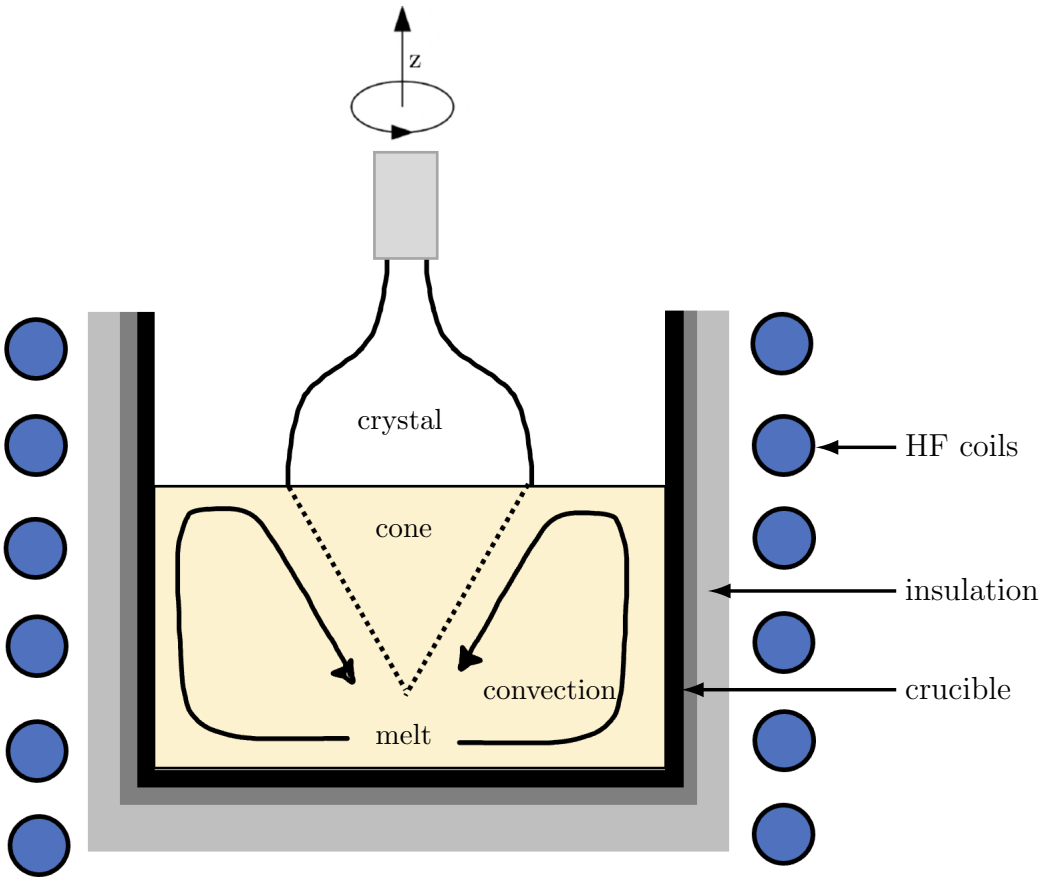

Figure 3.5: Sketch of the growth process at TUM. The HF coils inductively heat the crucible. The bottom of the crucible does not get as warm as the sides forming a temperature gradient. This and the rotation of the crystal cause convection in the melt. The colder bottom also induces a vertical gradient in the melt, causing a cone formation below the melt surface.

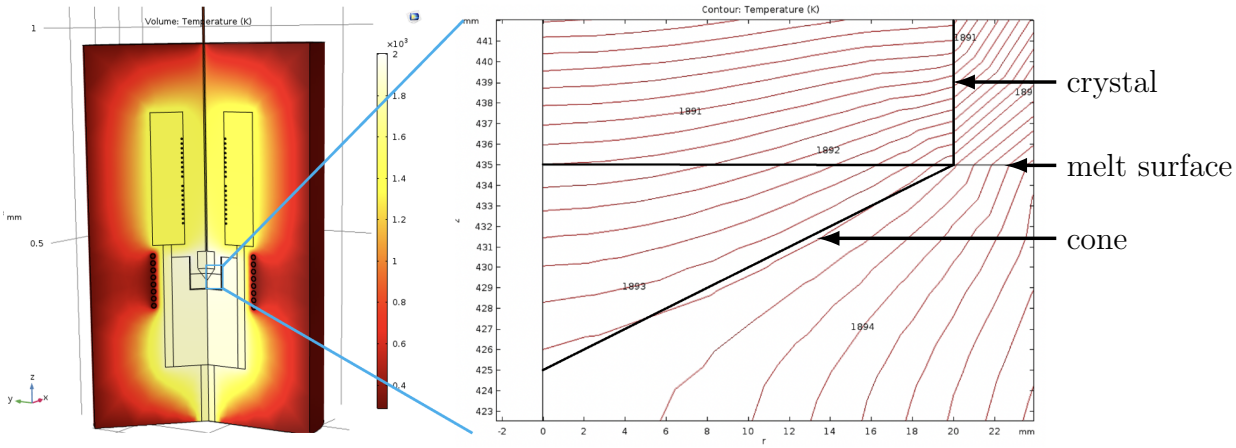

Figure 3.6: Left: Colour-coded temperature during growth in the TUM Czochralski furnace. The implemented parts are shown in black. The simulation contains the after heater, the HF coils, insulation, quartz glass, melt, crystal and growth atmosphere. The crucible, insulation and crystal are the hottest parts of the furnace. Right: Zoom in to the inside of the crucible. The horizontal black line shows the melt surface. The crystal and cone growing below the melt surface are shown in black. The cone grows along the isotherm going through the triple point between melt, crystal and growth atmosphere. Figures are taken from [92].

3.3.1 Simulation of Temperature Gradients in the Czochralski Furnace

Part of this simulation was carried out together with F. Hamilton in the scope of a bachelor's thesis [92] and with the help of the Institut für Kristallzüchtung (IKZ) Berlin. The software package used is the finite element software COMSOL multiphysics [94]. For this, the Czochralski furnace was implemented in the software and relevant physics processes like thermal conduction, radiation, convection etc., were considered in the simulation. Details about the physics packages used and how the geometry was implemented can be found in [92]. The simulation provides information about the overall temperature gradients in the oven and, most importantly, the melt. Figure 3.6 (left) shows the colour-coded temperature within the Czochralski furnace during the growth process. The implemented parts of the furnace, including the after-heater, the crucible, insulation, quartz glass, coils, melt and crystal, are shown in black. As expected, the crucible and surrounding parts have the highest temperatures, and the temperature decreases for points further away from the crucible. Figure 3.6 (right) shows the isotherms in the right half of the crucible. The melt surface is the horizontal thin black line, and the $CaWO_4$ crystal with a thicker black line. The isotherm defining the boundary between the solid crystal and the melt runs through the triple point between $CaWO_4$ crystal, $CaWO_4$ melt and the growth atmosphere. The cone below the melt level is forming along this isotherm. In addition, the vertical gradient along a vertical line running through the crystal was investigated [92].

Different ideas to reduce the thermal gradients were tested with the help of the simulation. On the one hand, the growth atmosphere and the growth rate were changed. On the other hand, two rhodium disks, one at the bottom for additional heating of the crucible from below and another with an inner diameter of 60 mm on the top of the insulation to reflect heat radiation into the melt were tested [92]. One of the key results of the simulation was that a combination of a reduced growth speed from 12 mm/h to 4 mm/h together with the implementation of the rhodium disk at the bottom for additional heating and on top for back-reflection of heat radiation show the most significant reduction of thermal gradients and hence of the lowest expected thermal stress in $CaWO_4$ [92].

3.3.2 Implementation of Rhodium Disks into the Furnace

Following the results obtained from the simulation, a small rhodium disk of 60 mm was cut from a rhodium disk with a diameter of 115 mm and height of 3 mm. The smaller disk is installed below the crucible for additional heating from below, and the larger disc with the centred 60 mm hole is placed above the insulation (see figure 3.7). To study the influence of both disks on the intrinsic stress in the $CaWO_4$ crystals, a series of crystals were grown with different combinations of the disks. First, the crystal TUM86 was grown with a reduced growth speed of 4 mm/h without the rhodium disks. The same growth settings were used for crystal TUM87 which was grown with only the top rhodium disk installed. The crystal TUM88 was grown with the small rhodium disk at the bottom and the top rhodium disk in place. Already during crystal growth, a positive effect of both discs was observed. The power needed to melt the $CaWO_4$ powder for growth 87 and 88 and the power required during growth was lower (13.6% for growth 88) compared to the growth 86 (22.1%), meaning that less heat was radiated away from the melt.

3.3.3 Comparison of Intrinsic Stress in $CaWO_4$ Samples

The underlying theoretical description of intrinsic stress in $CaWO_4$ crystals follows Hooke's law. In the most simplified case, Hooke's law describes the force F_s needed to extend or compress a spring with spring constant or stiffness k by a length x [95].

$$F_s = k \cdot x. \tag{3.4}$$

For a three-dimensional crystal, the problem cannot be described by the parameter x anymore. A certain amount of material can be compressed, stretched, and sheared simultaneously in all dimensions, leading to a solid body deformation [95] [96]. In addition, as $CaWO_4$ is an anisotropic material, the crystal behaves differently along the different axes. Due to the complexity of this material, it is not straightforward to solve the equation other than numerically, which would also need input from simulations using the finite element method. To get a feeling for the behaviour of

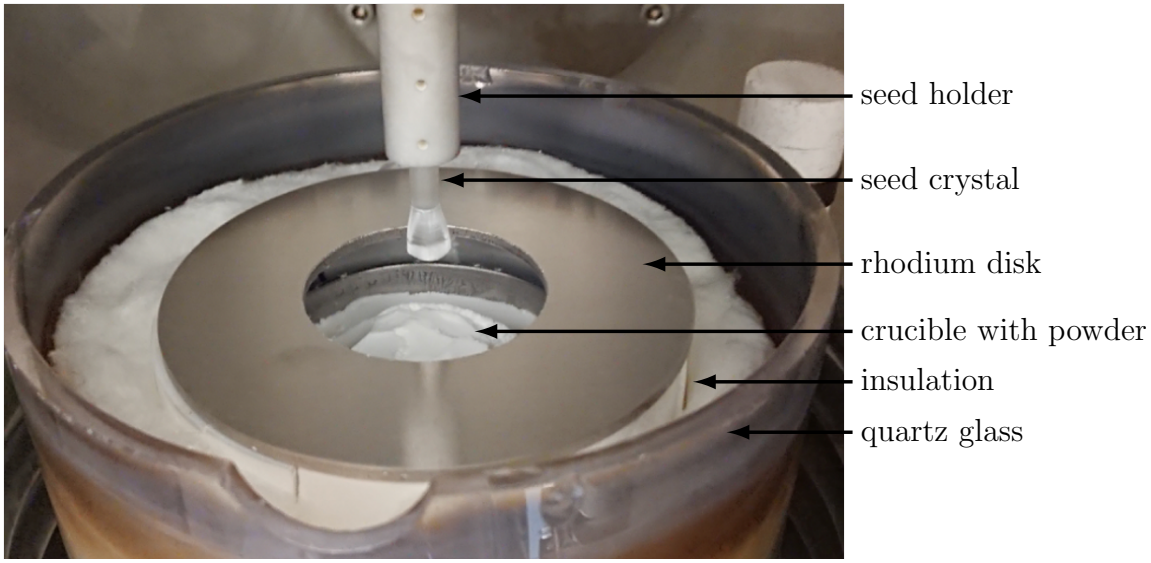

Figure 3.7: Picture of the modified Czochralski furnace. The small rhodium disc below the crucible is not visible. The top rhodium disk is placed on the ZrO_2 insulation. Below the disk, the crucible filled with $CaWO_4$ powder is situated.

$CaWO_4$ under stress and study the influence of external stress on the crystal lattice, dedicated measurements on point-like external stress were performed in the scope of a bachelor's thesis supervised as part of this dissertation (see [97]).

Investigation of Point-Like Stress on $CaWO_4$

For the investigation of the point-like stress, a $CaWO_4$ CRESST detector crystal was placed in a CRESST-III module, and two copper side plates were removed (see figure 3.8 (right)). This detector was placed into a plane polariscope setup called a photoelasticity setup.
The experimental setup (see Figure 3.8 (left)) consists of a white light source, a polariser, the sample, an analyser and a CCD (Charge Coupled Device) camera. It determines the stress distribution in a transparent sample through stress birefringence. The polarised light which goes through the sample is divided into wave components along the principal stress axes. The different refractive indices caused by the intrinsic stress lead to different phase velocities and phase shifts of the light. The light passes the analyser polarisation filter and is recorded by the CCD camera. The number of phase shifts is called fringe order, and successive dark and light bands are called fringes. In the case of elastic stress in a simplified two-dimensional stress state, the fringe order is proportional to the material-dependent stress fringe value times the difference in stress along the principle stress axes in the crystal [98].
To study the birefringence response of the $CaWO_4$ crystal to point-like stress in the photoelasticity setup and to get a feeling of the stress induced by the standard holding of the $CaWO_4$ crystal by the 3 $CaWO_4$ holding sticks held in place by bronze clamps, different loads were applied to the top holding stick and compared to the

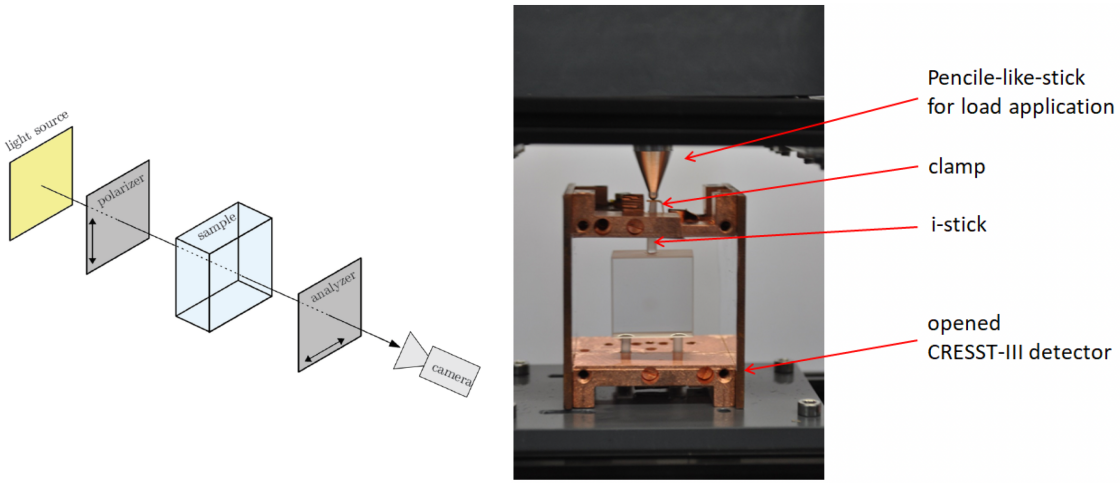

Figure 3.8: Left: Photoelasticity setup at TUM. It consists of a white light source, a polariser, the sample, an analyser and a CCD camera. Figure taken from [46]. Right: CRESST-III detector with opened side plates and installed $CaWO_4$ detector placed in the sample position of the photoelasticity setup. Three sticks hold the crystal. The upper stick can be fixed with the clamp, as in CRESST, or loaded with a pencil-like stick with a defined force.

load which is induced by the bronze holding clamp. A relation between load/stress σ and intensity I in the sole appearing fringe of

$$\sigma = I^{\frac{1}{3}} \tag{3.5}$$

was found, and the equivalent force applied to the crystal by the clamp was determined to be $\lesssim$5 N translating to an induced stress of σ_0 $\sim$556 MPa [97]. This external stress did not cause the formation of multiple fringes. An attempt to translate the results of the point-like applied stress to the intrinsic stress in the crystal showed non-physical results [97]. To study intrinsic stress, a combination of different approaches is proposed. First, the load has to be changed from a point-like load to a more distributed one. Second, the crystal should be measured at different temperatures as intrinsic stress influences thermal expansion. Most important, simulations with a finite element method have to be performed, implementing $CaWO_4$ as an anisotropic material with the stiffness tensor comparing the observed stress in the crystal with the simulation.

Nonetheless, the measurements showed a proportionality between stress and intensity of the stress birefringence if only one fringe is present. Hence, a qualitative comparison between similar crystal samples using the photoelasticity setup is possible. In addition, the number of fringes present in the sample can also be used to compare samples with multiple fringes.

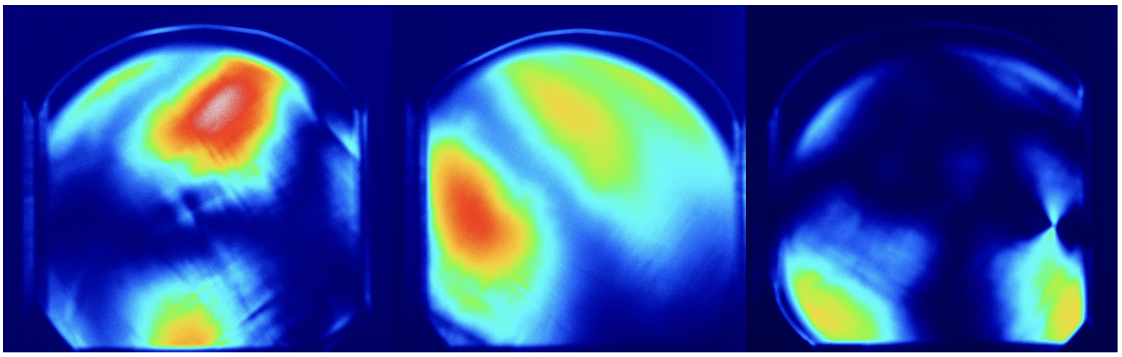

TUM86 TUM87 TUM88

Figure 3.9: Comparison of birefringence pattern taken by the CCD camera in the photoelasticity setup with a shutter time of 0.5s. The patterns are colour coded with the physics template of the Fiji image processing package. Compared are the crystal TUM86 (grown without rhodium discs), TUM87 (top rhodium disc) and TUM88 (top and bottom rhodium disc)

Comparison of Intrinsic Stress in TUM86, TUM87 and TUM88

For comparing the three crystal samples, discs with 5 mm height were cut from the cylindrical part of each crystal ingot and polished by the crystal laboratory. Afterwards, the samples were installed in the photoelasticity setup, sliding them into an u-shaped plastic piece with rail-like groves on the sides, which does not induce any stress from holding the sample. The CCD camera was programmed with a shutter time of 0.5 s and the black and white intensity pictures colour coded to highlight the intensity differences in each picture. For this, the image processing package Fiji [99] is used with the "physics" colour code settings. Figure 3.9 shows the birefringence pattern for all three crystal samples grown with different configurations of the Czochralski furnace. TUM86 without any rhodium discs, TUM87 with the top rhodium disc and TUM88 with both the top and the bottom rhodium disc. Comparing the colour-coded pictures, the intensity recorded by the CCD camera is highest for TUM86, followed by TUM87 and TUM88. Using the results obtained from [97], this points to the highest intrinsic stress in TUM86, 2nd highest in TUM87 and the lowest in TUM88.
Another observation is that the stress is located mainly on the edges of the crystal. This is because the crystal is grown with round edges, whereas the underlying crystal lattice is rectangular. Looking at the birefringence pattern, it seems like there is more stress also in the middle for TUM86 and TUM87 compared to TUM88, which agrees with the simulations performed in [92], which showed that the rhodium discs reduce the formation of a cone below the melt level which reduces thermal stress during growth. No higher-order fringes can be observed in any of the crystals.
However, the interpretation of the birefringence pattern should be taken with care as the intensity detected by the polariscope is not only dependent on the intrinsic stress in the crystal but can also be influenced by, e.g. the angle of the principal stress direction and the axis of the polarisation or small ($\mathcal{O}(1°)$) derivation of the

c-axis facing the CCD camera. A new experimental setup including two quarter wave planes and a monochromatic light source would reduce these effects [97].
The comparison hints toward successfully reducing intrinsic stress in TUM-grown $CaWO_4$ samples. Based on the results, the rhodium discs are kept in the Czochralski furnace.

3.4 Improving the Radiopurity of $CaWO_4$ Crystals

The radiopurity of $CaWO_4$ crystals can be improved in two ways: One is the principle of re-crystallisation in which $CaWO_4$ crystals are remelted in a cleaned crucible and regrown. This method reduces the impurity level in the $CaWO_4$ crystals due to segregation effects during growth. When the crystal lattice is formed, the probability for impurities to be built into the lattice is <1 and given by the so-called segregation coefficient, which is different for each element. During crystal growth, the impurity concentration in the melt increases. As the segregation coefficients are not concentration dependent, this also increases the impurity concentration in the crystal lattice forming an impurity gradient along the growth axis. The biggest impurity concentration is present in the rest melt after the growth. By removing the rest melt and remelting whole or only the top parts of existing $CaWO_4$ crystals, the impurity level of the new crystal can be reduced effectively. Up to now, the segregation coefficients are only known for a small number of elements reported in [46]. Hence, no statements can be made on the overall reduction of impurities in $CaWO_4$ by re-crystallisation. To determine the segregation coefficients during $CaWO_4$ crystal growth, the crystal TUM61 with known impurities was remelted, and TUM81 grown from it. Measurements of this crystal are planned for the near future. Feasibility studies for the determination of the segregation coefficient with this method were performed in [46], and a detector module to study the impurity level in TUM81 and other crystals is developed in the scope of this work (see chapter 9).
Another way to improve the radiopurity of $CaWO_4$ crystals is by reducing the impurities present in the raw materials $CaCO_3$ and WO_3 and by minimising the introduction of impurities during the production of $CaWO_4$ powder. The focus of this work is on this purification method. For this, the production process of $CaWO_4$ was optimised, starting from a chemical purification of the raw materials $CaCO_3$ and WO_3.[1] The materials are brought in aqueous solutions of $Ca(NO_3)_2$ and $(NH_4)_2WO_4$. In this state, the chemical extraction techniques Liquid Liquid Extraction (LLE) and Coprecipitation are applied to the solutions. Afterwards, the $CaWO_4$ powder is formed from the solutions via a precipitation reaction. A washing procedure is applied to the powder to remove solvable impurities from the $CaWO_4$ powder, followed

[1] The chemical purification was developed by Dr. Hong Hanh Trinh Thi and applied together in the scope of this work

by rinsing and calcination in a furnace. A detailed description of the development of the cleaning procedure is published in [46].
The purification procedure was performed in an ordinary laboratory which was modified to suit the requirements by, e.g. the installation of filters to the climate system and a dedicated HEPA-filter system. A tent functioning as a lock and changing room was installed at the door's entrance. The laboratory is only entered wearing laboratory coats, overshoes, hair-nets, masks, glasses and gloves. The whole powder purification and production took place in a flow box to further prevent contamination of the materials. The chemicals' quality was supra-pure (indicating a total metallic impurity level of 10 ppb) if not otherwise stated. Clean water was provided by a millipore machine operated with a conductivity of 18 MΩcm.
The following sections give an overview of the different steps applied to the raw materials and $CaWO_4$ powder in the scope of this thesis, starting with a description of the chemical extraction techniques applied to the aqueous solutions in 3.4.1. Afterwards, the precipitation reaction is explained in section 3.4.2, followed by the powder washing and calcination procedure in 3.4.3. In 3.4.4, the first results on the radiopurity of the purified powder are presented.

3.4.1 Chemical Extraction Techniques

Two chemical extraction techniques are applied to the aqueous solutions of the raw materials. On the one hand, a LLE removes heavy impurities like Uranium and Thorium. On the other hand, a Coprecipitation was applied for a general reduction of impurities in both solutions.

Liquid-Liquid-Extraction

This method is based on separating compounds due to their different solubility in two immiscible solvents, usually an organic solution and an aqueous solution. Figure 3.10 shows the basic concept of the technique. In this example, the aqueous solution is enriched with two impurities. The organic solution contains fewer of these impurities. For the LLE, both solutions are stirred continuously so that impurities can move from the concentrated to the concentration-poor phase until an equilibrium is reached. Afterwards, the mixture separates again due to the immiscibility of the solutions. The cleaned aqueous solution can be separated from the organic solution.
The LLE extraction was applied to the $CaCO_3$ powder to reduce its Uranium and Thorium contamination. Table 3.1 shows the results of High Purity Germanium (HPGe) screening of the $CaCO_3$ and WO_3 raw materials at LSC. Only in the $CaCO_3$ powder Uranium and Thorium contaminations could be measured. Hence, only the $CaCO_3$ powder is cleaned via LLE. For this, the extraction agent trioctylphosphineoxide (TOPO) with the structure formula $(C_8H_{17})_3PO$ is used. Due to its high polarity resulting from the dipolar phosphorus-oxygen bond (see figure 3.10 (right)), it is frequently used for the extraction of Uranium and Thorium [100][101].
For the LLE of the $CaCO_3$, it is first brought into an aqueous solution by dissolving $CaCO_3$ in nitric acid (HNO_3), forming $Ca(NO_3)_2$. The TOPO is dissolved in

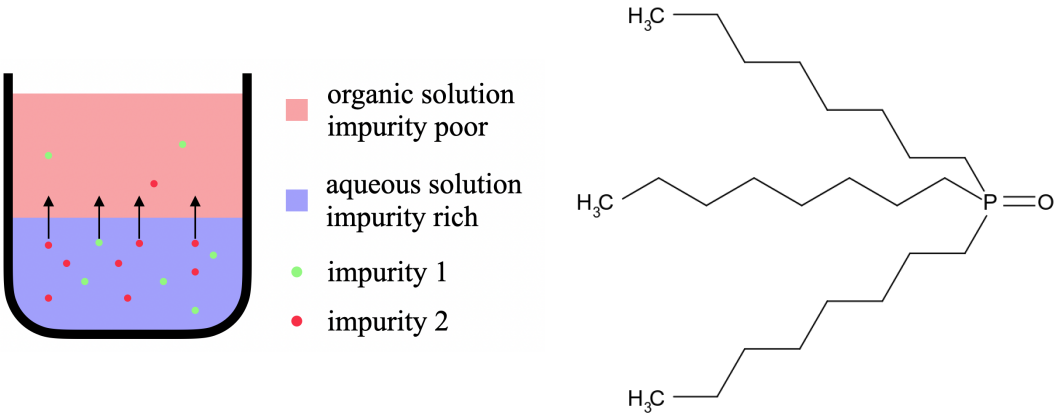

Figure 3.10: Left: Sketch of the principle of LLE. Two immiscible solutions (red: organic solution, impurity poor, purple: aqueous solution, impurity rich) containing different concentrations of impurities are mixed under continuous stirring. Due to a concentration gradient of the impurities, they transfer from the concentration rich to the concentration-poor phase until chemical equilibrium is reached. Afterwards, the solutions separate again. Right: Structural formula of trioctylphosphineoxide (TOPO). The dipolar phosphorus-oxygen bond creates a high polarity, resulting in a high efficiency for binding metals, particularly Uranium and Thorium [81].

sample		$CaCO_3$	WO_3
origin	isotope	activity [mBq/kg]	
^{232}Th chain	^{228}Ra	< 3.2	< 3.0
	^{228}Th	2.2 ± 0.6	< 1.7
^{238}U chain	^{234m}Pa	47 ± 10	< 40
	^{226}Ra	2.5 ± 0.6	1.8 ± 0.4
^{235}U chain	^{235}U	2.2 ± 0.5	< 2.0
	^{227}Ac	5.2 ± 1.2	< 3.2
other	^{137}Cs	< 1.0	< 0.80
	^{60}Co	< 0.7	< 0.63
	^{40}K	< 9.6	161 ± 10

Table 3.1: HPGe measurement at LSC of the raw materials $CaCO_3$ and WO_3. Errors are given with a confidence level (C.L.) of 68%, limits with 95% C.L. Results are taken from [46].

n-dodecane to create an organic solution. Before the TOPO solution is used to clean the $Ca(NO_3)_2$, it must also be cleaned via a LLE to reduce the initial trace contamination of the TOPO solution. This prohibits the contamination of the $Ca(NO_3)_2$ solution with contaminants of the TOPO solution and enhances the extraction capability of the TOPO solution. For the purification of the TOPO solution, several

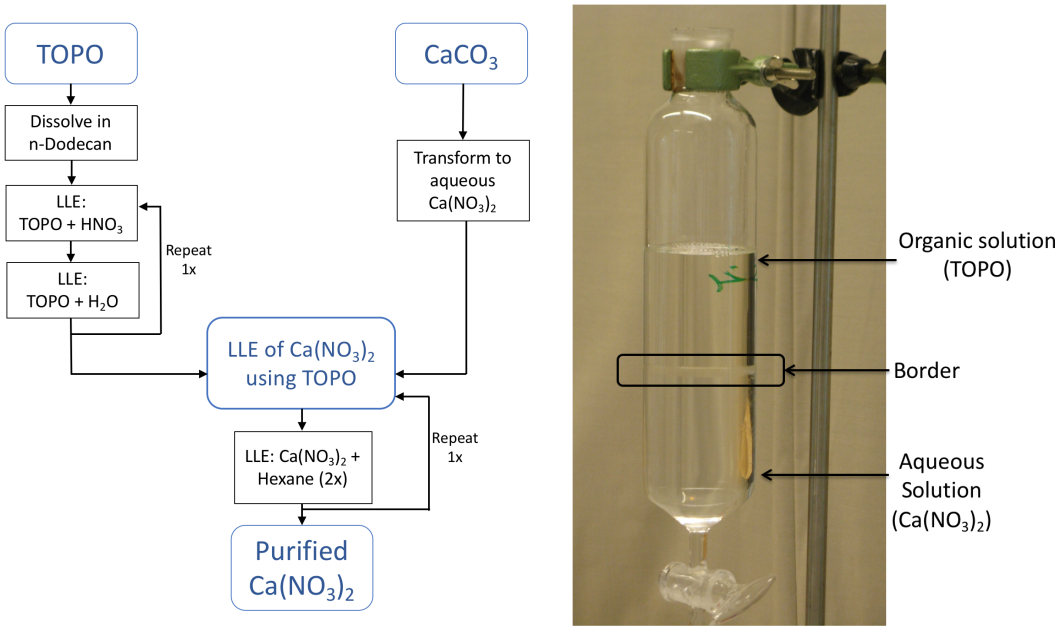

Figure 3.11: Left: Flowchart of the chemical purification of $Ca(NO_3)_2$ with the LLE method. The process starts with dissolving both TOPO and $CaCO_3$ into solutions. The TOPO solution is first cleaned by a LLE with HNO_3 and H_2O before it is used to perform a LLE of $Ca(NO_3)_2$. To remove remnants from the $Ca(NO_3)_2$ solution after the LLE with TOPO, the $Ca(NO_3)_2$ solution is cleaned twice by a LLE with Hexane. Right: Separation funnel with the organic solution TOPO and the aqueous solution $Ca(NO_3)_2$. A clear border between both solutions is visible. For the separation of both solutions, the lower solution is slowly extracted.

cycles of LLE with ultra-pure HNO_3 solution and clean water are performed. The whole process is shown in figure 3.11 (left). After the purification of the TOPO solution, the $Ca(NO_3)_2$ and the TOPO solution are mixed in the same concentration (mol/l) for 60 minutes, followed by a separation time of 15 minutes. Figure 3.11 (right) shows the clearly separated solution in the separation funnel. The $Ca(NO_3)_2$ solution is separated from the TOPO solution, and two additional LLE processes with $Ca(NO_3)_2$ and Hexane are performed to remove any remnants of the TOPO solution. This process of the LLE of $Ca(NO_3)_2$ using TOPO and twice Hexane is repeated once. Measurements showed that this process reduces the Uranium and Thorium content by a factor of $\geqq 35$ and $\geqq 7$ respectively [46].

Coprecipitation

Originally, coprecipitation was an unwanted side effect in separation chemistry [101]. When two solutes are mixed and react, the reactant which falls out contains an unproportionally high amount of undesired elements. These undesired elements attach via different mechanisms: The formation of mixed crystals and mixed chemical compounds, surface adsorption, and occlusion of mechanical inclusion [101]. A dominant

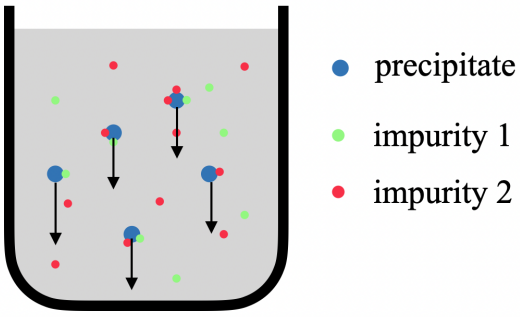

Figure 3.12: Sketch of the principle of coprecipitation. A small part of one solution is added to another, forming the solution shown in grey. They form a precipitate (blue), which falls out. The impurities present in the solution (green and red) attach to the precipitate and can be removed together with the precipitate afterwards.

process cannot be predicted since all the mentioned processes occur simultaneously [102]. The impurities are incorporated into the crystal lattice when mixed crystals are formed. Surface adsorption happens when the precipitate has a large surface area, and during occlusion, the impurities are not incorporated into the crystal lattice but enclosed during crystal growth, forming imperfections. Mechanical inclusions trap impurities between several crystal molecules [102]. This effect can efficiently extract unwanted impurities from the solution by forming a small amount of a precipitate filtered together with the impurities from the solution afterwards. The principle is shown in figure 3.12.
The coprecipitation process applied in this work is schematically shown in figure 3.13. In the first step, the pH value of the LLE cleaned $Ca(NO_3)_2$ solution is changed to nine by adding an NH_3 solution. The WO_3 is dissolved over several days in a mixture of NH_3 and H_2O to form $(NH_4)_2WO_4$. For the coprecipitation 2 % of each solution is removed with a pipette and added to the other solution under constant stirring. After a few seconds, the before transparent solutions turn milky, indicating the formation of $CaWO_4$ (see figure 3.14). The solutions are stirred for 30 minutes and are left to sediment for another 30 minutes before they are filtrated, removing the formed $CaWO_4$ and the impurities attached to it. The whole process is repeated once. It was shown in [46] that the coprecipitation removes elements like sodium, potassium, strontium and lead.

3.4.2 The Precipitation Reaction

The cleaned $Ca(NO_3)_2$ and $(NH_4)_2WO_4$ solutions are then undergoing a precipitation reaction in which the $CaWO_4$ powder is formed. For this, the solutions are under continuous stirring dropped in a host solution containing 5 % NH_3 (see figure 3.15). The $CaWO_4$ forms via

$$Ca(NO_3)_2 + (NH_4)_2WO_4 \rightarrow CaWO_4 + 2NH_4NO_3 \tag{3.6}$$

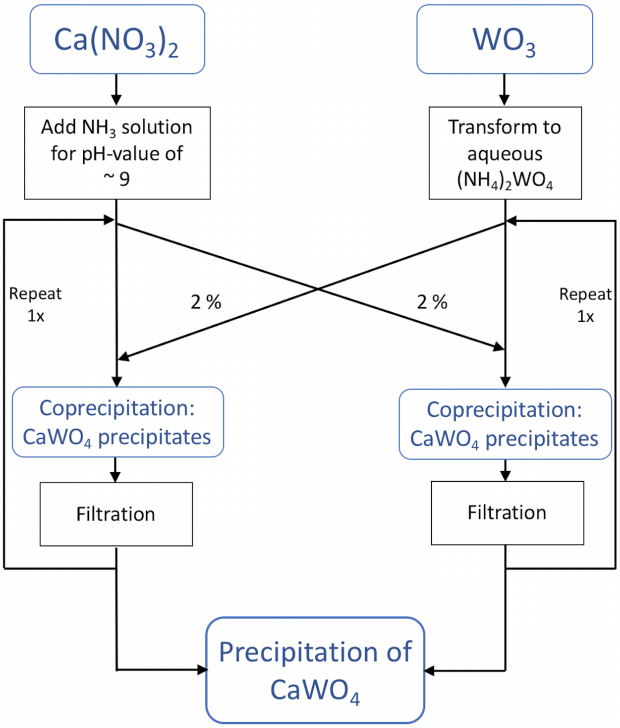

Figure 3.13: Flowchart of the coprecipitation processed developed at TUM. For the coprecipitation, the pH value of $Ca(NO_3)_2$ solution is changed by adding NH_3 solution. The WO_3 is transformed to $(NH_4)_2WO_4$. 2 % of each solution are added to the other solution. $CaWO_4$ precipitates, and impurities attach to it. The solutions are filtered, and the process is repeated. After this cleaning step, the $CaWO_4$ powder is produced via precipitation.

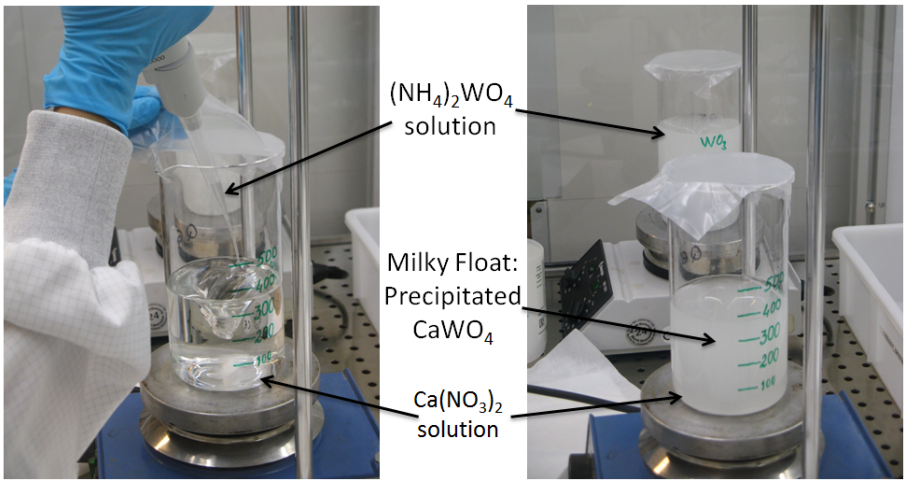

Figure 3.14: Left: 2 % of $(NH_4)_2WO_4$ solution are added to the $Ca(NO_3)_2$ which is stirred constantly. Right: The $Ca(NO_3)_2$ solution turns milky as $CaWO_4$ starts forming.

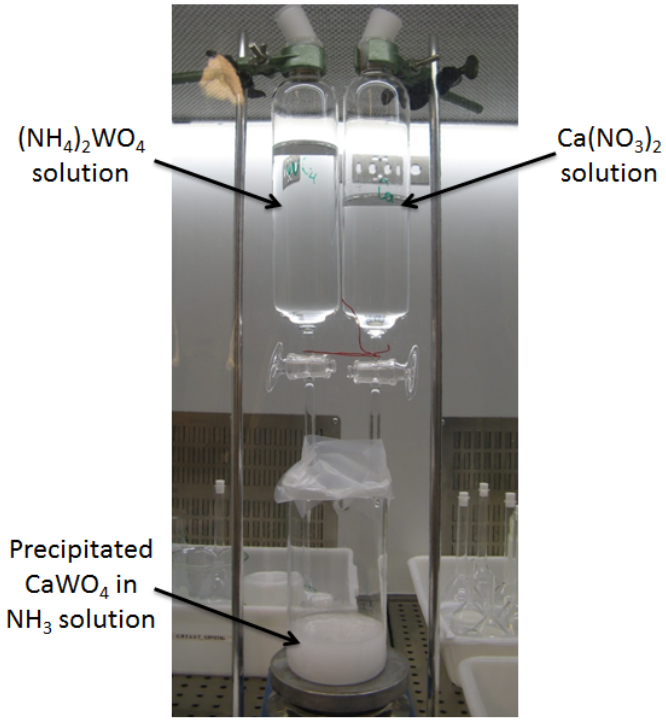

Figure 3.15: Precipitaion of $CaWO_4$. The left dropping funnel contains $(NH_4)_2WO_4$ solution, the right $Ca(NO_3)_2$. They are dropped into a 5 % NH_3 host solution, which is stirred continuously. The $CaWO_4$ forms, turning the solution milky.

Turning the host solution milky. To ensure a complete reaction, the solution is stirred for 3 h in which the $CaWO_4$ forms and falls apart again. This process is called re-crystallisation. After some time, the formation process stabilises. Afterwards, the $CaWO_4$ is left to sediment overnight.

3.4.3 $CaWO_4$ Powder Washing and Calcination

Following the precipitation reaction, the $CaWO_4$ powder undergoes another purification cycle, the washing and the calcination. As described in section 3.1, $CaWO_4$ is not soluble in an alkaline solution. However, impurities attached to $CaWO_4$, e.g. potassium or sodium, can be removed by, e.g. dissolving them during the washing procedure, schematically shown in the top part of figure 3.16.

For this, the NH_3 host solution from the precipitation reaction is carefully decanted (see figure 3.17 (left)), and 200 ml of fresh NH_3 solution is added. This mixture is stirred for 30 minutes and left to sediment for another 30 minutes before the NH_3 solution containing the dissolved impurities is decanted. The whole process is repeated twice, the last repetition is performed with ultra-pure NH_3 solution. Afterwards, the $CaWO_4$ is mixed with clean water and filled into a suction filter. A pump sucks out the water. In total, 2 l of clean water and 200 ml of ultrapure water are sucked

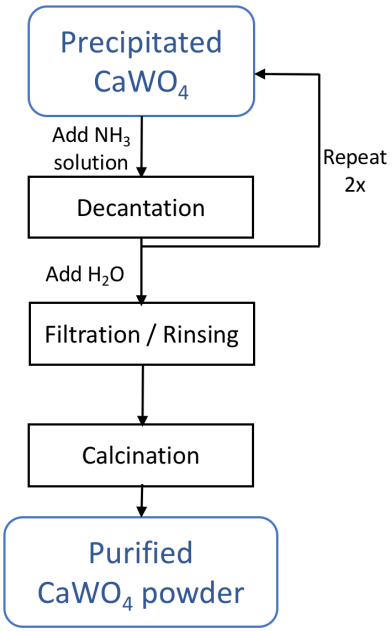

Figure 3.16: Flowchart of the washing and calcination procedure applied to the $CaWO_4$ powder. For the washing procedure, fresh NH_3 solution is added to the $CaWO_4$ powder, stirred for 30 minutes and allowed to settle, followed by removing the NH_3 solution. The process is applied three times in total with NH_3 solution followed by one cycle with clean water. Afterwards, the powder is rinsed and calcinated in a dedicated furnace.

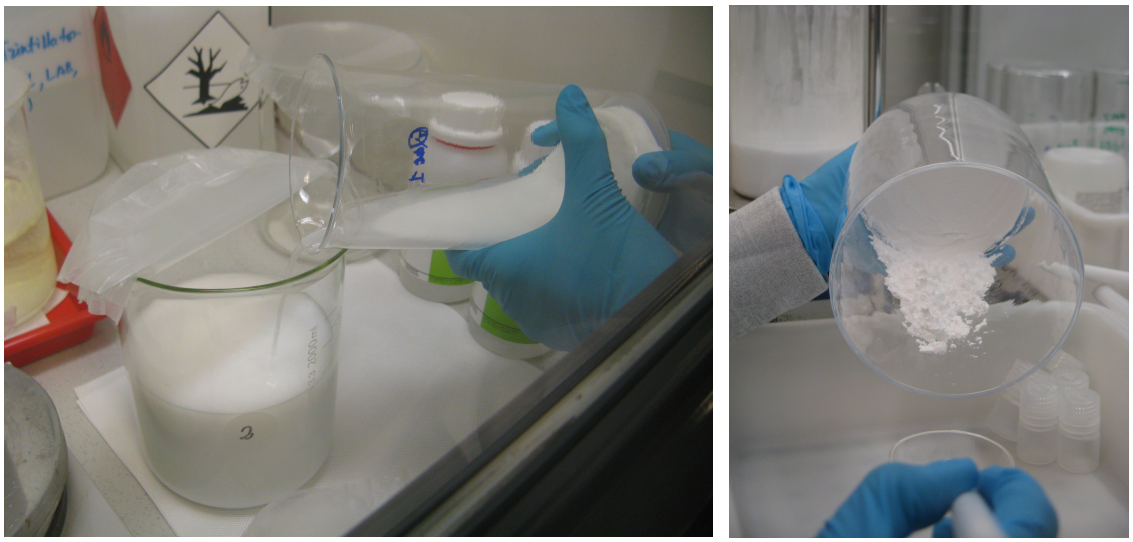

Figure 3.17: Left: Decantation of NH_3 solution used to wash the $CaWO_4$ powder. Right: Transfer of the dried $CaWO_4$ powder from the suction filter, which is used to rinse the powder, to the quartz glass used for calcination.

through the $CaWO_4$ to remove any remnants from the NH_3 solution. The filter containing the $CaWO_4$ is stored overnight in an oven at 60°C to dry the powder. Afterwards, the $CaWO_4$ powder is filled into a quartz glass (see figure 3.17 (right)), and 10 ml of ultrapure water is added to it to achieve a smooth surface of the powder. The quartz glass is placed in the oven at 90°C for 2 h followed by another 2 h at 210°C, which completely dries the powder, called calcination. If an excess of $(NH_4)_2WO_4(WO_4^{2-} + NH_3)$ is present, e.g. due to a slightly off stoichiometry, the high temperature reduces the oxidation number of VI to IV under the creation of a brownish molecule $WO(OH)_2(+N_2 + H_2O)$ which is swimming to the top forming a layer. This layer is removed from the quartz glass, and the pure $CaWO_4$ powder is collected. Each production cycle produces $\sim$50 g of purified $CaWO_4$ powder. In total, $\sim$1500 g has been produced with the purification procedure described in this work.

3.4.4 Results of the Powder Purification

During the development of the different purification steps, several screenings of the raw materials, the $CaWO_4$ powder and the solutions used to extract the impurities were done to determine the efficiency of each cleaning step. These screenings have been performed in the scope of [46]. In this work, the focus is set on the comparison between the final purified $CaWO_4$ powder and the powder produced by the state-of-the-art solid-state production method [46].
As $CaWO_4$ is only soluble in hot acid, typical screening methods like Inductively Coupled Plasma Mass Spectrometry (ICP-MS), where the material has to be dissolved, cannot be used to analyse the $CaWO_4$ powder. In [46], a so-called rinsing

method was developed, in which the $CaWO_4$ powder is leached with a solution of 1 % HNO_3 which reacts with the powder and dissolves impurities from the sample. The solution is afterwards analysed using ICP-MS. As only an unknown part of impurities is dissolved by this method, it cannot be used for an absolute determination of the impurities in the samples. However, a relative comparison of the contaminations in the solution hinting towards a reduction or increase of impurities can be performed. Table 3.2 shows results from a comparison of two powder samples produced from the same raw materials. One is produced via solid state reaction (left), and the other is produced via precipitation reaction with all purification steps above applied to it (right). The table is colour-coded with elements for which the concentration decreased by a factor >2, shown in green, and elements with an increased contamination level by a factor >2 in red. Overall a reduction of most impurities could be measured with this method suggesting a better total radiopurity of the purified powder [46].

Another widely applied screening method is HPGe spectroscopy. This non-destructive method detects radiation emitted by radioactive decays in the sample. It is hence only sensitive to radioactive impurities. To compare the two $CaWO_4$ powder samples, the HPGe screening was performed at the Laboratorio Subterraneo de Canfranc (LSC) in Spain [46]. The results of the screening campaign are shown in 3.3. Except for ^{228}Th, ^{226}Ra and ^{40}K for the solid-state produced powder and ^{40}K for the purified powder, the HPGe detector is not sensitive enough to measure the impurity level of the isotopes. The resulting limits are shown with a confidence level (C.L.) of 95%, measured values with 68% C.L.. The ^{40}K concentration was decreased by a factor of $\sim$3 whereas for ^{228}Th and ^{226}Ra minimal purification factors of $\gtrsim$4 and $\gtrsim$5 can be extracted from these measurements.

Both the ICP-MS rinsing method and the HPGe screening show promising results hinting towards a reduction of impurities in the chemically purified $CaWO_4$ powder. However, they cannot clearly state the absolute reduction of specific isotopes or the overall impurity reduction. One possibility to determine the radiopurity improvement is the operation of a $CaWO_4$ crystal grown from the purified powder as a cryogenic detector. In this way, the results could be directly compared to previously grown TUM crystals like TUM56 (DetA) or TUM40, which were operated as CRESST detectors and for which a radiopurity analysis was performed in [46] and [45] respectively.

sample	$CaWO_4$ (solid state, no purification)	$CaWO_4$ (precipitation, purification)
isotope	concentration [ppb]	
^{7}Li	1.3	0.12
^{9}Be	0.31	<0.0099
^{23}Na	$58 \cdot 10^3$	5
^{24}Mg	770	15
^{27}Al	920	0.49
^{39}K	190	1.1
^{45}Sc	0.045	0.15
^{53}Cr	2.2	0.34
^{55}Mn	0.71	0.019
^{59}Co	0.19	0.53
^{60}Ni	12	3.2
^{63}Cu	1.8	0.083
^{66}Zn	-0.54	0.22
^{72}Ge	0.0016	0.054
^{75}As	10	0.8
^{88}Sr	2.6	6.6
^{89}Y	0.38	<0.0024
^{111}Cd	0.097	0.036
^{115}In	0.036	0.003
^{118}Sn	1.4	0.038
^{121}Sb	0.059	0.019
^{137}Ba	7.8	0.12
^{139}La	0.0097	<0.0017
^{202}Hg	(250)	(150)
^{205}Tl	0.01	0.0097
^{208}Pb	-0.011	0.52
^{209}Bi	0.0018	0.0037
^{232}Th	(0.05)	(0.01)
^{238}U	0.15	< 0.0018

Table 3.2: Results from the ICP-MS rinsing method of two $CaWO_4$ powder samples, one produced via solid state reaction (left) and one produced via the precipitation reaction, including all purification steps (right). Concentration values which are decreased (increased) by a factor >2 are highlighted in green (red). Most isotopes show a reduced relative contamination level. Uncertainties are 30% of the given values. Vales are taken from [46].

sample		$CaWO_4$ (solid state, no purification)	$CaWO_4$ (precipitation, purification)
origin	isotope	activity [mBq/kg]	
^{232}Th chain	^{228}Ra	< 4.5	< 1.4
	^{228}Th	3.0 ± 0.9	< 0.71
^{238}U chain	^{234m}Pa	< 55	< 17
	^{226}Ra	4.7 ± 0.7	< 0.9
^{235}U chain	^{235}U	< 3	< 0.78
	^{227}Ac	< 4.8	< 1.1
other	^{137}Cs	< 1.1	< 0.50
	^{60}Co	< 0.8	< 0.09
	^{40}K	109 ± 10	39 ± 3

Table 3.3: HPGe measurement at LSC of two $CaWO_4$ powder samples. The left column contains values for $CaWO_4$ powder produced by the solid-state reaction. The $CaWO_4$ powder in the right column did undergo all purification steps described above. The values show an improvement in radiopurity of the isotopes ^{40}K, ^{228}Th and ^{226}Ra. For the other isotopes, the sensitivity of the HPGe-detector is not high enough to deduce any information on purification in terms of the respective isotopes. Errors are given with a confidence level (C.L.) of 68%, limits with 95% C.L.. Results are taken from [46].

Chapter 4

TUM93: From Crystal Growth to Successful Detector Operation at LNGS

In August 2019, as the central component of this dissertation, the crystal TUM93 was grown from the purified powder in the stress-optimised Czochralski furnace at TUM (see section 4.1). From this crystal ingot, three CRESST detector crystals were cut by the TUM crystal laboratory (section 4.2) and equipped with a TES by the Max Plank Institute for Physics (MPP). In the framework of this work, the crystals were tested in the cryostat facility at MPP with the support of the local group (see section 4.3), followed by the mounting of these crystals in three dedicated CRESST detector modules (section 4.4). As part of this dissertation, the CRESST setup at LNGS was cooled down, and the three TUM93 detector modules were optimised to low energy thresholds. This is described in section 4.5, and the data-taking periods up to July 2022 are summarised in 4.6. Finally, the exposure history to cosmic radiation and air of each TUM93 detector crystal is summarised in section 4.7.

4.1 Crystal Growth and Annealing of TUM93

To avoid contamination of the purified powder with residuals from former crystal growth processes, the TUM workshop cleaned the crucible mechanically by removing any rest melt, followed by a chemical cleaning with hydrofluoric acid at the Institut für Kristallzüchtung (IKZ) Berlin. Afterwards, the crucible was cleaned with hexane at TUM to remove any fat residuals before it was cleaned with a 5% HNO_3 solution of ultra-pure quality. In the last step, it was washed with ultra-pure water before being dried in a flow box. For the installation, the crucible was covered with a sterile cleanroom glove so no contamination with any insulation materials from the furnace could be introduced (see figure 4.1, left).
The purified powder has to be filled in two steps, melting the first batch before the second is filled, as the $CaWO_4$ material in this form has more volume than the

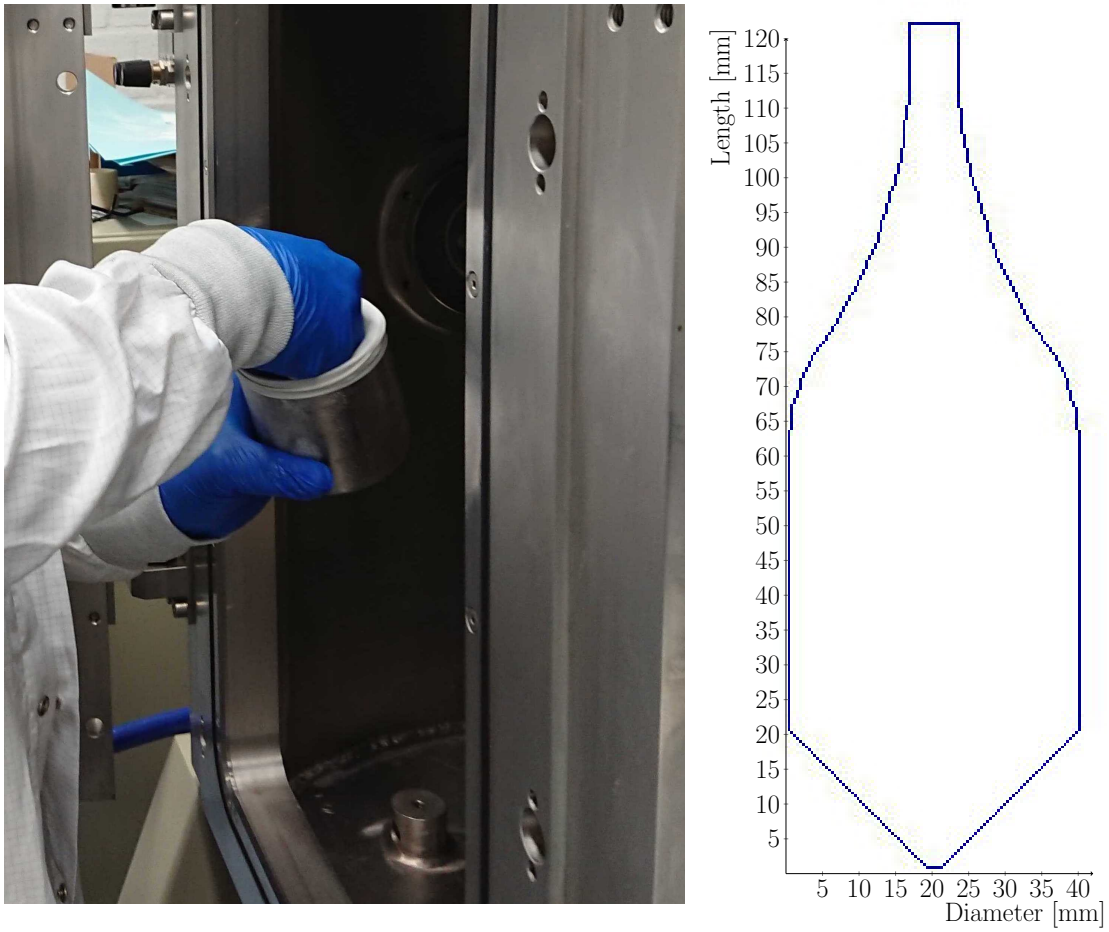

Figure 4.1: Left: Installation of the cleaned crucible in the Czochralski furnace. A clean room glove covers the crucible to avoid contamination of its inside. Right: Predefined geometry of the crystal TUM93 as given to the growth program of the Czochralski furnace.

crucible. In the first step, 939 g was filled and melted before the remaining 565.1 g of powder was added for a total mass of 1504.1 g of powder. The pre-defined crystal geometry given to the growth program is shown in figure 4.1 (right). The seeding was performed at a generator power of 13.6 %, corresponding to the power required to keep the melt at its melting point. The growth took $\sim$30 h and the ingot was held in the after-heater at 1400°C for 24 h and was slowly cooled down afterwards. The final crystal is shown in figure 4.2. It had a length of 122 mm and a mass of 596.81 g. The difference between the seed crystal (dull surface) and the grown crystal (clear surface) is visible.

For the annealing procedure, oxygen with a purity of 99.999% was used to avoid contaminations with other gases during the process. Afterwards, it was stored in the nitrogen locker in the shallow UnderGround Laboratory (UGL) at TUM to avoid cosmic activation before being given to the TUM crystal laboratory for cutting.

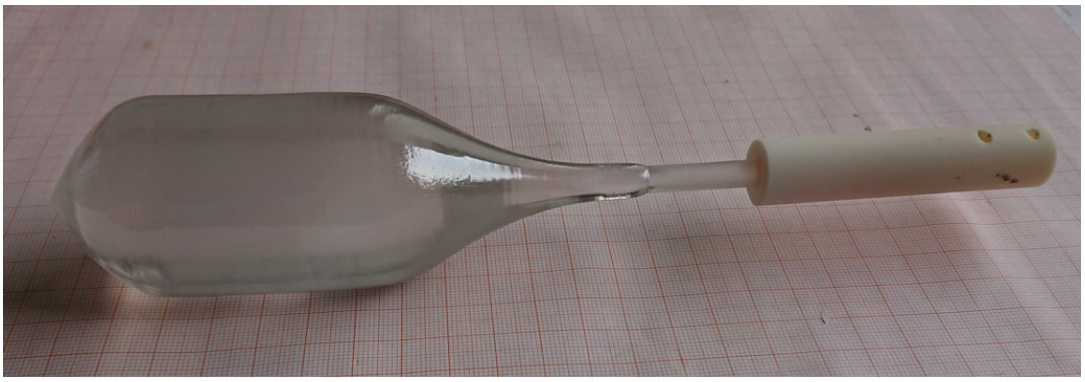

Figure 4.2: Crystal TUM93 just after its growth with a length of 122 mm and a mass of 596.81 g. The crystal still has a slightly grey colouration due to oxygen vacancies. In the next step, the crystal is put into the annealing furnace.

4.2 Fabrication of Three CRESST Crystals

Due to segregation effects during crystal growth, the top part of the crystal is expected to be the cleanest part. Hence, the goal was to cut the CRESST crystals from the highest possible part of the ingot. Unfortunately, TUM93 cracked during the first cut, performed with a diamond saw. The crack originated above the cutting area and went toward the seed (see red arrow in figure 4.3 on the top left). It made the upper part of the crystal not useable for the CRESST detector crystal production. Hence, three crystals with dimension $(20{\cdot}20{\cdot}10)\,\mathrm{mm}^3$ were cut from the lower part of the crystal shown in figure 4.3 on the top right. They are named TUM93A, TUM93B and TUM93C, with TUM93A being the crystal nearest to the shoulder and TUM93C closest to the tail of the ingot. The crystal sides are then ground using SiC powder (grain size 600), which is foamed with water. The measured roughness depth, in this case, is $1\,\mu$m. The side used to produce the TES is polished with silicic acid. After polishing and grinding, the crystals were immediately brought to the nitrogen locker to avoid exposure to radon in the air, as the crystal laboratory is located in a basement.[1]
Each detector crystal was equipped with an evaporated W-TES by the MPP group with the number WI-658-A for TUM93A and WI-658-B and WI-658-C for TUM93B and TUM93C, respectively. All TES were produced in the same evaporation run, hence the same run number in their names. The working principle of such a TES is explained in section 2.2.1.

4.3 Transition Tests

Before mounting the detector crystals in CRESST modules, they must be tested in a test facility at MPP to ensure that the TES is working and has the right transition temperature for operation in the CRESST facility. For these tests, the three crystals

[1]The cutting and polishing was performed by the crystal laboratory at TUM

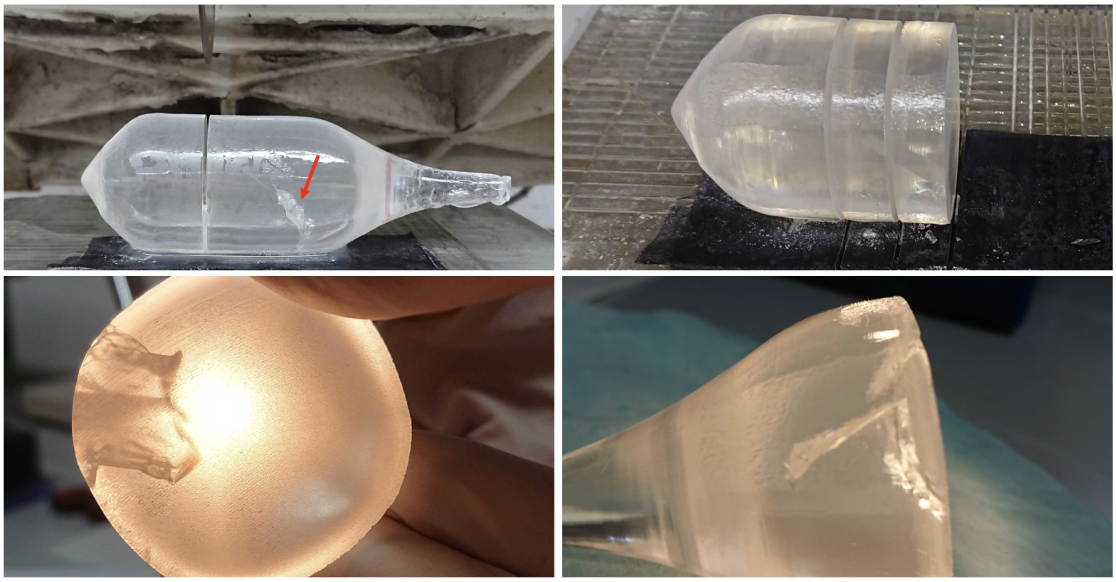

Figure 4.3: Cutting of CRESST detector crystals. During the first cut, TUM93 cracked ∼20 mm above. The crack is shown in more detail in a side view (bottom right) and front view (bottom left). Two CRESST detector crystals were cut from the ingot between the crack (top right) and the first cut and another one from the bottom.

were installed in a test module as shown in figure 4.4, left. The TES are connected to the copper pads via wire bonding before copper plates enclose the module. The module containing all three crystals was installed in Cryostat 1 and measured in run 184. Only TUM93B and TUM93C showed transitions in this run due to a failure in the cabling of TUM93A. Hence, TUM93A was measured in run 185 in the same facility. The measured transitions for all three modules are shown in figure 4.4 (right) for TUM93A in red, TUM93B in blue and TUM93C in black. On the y-axis, the response of the TES as a function of the temperature is shown. When the resistance of the detector changes as the tungsten becomes superconducting, less current flows through the SQUID branch and the signal measured becomes smaller. All transition temperatures are between 11 mK and 18 mK, which is suitable for an operation in CRESST, which operates the detectors at $\mathcal{O}(15\,\mathrm{mK})$. The crystals were cleaned and stored in a nitrogen cabinet following the transition tests.

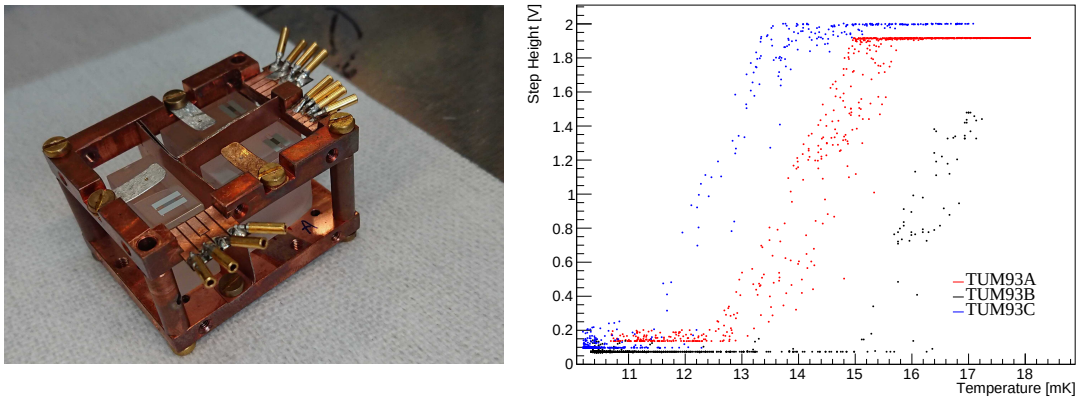

Figure 4.4: Left: Test module with TUM93A, TUM93B and TUM93C installed in it. The detectors are connected to the copper bond pads by wire bonding. Right: Recorded transition during a test run in cryostat 1 at MPP. TUM93A (red) has a transition between 13 mK and 15 mK, TUM93B (black) between 15 mK and 17 mK and TUM93C (blue) between 11 mK and 13 mK.

4.4 Module Design

The detector modules were designed in the following way: The modules are optimised for low energies to study the LEE and the low energy background. Due to the purification, the flat background is expected to be reduced. From the reduction of the intrinsic stress, the rate of the low energy excess should also be reduced if the origin is intrinsic stress. To study the effect of external stress through, e.g. the holding structure, part of it is replaced by softer holding sticks from copper. Hence the standard CRESST-III modules are used, and only the holding sticks are modified: To study α-decays simultaneously to operating the detectors at the lowest energies, two modules have one instrumented $CaWO_4$ holding stick to which part of the energy is transferred, making it possible to reconstruct high energetic events in the crystal. As the number of available readout channels in CRESST is limited, only two detectors have this instrumented stick. Otherwise, all $CaWO_4$ sticks are replaced by copper sticks. The i-stick is installed in modules TUM93A and TUM93B, and only copper sticks in TUM93C. Figure 4.5 shows the module TUM93A in a side view (top left) in which the instrumented stick is nicely visible and in the front view (top right) after the TES were connected to the bond pads via wire bonding. The module TUM93B is shown on the bottom left in a fully mounted configuration with the electrical connectors for the main detectors and the instrumented stick installed on the module. TUM93C is shown on the bottom right in a back view with the back copper plate opened. A screw thread is drilled into the rear plate in which a ^{55}Fe source is screwed for the low energy calibration of the modules. All three modules have been mounted in the CRESST setup. Their exact location is indicated in figure

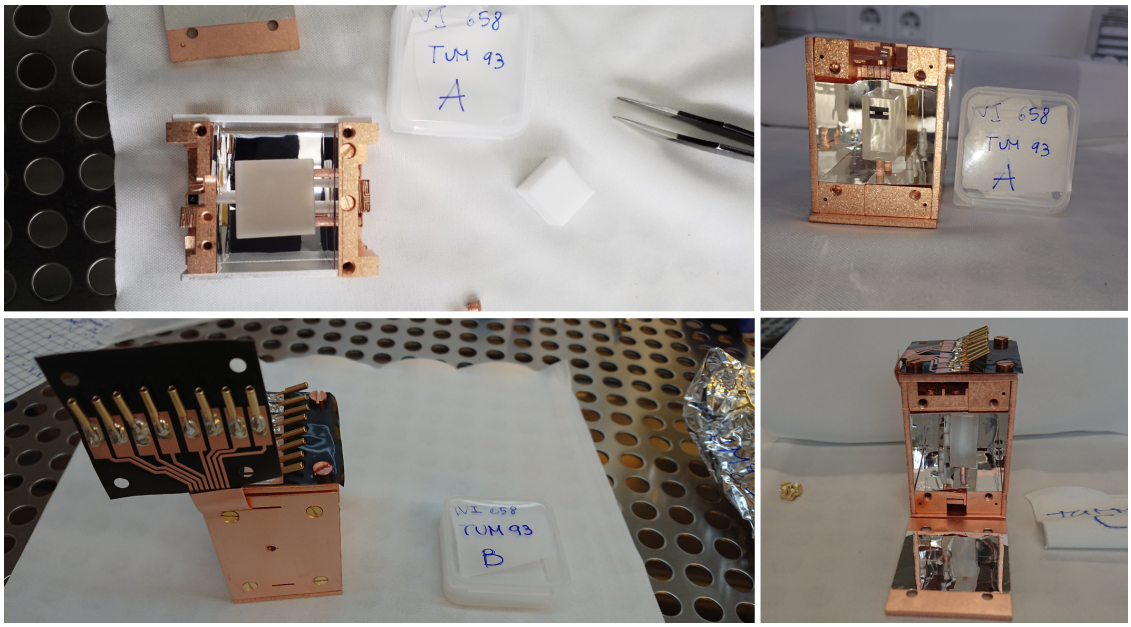

Figure 4.5: Preparation of all three TUM93 detector modules. Top left: TUM93A in a side view. The top and side copper covers are removed. Two copper sticks and one instrumented $CaWO_4$ stick hold the crystal. The TES is visible on the left of the stick. Top right: Front view of TUM93A fully installed and with all three TES bonded. Bottom left: Module TUM93B fully mounted just before being packed for shipment to Italy. The phonon and light detectors can be connected via the connectors on top of the module. The i-stick is connected via the vertical pad with the connectors. Bottom right: Back view of module TUM93C. A screw thread is visible in the back plate of the module. An ^{55}Fe source is mounted in this thread. The detector is held by three copper sticks and does not have a third channel. Hence only one connector pad is visible for this module.

2.15. As part of this thesis, the whole setup was first cooled down in February 2020 and, after a delay due to the COVID pandemic in August 2020 for a second time, this time by the local group. The detector setup started in September 2020.

4.5 Optimisation of Detector Performances

For the operation of each detector, the so-called working point (WP) has to be determined. It is the setting where the detector can be operated stably and has the highest sensitivity. This WP depends on a variety of factors. It strongly depends on the transition temperature of the TES and the shape of the transition. The shape depends on the bias current sent through the W-film. A bias current is chosen for the optimisation, and the detector is heated into its transition by finding a suitable heater setting. Afterwards, several test pulses (TPs) and control pulses (CPs) are sent to the detector, and the detector's response is recorded. For this, the detector is heated just out of the transition to its normal conducting phase and

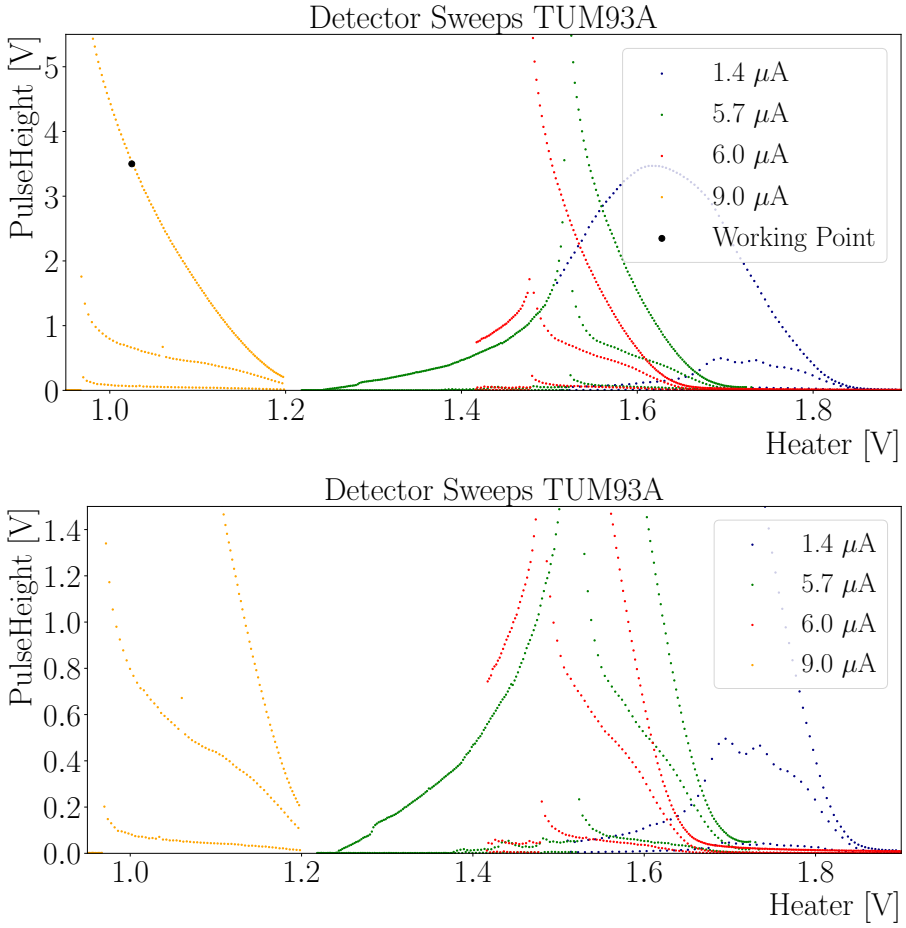

Figure 4.6: Results of heater sweeps of detector TUM93A-Ph. The pulse height of one control pulse and two test pulses is plotted against the heater voltage for different bias currents for the full pulse height spectrum (top) and zoomed in to lower pulse heights (bottom). The final operation point is highlighted in black.

slowly cooled down with a pre-set rate. This process is called a detector sweep, and an example is shown in figure 4.6 for different bias currents sent to the TUM93A detector. The recorded pulse heights of the TPs and CPs are plotted against the heater value (DAC). In the beginning, the pulses are small as the TES is near its normal conducting phase. The colder the temperature, the higher the pulses get until the steepest part of the transition. Afterwards, the pulses become smaller again. These sweeps are performed for several bias currents. Figure 4.6 (top) shows sweeps with several bias currents for the detector TUM93A-Ph for 1.4 μA (dark blue), 5.7 μA (green), 6.0 μA (red) and 9.0 μA (orange) and the bottom shows a zoomed version of the plot. The CP curve is always the top curve, and two TPs are sent, representing the two lower curves.

The goal of the detector setup is to choose the WP in the following way: The CP height should be in the steepest part of the CP curve so that a slight change in temperature leads to a large difference in the CP height. In this way, the active

stabilisation loop can react fast. At the same time, the curve of the lowest TP should be as flat as possible and as high as possible. A flat area in the lowest TP curve makes sure that a change in temperature does not change the energy response of the detector in the low energy range (see figure 4.6 (bottom)). The height of the lowest TP defines how sensitive the detector is to low-energetic pulses. These three requirements must be considered when choosing the bias current and the WP. As a rule of thumb, higher bias currents provide higher sensitivity. However, at a certain bias current, the TES starts to get hysteresis effects, causing instabilities in the TES resistance which should be avoided. These effects occur above a certain threshold in bias current and only happen for TES resistances below the resistance of the shunt. For details, see [103]. Sometimes, the right working point can only be chosen after taking data in different configurations and comparing the results from the preliminary analysis.
When the working point is chosen, a calibration data set (usually with ^{57}Co and ^{55}Fe) is taken with ∼10 test pulse heights sent to the detector. The data is analysed, and the CPE factor (Convert Pulseheight to Energy) is calculated. This value describes the energy a 1 V injected test pulse corresponds to. As a pre-defined test pulse pattern is sent to all detectors simultaneously, this value should be similar in all detectors. For this data-taking campaign, it was chosen to be 3 $\frac{keV}{V}$ for the PDs and 10 $\frac{keV_{ee}}{V}$ for the LDs. This means that the energy range of up to 30 keV gets covered with Tps for the PD and for the LDs, the energy range up to 100 keV of detected scintillation light in the energy units of the PD is covered.
As the calculated CPE value from the analysis usually does not correspond to the pre-defined CPE value, the settings have to be adjusted accordingly without changing the WP of the detector. Afterwards, the sweeps are repeated with the new values and compared to the old ones to ensure that the WP did not change. These sweeps are shown in figure 4.7 for all three TUM93 detectors with the final bias currents and working points indicated in the plot.
The module TUM93B already had problems during cooldown when it took several days to go into transition. Also, the detector setup was challenging due to a structure in the sweeps of the LD and problems of the PD with too high bias currents, which disturbed other detectors. Hence, the sensitivity of this detector is lower compared to TUM93A and TUM93C.

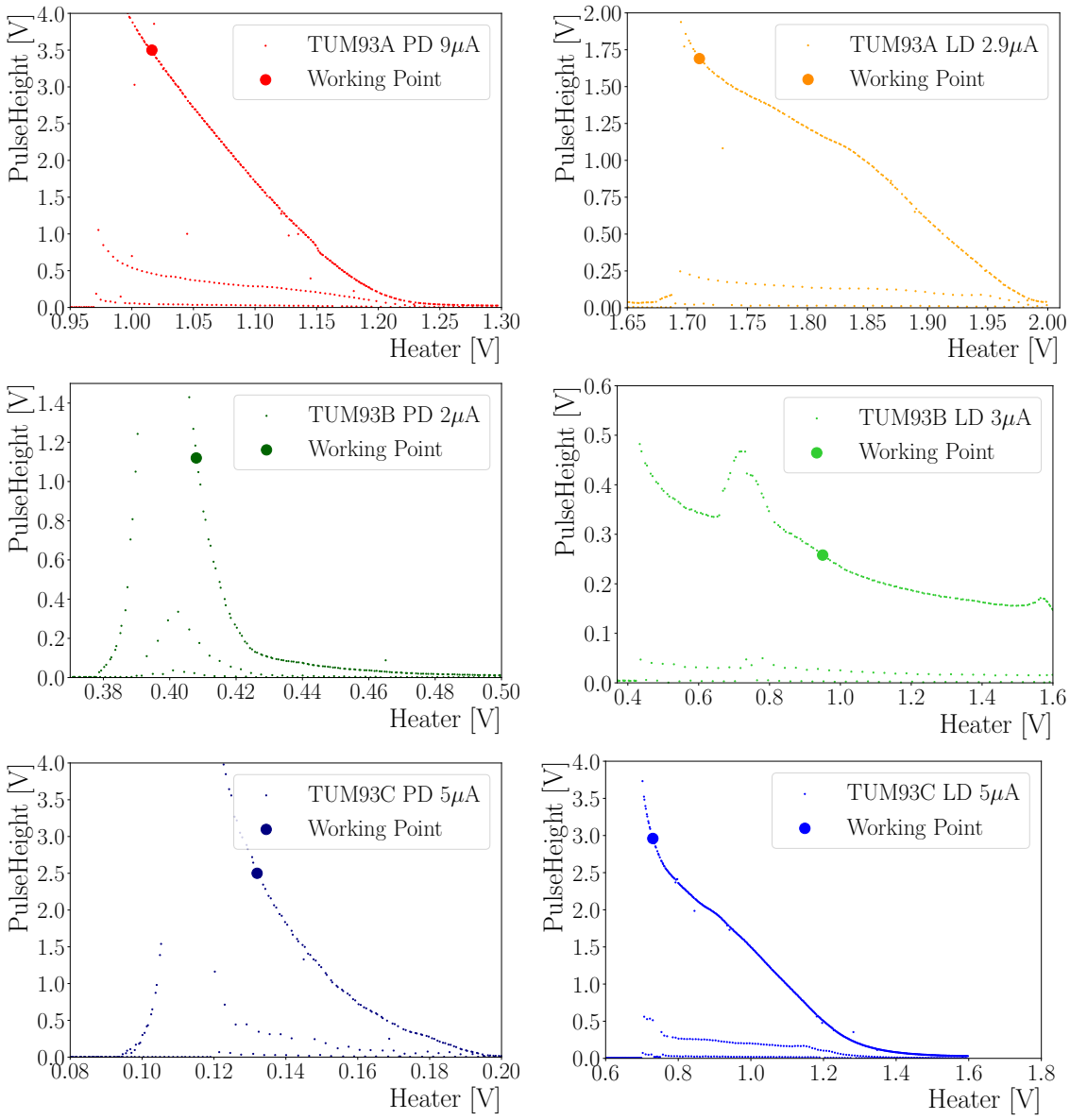

Figure 4.7: Temperature sweeps after the CPE value was set for all TUM93 detectors with the final bias current. The solid dot represents the chosen working point for each detector.

4.6 Data Taking Periods

The background data taking (*Bck*) was started in November 2020. The data-taking is, at the time of writing, still ongoing. The whole data-taking period of the ongoing CRESST run is shown in figure 4.8 until July 2022, the amount of data considered in this work.
At the beginning of the run, the *Bck* data is taken blindly to exclude any bias in the DM and LEE analysis. Only a small percentage of ∼20%, the non-blind data set or training data (indicated by the red fraction), is analysed. This blinding scheme was applied until August 2021. In this data set, problems with magnetic field conditions appeared due to crane maintenance in Hall A at LNGS. Hence, this period was excluded from the blind data set. After the *Bck* set was taken, a neutron calibration (*Ncal*) was performed with an AmBe source to calibrate the nuclear recoil region for each detector for the DM analysis. Following the *Ncal*, another data set, the *PostCal* data set, was taken to study whether a neutron calibration affects the detectors' LEE rate. Starting from this data set, the data was acquired in a non-blind way to allow fast feedback by the analysis team on the LEE rate investigation. To study the temperature dependence of the LEE rate, the detectors were warmed up to a temperature of 60 K and cooled back down to their operation point in the period from October to December 2021. No data was taken in this period. A dedicated data set followed the warm-up, called the after warm-up (*Awu*) data set. In this data set, three other smaller warm-ups were performed to temperatures of 600 mK (Awu II), 200 mK (Awu III), and 3.5 K (Awu IV) and their effect on the LEE rate was studied.

Data Set	Bck	PostCal	Awu I	Awu II	Awu III	Awu IV
	04.11.20	21.09.21	17.12.21	16.03.22	03.05.22	18.06.22
	06.08.21	18.10.21	25.02.22	27.04.22	03.06.22	06.07.22

Table 4.1: Data taking periods from November 2020 to July 2022.

An overview of the data sets is given in table 4.1 indicating the periods in which the data sets were taken. The exposures of these data sets are provided in section 7.1 for the LEE and DM analysis and in section 6.2 for the radiopurity analysis as different sub-sets of data were used for them.

4.7 Storage of Crystals / Exposure to Cosmic Radiation

To enable simulations on the cosmic activation of TUM93 and reduce its exposure to it, the crystal was stored underground in a nitrogen locker as much as possible. Table 4.2 shows the exposure history of the powder and the crystal TUM93 and the detector crystals TUM93A, TUM93B and TUM93C. They have a different history

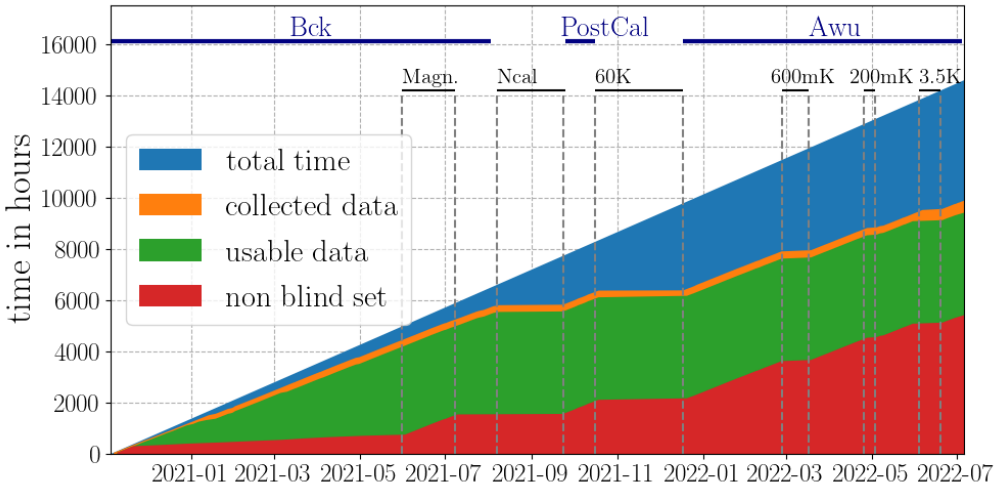

Figure 4.8: Collected data since the start of the data taking in the LEE explorative CRESST run. The blue curve indicates the total time since the start of the data taking, and the percentage of data taken in this time is orange. Green represents the useable time of recorded data (time periods without problems), and red represents the non-blind data set relative to the useable data. A period of data with influence from external magnetic field changes (Magn.) was excluded from the LEE analysis data set. In other periods no background data was taken as a neutron calibration (Ncal), and several warm-ups of the detectors to various temperatures were performed.

due to the crack in the top part of the crystal ingot. TUM93A underwent another annealing procedure to reduce any stress caused by the crack. In addition, TUM93A had to be tested twice as the first TES transition test was unsuccessful due to problems with the detector readout electronics. Several abbreviations indicate the different locations. They are the UGL at TUM with an overburden of 15 m.w.e., the crystal laboratory (CL) located in the basement of a two-story building at TUM, the MPP, also a two-story building and the Hut at MPP, which has no overburden. The crystals were cut in the basement of a two-story building (MS).
Due to the precise tracking of the exposure history of this crystal, simulations could be performed by H. Kluck to study the expected background spectrum originating from it [104]. Figure 4.9 (left) shows the build-up of the cosmogenic activation of ^{3}H for the different periods of TUM93 since its growth. The black curve indicates individual periods of exposure, and the red curve the cumulative exposure. The orange-shaded area marks the data-taking start. From these simulations, an expected cosmogenic background spectrum is derived for a time period of T $\sim$ 240 d and is shown in figure 4.9 (right). Individual components are displayed as coloured, unfilled histograms, the sum by the grey-filled histogram. The derived background spectrum is compared to the measured cosmogenic background in module TUM40. These results are essential for creating a full background model for the three TUM93 CRESST crystals. A detailed description of the simulations is presented in [104].

From	To	Production Step	Location	Atmosphere
-	06.08.19	Powder, Nitrogen Cabinet	UGL, TUM	Nitrogen
06.08.19	12.08.19	Powder, Furnace	Basement, CL	Argon
12.08.19	13.0819	Crystal Growth	Basement, CL	Argon
13.08.19	17.08.19	After Heater	Basement, CL	Argon
17.08.19	21.08.19	Annealing	Basement, CL	Oxygen
21.08.19	28.08.19	Nitrogen Cabinet	UGL, TUM	Nitrogen
28.08.19	-	Crystal Cutting	Basement, MS	Air
A				
02.09.19	09.09.19	Annealing	Basement, CL	Oxygen
03.09.19	13.09.19	Surface Polishing	Basement, CL	Air
13.09.19	18.09.19	Nitrogen Cabinet	UGL , TUM	Nitrogen
18.09.19	02.10.19	TES Production	Basement, MPP	Vacuum
02.10.19	02.10.19	TES Test Preparation	Basement, MPP	Air
02.10.19	15.10.19	Cryostat	Hut, MPP	Vacuum
15.10.19	15.10.19	TES Test Preparation 2	Basement, MPP	Air
15.10.19	21.10.19	Cryostat	Hut, MPP	Vacuum
21.10.19	03.02.20	Nitrogen Cabinet	Basement,MPP	Nitrogen
03.02.20	03.02.20	Car Transport Italy	-	Nitrogen
03.02.20	-	Installation CRESST	CRESST	Air/Vacuum
B/C				
07.09.19	07.09.19	Surface Polishing	Basement, CL	Air
07.09.19	18.09.19	Nitrogen Cabinet	UGL	Nitrogen
18.09.19	02.10.19	TES Production	Basement, MPP	Vacuum
02.10.19	02.10.19	TES Test Preparation	Basement, MPP	Air
02.10.19	15.10.19	MPP cryostat	Hut, MPP	Vacuum
15.10.19	03.02.20	Nitrogen Cabinet	Basement,MPP	Nitrogen
03.02.20	03.02.20	Car Transport Italy	-	Nitrogen
03.02.20	-	Installation CRESST	CRESST	Air/Vacuum

Table 4.2: Overview of the history of the TUM93 crystals. All three crystals had a common history until they were cut from the ingot. Afterwards, the crystal TUM93A was treated differently than TUM93B and TUM93AC. As TUM93A was cut near the crack in the crystal ingot, it underwent another annealing procedure to avoid cracks during the crystal polishing. In addition, crystal TUM93A had to be tested twice in the MPP cryostat facility, as the first test was unsuccessful. The different locations are the UGL at TUM with an overburden of 15 m.w.e., the crystal laboratory (CL), located in the basement of a two-story building at TUM, the MPP, also a two-story building and the Hut at MPP which has no overburden. The crystals were cut in the basement of a two-story building (MS).

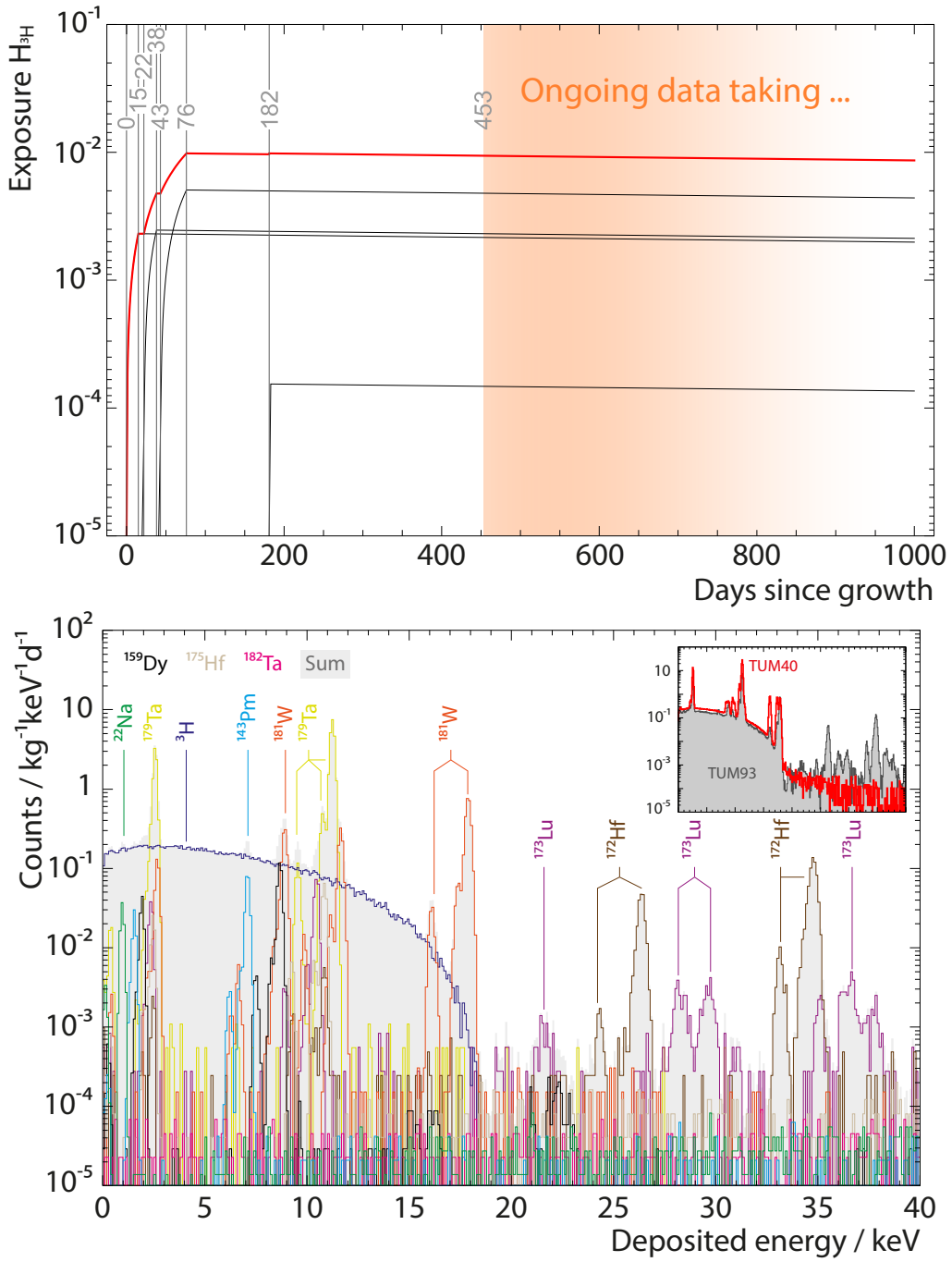

Figure 4.9: Top: Production of ^{3}H through cosmic activation in TUM93. The black periods indicate the individual periods of exposure, and the red curve is the cumulative exposure. The orange-shaded area indicates the data-taking. Bottom: Expected cosmogenic background in TUM93. Individual components are represented by the coloured histogram and the sum by the grey-filled histogram. Both figures are taken from [104].

Chapter 5

General Analysis Methods

In this work, the detector module TUM93A is analysed in detail over a broad energy range, from the study of the LEE at several eV to an analysis of the background up to 800 keV and an α-decay study in the energy range $\mathcal{O}$(MeV). In addition, a radiopurity analysis of the modules TUM93B and TUM93C is performed. These analyses have several basic steps in common, which are described in this chapter. These steps are mostly state-of-the-art analysis steps, with the exception of two energy reconstruction methods developed in this thesis. The specific steps applied to the low energy and radiopurity analyses are discussed in chapters 7 and 6, respectively. The main software package utilised in this work is CAT (Cryogenic Analysis Tools) [43].[1] It is based on the ROOT analysis framework [105] and is easily extendable by user-written macros. The following sections give an overview of the continuous data stream, recorded from the detectors in section 5.1 and the different analyses performed with CAT in section 5.2. Afterwards, the basic analysis parameters are described in section 5.3 followed by a summary of different pulse reconstruction methods in section 5.4. The Optimum Filter threshold trigger is described in section 5.5. Finally, basic data selection criteria are described in section 5.6.

5.1 Description of the Continuous Data Stream

In CRESST-II, the data was recorded by a DAQ with a hardware trigger threshold which recorded each signal exceeding a pre-defined threshold after passing a Bessel filter. This conventional DAQ has disadvantages, e.g. fixed window lengths or preset trigger thresholds. Therefore, in CRESST-III, the data is additionally recorded with a continuous DAQ with a sampling rate of 25 kHz. The whole output of the detector, the stream, is digitised and saved to disc. This provides high flexibility in the processing of the data. It allows for different sizes of event windows, software-based trigger algorithms which can be changed and optimised iteratively, as well as a change in trigger groups of detectors, high statistics simulation on the stream to determine trigger and signal survival probabilities and a high statistics study of

[1] CAT is developed by M. Stahlberg (MPP)

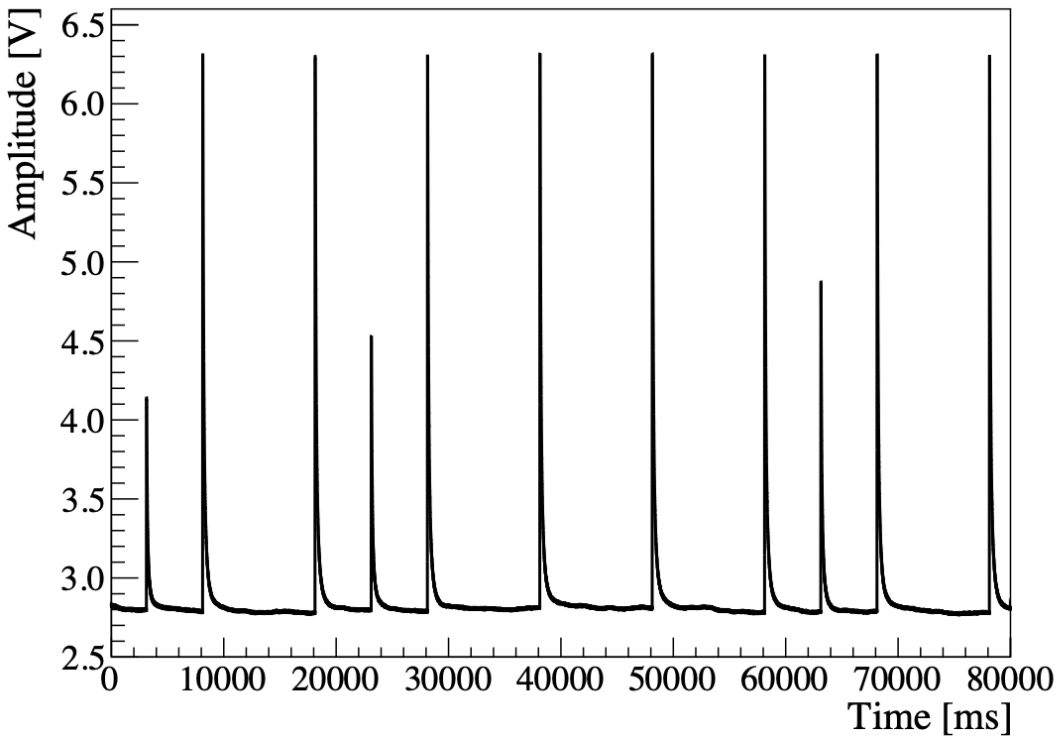

Figure 5.1: 80 seconds of the recorded stream for detector TUM93A-Ph. The baseline state of the SQUID determines the baseline level and is at ∼2.8 V in this case. Several control and test pulses are on the stream. The control pulses are sent before and after each TP. The TPs are sent with different amplitudes and are visible between the large control pulses. In addition, empty baseline traces are regularly recorded by the standard DAQ instead of a TP.

the baseline and the detector noise. A significant advantage of the continuous data stream is the possibility of applying an optimised filter to the data before triggering, which can help reduce noise and lower the trigger threshold. Figure 5.1 (left) shows a period of the continuous data stream of TUM93A-Ph, the phonon detector of module TUM93A. A pattern of CPs and TPs is visible on the stream. The CPs represent the pulses with the highest pulse heights, the TPs are the smaller pulses. All analyses performed in this work are based on the continuously recorded data stream.

5.2 Analysis Chains

In total, three different analyses were performed on the TUM93 detectors:

- Radiopurity analysis using the e^-/γ-band of TUM93A and TUM93C (see section 6.4).

- Radiopurity analysis using the α-band of TUM93A, TUM93B and TUM93C (see section 6.3).

- Low-energy / DM analysis with TUM93A-Ph as the main detector and TUM93A-L as the light (veto) detector, and with the TUM93A-L detector as a stand-alone detector to study the difference between both detectors (see chapter 7).

All these different analyses have the same basic steps at the beginning described in the following.

5.3 Analysis Parameters

A typical event recorded by TUM93A-Ph is shown in figure 5.2. The standard record length is 16384 samples with a time base of 40 µs. This corresponds to a total record length of 655.36 ms. One-quarter of the pulse is the so-called pre-trigger region which gives information about the baseline before an event and is needed to calculate some pulse parameters. In the following, the most important standard pulse parameters, as they are automatically calculated by CAT, are explained:

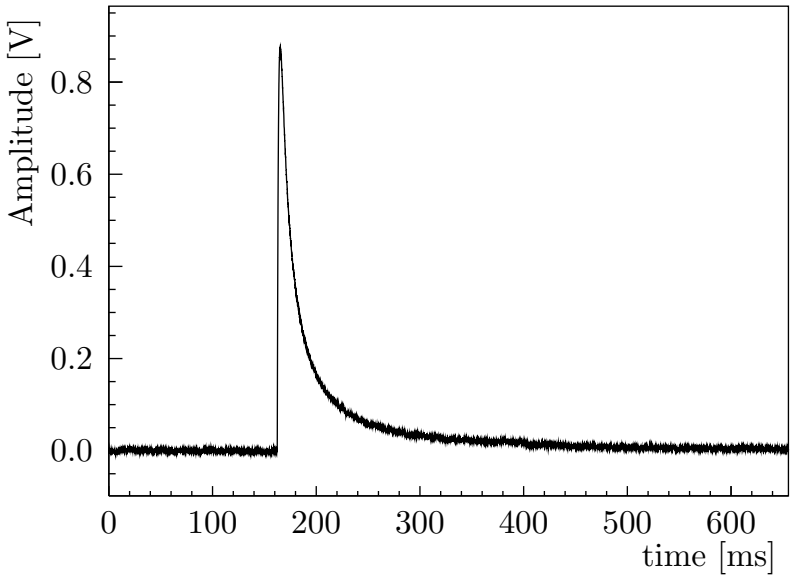

Figure 5.2: Typical particle event recorded by the DAQ. It consists of 16384 samples with a time base of 40 µs corresponding to a record length of 655.36 ms. One-quarter of the pulse is the pre-trigger region (from the start of the record window until 160 ms) which provides information about baseline parameters.

TimeStampDAQ: This parameter stores the CPU timestamp in Unix time at

which the pulse is recorded. For this, the time since the file start is added to the Unix time of the file start. The unit is [s].
Measuring Time: Instead of giving absolute time information as the TimeStamp-DAQ, the Measuring Time parameter gives the time since the start of each written file for each event in [h].
BaseLineDiff: The baseline difference between the average of the first 50 and the last 50 samples of the record window is evaluated and given in [V].
BaseLineRMS: This parameter describes the Root-Mean-Square of a linear fit to the pre-trigger range of the pulse and provides a measure for the noise condition of the detector. The unit is [V].
PulseHeight: The PulseHeight is defined as the difference between the maximum of a pulse and the baseline level. It is given relative to the baseline voltage in [V]. To determine this parameter, a moving average of 50 samples is used by CAT to reduce noise effects on evaluating this parameter.
PeakPositon: The parameter PeakPosition gives the time since the start of the record window at which the pulse reaches the PulseHeight value. The unit of this parameter is [ms].
Onset: The Onset parameter gives the time of the first sample (going backwards from the PeakPosition) at which the sample falls below three times the Baseline RMS in [ms]
DecayTime: The time between the PeakPosition and the sample at which the pulse decayed to 10 % of its original PulseHeight.
RiseTime: This parameter is defined as the time between the Onset of the pulse and the time when the pulse height reaches 90% of the PulseHeight of the pulse
MinimumDerivative: This value describes the minimum value of the derivative of the pulse, numerically evaluated as the difference between two consecutive samples.
Delta-V: The parameter is not implemented in CAT but can be calculated by dividing MinimumDerivative/BaseLineRMS for each pulse. It is sensitive to delta spikes which originate from electronic spikes.
TestPulseAmplitude (TPA): The injected test pulse amplitude in [V] as set on the pulser is saved in the TPA parameter. It is later used to linearise the detector.

5.4 Pulse Amplitude Reconstruction

The PulseHeight parameter, calculated for each pulse, is only a rough estimator for the real energy of an event. It is, e.g. biased due to noise, as the maximum of the pulse is more likely located at a positive noise fluctuation. The noise can also hide small pulses and worsen the detector's analysis threshold. In addition, the PulseHeight parameter can only be used to estimate the energy of pulses from the completely linear range of the TES as the pulse shape changes outside of this linear region. For very high energetic pulses, the SQUID can lose so-called Flux-Quanta, meaning that the baseline reconstruction fails and the PulseHeight parameter is lower than it should be. As this work focuses on the analysis of the low energy region $\mathcal{O}$(10-100 eV), medium energy region $\mathcal{O}$(10-100 keV) and the very high energy region

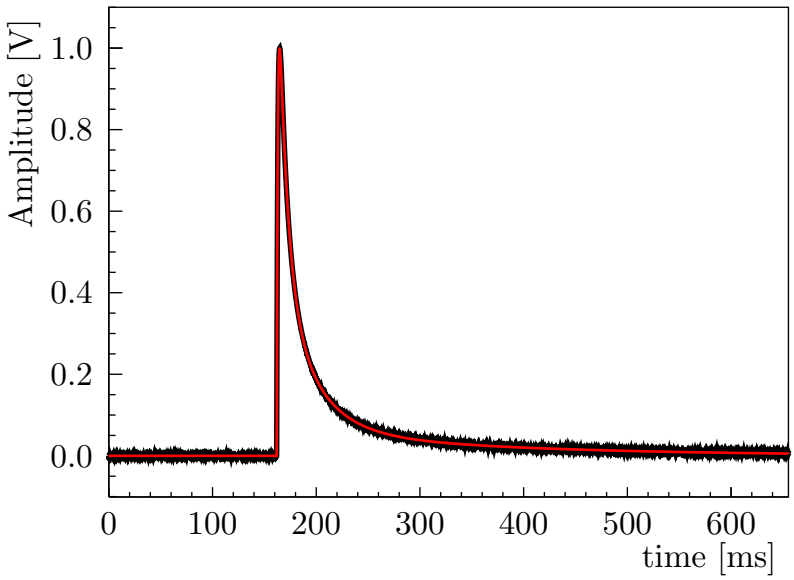

Figure 5.3: Template created for TUM93A-Ph from the 5.9 keV iron peak (black) and parametric fit of the template (red). The parametric fit eliminates the noise on the template.

$\mathcal{O}$(MeV) of the detectors, different reconstruction algorithms are used to reconstruct the energy of each event. The four different reconstruction methods are described in the following:

5.4.1 Template Fit

The template fit, also called standard event fit, is based on the assumption that all signals can be described by an analytical function or a typical pulse shape described in [42]. A template with the desired pulse shape (for a specific event class) has to be created as a first step. For this, several pulses from a similar energy range of a detector in the fully linear range of the TES (e.g. a calibration line) are averaged and normalised to one. The pulses are selected carefully so they do not contain artefacts. In addition, the number of pulses should be at least $\mathcal{O}(100)$ to reduce the noise in the averaged template. Figure 5.3 shows a template for TUM93A-Ph averaged from events of the 5.9 keV iron line as an example. To further reduce the noise on the template, a parametric fit of it is performed using again the pulse model described in [42] (see figure 5.3 red).
This parametric template is fitted to all particle pulses together with a baseline fit. An algorithm is minimising the root mean square (RMS) between the pulse and the template/baseline by shifting the pulse horizontally and vertically and scaling it to the best-fit amplitude (see figure 5.4 left). The fit parameters are stored for each pulse:

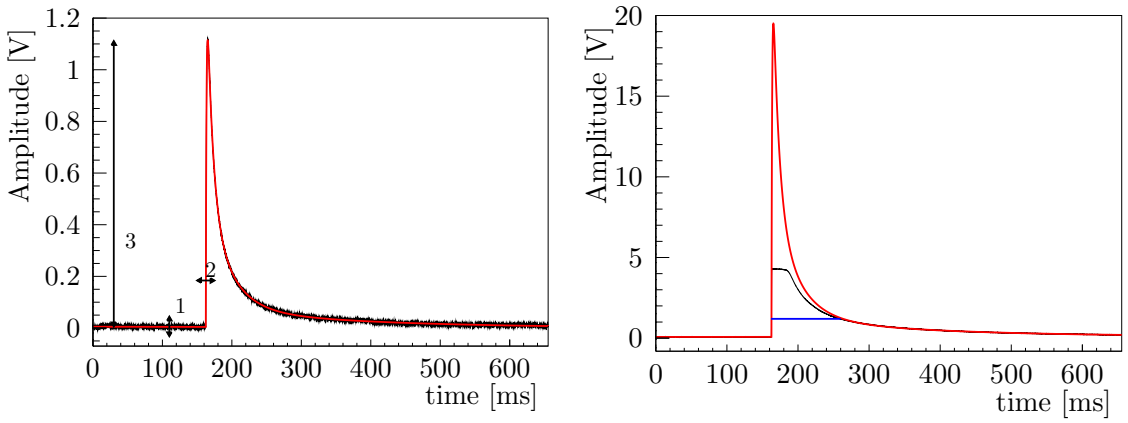

Figure 5.4: Left: Fit of the template (red) to a particle pulse (black). The template is shifted vertically (1), horizontally (2) and scaled (3) to minimise the RMS. In addition, the baseline is fitted by a baseline model. Right: Truncated template fit to a saturated pulse. The Fit uses information about the pulse (black) below the truncation limit (blue) and ignores any pulse samples above this limit. The scaled template is shown in red.

Amplitude: The amplitude is the height the template had to be scaled to fit the pulse best. It is a more robust estimator than the PulseHeight parameter described above and is given in units of [V].
RMS: The RMS estimates the difference between template and pulse. This value should be similar for all pulses [V] of the same pulse class.
OptimumShift: The time the template had to be shifted to fit the event best in [ms].

Truncated Template Fit

As described above, the template fit assumes that the fitted pulses have the same pulse shape as the template. This assumption is, however, only valid in the linear range of the TES transition. As described in section 2.2.1, the transition curve is linear in its steepest part and flattens towards the top until the TES is completely normal conducting. This effect strongly influences the pulse shape of pulses with higher energies heating the TES above this linear range. Their pulse shape starts to differ. They become truncated. The truncated template fit considers this by ignoring all the pulse samples above a certain so-called truncation limit and only fitting the template to the subset of the pulse below this limit (see figure 5.4 right). In black, a saturated pulse is shown. The blue line indicates the truncation limit, and the red pulse is the scaled template fitted to the pulse below the truncation limit.
To determine the truncation limit, all particle pulses are fitted with the standard template fit. The results are plotted in an RMS vs fitted amplitude histogram (see figure 5.5 for an example of the detector TUM93A-Ph). For this detector, the RMS

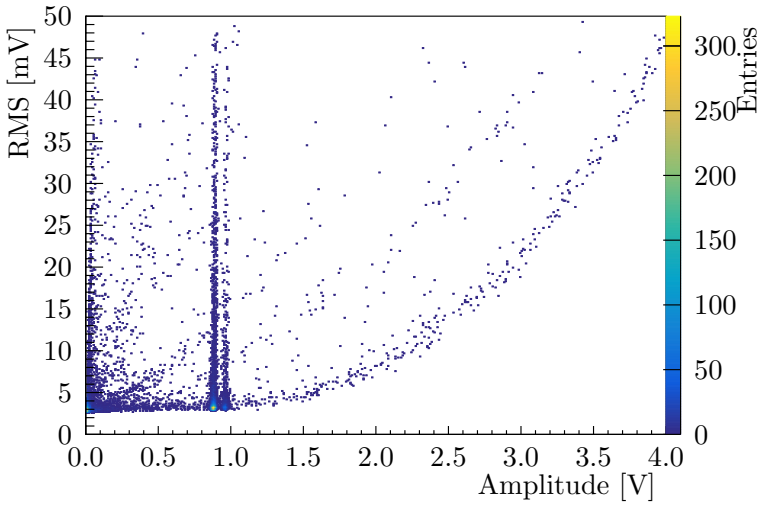

Figure 5.5: Truncation limit determination for TUM93A-Ph. All events are fitted with a template fit. The fit RMS is plotted against the reconstructed amplitude. Visible are the two iron calibration lines at around 0.9 V. The RMS rises at a value between 1.3 V and 1.5 V. The truncation limit was chosen at 1 V in a conservative approach.

starts to rise at a value of 1.3-1.5V. In a conservative approach, the truncation limit should always be slightly below this value. For this detector, it was determined to be at 1 V.

5.4.2 Parametric Fit

The standard truncated fit cannot be applied to reconstruct truncated pulses for some detectors. This is the case for the detector TUM93A-L and was also observed for the LD Michael of module TUM40 from a CRESST-II data taking campaign. In figure 5.6, the test pulses of the TUM40 phonon detector (left) are compared with the test pulses of the TUM40-LD Michael, taken from [106]. The pulses are normalised by the injected test pulse energy in volts. The standard pulse model assumes that the pulses below a specific energy (the truncation limit) follow the standard pulse model, so we use the truncated fit to estimate their energies. This is visible for TUM40 on the left. All pulses overlap in the lower part of the test pulses. For the detector Michael, this is not the case. The more energy the pulses have, the narrower they get when scaled by the injected energy. This means that the template fit cannot determine the right energy. This effect is called self-heating and was studied in [106, 103]. It describes a temperature-dependent loss of heat in the TES. In [103], it was also shown that this effect is visible when taking a transition curve with the same bias current used for the operation of the TES.
Hence, using a parametric fit model, which describes the shape of the transition,

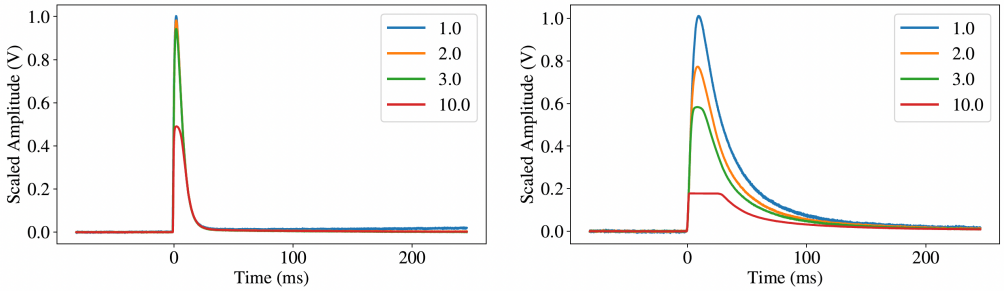

Figure 5.6: Comparison of the test pulses of TUM40 (left) and Michael (right) scaled by their injected voltage. The test pulses of TUM40 follow the pulse model assumption in which the width of the pulses below the truncation limit scales linearly with the injected voltage/energy. For the detector Michael the test pulses do not scale linearly with the injected voltage. Hence no truncated template fit can be applied to reconstruct the pulses. Figure taken from [106]

can take the self-heating of the TES into account. The parametric fit considering the transition curve was developed in [43] and extended for the use in this thesis. It expands the standard parametric pulse model by parameters describing a generalised Richards curve representing the transition's shape and the pulses' truncation.
The curve is described by the formula:

$$Y(x) = A \cdot \left(1 - \left(\frac{C + Q}{C + Qe^{-Bx}}\right)^{1/\nu}\right)[43] \tag{5.1}$$

Which is constructed in a way that Y(0) = 0. This formula can be further simplified by introducing the parameter R as C/Q:

$$Y(x) = A \cdot \left(1 - \left(\frac{R + 1}{R + e^{-Bx}}\right)^{1/\nu}\right). \tag{5.2}$$

This formula is fitted to the measured transition curve of TUM93A-L starting at the operation point (see figure 5.7, left). The curve is scaled to represent the PulseHeight or the measured voltage on the y-axis plotted against the injected voltage on the x-axis. The Richards curve is fitted in the upper part where the saturation has the strongest effect.
For a combination of the standard parametric fit model and the transition curve description, the parameter x is replaced by the pulse shape of the signal ΔT(t), obtained from a parametric fit of a non-truncated template [43].
The fit function is thus described by

$$Y(t) = A \cdot \left(1 - \left(\frac{R + 1}{R + e^{-Bn\Delta T(t,O)}}\right)^{1/\nu}\right)[43]. \tag{5.3}$$

With the parameters $\Delta T(t, O)$ fixed beside the onset of the pulse O and the amplitude from the pulse model. The transition curve parameters obtained from the transition curve fit are also fixed. The parameter n is the linear scaling factor. It is used to normalise the fit so that the amplitude determined in the non-saturated

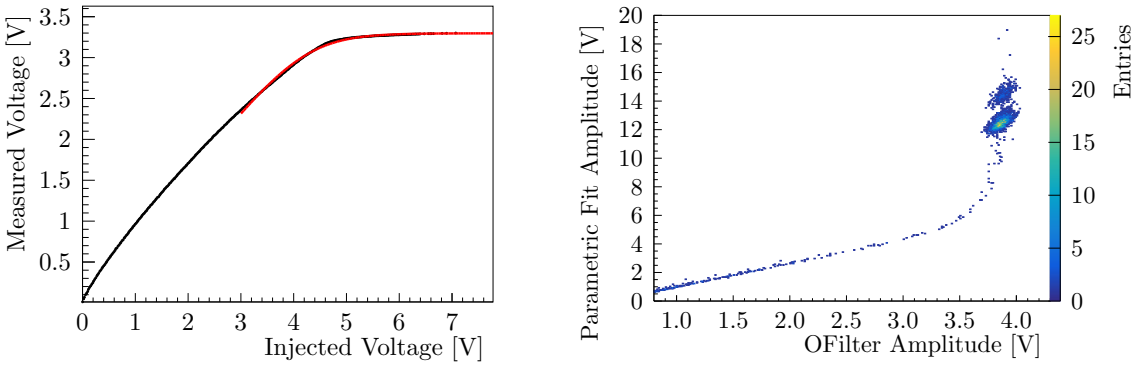

Figure 5.7: Left: Fit of the generalised Richards curve to the top part of the transition of TUM93A-L. The transition curve is scaled to represent the injected voltage on the x-axis and the reconstructed voltage by the detector on the y-axis. The self-heating effect is included in the pulse shape of the transition. Right: Results of the amplitude determined with the parametric fit of TUM93A-L as a function of the amplitude determined by the Optimum Filter reconstruction method described in the following. The parameter n is set to one for this fit. It has to be tuned so that both amplitudes agree with each other. Afterwards, the two nicely resolved direct LD hit iron peaks can be used to calibrate the detector.

region corresponds to the amplitude of a different reconstruction method, like the template fit or the Optimum Filter described later. Figure 5.7 (right) shows the results of the parametric fit to TUM93A-L with respect to the determined amplitude of the Optimum Filter of TUM93A-L applied to the same data set. The factor n is set to one for this fit. It is then adjusted so that both amplitudes agree in the linear region. Afterwards, the two ^{55}Fe lines reconstructed by the parametric fit are used for the energy calibration of the detector. The reader is referred to [43] for a more detailed description of the fit.

5.4.3 Saturation Time

This method was developed in the scope of this thesis. It can reconstruct saturated pulses which suffer from SQUID Flux-Quantum-Losses (FQLs) or pile-ups. As described in section 2.2.1, a fast rise of the signal in the SQUID can cause FQLs meaning that the absolute baseline value of the SQUID changes. This happens mostly for very high energetic events, and for α-decays with energies $\mathcal{O}$(MeV), nearly all pulses suffer from FQLs. Figure 5.8 (left) shows an example of an α-event. The baseline value drops by $\sim$1.5 V. As the FQLs are lost in the rise of the pulse, the saturated PulseHeight, which is around 4 V for this detector, is also reduced by a value of 1.5 V.

The truncated template fit assumes the baseline level to be constant. Hence, it can not be applied to these pulses. This can be solved by a program that first checks whether the pulse is saturated and afterwards determines the difference between the

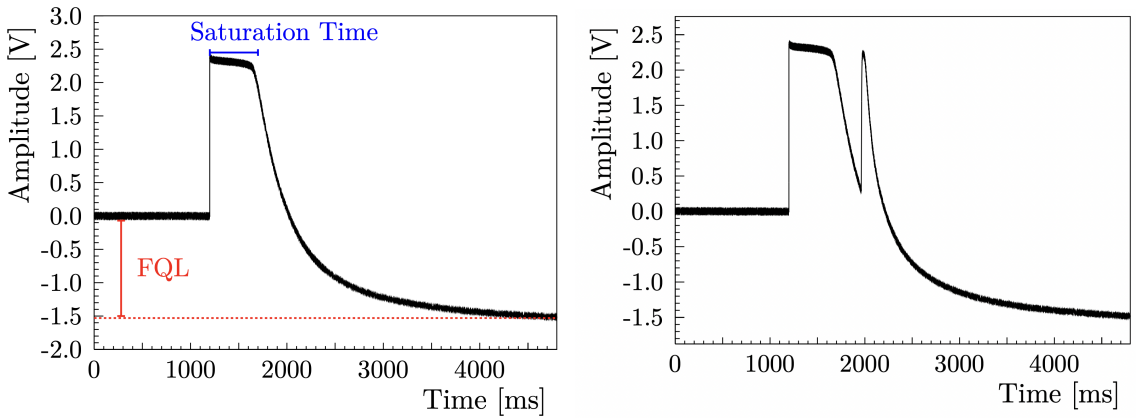

Figure 5.8: Left: Typical α-decay pulse. The high energy deposited in the crystal causes the pulse to have a fast rise time, leading to an FQL in the squid. This shifts the baseline level down (see red line) and also reduces the PulseHeight (which should be around 4V) by the same amount. This effect is corrected by shifting every sample after the onset up by the FQL value. Right: Pile-up of a test pulse with an α-event. These pile-ups make reconstruction with, e.g. a truncated template fit impossible.

baseline level in the pre-trigger range and the PulseHeight of the saturated Pulse. This value is compared with the nominal PulseHeight of a saturated pulse without FQLs. After the Onset, all pulses samples are shifted upwards by this difference. The result is a pulse corrected for the SQUID's FQLs. A truncated template fit could now be applied to the pulses. This, however, does not work for α-decay pulses as the pulses are several seconds long. In CRESST, we send test and control pulses every 5 seconds so a pile-up with an α-event is visible in most of the α-pulses (see fig. 5.8 right).
The saturation time analysis is designed to be insensitive to these parts of the pulse to deal with the pile-ups located in the pre-trigger range and the decaying flank of the pulse. The method determines the baseline in a few samples before the onset and the saturation time in channels from the Onset until the pulse reaches 90% of its corrected PulseHeight, indicated by the blue line. This makes the method sensitive to the time the pulse stays in saturation which is connected to the energy deposited in the crystal. In addition, the integral of the pulse in this area can be calculated. The saturation time reconstruction is impossible for pulses not wholly saturated, i.e., the TES does not reach its full normal conducting state. Hence, the method cannot be used for a calibration down to low energies of the detector. With the additional integral calculation, also non-saturated pulses can be reconstructed.

5.4.4 Optimum Filter

Another reconstruction method is used to analyse the low energy events in CRESST, the so-called Optimum Filter (OF or OFilter). The speciality of the OF is that it

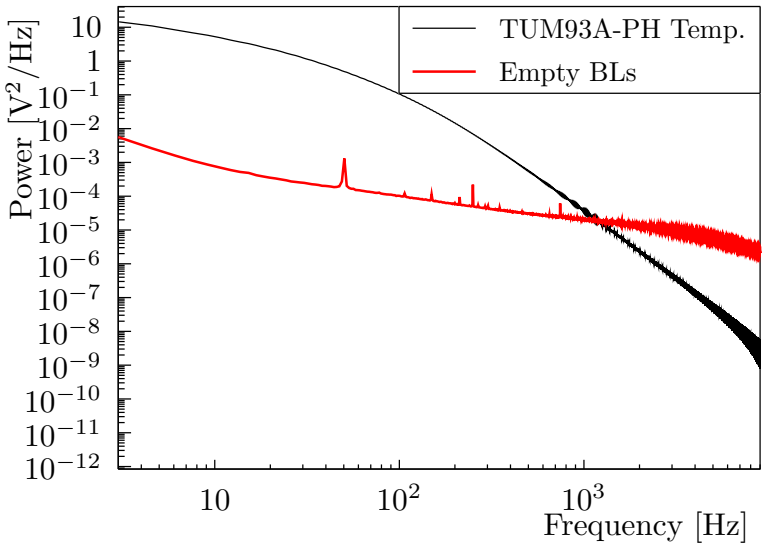

Figure 5.9: Noise power spectrum (NPS) of the detector TUM93A-Ph (red). It is created from randomly collected empty baselines/noise traces of the data stream. In comparison, the frequency representation of the parametric template of TUM93A-Ph is shown in black.

maximises the Signal-to-Noise ratio following the idea by Gatti and Manfredi [107]. The OFilter amplifies pulse-like frequencies and suppresses noise-like frequencies. Each pulse trace is a combination of its amplitude A, normalised pulse shape s(t) and white noise with value n(t). So it can be described by

$$y(t) = A \cdot s(t) + n(t) \tag{5.4}$$

With the Noise Power Spectrum (NPS) N(ω), a measure of the frequency composition of the baseline, i.e. the Fourier transformation of n(t). The transfer function of the optimum filter in frequency space H(ω) is

$$H(\omega) = K \cdot \frac{\widehat{s}^*(\omega)}{N(\omega)} \cdot e^{-i\omega\tau_M} \tag{5.5}$$

Where K is a normalisation constant set in a way that the OFilter amplitude corresponds to the truncated fit amplitude, $\widehat{s}^*(\omega)$ is the complex conjugate of the Fourier transform of the pulse shape, and τ_M is the phase. The transfer function is used to re-weight a recorded pulse in the frequency domain. In the process of Fourier transforming, the phase information of the pulse is lost. Hence, the back-transformed filtered pulse is symmetric around the onset.
Knowledge about the NPS and normalised pulse shape is needed for the method. For the normalised pulse shape, the same template as created for the template fit can be used (see figure 5.3). The NPS is created from a number $\mathcal{O}$(100-1000) noise samples, called empty baselines. They are selected randomly during data taking. An NPS from the empty baselines of TUM93A-PH is shown in figure 5.9 (red). It features,

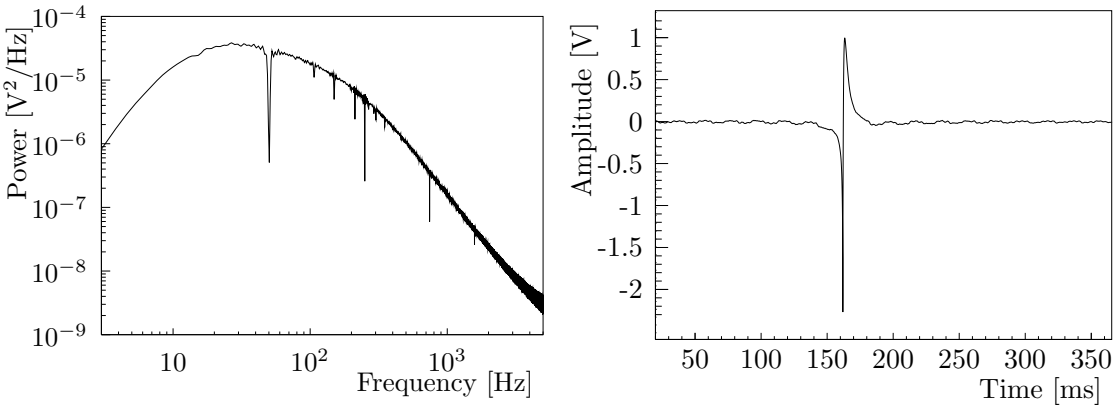

Figure 5.10: Left: Transfer function of TUM93A-Ph. Prominent noise frequencies such as the 50 Hz noise are removed. Right: Backtransformed template of TUM93A-Ph after the filter kernel was applied to it.

e.g. a prominent peak from 50 Hz noise and multiples of 50 Hz. The template is shown in black. No peaks are visible, as the parametric template contains no noise. Both NPS and the template are then used to create the transfer function. It is shown in figure 5.10 (left), which is used to re-weight the pulse in the frequency domain. The back-transformed template is shown on the right. A maximum search looks for the maximum of the back-transformed pulse. Similar to the template fit, the OF saves several parameters of the fit:

Amplitude: The amplitude is the reconstructed height by the OF. In the linear range of the TES, it is a good energy estimator [V].

RMS: This parameter gives the Root-Mean-Square of the fit between the filtered and back-transformed pulse and the filtered template scaled to the same amplitude [V].

Maximum: The maximum value of the pulse after the filtering and back-transformation process [V].

MaximumPosition: This parameter gives the maximum position in channels of the filtered pulse and is determined by the maximum search similar to the template fit. This parameter is given in channels.

5.5 Optimum Filter Threshold Trigger

As already described in section 5.1, the continuous recording of the data has the advantage that, e.g. the threshold and window length can be optimised for each detector. This work applies an optimum filter-based trigger to maximise the signal-to-noise ratio in the data set. For the optimum filter threshold trigger, an OFilter has to be created following the recipe described in section 5.4.4. For this, either the data recorded by the conventional DAQ or the stream data triggered with a moving average trigger is used. The OFilter is afterwards applied to the whole

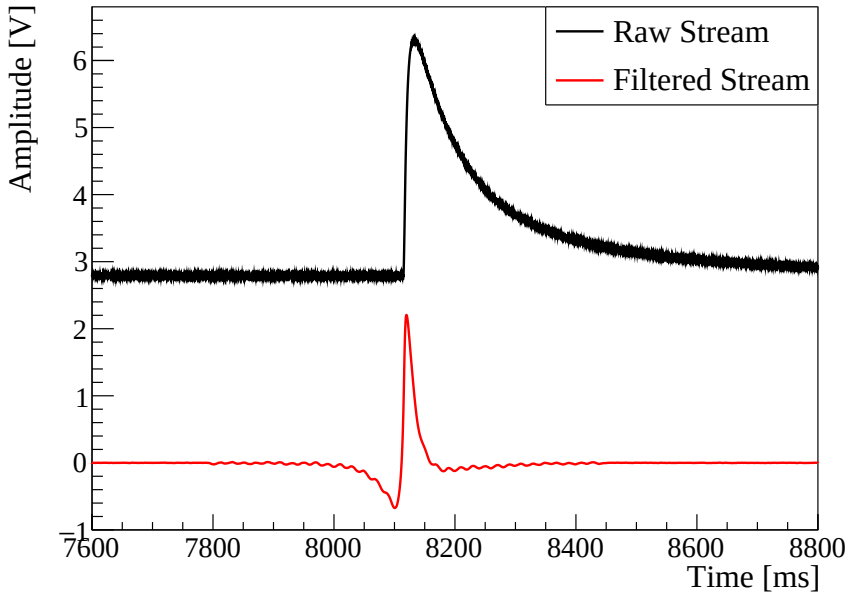

Figure 5.11: Comparison of a test pulse seen in the raw data stream (black) with the same signal filtered by an optimum filter (red). The OFilter is optimised to the pulse shape of particle events, not TPs. Hence the back-transformed pulse shows an asymmetry.

stream (black), resulting in a filtered stream with an optimised signal-to-noise ratio shown in figure 5.11 in red.

In CRESST, the threshold is optimised based on a pre-defined criterion, the number of noise triggers for a particular exposure. Following the analysis approach of DetA published in [37], one noise trigger per kilogram day of detector operation is aimed for. For this, following [108], a set of empty baselines, i.e. pure noise samples, is fitted with the OFilter. This results in an amplitude distribution which represents the filtered maximum value of each noise trace (see blue histograms in figure 5.12 on the top left (TUM93A-Ph) and top right (TUM93A-L)).

Assuming this distribution to be Gaussian, the probability distribution $\mathrm{P}_d(\mathrm{x}_{max})$ expresses the probability of one sample being equal to x_{max} and all other samples being smaller

$$P_d(x_{max}) = \frac{d}{\sqrt{2\cdot\pi}\cdot\sigma}\cdot e^{-\left(\frac{x_{max}}{\sqrt{2}\cdot\sigma}\right)^2}\cdot\left(\frac{1}{2}+\frac{erf(x_{max}/(\sqrt{2}\cdot\sigma))}{2}\right)^{d-1} \tag{5.6}$$

with d the length of the trigger window and σ the resolution [108]. This function is fitted to the Ofilter amplitude distribution (black fit line, top left). The resulting probability distribution is now used to calculate the total noise trigger rate (NTR) above a threshold x_{th} by

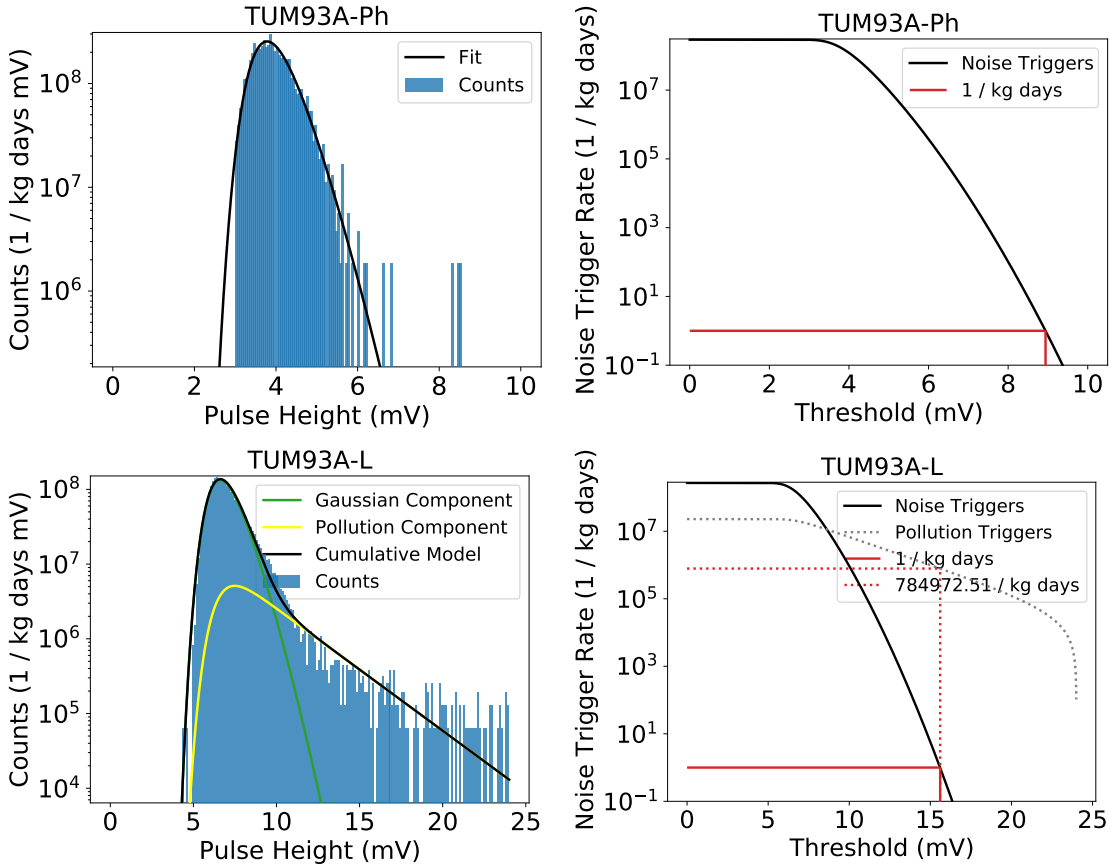

Figure 5.12: Threshold determination of TUM93A-Ph (top) and TUM93A-L (bottom). For TUM93A-Ph, the amplitude distribution of empty baselines follows a Gaussian distribution. For TUM93A-L, several low-energy excess events pollute the empty baselines. Hence, the data is fitted with a Gaussian and exponential component for the threshold determination. The threshold depends on the number of accepted noise triggers, as shown in the two right plots. The red line indicates the threshold for one accepted noise trigger per kgd exposure.

$$NTR(x_{th}) = \frac{1}{t_{win} \cdot m_{det}} \int_{x_{th}}^{\infty} P_d(x_{max}) dx_{max} \tag{5.7}$$

with t_{win} the trigger time window and m_{det} the detector mass [108]. The distribution of the NTR(x_{thr}) is shown in figure 5.12 on the bottom left for TUM93A-Ph. From this distribution, the threshold can be chosen according to the previously defined noise trigger rate.
The approach described above works well for a purely Gaussian maximum value distribution. For some detectors in Run36, this assumption of a Gaussian distribution is, however, not valid. Due to low thresholds, the rate of excess events was so high in many light detectors that empty baselines had a significant amount of LEE events on their traces. Standard data quality cuts cannot remove these without creating a significant bias on the threshold determination. To target this effect, formula 5.5 was modified to account not only for a Gaussian maximum distribution but also for an exponential part in the maximum distribution.[1] This extra exponential part is called the pollution component as it represents the LEE pollution of the empty baselines (see the yellow fit line in figure 5.12 top right). For both components, the Gaussian (green) and the pollution (yellow), a trigger rate vs threshold curve is derived using formula 5.5. The result is shown in figure 5.12 on the bottom right. The solid line shows the noise trigger rate depending on the threshold, whereas the grey dotted line shows the corresponding expected LEE rate. This method was applied to the detector TUM93A-L.
The stream is triggered with the threshold defined above. In the next step, the data set is created from the trigger time stamps. The information about test and control pulses, triggered particle events, number of channels, trigger groups and other settings are merged, and the data set is tuned for a specific analysis. This allows maximum flexibility. Only the PD is triggered for a standard DM analysis in CRESST, and the LD is read out in coincidence. In the case of an LD-only analysis, the LD is triggered, and the PD is read out in coincidence as a veto detector. For the high energy analysis, the triggering detector is also the PD. The values for the different trigger thresholds are shown in table 7.3 in section 7.2.5.

5.6 Basic Data Selection

Afterwards, the data is cleaned with some basic selection criteria by cutting away unstable periods in the measurement and coincidences with signals in the muon veto to avoid signals from muons in the data.

Stability Cut

The CPs not only serve the purpose of active stabilisation of the detector but are also used to monitor the stability offline. Figure 5.13 (left) shows the reconstructed

[1] The extended model was developed by F. Wagner [109]

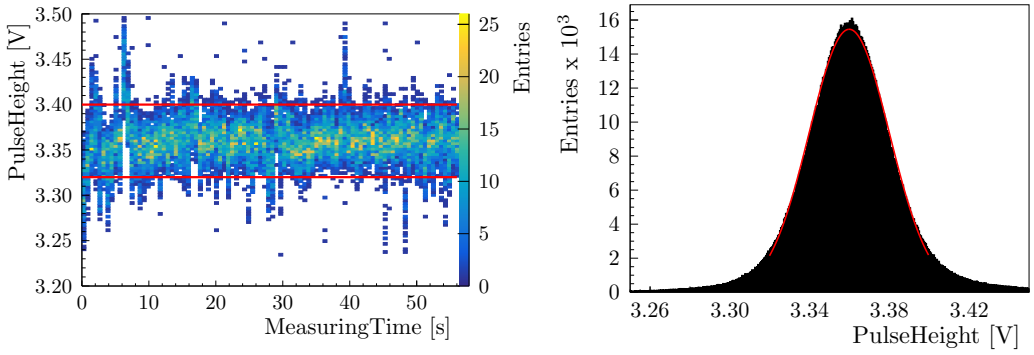

Figure 5.13: Left: PulseHeight of control pulses over time for one file of TUM93A-Ph. The outliers show time periods when the detector was unstable, which should be removed for the analysis. Right: Histogram of the control pulse PulseHeight of all control pulses of TUM93A-Ph. The distribution is fitted by a Gauss function. The fit results are used for the definition of the stability criterion. The red lines in the 2D histogram indicate the stability criterion for a 2 σ cut.

PulseHeights of control pulses for one file versus the measuring time. Some unstable periods are visible where the control pulse height deviates from the usual one. The stability cut removes such time intervals. For this, the PulseHeight of all control pulses is plotted (see figure 5.13 right) and fitted with a Gaussian. Depending on the type of analysis, a stability criterion of typically two or three sigmas with respect to the mean of the Gaussian is selected. Time periods with control pulse heights outside of this criterion are cut away. A stable period is defined by a minimum of two consecutive control pulses.

Muon Veto Cut

Whenever a muon passes one of the muon veto panels surrounding the experiment, there is a probability that this muon causes an event in one of the detectors. To veto these events, all panels are read out when one of the panels is triggering, and the DAQ records the information. A muon interaction in both a panel and the detector appears almost simultaneously. However, due to the time resolution of the cryogenic detector, for each muon event, a conservative window of ± 5 ms or ± 2 ms is vetoed, depending on the analysis.

In addition to these two cuts, other data quality cuts are applied to the data. They, however, depend on the specific analysis and are described in the corresponding sections of chapter 7 and 6.

Chapter 6

Results of the Radiopurity Analysis

In this chapter, the radiopurity analysis of the TUM93 detectors is discussed. Section 6.1 gives an overview of the natural decay chains and the possibility of using secular equilibrium assumptions to determine the impurity-induced intrinsic background in the ROI. Section 6.2 explains the different data sets used for this study. The specific analysis steps, deviating from the standard analysis and developed in the context of this dissertation, are described in section 6.3 for the α-decay analysis and in section 6.4 for the e^-/γ-background analysis. The results of the radiopurity analysis are shown in section 6.5. A new module to perform radiopurity analyses on the crystal ingots at TUM is developed in section 9.

6.1 Radiopurity Determination of $CaWO_4$ Crystals

The background in the energy region for DM search is composed of many contributions, e.g. from cosmic activation of detector components, external radiogenic contaminations or intrinsic impurities in the target material. Disentangling these contributions requires a deep understanding of particle interactions in all the parts of the experiment by simulations. An essential step for this understanding is the investigation of the whole energy range of the detector up to several MeV, the energy region in which α-decays are located. As α-decays are a two-body decay, producing a mono-energetic energy deposition in their own LY band, the decays of single isotopes can be detected without other backgrounds, and the activity of each isotope can be determined. In this way, different $CaWO_4$ crystals can be compared concerning their intrinsic radiopurities and overall background in the region of interest. Most intrinsic impurities are part of the three main natural decay chains ^{238}U, ^{235}U and ^{232}Th. Hence, through the analysis of α-decays, the concentration of impurities in the target material can be determined. With this information, the content

of β-decaying nuclides produced by these decay chains can be evaluated, and their contribution to the ROI for DM search can be calculated.
A decay chain represents a series of radioactive decays starting from the mother nuclei (^{238}U, ^{235}U, ^{232}Th) down to a stable isotope of lead (^{206}Pb, ^{207}Pb, ^{208}Pb). Figure 6.1 shows the three natural decay chains with β-decaying isotopes in blue and α-decaying isotopes in red. When the decay chain is in equilibrium, each decaying isotope has the same activity as the isotope with the longest half-life time, called secular equilibrium. This secular equilibrium is reached after several half-life times of the mother nuclei. For the natural decay chains, this is $\mathcal{O}(10^8\text{-}10^{10}\,\mathrm{y})$. The secular equilibrium can be broken by, e.g. cleaning procedures of the material or during crystal growth as segregation effects can cause different elements to stay more likely in the melt. In this case, only isotopes with half-lives of less than the time period from the equilibrium breaking to the measurement of the decays are in secular equilibrium. For these isotopes, the same activity is expected. The secular equilibrium groups found in the crystal TUM40, the first TUM-grown $CaWO_4$ crystal operated in CRESST, are indicated in figure 6.1 by the labels g1, g2, g3 and g4. These groups are in secular equilibrium as the decay times are shorter than the time from the crystal growth to the cryogenic measurement. Hence, within these groups, secular equilibrium is expected. From the detected α-decay rate, a contribution to the overall background in the ROI of TUM40 from 1-40 keV of 30.4 % was determined with the help of Monte Carlo simulations [45, 110, 111].
The primary goal of the powder purification was to reduce the intrinsic activity in the ROI to enhance the sensitivity of CRESST. To assess whether the chemical purification of the $CaWO_4$ material at TUM significantly impacted the overall reduction of the background rate in the ROI, an α-analysis is conducted in the scope of this work to identify the activity of individual α-decaying isotopes. Subsequently, the β/γ-background is analysed over a large energy range, up to 740 keV. The contribution of the intrinsic background to the overall background is calculated, and the results are compared to previously measured TUM-grown crystals TUM40 and TUM56.

6.2 Analysed Data Sets

The different data sets used for the radiopurity analyses of the TUM93 detectors are shown in table 6.1. For the analysis of the e^-/γ background, the *Bck* data set taken from November 2020 to August 2021 was used together with ^{57}Co calibration data (*CoCal*) recorded in October 2020. For the α-background analysis, in addition to the *Bck* data set, the After-Warm-Up (*Awu*) data set started after the first warmup of the carousel, which was performed for the study of the low energy excess was used to provide better statistics.
The α background analysis was performed with two different methods for TUM93A, the i-stick analysis and the saturation time analysis. As the i-stick had stability problems and a change in working point during the *Bck* data set, only a reduced *Bck* data set was analysed. A complete list of data segments included in the different

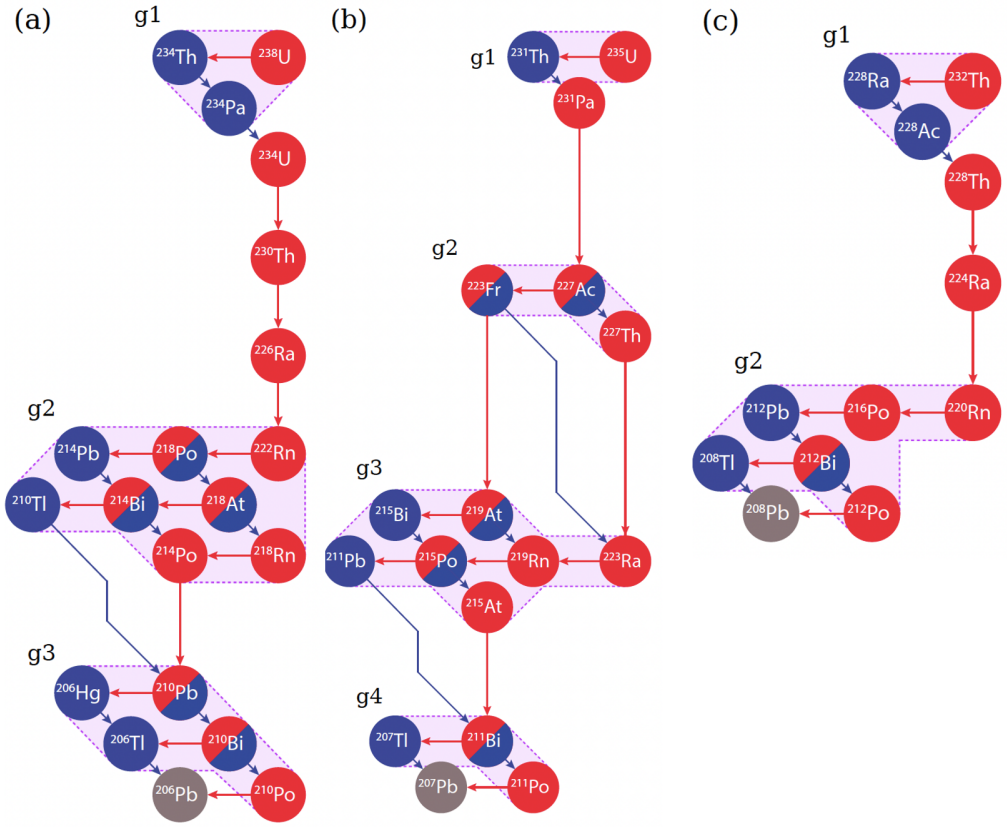

Figure 6.1: Secular equilibrium groups in the three natural decay chains of ^{238}U, ^{235}U and ^{232}Th as derived from the detector module TUM40. α-decaying isotopes are shown in red and β-decaying isotopes in blue. Figure adapted from [111].

analyses is shown in appendix B. In the following, the specific steps for the α-decay analysis yielding the activities of the individual isotopes and the e^-/γ-background analysis are explained.

6.3 Specific α-Decay Analysis Steps

This section covers the analysis of highly energetic α-decays in the $CaWO_4$ detector crystals. As α-decays have Q-values in the order of several MeV, the pulses measured by the TES are fully saturated, and nearly all events cause FQLs in the SQUID, which makes a reconstruction via the truncated fit on the PD impossible. Figure 6.2 shows a typical α-event recorded by the module TUM93A. The PD (black) is entirely saturated and suffering from FQLs. The LD (red) is saturated, too. In most cases, the LD SQUID does not show FQLs from the light signal caused by an α-decay in the primary detector. In addition, part of the deposited energy is transmitted to the i-stick (green) for detector TUM93A.

In the following, two different analysis approaches for determining the α-decay en-

Analysis	Module	Bck [kgd]	Awu [kgd]
e^-/γ	TUM93A	3.73	-
	TUM93C	4.94	-
α (I-stick)	TUM93A	4.23	3.31
α (Sat. Time)	TUM93A	4.94	3.31
	TUM93B	4.94	3.31
	TUM93C	4.94	3.31

Table 6.1: Raw exposures of all data sets considered in the radiopurity analysis.

ergies in TUM93A, TUM93B and TUM93C are presented. First, the i-stick analysis of TUM93A and, afterwards, the analysis using the saturation time of the phonon detector for all three detector modules.

6.3.1 I-stick Analysis

The i-stick analysis is applied to TUM93A only, as it is the only detector in the ongoing data-taking campaign with an operated holding stick made from $CaWO_4$. For the i-stick analysis, mainly TUM93A-L and the i-stick channel are used. This method to reconstruct α-decays was already applied on several detectors in Run34 in [46]. As the i-stick had some instability issues during the whole run, a strict stability cut is applied to the control pulses recorded for this channel. This reduces the exposure significantly but is needed for a correct reconstruction of the events.

Amplitude Reconstruction

To determine the amplitude in the light and i-stick channel, the OFilter cannot be applied due to a saturated signal in the LD and changing noise conditions in the i-stick. As mentioned in section 5.4.4, the OFilter can only be applied to non-saturated pulses and relies on a constant noise level described by an NPS in the frequency domain. Hence, the template fit is applied to both channels. Figure 6.3 shows a fit (in green) to the signal (black) measured by the i-stick for an α-decay in TUM93A-Ph. A truncated fit using the same settings as for the α-events is applied for the TPs of both channels.

Data Quality Cuts

Great care has to be taken for the cuts applied to the α-decay data set. The reason is that FQLs and pile-ups can not be correctly modelled by simulation, so no cut efficiency can be determined and the α-activity cannot be corrected for wrongly removed events. In addition, the α-decay analysis is, to a certain degree, a simple counting of events with low statistics, so using a survival probability to correct $\mathcal{O}(1)$ event is not possible. Hence, all cuts applied to the data must be checked so that

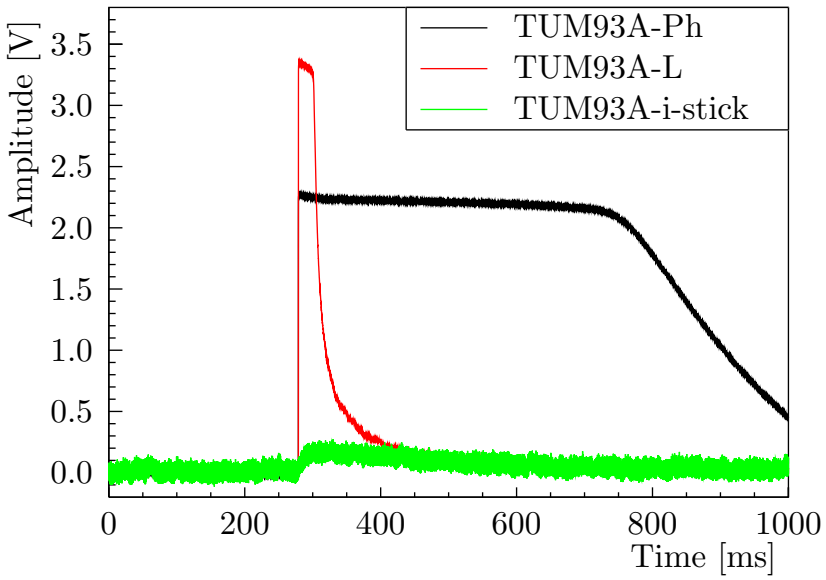

Figure 6.2: α-decay recorded by all three channels of the Module TUM93A. The PD signal is shown in black. It lost some FQ. The LD signal is shown in red, and the i-stick pulse is plotted in green. For a highly energetic event like an α-decay, part of the energy gets transmitted to the i-stick and the i-stick measures a signal.

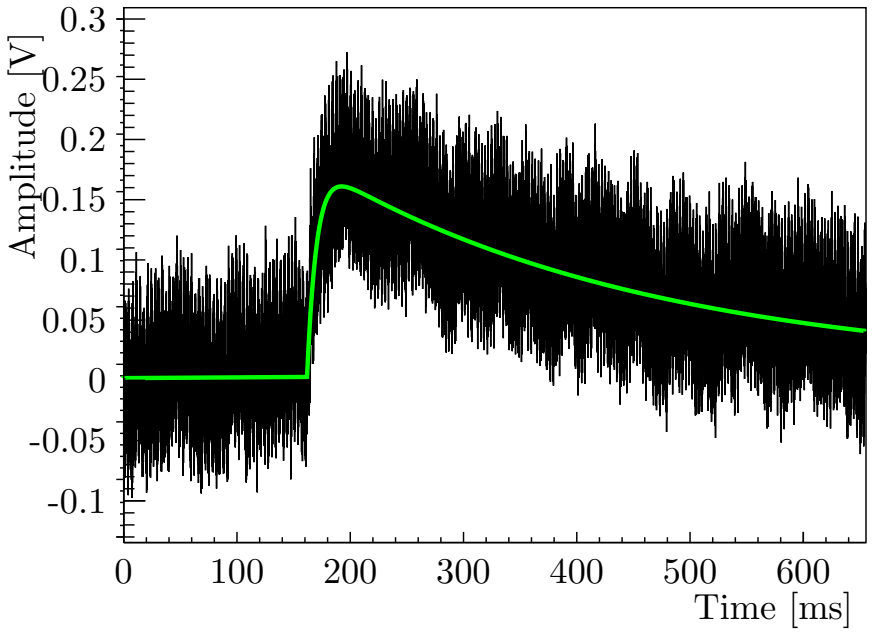

Figure 6.3: Template fit (green) to a degraded alpha decay signal recorded by the i-stick (black).

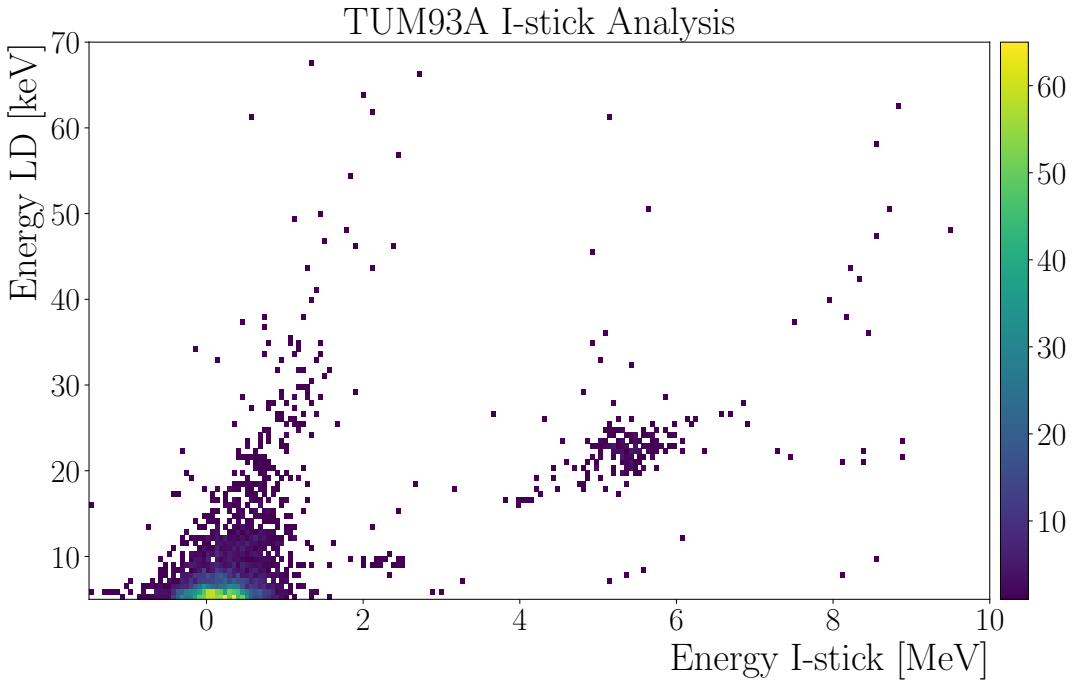

Figure 6.4: 2D-Histogram of high energy events in TUM93A after the cuts were applied. The reconstructed LD energy is plotted against the reconstructed i-stick energy. The α-band is clearly separated from the e^-/γ-band.

they do not remove a single reconstructable α-event. As the number of α-events is $\mathcal{O}(100)$ events, this is done on an event-by-event basis. The cuts can be more strict for TPs.
The cuts applied to the data set are: A muon coincidence and stability cut on i-stick and LD reducing the effective exposure, a BaseLineDiff cut removing events which feature a 5V higher average baseline value in the last 50 samples compared to the pre-trigger baseline, removing SQUID resets in both channels. In addition, a BaseLineDiff cut is applied to the i-stick to remove events with FQLS on the i-stick originating from direct hits in the stick. As the last cut, all events for which the i-stick is completely saturated are removed as they show signals which cannot originate from a transmission from the phonon detector. Figure 6.4 shows the resulting 2D-Histogram with the reconstructed energy in the LD vs the reconstructed energy in the i-stick. A clear separation of the e^-/γ-band and the α-band is visible. The outliers below the α-band originate from wrongly reconstructed LD amplitudes due to FQLs in the LD.

Energy Calibration

The ^{55}Fe calibration lines cannot be used for the energy calibration of the stick as their transmitted energy is below the detectable amplitude in the i-stick. Hence, the calibration has to be performed using the α-spectrum, identifying lines originating from α-decays. Before this is possible, the i-stick TPs are used to create a TPR

object as described in section 7.2.1. The corrected spectrum is then used to identify α-lines which are used for a linear calibration. The LD is calibrated via the direct hits of the ^{55}Fe source in the LD.

Survival Probability

No simulation could be performed for the α-i-stick analysis as the implemented simulation tool cannot model the highly energetic events. The trigger efficiency (which is a constant value above the threshold) is taken from the low-energy analysis (described in section 7.2.3) to estimate the survival probability. In addition, the fraction of unstable periods is accounted for. As the α-events in the data set are $\mathcal{O}(100)$ events, all cuts are carefully tuned not to remove any α-events. For this, the events removed from the α-LY band are carefully inspected on an event-by-event basis for each cut.

6.3.2 Saturation Time Analysis

The saturation time reconstruction method described in 5.4.3 is used for this analysis. The advantage of the method is that it uses the PD together with the LD and does not need the i-stick for the reconstruction. This makes it also applicable to other detectors than TUM93A, which were not equipped with an i-stick (TUM93C) or have a non-working i-stick (TUM93B). Also, for TUM93A, the reconstruction method has advantages. As described before, the i-stick has many unstable periods, significantly reducing the actual measurement time. Using the PD instead of the i-stick provides higher statistics for the α-decay analysis. In addition, due to the changing noise conditions in the i-stick, the energy resolution of the saturation time reconstruction is better than that obtained by the i-stick reconstruction.

Amplitude Reconstruction

The PD is reconstructed with the standard saturation time determination. Depending on the detector, the LD can either be reconstructed using a truncated template fit, with the saturation time or a numerical integral calculation from the onset to the saturation time value. As the LD is only used to separate the e^-/γ-band from the α-band, the method which enhances the separation should be used. This can be different for each detector. In this work, the saturation time, in combination with the integral of the LD up to the point where the event decayed to 90% of its saturated pulse height, showed the best results.

Data Quality Cuts

Similar to the i-stick analysis, a muon veto cut is performed to exclude muon events from the data. In contrast, no stability cut is applied to the data. As described in 5.4.3 α-events often pile up with control pulses due to the length of the pulses. This leads to a wrong reconstruction of the control pulses, marking the time period as

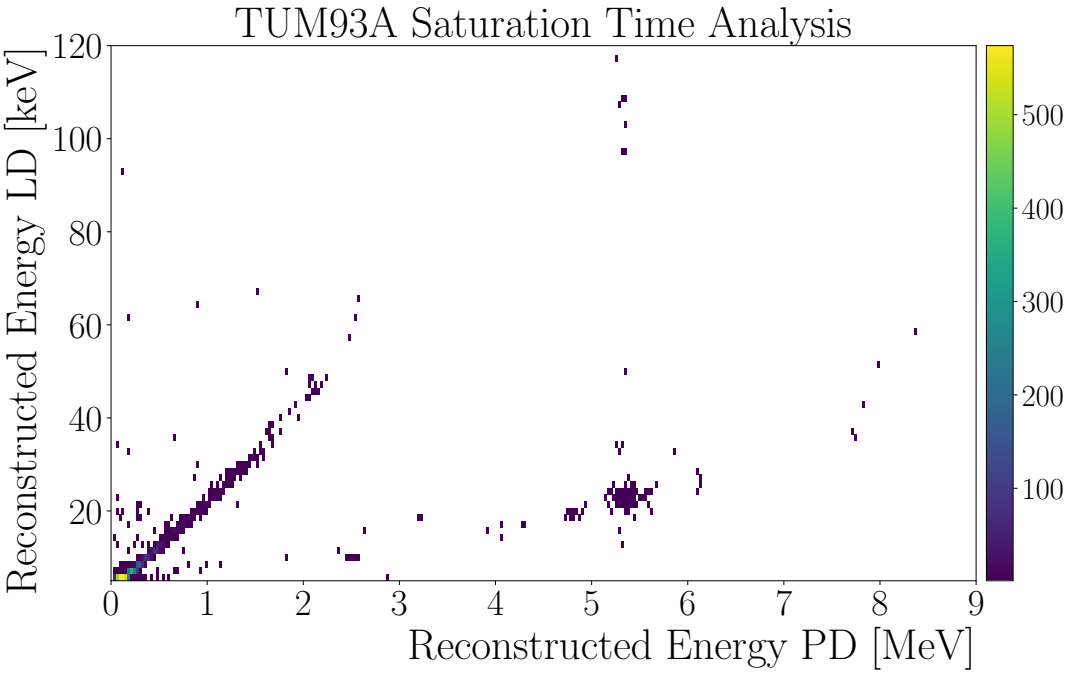

Figure 6.5: 2D-Histogram of events in TUM93A after the cuts were applied. The reconstructed LD amplitude is plotted against the fitted Saturation Time in the PD. The α-band is clearly separated from the e^-/γ-band.

unstable. Cutting on the stability of the PD removes nearly all α-events. As the reconstruction is performed on $\mathcal{O}$(MeV) events, a slight fluctuation in the working point of $\mathcal{O}$(eV) is negligible. Even a fluctuation O(keV) would only influence the reconstruction in a lower per cent region. Hence a working point correction is not needed. Two other cuts are applied, a PulseHeight cut on the PD removing all events with a PulseHeight >5V, which is 1V above the maximum saturated PulseHeight of the PD. This cut is designed to remove unphysical effects like SQUID resets. In addition, a RiseTime cut is applied on the PD, removing events with a RiseTime above a certain value. Highly energetic events have a much faster rise time compared to low energetic events. This removes events which have, e.g. mainly an LD signal or are due to other artefacts reconstructed wrongly by the saturation time fit. Figure 6.5 shows the energy-calibrated reconstructed events in the LD, calibrated via the direct hits of the ^{55}Fe events in the LD, against the energy-calibrated saturation time for the PD of TUM93A. Both the e^-/γ band and the α-band are clearly separated. Compared to the data reconstructed with the i-stick method, a better energy resolution and separation with this method are visible.

Survival Probability

Also, no simulation could be performed for the saturation time analysis as the implemented simulation tool cannot model the high-energetic events. Similar to the i-stick analysis, the trigger efficiency is taken from the low-energy analysis. The cuts are tuned to remove no valid α-events from the α-LY band.

Energy Calibration

Due to the pile-up of α-events with TPs and CPs and their subsequent wrong reconstruction, no TPR object is created for this analysis. As mentioned before, small fluctuations in the operation point of the PD have only a small influence on the reconstruction of the saturation time. The energy calibration is performed by identifying lines in the α-spectrum. Prominent lines are the ^{180}W decay line at 2.52 MeV, ^{226}Ra at 4.88 MeV, the ^{210}Po surface background line at 5.30 MeV and the ^{218}Po line at 6.11 MeV. These data points are then fitted by an exponential function which describes the correlation between saturation time and the original amplitude of the pulse as shown in figure 6.6. The exponential behaviour is derived from a simplified pulse model based on [42]. For a pulse described by an amplitude A via $A \cdot exp(-t/t_{decay})$ the saturation time t_{sat} for a given saturation voltage V is described by

$$t_{sat} = t_{decay} \cdot ln\left(\frac{A}{V}\right) \tag{6.1}$$

so the reconstructed amplitude A is proportional to $exp(t_{sat})$.

6.4 Specific Analysis Steps for the e^-/γ Background

This section covers the specific analysis steps applied for the e^-/γ background analysis of the modules TUM93A and TUM93C up to energies of several hundred keV. In this energy region, pulses are mostly saturated. Hence a truncated template fit is applied to both the PD and the LD. TUM93B could not be analysed in this energy region as no calibration data is available for this energy range. Due to a bad energy resolution, no peaks could be identified in the higher energy region.

Energy Calibration

Since the TPs sent in regular intervals to the detectors cover an energy range up to 30 keV, a time-dependent correction of the working point can only be performed up to this energy. A reconstruction above this value is strongly dependent on the extrapolation method of the transfer function and can have large errors. Hence, no TP correction is applied to this data set. Instead of the time-dependent correction and linearisation of the reconstructed amplitudes with the test pulses, lines at higher energies are used to calibrate the whole energy range. For this, the ^{57}Co

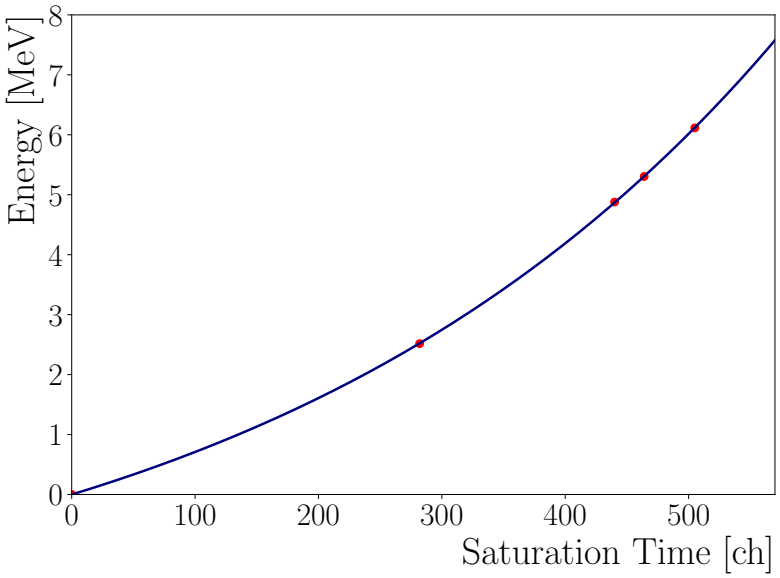

Figure 6.6: Exponential conversion function from the saturation time in channels to energy in MeV for detector TUM93A. The lines used for the fit originate from the decays of ^{180}W (2.52 MeV), ^{226}Ra (4.88 MeV), surface ^{210}Po (5.30 MeV) and ^{218}Po (6.11 MeV).

calibration data is used, which also contains lines from the internal ^{55}Fe calibration source. The values of the most prominent lines observed for the ^{57}Co calibration are summarised in table 6.2, the values of the ^{55}Fe lines in table 7.2. The interaction of high energetic γ's from the ^{57}Co source with energies of 122.1 keV and 136.5 keV can remove electrons from the shell of the target crystal atoms. Electrons from outer shells fill these vacancies via the emission of X-rays. If this happens close to the detector surface, the X-ray can escape and a reduced energy, an escape line, with the energy of the ^{57}Co γ-line minus the X-ray energy is detected.
Figure 6.7 shows the energy-calibrated spectrum for the CoCal data set of TUM93C. All four 122.1 keV W escape lines are visible in the spectrum as well as the two emission lines, the ^{55}Fe lines and the two ^{57}Co γ lines. For the calibration, both ^{55}Fe lines, the W $K_{\alpha 2}$ and W $K_{\alpha 1}$ escape lines, as well as the two ^{57}Co lines, are fitted with a Gaussian and the best fit mean value is plotted against their nominal energy (see figure 6.8). A second-order polynomial is fitted to it with the offset set to zero. This function is then used for the energy calibration of the background spectrum of the detector.

6.4.1 Data Selection

Afterwards, the data is cleaned from artefacts and wrongly reconstructed pulses. A BaseLineDiff cut aims to remove SQUID resets and FQLs together with pile-ups from the data. To remove wrongly reconstructed pulses from the data, a cut on the

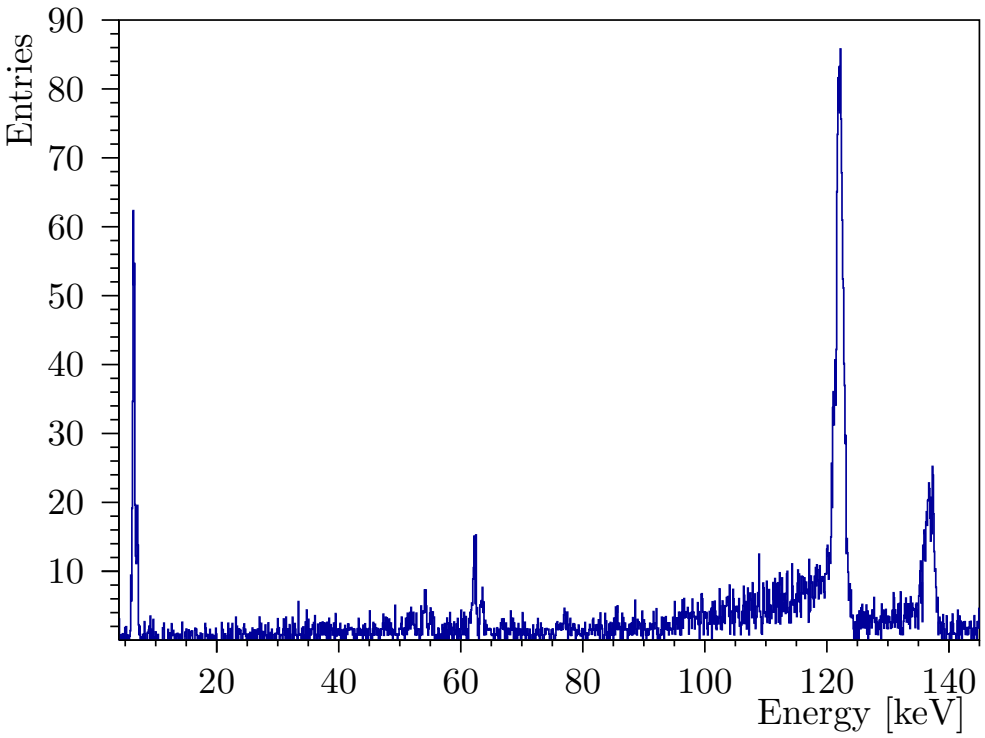

Figure 6.7: TUM93C spectrum of the ^{57}Co calibration data set. The two ^{57}Co γ emission lines at 122.1 keV and 136.5 keV are prominent. Also, the four 122.1 keV escape lines are resolved with smaller intensities. Two ^{55}Fe calibration lines are visible at smaller energies.

type	line origin	energy [keV]	intensity
emission	^{57}Co	122.1	85.6
emission	^{57}Co	136.5	10.7
X-ray	W $K_{\alpha 2}$	58.0	34.8
X-ray	W $K_{\alpha 1}$	59.3	60.5
X-ray	W $K_{\beta 1}$	67.2	13.1
X-ray	W $K_{\beta 2}$	69.1	4.5
escape	$W_{122.1\,\mathrm{keV}}$ $K_{\beta 2}$	53.0	-
escape	$W_{122.1\,\mathrm{keV}}$ $K_{\beta 1}$	54.9	-
escape	$W_{122.1\,\mathrm{keV}}$ $K_{\alpha 1}$	62.8	-
escape	$W_{122.1\,\mathrm{keV}}$ $K_{\alpha 2}$	64.1	-

Table 6.2: Prominent lines from the ^{57}Co decay with the most prominent escape lines. Their relative intensity distribution corresponds to the distribution of the X-ray lines. The 136.5 keV escape lines are not listed as their intensities are too small to be seen in the data. [112]

RMS parameter of the truncated fit is applied to the data. In the last step, a light yield cut is applied to remove events outside the expected light yield region. In this

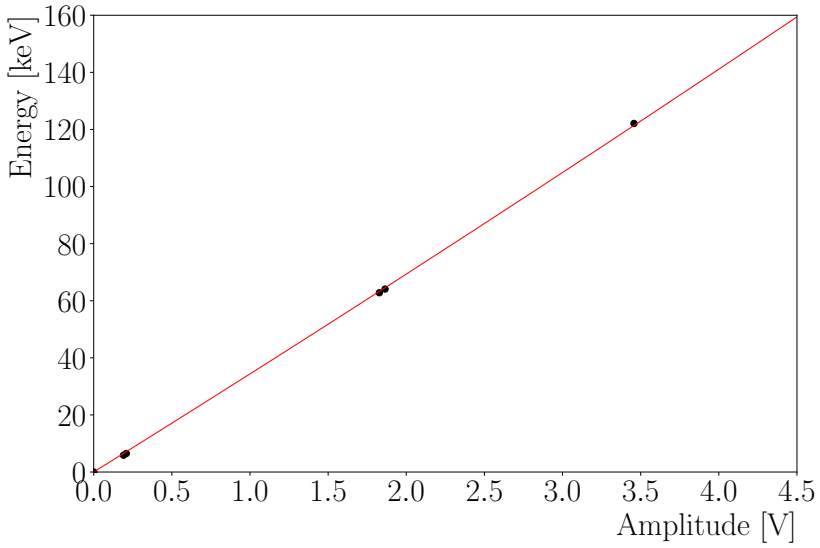

Figure 6.8: Conversion function from reconstructed amplitude to energy for TUM93C. The black data points represent the two ^{57}Co γ emission lines, the $K_{\alpha 2}$ and $K_{\alpha 1}$ escape lines and both ^{55}Fe calibration lines. They are fitted by a polynomial of the second order, which is used to convert the reconstructed amplitudes to units of energy.

way, events where the light detector was hit directly or some part of the energy was lost from the detector, causing the scintillating foil to emit extra light, are excluded from the analysis.

6.4.2 Survival Probability

For the survival probability, parametric templates are simulated on the whole data stream and processed afterwards. The process is described in more detail in section 7.2.3. The simulations were performed up to an energy of 100 keV as the simulation for energies above produced non-physical results. One of the reasons is, e.g. that scaling the template up by a large factor causes a too-low number of points in the rising flank of the pulse, which can cause a wrong calculation of basic analysis parameters. Due to the truncation of real pulses, this effect is not present for them. As the cuts were chosen in an energy-independent way, a constant survival probability can be assumed above this value. Figure 6.9 shows the simulated survival probabilities for both TUM93A and TUM93C for the energy range up to 100 keV.

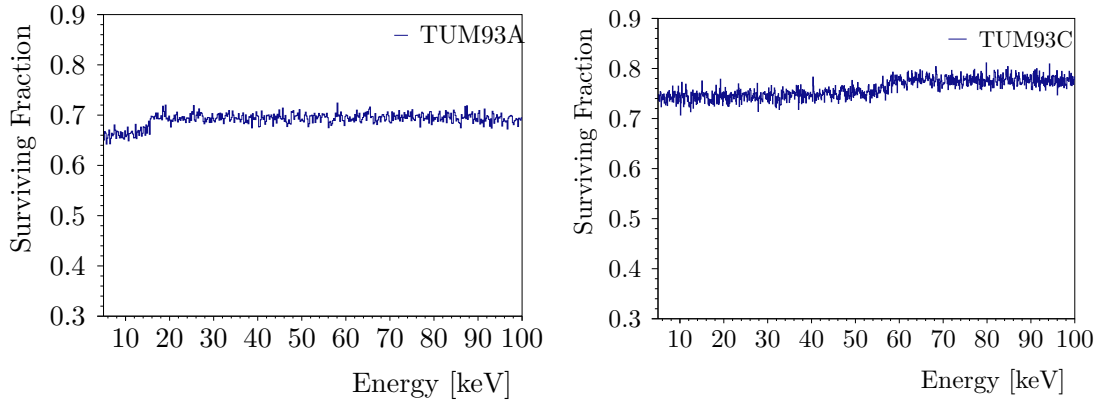

Figure 6.9: Survival probabilities for detectors TUM93A and TUM93C up to an energy of 100 keV. Both probabilities are assumed to be constant for energies above 100 keV.

6.5 Results of the Radiopurity Analysis

In this section, the α-activity of the TUM93 crystals is determined and used to describe the continuous β-background assuming secular equilibrium in the three natural decay chains.

6.5.1 Determination of α-Activities

The energy-calibrated 2D histograms for the α-decay analysis of the combined Bck and Awu data sets are shown in Figure 6.10 for the TUM93A i-stick analysis (top left, named TUM93Ai from now on), the TUM93A saturation time analysis (top right) as well as for TUM93B and TUM93C (bottom left and right). Results of a reduced data set were also published in [113] for the i-stick analysis. The reconstructed energy in the LD is plotted versus the reconstructed energy in the i-stick or PD. Even though the resolution differs significantly for each analysis, several common features are present. First, events with a much higher light signal ($\sim$ 100 keV) are observed at energies between 5 MeV and 6 MeV.
These events originate from ^{210}Po α-decays at 5.4 MeV. When the decay happens on the surface of the crystal, either the α-particle may escape from the surface, and only the recoil of the ^{206}Pb daughter nucleus with an energy of $\sim$100 keV is detected or the ^{206}Pb escapes and only the α-particle with an energy of 5.30 MeV is measured [114]. As roughly 25% of the detector surface is faced by the LD, the escaping ^{206}Pb nucleus can hit the LD and, hence, a 100 keV higher light signal is measured, as seen in the data. Therefore, roughly four times the amount of events detected with the excess light can be attributed to ^{210}Po surface decays for which the daughter nucleus escapes the crystal. The large spread in energy of these ^{206}Pb hits is due to a worsening performance of the LDs at higher energies. The TUM93C LD has the worst resolution in this energy range.

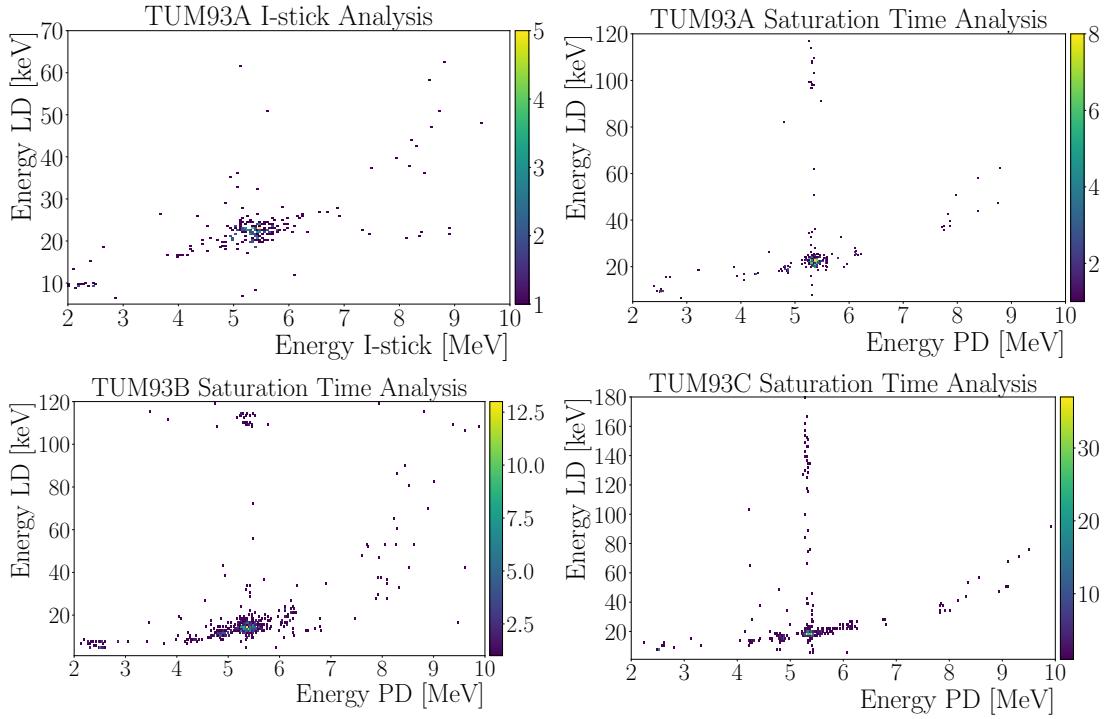

Figure 6.10: 2D Histograms of the resulting α-bands from the analysis of TUM93A with the i-stick (top left) and the saturation time (top right) as well as the saturation time analyses for TUM93B (bottom left) and TUM93C (bottom right).

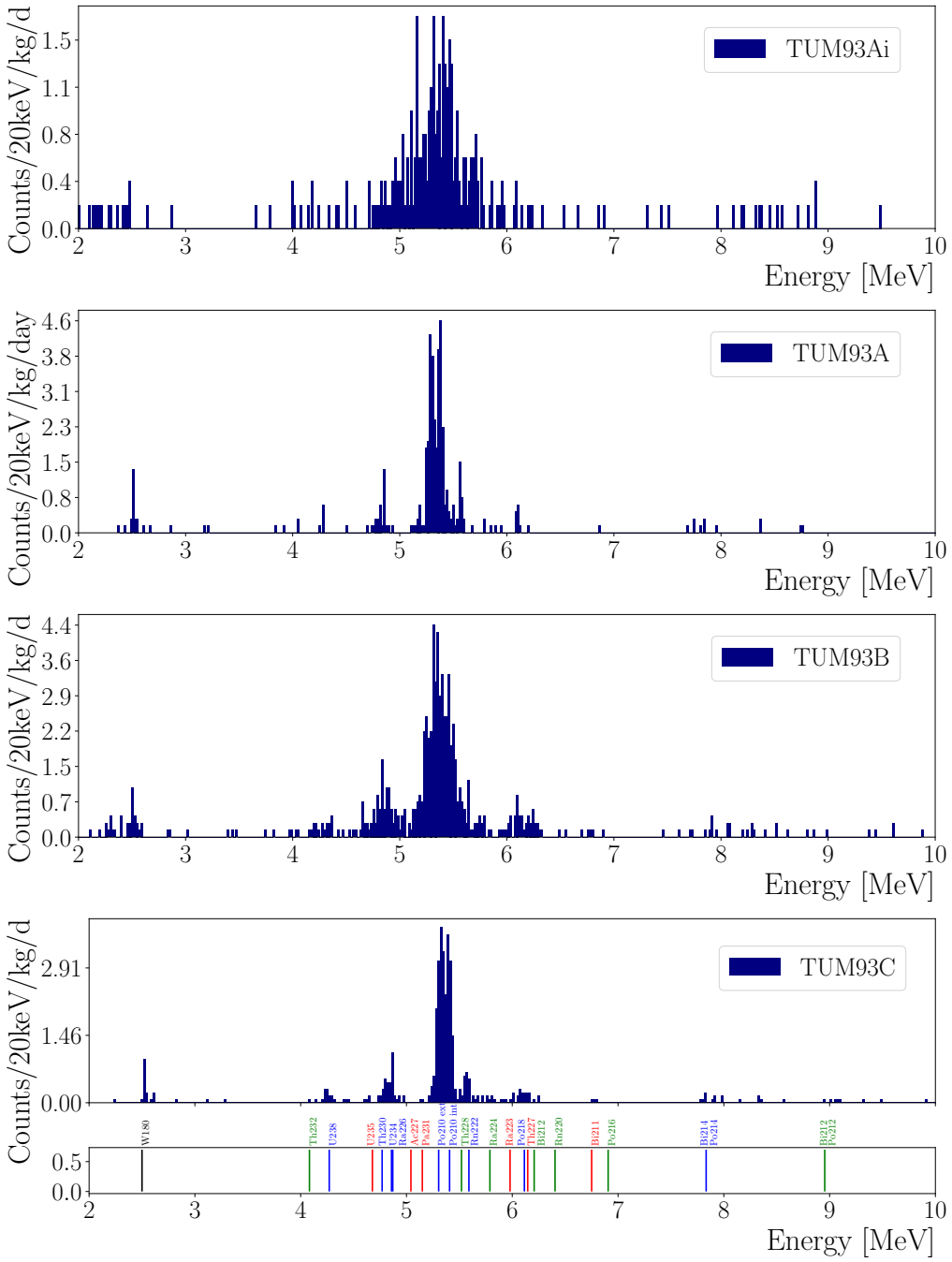

Figure 6.11: Energy spectra for the α-decays detected in the TUM93A i-stick analysis, TUM93A, TUM93B and TUM93C saturation time analyses (from top to bottom). In addition, the expected α-decay energies for the three natural decay chains ^{238}U (blue), ^{235}U (red) and ^{232}Th (green) are shown. Line energies taken from [45].

A second feature in the data is the decay line of ^{180}W, located at 2.52 MeV at the lower end of the α-band. ^{180}W is a naturally occurring isotope of Tungsten with an abundance of 0.12 %. Its half-life of $(1.8\pm0.2)\cdot10^{18}$ years was determined by CRESST in 2004 [115]. With a $CaWO_4$ crystal mass of 24 g and an exposure of 9.1 kg d, 11 ± 3 counts of ^{180}W are expected for TUM93C and 12 ± 3 counts for TUM93A. The discrepancy originates from both modules' different efficiencies. Observed are 15 ± 3 counts for TUM93A and 17 ± 5 counts for TUM93C between 2.45 and 2.58 MeV. As the values agree within their uncertainties, this line can be identified as the ^{180}W decay line.

Depending on the detector resolution, additional lines can be identified in the histograms. The energy spectra are shown together with the literature values for the α-decays in figure 6.10 from top to bottom for TUM93Ai (5.23 kg d net exposure), TUM93A (6.53 kg d net exposure), TUM93B (6.89 kg d net exposure) and TUM93C (6.87 kg d net exposure). Indicated are the locations of the ^{180}W line as well as all the α-lines from the natural decay chains ^{238}U (blue), ^{235}U (red) and ^{232}Th (green). For the ^{214}Bi/^{214}Po and ^{212}Bi/^{212}Po decays only the lower energy limits are shown as the decays consist of an α-decay followed by a β-decay with a half-life shorter than the detector time resolution. For ^{210}Po, both the full energy line (int.), as well as the reduced line (ext.) are indicated. The spectra seem dominated by the ^{210}Po backgrounds for all detector crystals.

Even though the rate seems to be dominated by ^{210}Po intrinsic and surface backgrounds, a conservative α-decay rate, including intrinsic and surface α-backgrounds was calculated for all four analyses summing up all α-decay events originating from natural decay chains. The results are summarised in table 6.3. For TUM93A, the activity determined by the i-stick and saturation time analyses is calculated. They agree well with each other providing a cross-check for the newly developed saturation time method.

As described in section 3.4, due to segregation effects, the top part of the crystal ingot is usually the cleanest part of it, with impurities rising towards the end of the crystal. Hence, TUM93A is expected to have the lowest α-decay rate, TUM93B the 2nd lowest and TUM93C the highest. From the overall rate, TUM93B shows the highest activity. This might be due to a mix-up of both crystals during cutting, polishing, TES production, testing or mounting. As the crystals do not have a specific label, this is possible but cannot be checked.

A fit to the data must be performed to study the intrinsic overall α-decay rate and the α-decay rate of single isotopes. This is only possible for the spectra of TUM93A (sat. time) and TUM93C as these have detector resolutions of 23.5 keV and 24.6 keV, respectively, which makes an analysis of the different lines possible. The resolutions of TUM93B ($\sim$72 keV) and TUM93A (i-stick) ($\sim$260 keV) are too bad to resolve single lines, so no line analysis was performed.

Both detectors were fitted by multiple Gaussians with starting values at the nominal line position and a Poisson uncertainty assigned bin-wise to the data. The fit uncertainty considers these Poisson uncertainties and is given with 68 % C.L. The width of the Gaussian peaks is a global variable for all the peaks. Figure 6.12 (top) shows

Detector	Counts	Exposure [kg d]	α-rate [μBq/kg]
TUM93Ai	243	7.54	538 ± 69
TUM93A	302	8.25	516 ± 62
TUM93B	547	8.25	919 ± 79
TUM93C	505	8.25	761 ± 76

Table 6.3: Total α-decay rate of all α-decaying isotopes of the three natural decay chains (^{238}U, ^{235}U, ^{232}Th) in an energy range from 3 MeV to 10 MeV for the TUM93 detectors.

the fit to the data set of TUM93A, and figure 6.12 (bottom) the fit to TUM93C. In both cases, a subplot indicates the expected energies for the different isotopes of the three natural decay chains ^{238}U (blue), ^{235}U (red) and ^{232}Th (green). Lines that could not fit the data due to a count rate of fewer than five events are shown as dashed lines. For these isotopes, a one-sided upper Poisson limit with 90 % C.L. taken from table 40.3 in [116] is given.

The results of these fits are summarised in table C.1 in appendix C. Table 6.4 shows the fit results for both TUM93A and TUM93C, stating only the activity of the first isotope of a secular equilibrium group for each decay chain for clarity. For $CaWO_4$, the secular equilibrium is usually broken at ^{226}Ra, confirmed by the values in table C.1. For the ^{238}U chain it is additionally broken at ^{210}Pb (half-life ∼22 y) which is a β-decaying isotope, hence the α-decaying values of the daugther ^{210}Po are given below it. The activity of ^{210}Pb is derived from the detected activity of $^{210}\mathrm{Po}_{\mathrm{internal}}$. For this, the decay rate of ^{210}Po was studied over time by looking at the rate between 5.25-5.45 MeV as shown in figure 6.13 for TUM93A.

There was no evidence (over 500 days) for a decrease of the ^{210}Po rate. Hence secular equilibrium with ^{210}Pb is assumed. The secular equilibrium groups are defined similarly for the other two decay chains and are broken at ^{223}Ra and ^{224}Ra.

All activities are compared to activities measured for the crystal TUM40 in [45], and purification factors are calculated for each isotope (purification factors >10 highlighted in green, <1 in red). A comparison with the crystal TUM56, produced from the same raw material without chemical purification, is shown in appendix C. As no single line analysis was published in [46] due to the non-sufficient resolution of the detector, groups of activities are compared between TUM93A, TUM93C and TUM56 in table C.2, showing similar improvement factors as concerning TUM40.

Besides the secular equilibrium group of ^{210}Pb, the activities are reduced in all parts of the three decay chains. This hints towards an introduction of ^{210}Pb during the purification process either by direct contamination with ^{210}Pb or contact with radon. In addition, the observed activity is higher in TUM93C compared to TUM93A. This is expected as the crystal TUM93C was cut from a lower part in the ingot with TUM93A cut as the topmost crystal. Due to segregation effects during Czochralski growth, an increased impurity level is expected towards the lower part of the crystal (see section 3.4).

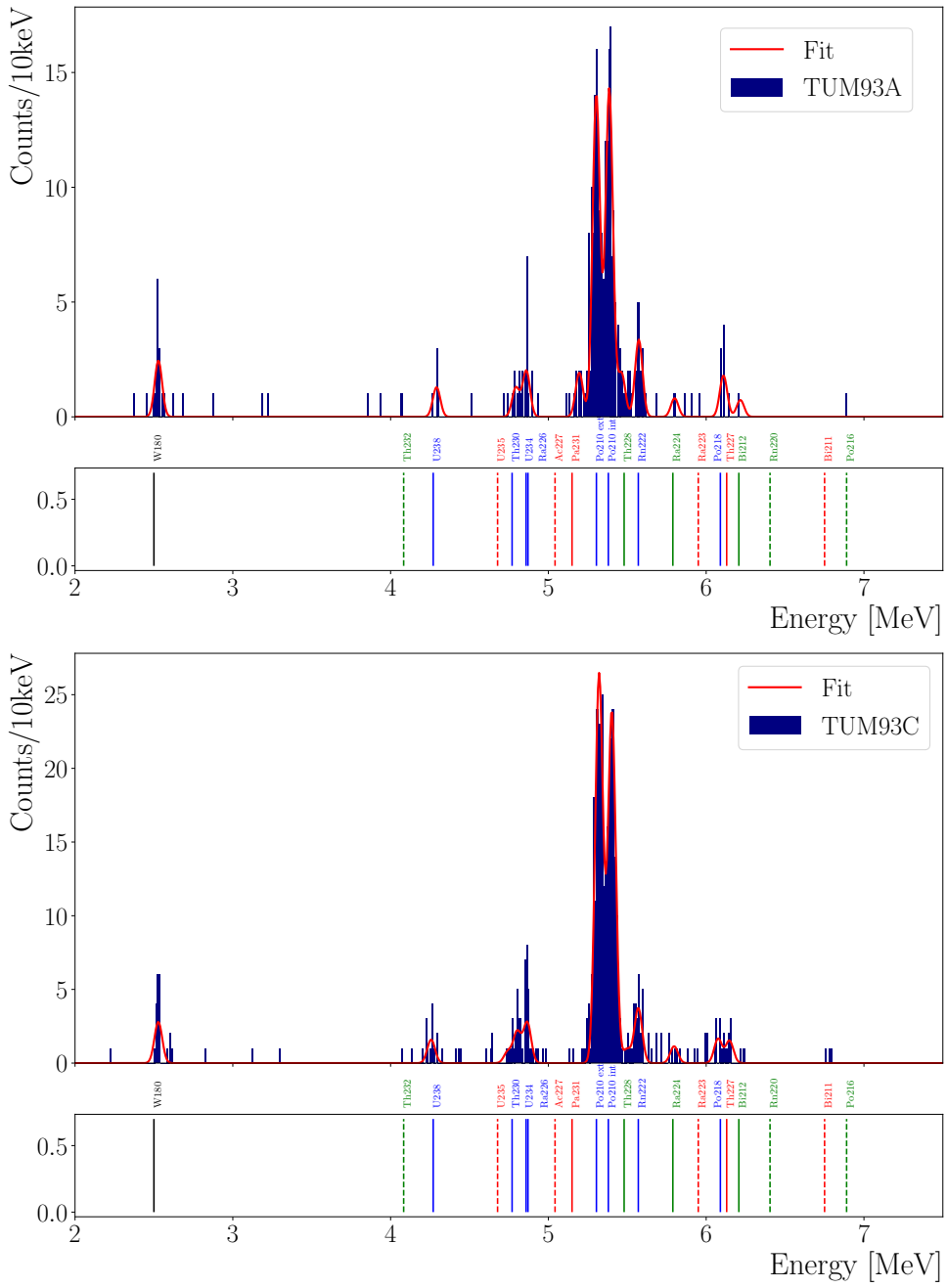

Figure 6.12: Top: Fit of the α-decay energy spectrum for TUM93A. The resolution of the detector is 23.6 keV. Expected energies of the ^{238}U (blue), ^{235}U (red) and ^{232}Th (green) decay chains are shown below. Bottom: Fit of the α-decay energy spectrum for TUM93C. The resolution of the detector is 24.6 keV. The expected α-decay lines are indicated as reported in [45]. The dashed lines were not fitted in the data due to non-sufficient statistics.

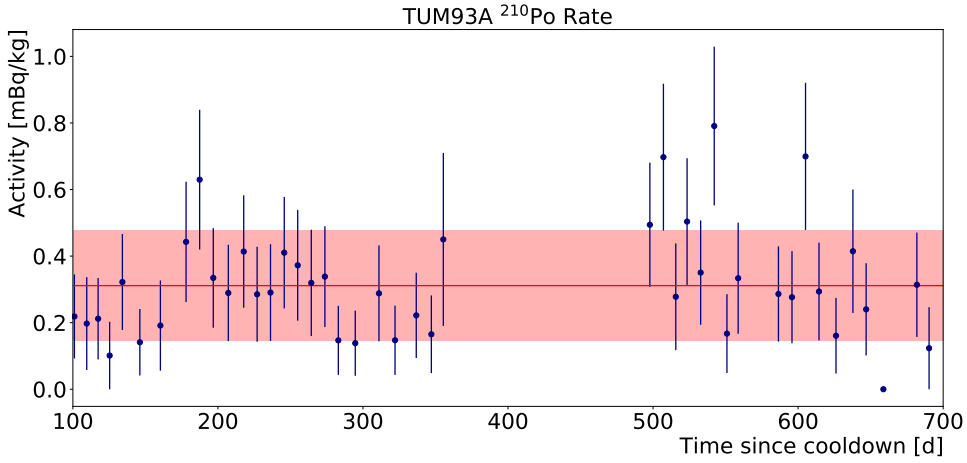

Figure 6.13: Rate in mBq/kg of the ^{210}Po decays detected in the TUM93A crystal in an energy range between 5.25-5.45 MeV. The data is binned in four data segments each, corresponding to ∼200 h per bin. In addition, the mean and standard deviation are shown in red.

Isotope	Activity [μBq/kg]			Improvement	
	TUM93A	TUM93C	TUM40 [45]	A-TUM40	C-TUM40
^{238}U	13.6 ± 5.5	16.6 ± 5.3	1010 ± 20	74.5	60.9
^{226}Ra	35.3 ± 6.2	38.9 ± 7.9	38.1 ± 4.9	1.1	1.0
^{210}Pb	149.7 ± 12.5	248.4 ± 18.6	7^{+36}_{-7}	0.05	0.03
^{210}Po int.	149.7 ± 12.5	248.4 ± 18.6	17.8 ± 4.0	0.12	0.07
^{210}Po ext.	147.4 ± 12.2	274.4 ± 19.4	-	-	-
^{235}U	<6.9	<11.3	39.5 ± 4.4	>5.7	>3.5
^{223}Ra	<6.9	<13.4	104 ± 7	>15.1	>7.7
^{232}Th	<9.4	<11.3	9.2 ± 2.3	>1.0	>0.8
^{224}Ra	<9.0	11.9 ± 5.2	19.8 ± 8.1	>2.2	1.7
	Surface Activity [μBq/cm^2]				
^{210}Po ext.	0.22 ± 0.02	0.41 ± 0.03	-	-	-

Table 6.4: Derived α-activities in TUM93A and TUM93C in comparison to the crystal TUM40 analysed in [45]. For TUM40, no number for the surface ^{210}Po rate has been published. The parent isotope of each secular equilibrium group is stated. Purification factors >10 are highlighted in green. A red factor corresponds to an increase in rate. The uncertainties are a combination of fit and bin-wise Poissonian errors given to the fit for the isotopes, which could be fitted by a Gaussian distribution. For the other isotopes with a small number of counts, a 90 % C.L. Poisson upper limit was derived according to table 40.3 in [116].

Also, the surface contamination is higher in TUM93C (by a factor of two), which is to a certain extent expected, as also the bulk contamination is higher by a factor of 1.6. In addition, it might originate from the storage difference between TUM93A and TUM93C shown in table 4.2.
Due to the fit, the surface background of ^{210}Po could be quantified, allowing a calculation of the intrinsic α-background of TUM93A and TUM93C shown in table 6.5. The values are compared to the intrinsic total α-activity measured in TUM40. An improvement in the overall intrinsic activity by a factor of 8.3 for TUM93A and 6.3 for TUM93C is calculated. This means that the intrinsic radiopurity of the TUM93 crystal was significantly improved by chemical purification.

Detector	α-activity [μBq/kg]	Improvement TUM40
TUM93A	369 ± 19	8.3
TUM93C	487 ± 22	6.3

Table 6.5: Intrinsic α-decay rate of all α-decaying isotopes of the three natural decay chains (^{238}U, ^{235}U, ^{232}Th) in an energy range from 3 MeV to 10 MeV for the TUM93 detectors. Improvement factors for comparing the intrinsic α-decay rate of TUM40 are given.

6.5.2 Extrapolation of Intrinsic e^-/γ-Activities from the α-Analysis

In the next step, the knowledge about the activity of the secular equilibrium groups in TUM93A and TUM93C is used to describe the background in the e^-/γ-band of TUM93A and TUM93C. The measured e^-/γ-background spectra of TUM93A and TUM93C up to an energy of 740 keV are shown in figure 6.14 (left) and zoomed in to an energy region up to 100 keV (right). The energy range is cut at 740 keV as the pulses in TUM93C start to cause flux quantum losses in the SQUID starting from this energy and cannot be reconstructed anymore.
In addition, a median rate is calculated for several energy ranges and shown in table 6.6. The rates agree well between the two detector modules.

Module	TUM93A	TUM93C
Energy Range [keV]	Rate [counts/(keV kg day)]	
10-100	3.33 ± 0.23	3.39 ± 0.20
10-40	4.46 ± 0.47	4.36 ± 0.39
30-40	2.93 ± 0.66	3.48 ± 0.60

Table 6.6: Rate in the e^-/γ-band of TUM93A and TUM93C for different energy regions. They agree well within their statistical uncertainties.

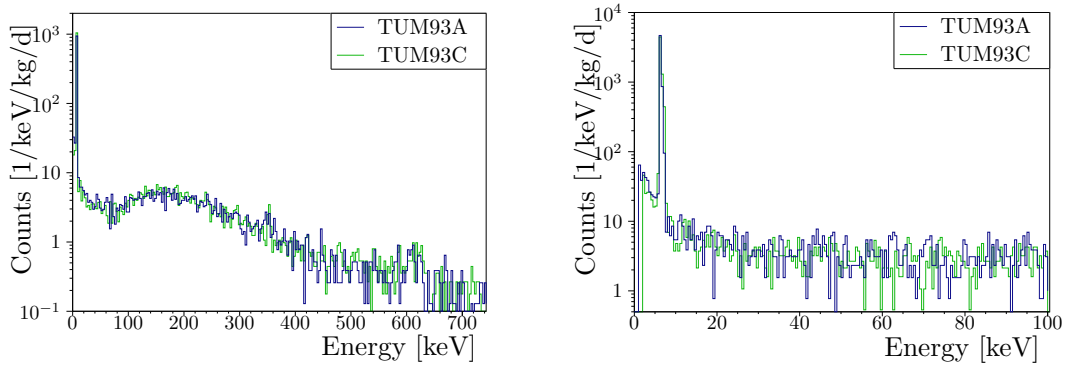

Figure 6.14: Left: Efficiency corrected energy spectra of TUM93A and TUM93C up to an energy of 740 keV. Right: Zoomed version up to an energy of 100 keV for both detectors. The spectra agree well with each other.

To determine the expected energy spectrum in the e^-/γ-band caused by intrinsic background, so-called templates derived from Monte-Carlo simulations are scaled according to the α-activity derived for TUM93A and TUM93C.
For this, $\mathcal{O}(100\text{k})$ decays of each isotope of the three natural decay chains are simulated in a $CaWO_4$ detector crystal in a fully implemented detector geometry.[1] DetA had a similar module design as TUM93A and TUM93C, only the detector resolutions were updated to match TUM93A and TUM93C. The outcome of these simulations is a list of normalised energy spectra in which the energy deposition in the crystal produced by each nuclide of the decay chains is represented. The templates for the decays of ^{210}Pb and ^{227}Ac are exemplarily shown in figure 6.15. For ^{227}Ac, the events are spread over a large energy region as ^{227}Ac can undergo both an α- and a β-decay. ^{210}Pb is purely β-decaying, and in 80 % of the cases it decays into an excited state of ^{210}Bi and emits a γ of 46.6 keV leading to the two structures in the template. The templates represent these effects correctly and help model each decay signature.
In the scope of this work, the integral of these templates was normalised to 1, representing a probability density function (PDF) for each decay. For a description of the background, the PDFs are scaled with the activities of their secular equilibrium group determined in the α-anlysis:

$$\text{Activity}_{e^-/\gamma}(E) = \text{PDF(E)}_{\text{normalised}} \cdot \text{Activity}_{\alpha-\text{line}} \tag{6.2}$$

and summed up afterwards.
Figure 6.16 shows the measured spectrum of TUM93A with the intrinsic contributions from the ^{238}U-chain in green, the ^{235}U-chain in orange and the ^{232}Th-chain in red. The sum of all contributions is shown in blue. The spectrum on the top shows an energy range of up to 500 keV, whereas the lower one shows a spectrum of up to 40 keV. In an energy range up to 40 keV, the expected rate from

[1] This work was performed for the module DetA by A. Karl in [117]

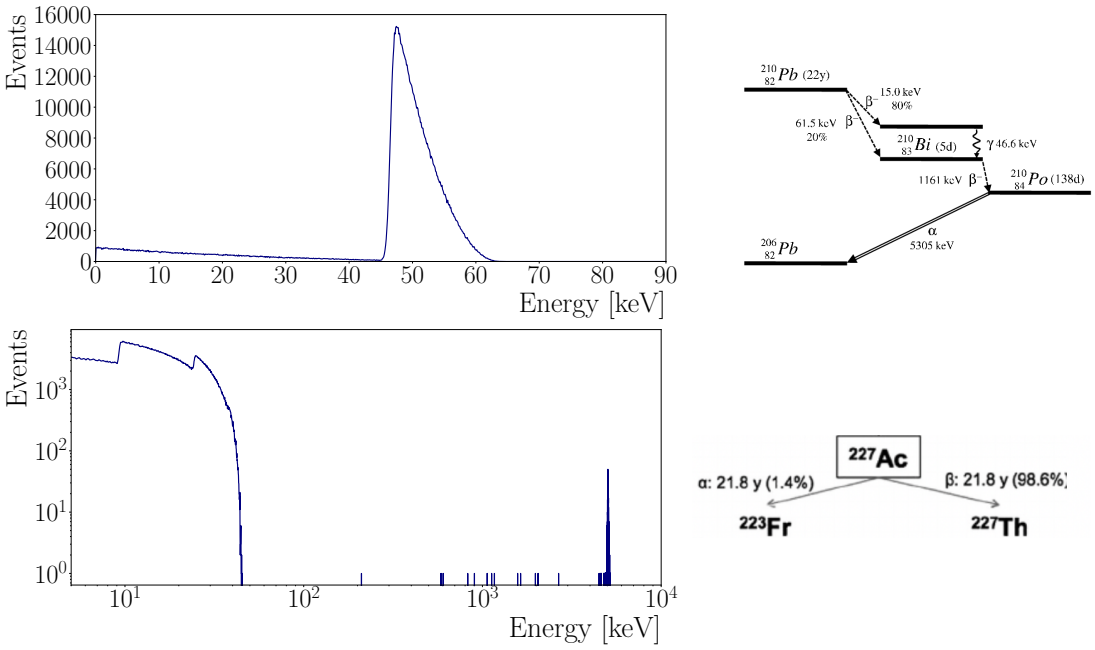

Figure 6.15: Left: Simulated templates for the ^{210}Pb decay (top) and for the decay of ^{227}Ac (bottom). The y-axis shows the raw amount of detected events for the simulation. Right: ^{210}Pb scheme from [118] and ^{227}Ac scheme from [119].

intrinsic contributions is 0.13 counts/keV/kg/d, and in an energy range below 5 keV 0.15 counts/keV/kg/d.

These results are compared to the detector TUM40 for which the same simulation was performed using the activities reported in [45]. The energy spectrum measured with TUM40 is taken from the analysis reported in [120]. The comparison of both TUM-grown crystals is shown in figure 6.17 for an energy range of up to 500 keV (top) and up to 40 keV (bottom). In this comparison, it is visible that the measured background in TUM40 is lower compared to TUM93A. Even though the background originating from intrinsic contaminations from the three natural decay chains over a broad energy range could be reduced by up to one order of magnitude, as shown by the ratio between the two simulated intrinsic background components. At ∼50 keV, the TUM93A intrinsic background exceeds the TUM40 background due to a significant contribution of ^{210}Pb, for which the PDF of the decay shows a peak at 50 keV. This observation is expected due to the high ^{210}Po α-rate detected in TUM93A, which was also higher compared to TUM40. At ∼100 keV, the improvement is the highest due to a significant reduction of ^{234}Th, for which the energy distribution of the decay shows a maximum at this energy. In the energy region below 5 keV, a reduction factor of ∼8.2 in the intrinsic activity is observed. This low-energy region is especially interesting for CRESST as LY bands overlap due to a finite energy resolution and background discrimination worsens.

With the help of the simulations, the contributions of individual isotopes on the background level can be investigated and compared between TUM40 and TUM93A.

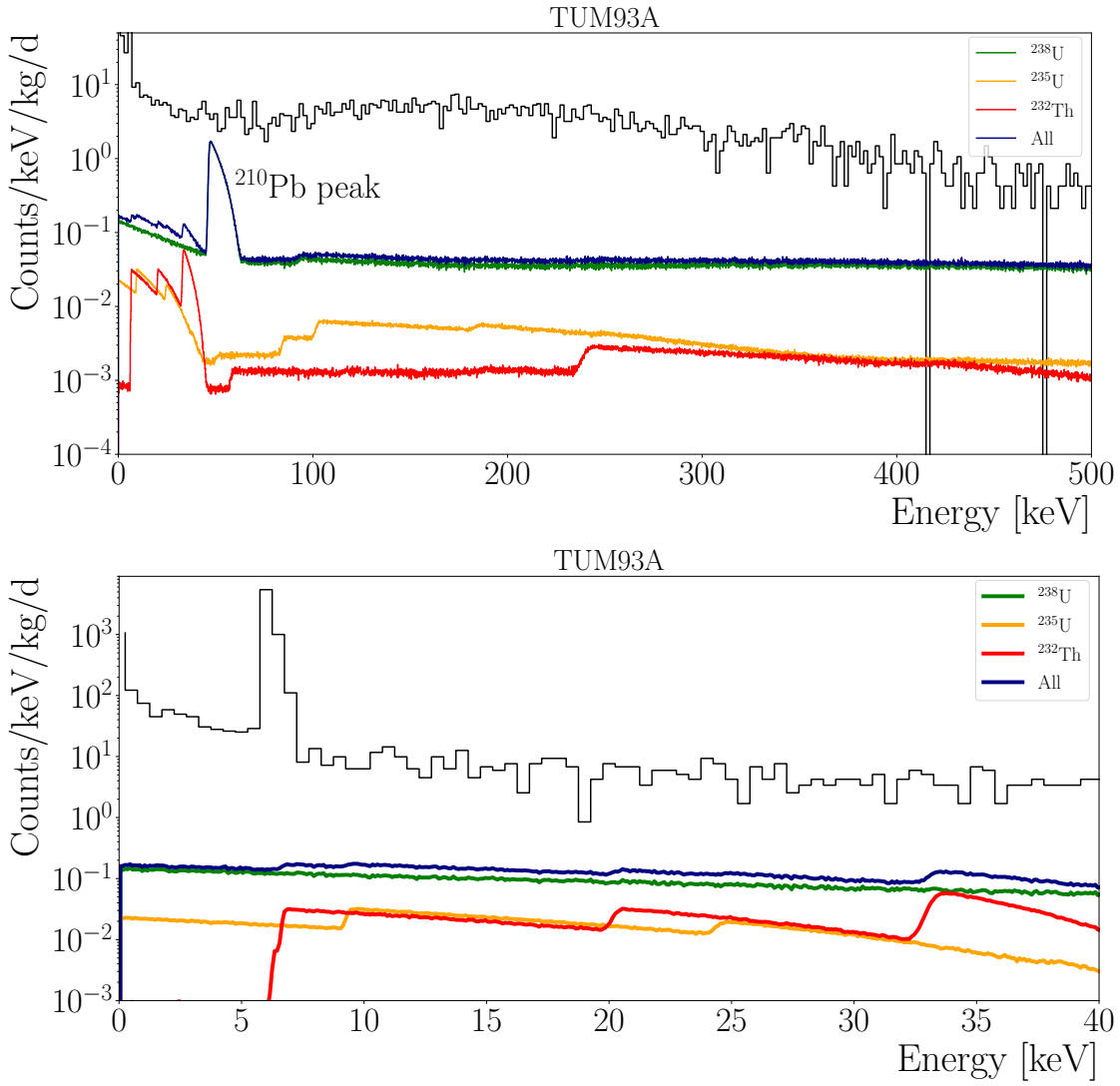

Figure 6.16: Energy spectrum of the efficiency corrected events in the e^-/γ-band recorded by TUM93A. The blue line indicates the sum of all background sources originating from the three natural decay chains ^{238}U (green), ^{235}U (yellow) and ^{232}Th (red) as derived from secular equilibrium assumption with α-decaying isotopes in the decay chains (see text). Top: Energy region from 0 to 500 keV. The high ^{210}Pb contamination present in the crystals is visible from the peak at ∼50 keV. Bottom: Zoomed energy region up to 40 keV. Only a dub-dominant fraction of the measured spectrum is described by the intrinsic background shown in blue. The remaining fraction is caused by different contributions. Below the ^{55}Fe peaks at 5.9 keV and 6.5 keV an additional flat background component from the source is visible in a higher background level.

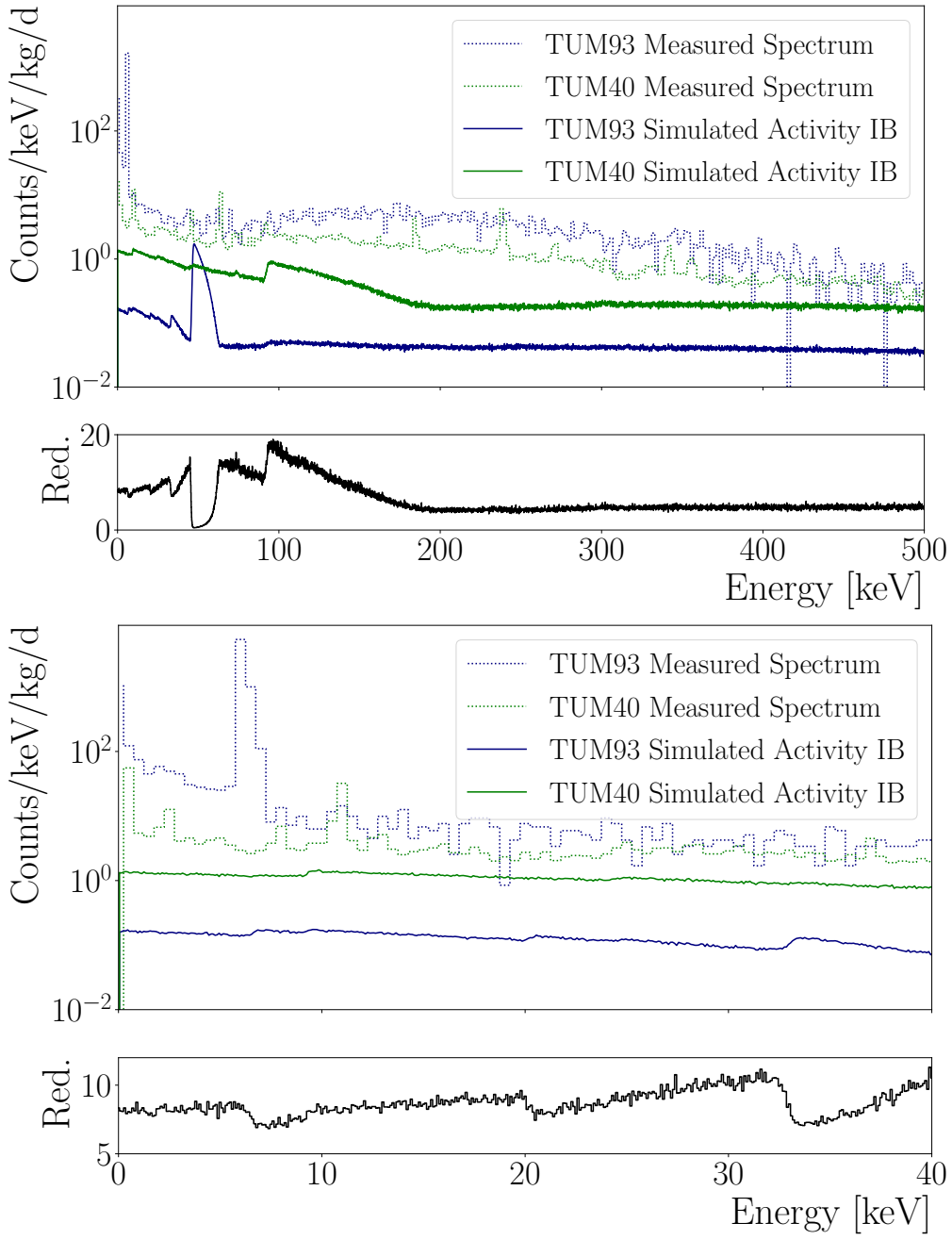

Figure 6.17: Comparison of the recorded data and the simulated sum of all intrinsic background (IB) sources originating from the three natural decay chains for the crystals TUM93A (blue) and TUM40 (green) for an energy range up to 500 keV (top) and 40 keV (bottom). The TUM40 energy spectrum is taken from the analysis performed in [120]. The ratios between the TUM40 and TUM93A simulated spectra are shown in the residual plots as reduction factors.

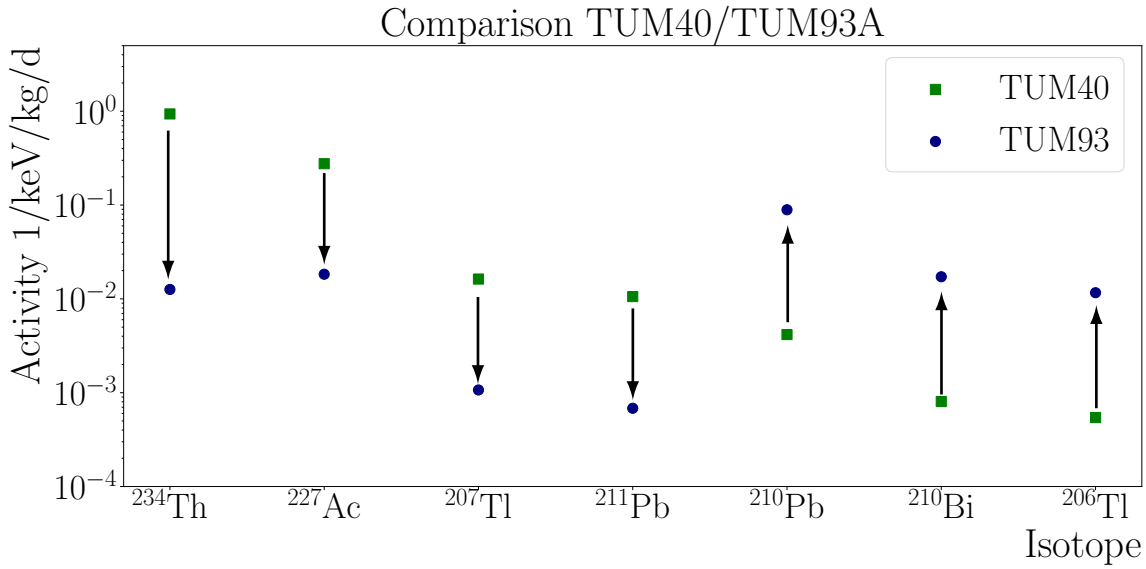

Figure 6.18: Change in activity of the most prominent isotopes in the energy range below 5 keV in TUM40 (green) and TUM93A (blue). The isotopes are sorted by their activity in TUM40, starting with the highest on the left. The arrows show whether the activity was decreased (downward arrow) or increased (upward arrow) in TUM93A compared to TUM40.

The scaled templates for the individual isotopes of all three decay chains are shown in figures E.1, E.2 and E.3 in Appendix E for both TUM93A and TUM40. Figure 6.18 shows the simulated activities for the isotopes which contribute most to the activity at a selected energy range below 5 keV for TUM40 in green and TUM93A in blue. The four isotopes with the highest activity in TUM40 could be reduced by a factor of 74 for ^{234}Th, 15 for ^{227}Ac and ^{207}Tl and by a factor of 16 for ^{211}Pb. The three isotopes with the highest activity below 5 keV of TUM93A are ^{210}Pb and its daughters ^{206}Tl and ^{210}Bi, for which the activity is higher by a factor of 21 compared to the activity in TUM40. It is not clear yet in which process of the purification the ^{210}Pb was introduced. Reducing the ^{210}Pb contamination to the same level as observed in TUM40 would yield an overall reduction factor below 5 keV of 30 instead of 8 for the TUM93A detector. For a possible future purification campaign, the focus should be on additionally minimising the ^{210}Pb introduction. Overall the achieved radiopurity is a milestone for the $CaWO_4$ production at TUM, showing that the chemical purification successfully reduced the background originating from natural decay chains in the region of interest for low mass DM search.

6.5.3 Determination of Other Background Components in the ROI

Even though the absolute level of intrinsic background could be reduced in the TUM93 crystals compared to TUM40, the overall background level in TUM93A

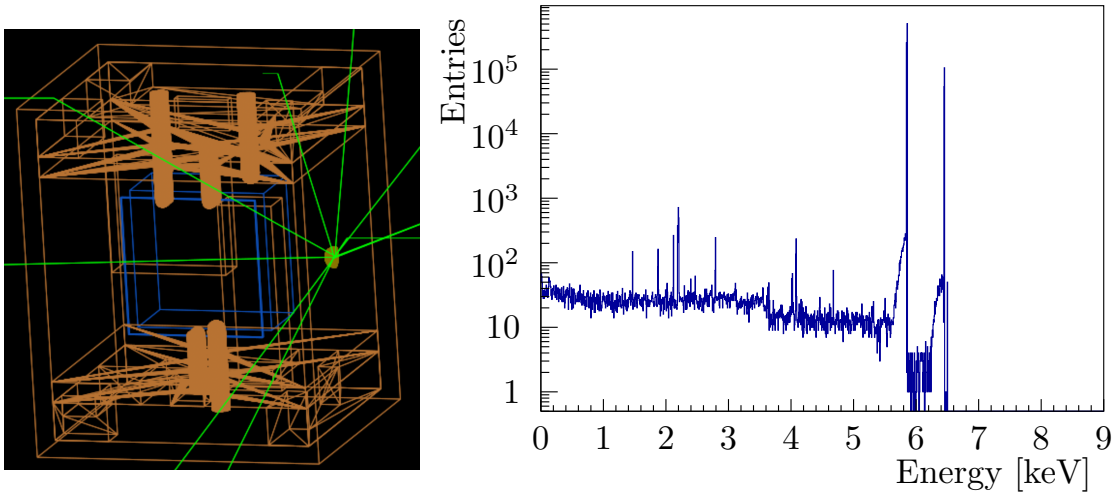

Figure 6.19: Left: Implementation of the geometry of TUM93C in the CRESST simulation software ImpCRESST. The iron source is located at the back of the module and is the starting point for the green trajectories. The $CaWO_4$ crystal and the LD are shown in blue, and the copper structure in orange. Right: Resulting template for the ^{55}Fe simulation. The energy spectrum detected by the PD for events induced by the source is shown on a logarithmic scale. Above $\sim$6.5 keV no events are caused by the detector's ^{55}Fe source. Figures by S. Banik.

and TUM93C are higher compared to TUM40. This is visible when comparing the measured spectra of TUM93A and TUM40 as shown in figure 6.17. Especially below the ^{55}Fe lines, a higher background is observed for TUM93A. To understand this effect, the ^{55}Fe source was implemented in a CRESST-III detector geometry[1] (see figure 6.19), and the expected energy distribution is computed with the help of Monte Carlo simulations. The results show that no source contribution is expected above $\sim$6.5 keV and a flat background is produced below the characteristic X-ray lines. This flat background is visible as an order of magnitude higher background in TUM93A compared to the TUM40 background level in the energy region below 5 keV. Also, at higher energies, a higher background level is present in TUM93A, implying that other background components are increased in TUM93A compared to TUM40. Only 2.1 % of the background in the energy region of 10-40 keV can be explained by the intrinsic contamination in TUM93A.

For a better understanding of the origin of the other 97.9 % of the background, a complete simulation including the detector holder, all the materials surrounding it, the shieldings and cosmic activation of the materials is needed.

The CRESST simulation group is currently developing this background model, adding spectral templates from other materials surrounding the detectors in addition to the templates for the intrinsic contaminations or intrinsic radiation (IR). For this, templates for intrinsic cosmogenic (IC), holder radiogenic (HR), shield-

[1] by S. Banik from the CRESST simulation group

ing radiogenic (SR), holder cosmogenic (HC), shielding cosmogenic (SC) and foil radiogenic (FR) backgrounds from the DetA simulation are used.

A complete set of templates is fitted to the combined data set for the e^-/γ-band and the α-region. A likelihood approach fits both the TUM93A and TUM93C data sets correlatedly, as many components, like the shielding radiogenic background, must be the same for both detectors. This makes the fit more robust. A first likelihood fit to the TUM93A and TUM93C data set was performed by J. Burkhart, who developed the approach in [121]. The results for TUM93A are shown in figure 6.20 and the results for TUM93C in appendix D in figure D.2. The top figure shows the fit to the α-region with templates scaled to the data. The templates cannot describe the 5.3 MeV peak as no surface ^{210}Po template was simulated yet for this detector. These simulations are currently in preparation. The bottom plot shows the results of a likelihood fit to the data, using the templates simulated for all components as mentioned above. The intrinsic cosmogenic component was limited according to the expected cosmogenic activation, as shown in figure 4.9. The other components of the fit are not limited by any constraints yet, and the fit assigns most of the background to radiation from shielding components. The likelihood fit, however, only has a coverage of 92 % of the data, highlighting the need to optimise the simulation further to describe the data more accurately.

Nonetheless, the preliminary results can be used to verify the results of the intrinsic background simulations performed in the scope of this work. Due to the correlated fit in the likelihood approach of the e^-/γ-band and the α-band for the intrinsic contamination, the IR component is restricted by the α-region from the assumption of secular equilibrium groups.

A comparison between the intrinsic contamination curves derived in the full simulation (red) and the intrinsic simulation performed in this work (blue) is shown in figure 6.21. The curves agree well with each other. The red curve has an additional component from ^{40}K, which could not be simulated in the scope of this work, as it is not part of the three main natural decay chains.

Even though the likelihood results are still preliminary, the fraction of the IR background from the overall background can be compared for detector modules containing different crystals. The likelihood approach assigns a fraction of 3.0 % of IR coverage (including ^{40}K) of the whole background in the energy region 10-40 keV for TUM93A and 3.4 % for TUM93C. The results are compared to the IR coverage of the crystals TUM40 and Lise (a CRESST-II module consisting of a commercial $CaWO_4$ crystal), fitted by the same approach in table 6.7.

The table shows that the intrinsic background of the commercial crystal Lise mainly dominated the overall background of the CRESST-II module containing a commercial crystal. This fraction could be reduced significantly by using TUM-grown crystals. With the current crystal quality of TUM93, it is only a sub-dominant fraction of the background, a significant milestone for the TUM crystal growth program. To further reduce the background level, other setup components have to be understood with the help of optimised simulations and decreased subsequently. In the following,

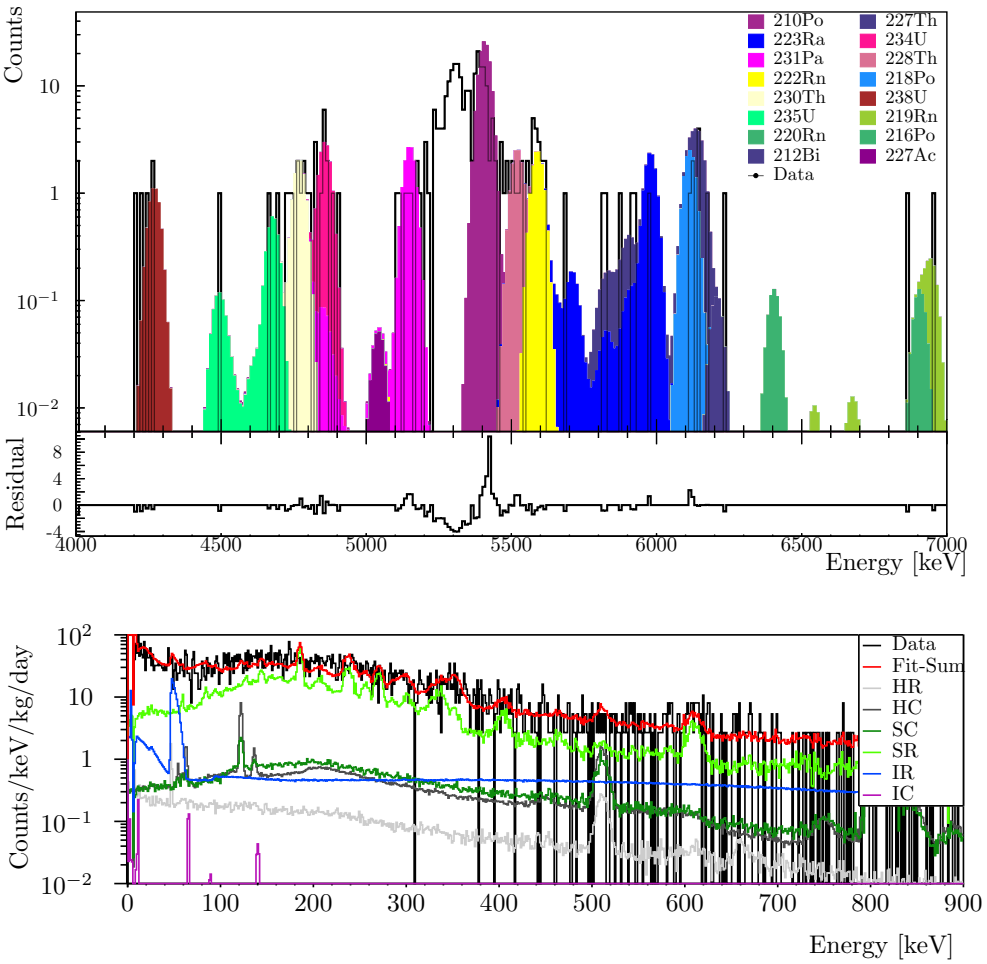

Figure 6.20: Results of the combined likelihood fit to both the α-region and the e^-/γ-band of TUM93A. Top: Template fit to the α-region of TUM93A with the different isotopes. As surface backgrounds are not included in the simulations, the surface ^{210}Po peak is not yet fitted with this model. Bottom: Likelihood fit of the various background components to the TUM93A e^-/γ-band spectrum. The intrinsic contaminations, fitted correlated with the α-activities, are shown as a blue curve. Other background components from the holder are shown in grey, the shielding in green and the cosmogenic activation of the crystal in magenta. The overall fit coverage in this energy region is 92 %. Fit performed by J. Burkhart.

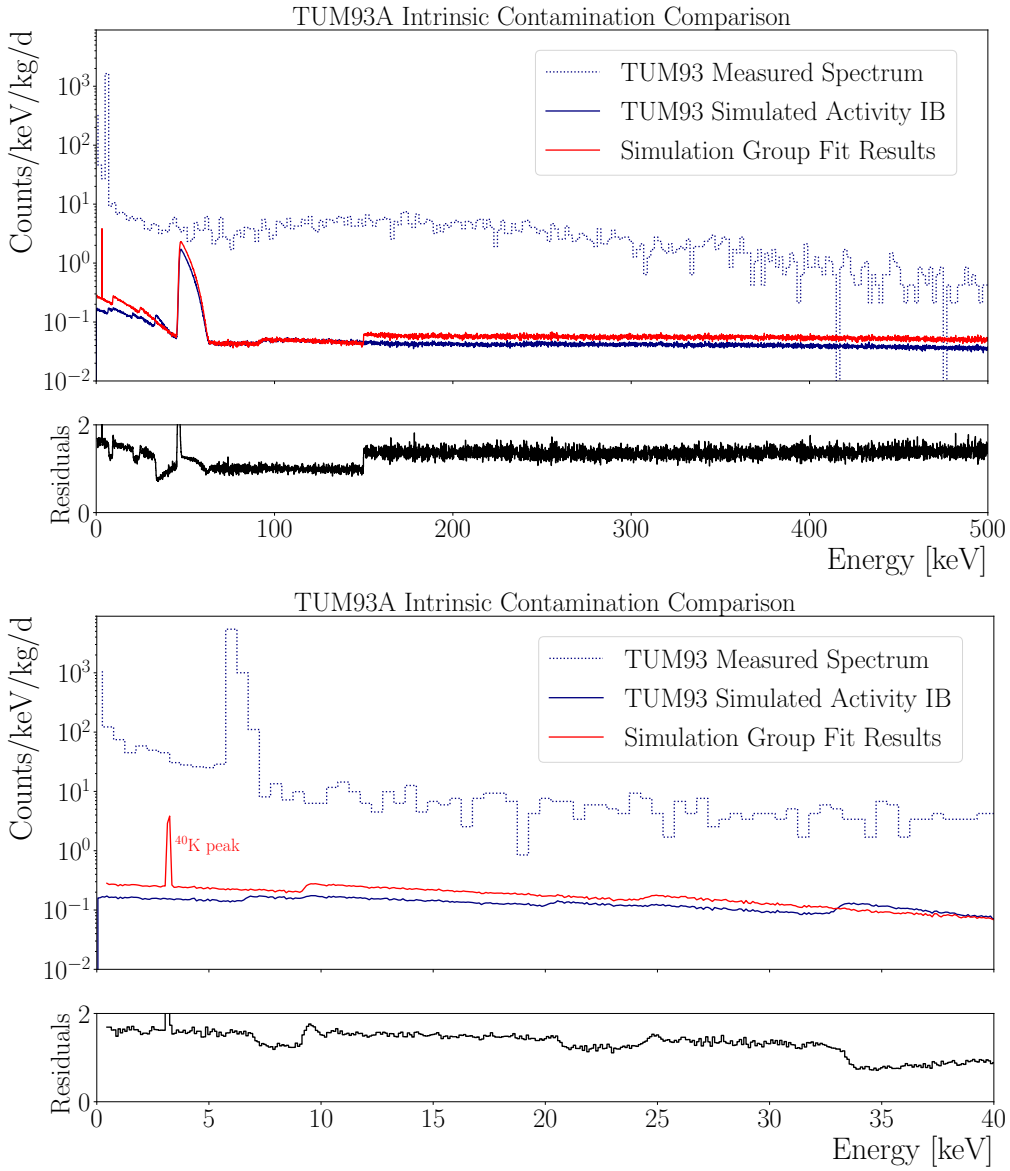

Figure 6.21: Comparison of the simulated intrinsic contaminations of this work (blue) with the results derived by the CRESST simulation group in red. A ^{40}K peak is visible above 3 keV. As this isotope is not part of the three natural decay chains, it was not simulated in the scope of this work as no related α-decays can be used for secular equilibrium assumptions.

Detector	IR Coverage [%] (including ^{40}K) 10-40 keV
TUM93A	3.0
TUM93C	3.4
TUM40	44.5
Lise	80.0

Table 6.7: Described fraction of the e^-/γ-background by intrinsic contaminations (IR coverage). Numbers for TUM40 and Lise from [121]. The TUM93 results are derived by J. Burkhart. The total coverage of the fit is 92 % for TUM93A and 102% for TUM93C.

the ultimately possible sensitivity of CRESST with this quality of $CaWO_4$ crystals is discussed further.

6.5.4 Sensitivity Projections

This section studies what sensitivity can be achieved with the TUM93A crystal quality compared to the TUM40 crystal quality, assuming all other background components, especially the LEE, can be understood and eliminated in the future. For this, the simulated intrinsic background is used as a baseline for an exclusion limit simulation similar to the approach used in section 2.4. The exclusion limits are simulated for a threshold of 54 eV (the current TUM93A threshold) and a threshold of 10 eV for both TUM93A and TUM40. The threshold of 10 eV was reached in the ongoing data campaign, and the next-generation detectors are expected to have thresholds in this energy region. The simulated exposure for the limits ranges from 10 kgd, roughly approximating the collected exposure in the ongoing campaign, up to 1000 kgd, which is the exposure goal for the upcoming CRESST upgrade. The resulting exclusion limits with 2-σ uncertainty bands are shown in figure 6.22 for the case of a 10 kgd (top) and 1000 kgd (bottom) exposure for a threshold of 54 eV (TUM93A, dark blue) and 10 eV (light blue for TUM93A, green for TUM40). Independent of the exposure, the exclusion limits at low DM masses strongly depend on the detectors' threshold and underline the need for a further threshold reduction. At an exposure of 10 kgd, no difference in the simulated limit for TUM93A and TUM40 is visible, whereas, for 1000 kgd of exposure, the TUM93A crystal quality can yield better DM exclusion limits implying that a reduction of the intrinsic contamination of the $CaWO_4$ crystals becomes especially important for larger exposure.
To better visualise the sensitivity gain with exposure for different DM masses and thresholds, the results are shown in a DM-cross-section vs exposure plot for four selected DM masses of 0.3 GeV/c^2, 0.82 GeV/c^2, 2.0 GeV/c^2 and 5.0 GeV/c^2.
For lower DM masses, the impact of the threshold on the sensitivity is higher than the impact at higher masses, as expected. For DM masses $\mathcal{O}(5\,\mathrm{GeV/c^2})$, the sensitivity no longer depends on the threshold. For the low-mass DM region, which is the mass region in which CRESST is setting the most competitive limits, the crystal

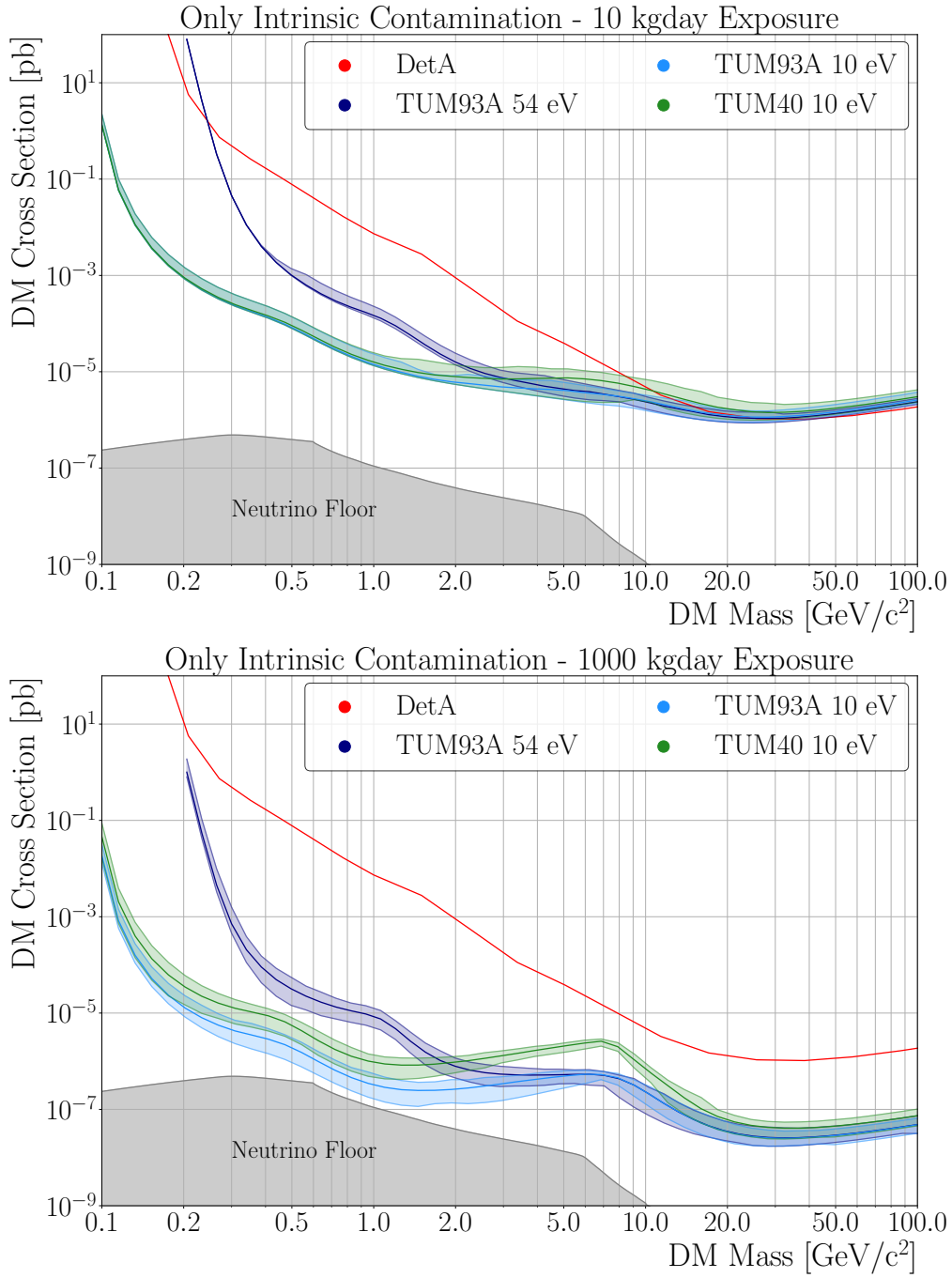

Figure 6.22: Exclusion limit projections for TUM93A (54 eV threshold, dark blue and 10 eV threshold, light blue) and TUM40 grade crystal (10 eV threshold, green) with only intrinsic background, for a 10 kgd exposure (top) and 1000 kgd exposure (bottom).

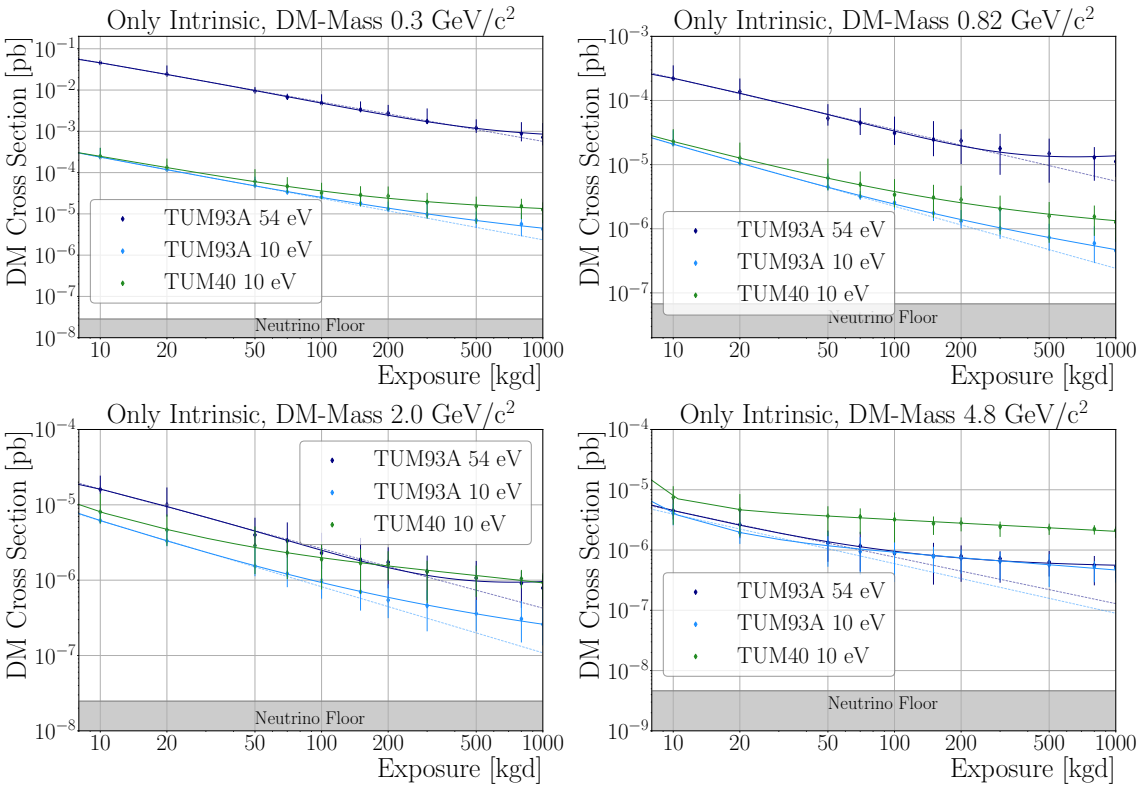

Figure 6.23: Sensitivity projections for TUM93A (54 eV threshold, dark blue and 10 eV threshold, light blue) and TUM40 grade crystal (10 eV threshold, green) . Four different DM Masses are compared: 300 MeV/c² (top left), 820 MeV/c² (top right), 2.0 GeV/c² (bottom left) and 4.8 GeV/c² (bottom right). The dashed lines correspond to the background-free improvement of the limits, the solid lines are fits to the data points.

quality provides a near-background-free measurement of up to 50 kgd for TUM93A-grade crystals and up to only 10 kgd for TUM40 grade crystals. For higher exposures up to 1000 kgd, the sensitivity gain deviates from the dashed line, corresponding to the sensitivity gain for a background-free measurement. The measurement with the TUM93A-grade material would not be background-limited at this exposure as the sensitivity curve is not yet approaching a horizontal line. For TUM40-grade crystals, however, the sensitivity curves flatten earlier. This effect is also visible for higher DM masses. The TUM40 sensitivity projections are always weaker than the TUM93A projections due to the higher background level, and the sensitivity simulations deviate from the background-free projections already for small exposures.

6.6 Discussion

The crystal TUM93 shows a significantly reduced α-activity of $(369 \pm 19)\mu$Bq/kg which is a factor 8.3 lower compared to TUM40 activity. Comparing the intrinsic

activities of the β- and γ-decaying isotopes of the three natural decay chains, created via simulations and secular equilibrium assumptions of the secular equilibrium subgroups, the reduction factor in the energy region below 5 keV is similar, namely a factor of $\sim$8.2, which means that the purification also impacts the background in the low energy region most relevant for low-mass DM search. The four most prominent isotopes of TUM40 in this energy region could be reduced by at least an order of magnitude.

In contrast, the measured spectrum of TUM93A shows a higher count rate than TUM40, implying that other background components are more prominent in TUM93A than TUM40. To understand this effect, simulations of the entire CRESST geometry are currently in preparation by the CRESST simulation group. Preliminary results based on a likelihood fit to both the α and e^-/γ-spectra yield a comparable intrinsic contamination level and provide a cross-check for the results derived in this work. The simulation has to be optimised for all other components in the future, as the current fit coverage is only 92 %. For this, screening results of different components of the detector holders and the shielding have to be included, and additional isotopes resulting not only from natural decay chains but also from radioactive isotopes created, e.g. by nuclear weapon tests, have to be simulated.

The intrinsic background spectra were used for sensitivity projections with different thresholds, which show that a lower threshold improves the DM exclusion limit significantly at lower DM masses and that depending on the DM mass, a near background-free measurement is possible with the TUM93A crystal quality up to an exposure of 50 kgd and above that a non-linear improvement of the limit with exposure until 1000 kgd (the design goal of the CRESST upgrade). With the TUM40 crystal quality, the sensitivity curves deviate earlier from the background-free measurement cases, and the reachable sensitivity is always smaller compared to the TUM93A-grade crystals.

These projections present the ultimate sensitivity which can be reached with the two different radiopurity levels of the TUM93 and TUM40 crystals without other backgrounds and especially without the LEE present. As mentioned above, the intrinsic impurities only contribute a small percentage to the overall background level in the ROI. Exchanging the TUM93A intrinsic purity in the TUM93A measured spectrum with the TUM40 intrinsic purity would only raise the overall background by $\sim$2-5 % in the energy region above the ^{55}Fe X-ray peaks, and below the difference is negligible. Hence, removing the calibration source, LEE and other background sources are required before the purity difference between TUM40 and TUM93 becomes relevant. If these sources are reduced in the future, TUM93A-grade crystals will provide a powerful tool to enhance CRESST's sensitivity.

For the decision on which crystals to use in the upcoming CRESST upgrade, factors like the workforce needed to produce a certain quality have to be considered. With the chemical purification process described and applied to the powder in this work, only a few grams of $CaWO_4$ can be produced in one run. Hence, mass production is challenging. Therefore, other methods for purifying $CaWO_4$ crystals, like re-crystallisation, must be investigated. If the re-crystallisation process also signif-

icantly improves intrinsic radiopurity, it can provide a good compromise between workforce and background reduction in CRESST. A setup for a fast determination of α-activities in a whole crystal ingot was developed in the scope of this work and is described in chapter 9. This setup can investigate the impact of re-crystallisation on the intrinsic impurity concentration in $CaWO_4$ crystals.

Chapter 7

Results of the Low-Energy Analysis

In this chapter, the low-energy analysis of the TUM93A module is described. First, in section 7.1, the data sets analysed in this work are presented. Afterwards, specific analysis steps applied for the low-energy analysis to obtain DM limits and study the LEE for the TUM93A 2-channel detector and a light detector-only analysis are described in section 7.2. These analysis steps are based on the DM analysis published in [37] and were adapted for the LEE analysis in collaboration with the CRESST analysis team. A calculation of a DM exclusion limit, including band fits, is shown in section 7.3 and the characteristics of the LEE and intrinsic stress as the possible origin of it, are investigated in section 7.4.

7.1 Analysed Datasets

Four data sets have been processed for the low-energy analysis in this work, which are explained in section 4.6. The background data set (*Bck*), the neutron calibration (*Ncal*) with an AmBe source and the *PostCal* data set. In addition, the data set following a warmup of the carousel is analysed as the After-Warm-Up (*Awu*) data set. Approximately 20 % of the *Bck* data set were used as a *Training* set for the DM analysis on which the cuts and the energy calibration were fixed. For the DM analysis, the *Training* set is excluded from the *Bck* data set, forming the *Blind* data set. The raw exposures of these sets, assuming the detector masses from table 2.1, are shown in table 7.1. A list of all data segments included in the analysis is shown in tables B.1 to B.4 in appendix B.

7.2 Low-Energy Analysis Steps

This section focuses on the specific steps applied to the data set for the DM and LEE analysis of both the analysis of TUM93A as a 2-channel module with TUM93A-Ph as the primary detector and the LD as veto detector (called PD or TUM93A analysis

Detector	Blind [kgd]	Training [kgd]	Ncal [kgd]	PostCal [kgd]	Awu [kgd]
TUM93A-Ph	3.732	0.7112	0.9418	0.5446	3.311
TUM93A-L	0.09931	0.01778	0.02354	0.01362	0.088277

Table 7.1: Raw exposures of all low-energy data sets analysed for the low-energy analysis of TUM93A. The *Bck* data set is composed of the blind and training data sets.

in the following) and the TUM93A-L direct hit analysis (called LD or TUM93A-L analysis). For both analyses, the OFilter is selected to reconstruct the amplitudes, as it has the optimal signal-to-noise ratio per definition and yields the lowest threshold. For the PD analysis, the primary detector is triggered with a threshold of 8.22 mV, for LD analysis, the LD was triggered with a threshold of 17.8 mV. Both values are determined with the method described in section 5.5.

Amplitude Determination using the OFilter

The trigger OFilter writes several parameters for each pulse. One is the trigger position which is used to set the pulse maximum to the defined position and collect the pre-trigger range of one-fourth of the entire record window before the pulse. This ensures that every event has the same Onset and OFilter MaximumPosition value. In addition, the trigger filter amplitude (TFA) parameter is evaluated for each pulse. This is the OFilter amplitude determined by the trigger OFilter used for the trigger process. However, this parameter is only stored for the channel which was triggered. For an analysis with two or more channels where the other channels are used as veto detectors and are not triggered, no information about the amplitudes in these channels is stored. In addition, no information about the goodness of fit for the amplitude information is currently stored for the triggered channel. Therefore, the OFilter has to be applied to all pulse windows in all channels to provide a reconstructed amplitude and fit RMS.
The OFilter, when applied to a pulse, performs a maximum search on the back-transformed pulse, reconstructing the maximum of the pulse. For the low-energy analysis, two possible effects are taken into account. First, the window OFilter can suffer from boundary effects as the baseline is cut sharp at the beginning and end of the pulse window. This can lead to a wrong reconstruction causing the window filter to find a different maximum position than the trigger OFilter, which did not suffer these boundary effects. Second, no scintillation light is produced for small pulses; hence, none should be measured by the LD. Therefore, the resulting Amplitude should be a Gaussian distribution around 0 V. The OFilter, however, is always looking for a positive fluctuation and finds a maximum position where the fitted amplitude is positive. Applying the OFilter with free maximum search leads to an LY plot (LY = OFAmplitudeL / OFAmplitudePh) as shown in figure 7.1 (left). The LD should see no light for very low energies, and the LY band should

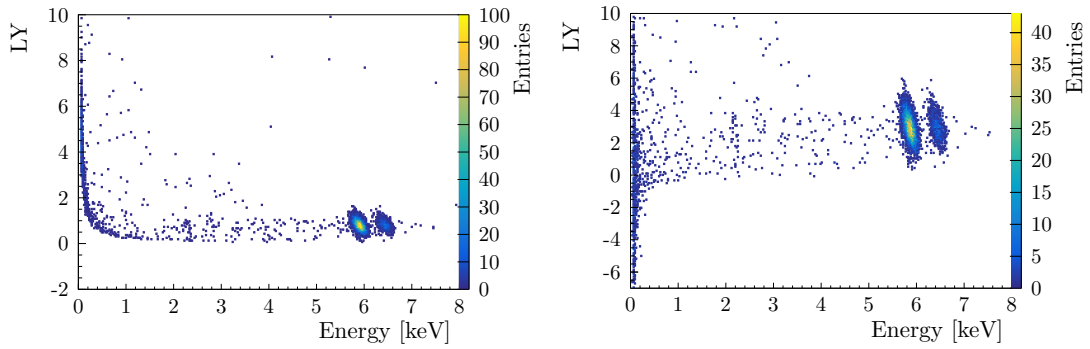

Figure 7.1: Left: LY Plot of TUM93A showing the full data set. Both ^{55}Fe lines are visible in the spectrum. The OFilter was applied to both channels without fixing the MaximumPosition. Instead of being symmetric, the LY band curves upwards at low energies due to the positive bias of the OFilter reconstruction for small amplitudes. Right: LY plot for a correctly reconstructed LD amplitude. The LY at low energies shows a symmetric distribution.

be a Gaussian distribution. Due to the positive bias of the OFilter, the LY band curves upwards.
The MaximumPosition is fixed to the primary detector's maximum position to prevent this positively biased reconstruction. Fixing the OFilter leads to a correct reconstruction of the LD amplitude, as shown in figure 7.1 (right).

7.2.1 Energy Calibration and Detector Response

As described in 2.2.1 the CRESST detectors are actively stabilised by CPs, which are highly energetic heater pulses injected into the detector. The DAQ evaluates the PulseHeight of these pulses, and a PID controller is actively changing the detector's temperature to keep it at its operating point. This stabilisation works for a rough compensation but is not sensitive to small or fast changes in the working point. Therefore, additional heater pulses, the TPs, are injected over a broad energy range into the detector. Using the reconstructed amplitudes of the TPs, the time-dependent behaviour of the detector can be corrected in the energy range covered by the TPs. As the TPs have a known relative energy to each other, they can also be used to linearise the detector. Afterwards, the time-corrected and linearised spectrum is used for the energy calibration.

Time-dependent Test Pulse Response

In the first step, the TPs have to be fitted with one of the methods described in section 5.4, which should be the same used to fit the particle events. Figure 7.2 shows the reconstructed amplitude of TPs from five files plotted versus their Unix time stamp for TUM93A-Ph. In total, ten different TP heights are sent to the detector.

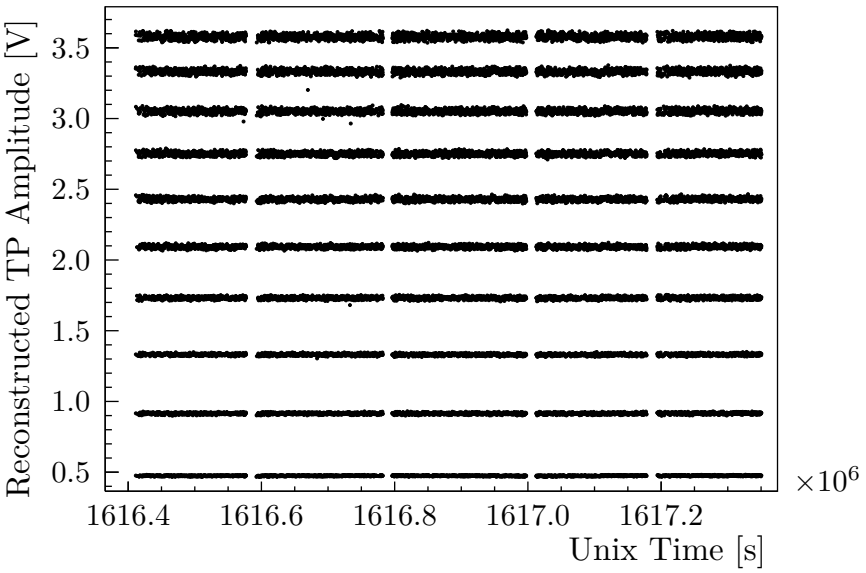

Figure 7.2: TPs of TUM93A-Ph of five example files plotted against the Unix time stamp. In total, ten different TP amplitudes are injected into the detector.

For the Test Pulse Response (TPR) object needed for the time-dependent correction of the data, the TPs are evaluated file by file. For each file and each TP amplitude, a spline fit is performed between the data points using a Gaussian kernel with a width of 30 min. Figure 7.3 shows four selected TP amplitudes from file bck-009 for TUM93A-Ph (black) and the spline fit for each TP amplitude in red. The spline fit shows that the working point changes slightly over time.

The following method is applied to correct the reconstructed amplitude for each particle event individually: All spline values are evaluated at the event's time. The spline amplitude, assumed to correspond to the reconstructed TP amplitude at this exact time, is plotted for each TP against the known injected amplitude (see black dots in figure 7.3 right). In the next step, the data points are fitted by a cubic spline (red curve); this is the transfer function forced to go through the (0/0) point. It translates the reconstructed amplitude of the spline function to a Test Pulse Equivalent (TPE) injected amplitude and includes non-linearity effects such as truncation of the pulses above 1 V. This process is repeated for each particle event such that the reconstructed amplitude for each event is converted to a value corresponding to the equivalent of the injected amplitude or, as typically named, the test pulse equivalent amplitude. As the injected amplitudes of the TPs correspond to different (but fixed) energies, the TPE parameter is an energy estimator, which is calibrated in the next step.

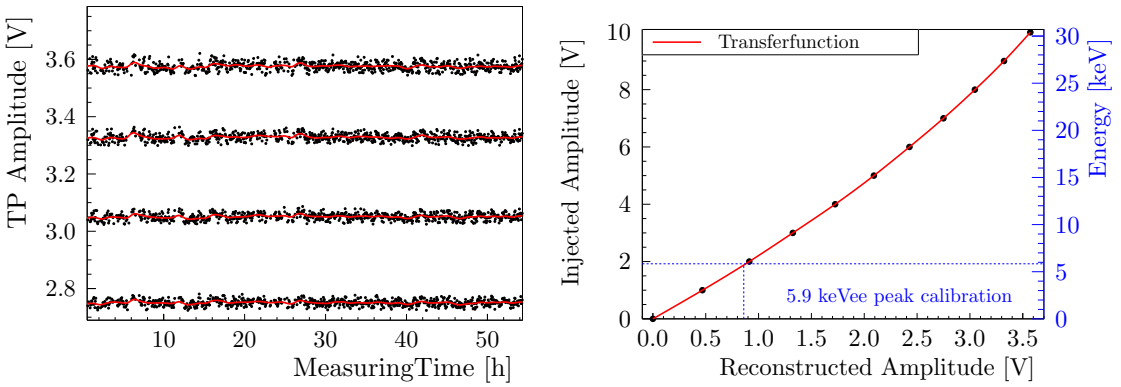

Figure 7.3: Left: Spline fit to four selected TPs of TUM93A-Ph for file bck-009. The spline represents the working point change over time. Right: Comparison of injected and spline amplitude for each TP at a certain time T. The points are fitted with a cubic spline producing the transfer function, which translates reconstructed energy to injected energy, an estimator for the energy. Using a calibration line, the injected energy axis can be converted to the energy axis by multiplication with the CPE factor.

Energy Calibration with Internal ^{55}Fe Source

In the ongoing data-taking campaign, the energy calibration is performed using the ^{55}Fe source mounted inside of the detectors. ^{55}Fe decays via electron capture to ^{55}Mn with a half-life of 2.737 years [122]. Table 7.2 shows the most prominent X-ray lines emitted from the source. The energies of these lines are for most detectors still within the fully linear range of the detectors. Hence, they can be reconstructed with the OFilter, and an energy calibration down to the detector's threshold is possible.

Xray shell	energy [keV]	intensity
Mn $K_{\alpha 2}$	5.888	8.5
Mn $K_{\alpha 2}$	5.899	16.9
Mn $K_{\beta 3}$	6.49	1.01
Mn $K_{\beta 1}$	6.49	1.98

Table 7.2: Prominent X-ray lines from the ^{55}Fe decay with intensities of more then 1% are shown [112]

For the calibration, the TPE amplitude of the events is plotted in a histogram and the 5.9 keV line is fitted with a Gaussian function (see figure 7.4). The Convert Pulseheight to Energy factor (CPE) is extracted from the fit, which converts the energy scale from equivalent injected amplitude to energy. This is shown in figure 7.3 (right). The 5.9 keV line from the ^{55}Fe source is used for calibration (blue line) of the energy axis (blue axis on the right). As a cross-check, the position of the second peak is determined and compared to the nominal value.

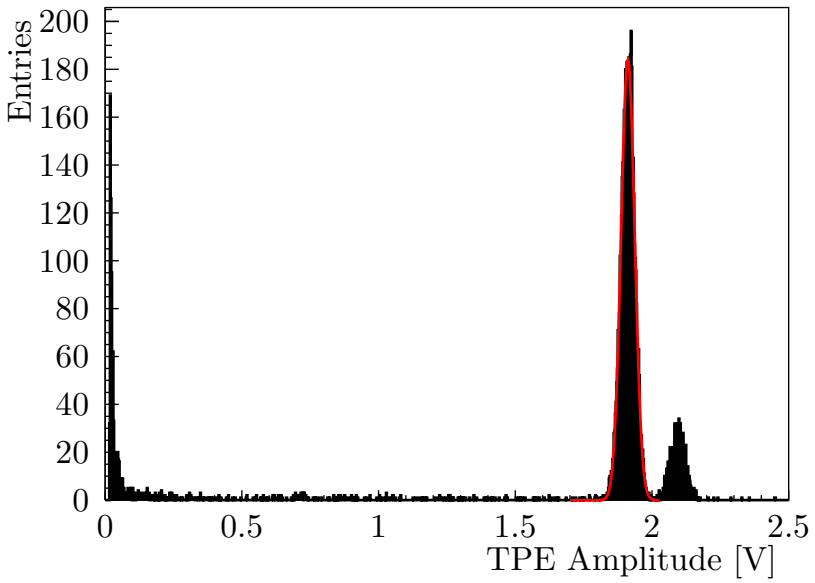

Figure 7.4: TPE amplitude for events of detector TUM93A-Ph. Two peaks from the iron source are visible. A Gauss fit is performed to obtain the mean of in TPE amplitude of the 5.9 keV peak (red). This value is used to calculate the CPE value, which converts the energy scale from TPE amplitude [V] to energy [keV].

7.2.2 Data Selection

In the next step, the data has to be cleaned from artefacts and wrongly reconstructed pulses. These artefacts can, e.g. be electronic spikes, SQUID resets and other effects which disturb the baseline and create an invalid event. Also, pile-ups with other particle events or heater pulses can lead to wrongly reconstructed amplitudes. In the following, the cuts applied for the low-energy analysis of TUM93A and TUM93A-L are explained in detail.

Delta Voltage Cut

This cut aims to remove so-called delta spikes from the data set. A delta spike is an electronic disturbance that causes the baseline level to drop for a few channels before returning to its original value (see figure 7.5 top left). These spikes cause the OFilter to trigger but are invalid pulses. A cut on the value DeltaVoltage described in section 5.3 is used for this.

BaseLineDiff Cut

High-energy pulses need a long time to decay back to their baselines. Depending on their energy, this time may be longer than the record window. If a pulse occurs close to the high energetic event, its baseline is not flat but still decaying (see figure 7.5 top

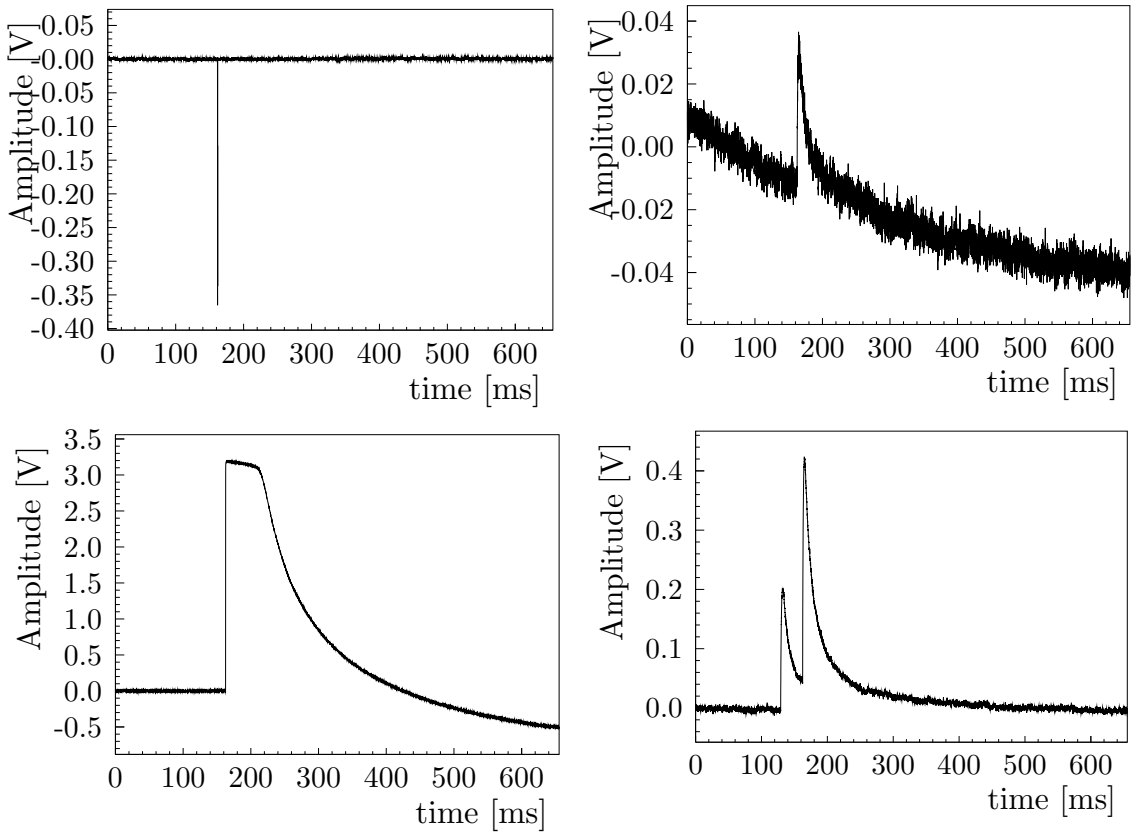

Figure 7.5: Collection of pulses cut away by the data quality cuts. Top left: Electronic spike on the pulse. This spike is cut away by the DeltaVoltage cut. Top right: Pulse sitting on a decaying baseline of a previous pulse. The reconstruction of these pulses is, in most cases, not correct. The BaseLineDiff cut removes these events. Bottom left: Saturated pulse with an FQL. The baseline on the right is lower than the pre-trigger baseline. The BaseLineDiff cut also removes these events. Bottom right: Pile-up event of one particle pulse with another particle pulse. The OFilter RMS of these events is higher than for normal events. The RMS cut can remove these events.

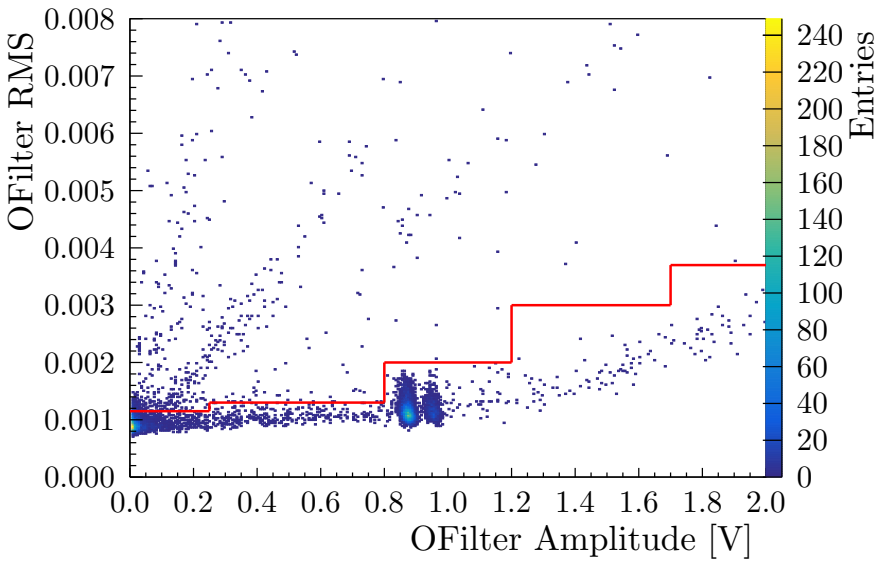

Figure 7.6: OFilter RMS plotted against the OFilter Amplitude. The RMS is energy-dependent, so a step cut is applied to the data. Above the iron line, the RMS starts to curve up as the pulses start to saturate.

right). This can affect the reconstruction of the amplitude. Therefore, these pulses have to be discarded. The parameter BaseLineDiff is sensitive to these pulses as the baseline of a pulse sitting on a decaying baseline is lower on the right side than on the left side, so the parameter becomes negative. At the same time, the parameter is sensitive to FQLs of the SQUID, which have a lower baseline level at the end of the pulse window than in the beginning (see figure 7.5 bottom left). High-energetic pulses not entirely decaying within the record window have positive BaseLineDiff values and can also be cut away with this cut, as these high-energetic pulses are not needed for the low-energy analysis. As the effect of a decaying baseline on the reconstruction of a pulse becomes more substantial with a smaller pulse height, the cut should be set rather stringent.

Comparison Trigger OFilter - Window OFilter

As described above, the OFilter applied to the pulse windows can suffer from boundary effects and reconstruct a wrong amplitude value. The TFA value (the amplitude determined by the trigger OFilter) is compared to the session OFilter amplitude to avoid an inaccurate reconstruction due to this effect. A difference of 2% from the trigger amplitude is allowed for each pulse. Pulses with larger differences between both amplitudes are discarded.

OFilter RMS Cut

Effects like pile-ups or artefacts on the pulse (see figure 7.5 bottom right) can influence the reconstruction of it. The OFilter calculates the RMS value for each fit. A

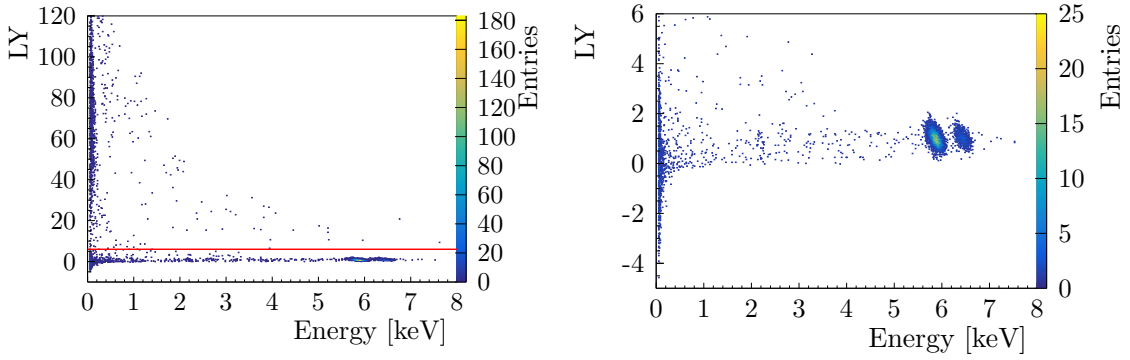

Figure 7.7: Left: Plot of the LY of all events surviving the data quality cuts for TUM93A against the measured energy in the TUM93A-Ph detector. The LY is normalised to 1 for the LY of ^{55}Fe γ-events. On the top left of the plot, events showing a significantly higher LY are located. They are called light-only events and have mostly a signal in the light detector. Right: Same spectrum after applying an LY cut which removes the light-only events visible in the left plot.

cut on this value ensures that only pulses with a pulse shape similar to the standard event used for the filter end up in the final data set. As the RMS value depends on the amplitude of the reconstructed pulses, a step-like cut must often be performed (see figure 7.6). The shape of this cut can be chosen freely as a cut-efficiency simulation later models the fraction of valid events removed by this cut.

Light Yield Cut

The abovementioned cuts are designed to remove invalid event classes that either originate from non-physical events or could not be reconstructed correctly. In the next step, a physically motivated cut, the LY cut, is applied to the data of the TUM93A analysis. It removes events which deposit mainly energy in the light detector instead of the primary detector. These events are so-called light-only events. Plotting the LY of all surviving events (normalised to one for ^{55}Fe events) against the energy detected by TUM93A-Ph they are located in the top left of the LY plot (see figure 7.7 left). The LY is cut at a value below these events to remove them. Figure 7.7 (right) shows the resulting selected events. So-called excess-light events that feature a phonon signal but also a large light signal compared to the e^-/γ-band remain in the data set and are visible above the e^-/γ-band in the right plot. This selected data after the LY cut is used for high-level analysis, like a derivation of dark matter exclusion limits and LEE studies. For the light-only analysis of TUM93A-L, this cut is used to remove events which have also triggered in the PD.

7.2.3 Survival Probability Determination

The applied trigger procedure and event selection, including stability, muon and data quality cuts, are designed to remove all artefacts of the data and provide a

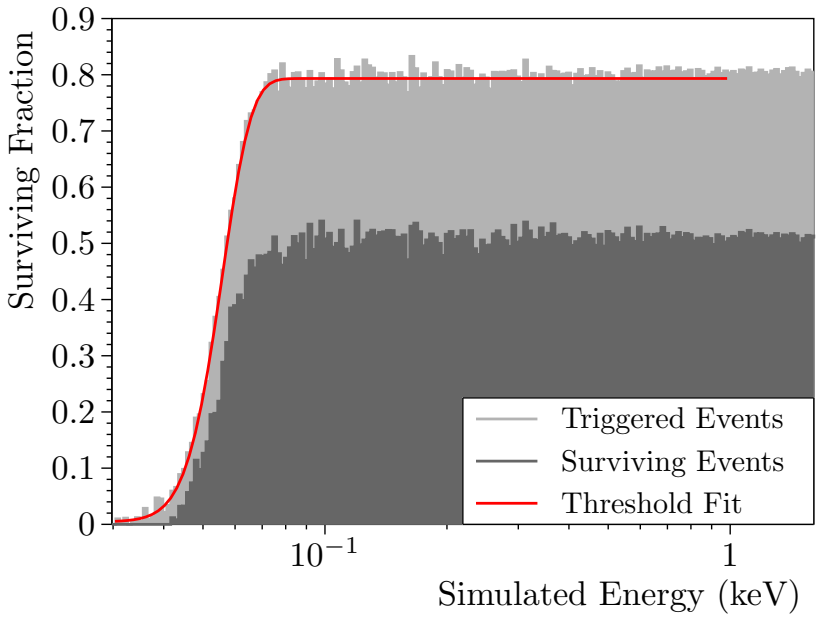

Figure 7.8: Surviving fraction of events for all events after triggering (light grey) and events after all cuts (dark grey)for TUM93A. An error function is fitted to the trigger efficiency to cross-check the detector's threshold in [keV].

data set with a selection of valid events for, e.g. a DM analysis or LEE study. However, these procedures also remove a significant fraction of good events from the data set. This fraction of valid events is represented by the so-called cut efficiency or survival probability, an energy-dependent number showing the probability that a valid event survives the selection criteria. For this, the whole data stream is randomly filled with simulated events of a specific rate and energy spectrum. The parametric template is scaled to a certain amplitude to build a simulated event. For the simulation of a flat energy spectrum, the detector response has to be used as input, which provides information about the working point of the detector at each time. The identical analysis chain of the blind data is applied to the simulated data. This includes triggering the stream with the OFilter threshold trigger, creating pulse windows with the same record lengths, calculating CMP parameters, applying the OFilter in the session and performing all data quality cuts (but not the LY cut) to the data set. The LY cut is not an artefact cut but removes actual events which, e.g. passed both detectors or the LD only. The simulation only simulates events with the correct LY value, so the cut is not applied to the data set.
From this data set, the trigger efficiency, which describes the energy-dependent probability that a pulse survives the trigger algorithm, and the cut efficiency, which represents the efficiency that a pulse survives in addition all analysis cuts, can be derived. As a first step, a reference list has to be created. This list contains all simulated events with the criterion that only one simulated event per pulse window is allowed. Pile-ups between simulation events are discarded as the simulated rate is

much higher ($\sim 0.2\,\mathrm{Hz}$) than the particle event rate in the detector, so the simulation pile-up does not correctly model the pile-up probability.
The reference list contains simulated events which pile up with test or control pulses. During the analysis of the blind data set, these events are removed in the first step since the information on when heater pulses were sent is stored in the data. To determine the trigger efficiency, both events piling up with test and control pulses and non-triggered simulated events are removed. The surviving events are used for the trigger efficiency calculation. In addition, the simulated time stamp is compared with the trigger timestamp, discarding events where the time difference exceeds two times the rise time. This ensures that the simulated event is also the event which was triggered by the algorithm and not some other pulse like a particle event with a higher amplitude, as the trigger algorithm always triggers on the highest pulse. This models the possibility of a small actual event not triggering in the detector due to a neighbouring larger event tagged as the triggered event. The trigger efficiency for TUM93A is shown in figure 7.8. It is plotted against the simulated energy, representing a particle event's "real" energy. The trigger threshold is a fixed value in units of [V]; however, due to the finite resolution of the detector, an error function can describe the trigger efficiency in units of [keV]. Fitting this error function to the trigger efficiency curve provides a translation from the threshold in [V] to the threshold in [keV] of the detector.
For the overall survival probability, all cuts like the stability, muon veto, and data quality cuts are applied to the data. Another cut is applied to ensure that simulated events that pile up with other events on the stream are not wrongly reconstructed and influence the low statistics region below the threshold, where single outliers can influence the limit calculation. A simulated event whose reconstructed energy differs from the injected energy by more than three times the detector's baseline resolution is removed. This cut reduces the survival probability slightly, leading to a weaker but more conservative exclusion limit.
For the calculation of Dark Matter exclusion limits, two different simulations are performed for each detector. First, a simulation over the whole ROI (as shown in figure 7.8) with a frequency of 0.2 Hz is done (a higher frequency increases the possibility of pileups also outside of the analysis window as simulated pulses might sit on decaying tails of previous simulated events). Afterwards, another simulation which focuses on the energy region around the threshold is performed, again with 0.2Hz, to increase the statistics around the threshold. This simulation is also used to determine the time-dependent survival probability and can be used for time-dependent studies of, e.g. the low-energy excess or the DM limit.

7.2.4 BandFit and Dark Matter Exclusion Limit Calculation

For calculating a Dark Matter exclusion limit, the ROI for DM search has to be defined. This is only possible for the TUM93A analysis with both the PD and the LD channels. As the dark matter signal is expected to be a nuclear recoil signal, only

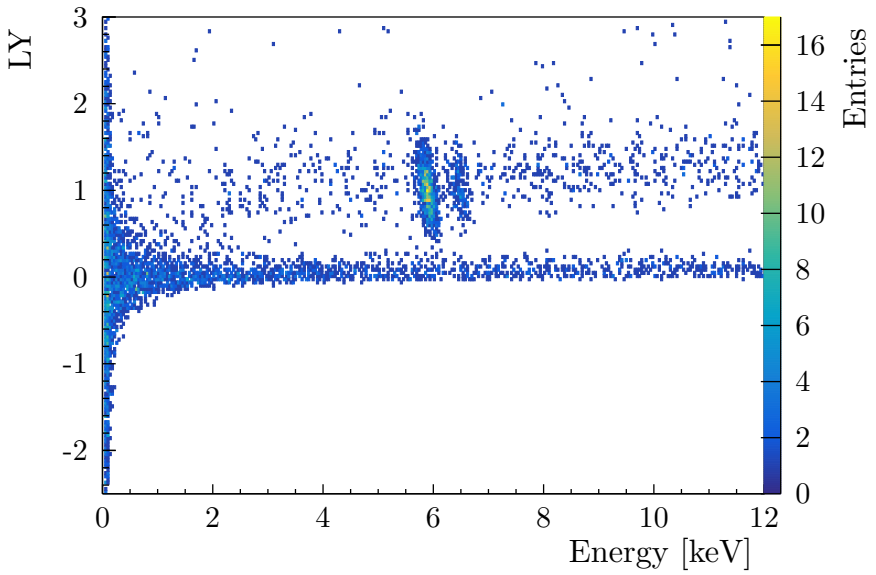

Figure 7.9: LY plot of the neutron calibration data of TUM93A. The data was processed with the same analysis chain as the blind data set. A populated nuclear recoil band is visible

events in the nuclear recoil bands are considered for the DM limit calculation. A dedicated neutron calibration (*Ncal*) is performed with an AmBe source to determine this ROI. The calibration data is processed the same way as the blind data set. The resulting LY plot for the neutron calibration of TUM93A is shown in figure 7.9.
For the definition of the ROI, a likelihood-based band fit is performed on both the background and neutron calibration data. The fit is done time-dependent.[1] The data from the ROI is then used to calculate a DM exclusion limit using the Yellin approach.

Band Description

This parametrisation was developed in [123], and a detailed description of the model is given in this reference. In a first approximation, the LY of the electron band can be described as a function of energy using a polynomial of second order:

$$L_e(E) = L_0 E + L_1 E^2 \tag{7.1}$$

with the two fit parameters L_0 and L_1. However, at lower energies, an effect called the scintillator non-proportionality bends the LY down towards lower energies [123]. This can be taken into account using an extra exponential factor:

[1] For this, Romeo, a Julia-based software package developed in [123, 124], is used

$$L_e(E) = (L_0 E + L_1 E^2)\Big[1 - L_2 \exp\Big(-\frac{E}{L_3}\Big)\Big] \tag{7.2}$$

Multiple secondary low-energy electrons are produced for events originating from γ-lines when the γ reacts with the detector material. Due to the above-described non-proportionality at low energies, the sum of the emitted light is lower than for pure electronic reactions, and the γ-band is quenched to slightly lower LY compared to the electron band. As before, a polynomial of second order can be used to describe the LY dependence on the initial energy, including the quenching factors $Q_{\gamma,1}$ and $Q_{\gamma,2}$

$$L_\gamma(E) = L_e(E[Q_{\gamma,1} + EQ_{\gamma,2}]) \tag{7.3}$$

The nuclear recoil bands are parameterised relative to the electron band. As the nuclear recoil bands do not show the non-proportionality effect, it is based on equation 7.1. For an element x, it can be written as

$$L_x(E) = (L_0 E + L_1 E^2) \cdot \epsilon \cdot QF_x \cdot \Big[1 + f_x \exp\Big(-\frac{E}{\lambda_x}\Big)\Big] \tag{7.4}$$

with QF_x, f_x and λ_x fixed constants determined for $CaWO_4$ in [125]. The scaling factor ϵ is individual for each crystal and is determined by the band fit [123].
For the width of the bands, the following effects have to be considered: The resolution of the light detector is composed of the baseline resolution of the light detector $\sigma_{L,0}$, statistic fluctuation in the number of produced photons which is proportional to $\sqrt{L}$ and described by the parameter S_1 and other uncertainties, e.g. from a position dependence described by the parameter S_2. The total resolution of the LD is

$$\sigma_L(L) = \sqrt{\sigma_{L,0}^2 + S_1 L + S_2 L^2} \tag{7.5}$$

Similarly, the phonon detector resolution is given by:

$$\sigma_P(E) = \sqrt{\sigma_{P,0}^2 + \sigma_{P,1}^2 E} \tag{7.6}$$

with $\sigma_{P,1}$ scaling with $\sqrt{E}$.
For the total width of the band, the resolution of the phonon detector cannot be directly included as the width of the band is defined in terms of light (L) and not energy (E). Therefore, the phonon resolution has to be multiplied by the slope of the corresponding band. The analytical derivation of the electron band is:

$$\frac{dL_e}{dE}(E) = \Big[(L_0 E + L_1 E^2)\frac{L_2 \exp(-\frac{E}{L_3})}{L_3}\Big] + \Big[(L_0 + 2L_1 E)\Big(1 - L_2 \exp\Big(-\frac{E}{L_3}\Big)\Big)\Big] \tag{7.7}$$

For the γ band, this is derived accordingly. With the description of the slope of each band, the with of the band can be written as

$$\sigma_x(E) = \sqrt{\sigma_L(L_x(E)) + \frac{dL_x}{dE}(E)\sigma_p(E)}[123] \tag{7.8}$$

Energy Spectra Description

In addition to a fit of the LY, the energy spectra are fitted to describe the distribution of events in each band. For this, the spectra $\frac{dN_x}{dE}$ are defined for each event type [123].
For the electron band, this is a constant plus a linear term.

$$\frac{dN_e}{dE}(E) = P_0 + EP_1. \tag{7.9}$$

For γ peaks, the parametrisation is individual as they originate from material near the detector or the detector itself and should correspond to characteristic lines. They follow a Gaussian distribution.

$$\frac{dN_{\gamma,x}}{dE} = \frac{1}{\sqrt{2\pi}\sigma_P(M_x)}\exp\Big(-\frac{(E-M_x)^2}{2\sigma_p^2(M_X)}\Big) \tag{7.10}$$

With M_x the mean line for a given peak x. The neutron spectra in the presence of a neutron source are described as

$$\frac{dN_{n,x}}{dE} = A_{n,x}\exp\Big(-\frac{E}{N_{decay,x}}\Big) \tag{7.11}$$

with $A_{n,x}$ the initial amplitude and the decay constant $N_{decay,x}$.

Dark Matter Limit Calculation

The DM exclusion limit is calculated using Yellin's Optimal Interval method [126] applied to all events in the ROI defined by the band fit. The method assumes that the measured events are distributed along a 1D interval with the shape of the expected signal and an unknown background.
This makes it a more robust tool than Poisson-based upper limit calculations, which perform poorly in the presence of unknown background and likelihood-based approaches that also require a description and understanding of all background components. As the LEE observed in CRESST and other low-threshold experiments represents a non-understood background, the Yellin Optimal Interval method provides a strong tool for calculating DM exclusion limits.
The optimum interval method used in this work is based on the so-called maximum-gap method, which uses information about the gaps between measured events to calculate a limit on the cross-section of DM particles. The gap between two measured points E_i and E_{i+1} is characterised by the expected number of events for a certain cross-section $\frac{dN}{dE}$

$$x_i = \int_{E_i}^{E_{i+1}} \frac{dN}{dE}dE[126] \tag{7.12}$$

The maximum gap method increases the intensity $\frac{dN}{dE}$ until the expected number of events are no longer consistent with the observed energy spectrum. The probability of a gap being smaller than the observed depends on two variables, the size of the gap, x, and the expected number of events around the gap μ

$$C_0(x,\mu) = \sum_{k=0}^{m} \frac{(kx-\mu)^k e^{-kx}}{k!}\Big(1+\frac{k}{\mu-kx}\Big)\text{[126]} \tag{7.13}$$

With m being the largest integer smaller than μ/x. For the exclusion limit, the cross-section of the DM particle σ (and hence also the parameter μ) is increased until $C_0(x,\mu)$=0.9 corresponding to an upper limit at 90% confidence level [126]. This maximum gap method struggles with a large number of background events in a spectrum. In this case, the method is changed to search for optimum intervals in which there are, e.g. only one or two events observed. For this, $C_n(x,\mu)$ is the probability that all intervals with ≦n events have ≦x expected events for a given dN/dE. The optimum interval then corresponds to the interval which indicates most strongly that a proposed cross-section is too high. This approach increases the statistics of the maximum interval method compared to the maximum gap method.

7.2.5 Resulting Energy Spectra

In this section, the key characteristics gained from the training set of each analysis are summarised, and the final energy spectra derived from the blind data set are shown.
The characteristic parameters resolution, threshold and truncation limit for both detectors are summarised in table 7.3 in units of V. The threshold of TUM93A-Ph was determined, assuming a Gaussian noise distribution. In contrast, the threshold of TUM93A-L was determined assuming an additional exponential pollution component as LEE events are present in the set of empty baselines used for the threshold determination (see section 5.5).

Detector	Resolution [mV]	Threshold [mV]	Truncation Limit [V]
TUM93A-Ph	1.2	8.22	1.0
TUM93A-L	1.9	17.8	0.7

Table 7.3: Baseline resolution, threshold and truncation limits for both TUM93A-Ph and TUM93A-L in Volt.

As TUM93A-L is both used as a light detector for TUM93A-Ph and as a standalone detector, the values in units of energy, shown in table 7.4, are given both in electron equivalent energy (ee) for the scintillation light detection and in absolute detected energy. The trigger threshold and the resolution in units of energy are acquired from the fit of the error function to the trigger efficiencies obtained by the stream simulation for TUM93A-Ph and TUM93A-L and by a simple conversion from V to

eV for TUM93A-L$_{ee}$. As TUM93A-L is not triggered when operated as a scintillation light detector, it does not have a threshold in energy units in this case.

Detector	Resolution [eV]	Threshold [eV]	Truncation Limit [keV]
TUM93A-Ph	8.12	53.95	6.73
TUM93A-L	1.5	13	0.524
TUM93A-L$_{ee}$	107	-	39.4

Table 7.4: Baseline resolution, threshold and truncation limit in energy units. For TUM93A-L, two different cases are displayed. Once, the values for an operation as a single detector, and once as a detector for scintillation light denoted by the "ee".

The CPE factors are derived following 7.2.1 using the direct hits of the 5.9 keV ^{55}Fe line as calibration for TUM93A-Ph and TUM93A-L and the detected scintillation light emitted from a 5.9 keV ^{55}Fe event in TUM93A-Ph for the CPE factor of TUM93A-L$_{ee}$. Table 7.5 summarises CPE factors derived in this work.

Detector	CPE factor [keV/V]
TUM93A-Ph	3.07
TUM93A-L	0.16
TUM93A-L$_{ee}$	12.63

Table 7.5: Summary of CPE factors obtained for the detectors TUM93A-Ph, TUM93A-L and TUM93A-L$_{ee}$.

For each analysis, the data quality cuts described in 7.2.2 were tuned to remove all artefacts and pile-up events to arrive at a clean energy spectrum. The cut values are summarised in B. Figure 7.10 shows the trigger and cut efficiencies for both the PD and LD analysis for each cut to show their impact on the survival probability. All cuts besides the OFilter RMS cut in the PD analysis are energy independent as a constant fraction of the events is removed. For the OFilter RMS cut, usually, step-like cuts are used as the RMS rises towards the truncation limit. This becomes visible as a step in the survival probability of the PD and is modelled correctly by the simulation. There is a significant difference in the fraction which gets removed by, e.g. the stability cut comparing the PD and LD analysis. This is because, in the LD analysis, only the stability of the LD is considered, whereas, in the PD analysis, the cut is applied to both detectors. As the PD is more often unstable, a bigger fraction is removed. Also, the BLDiff cut removes fewer events for the LD analysis as the pulses in the LD are faster, so the probability of a pulse piling up with other pulses or having a decaying baseline is reduced. The RMS cut on the PD removes a significant fraction of events in the PD analysis. This effect is also absent in the LD analysis, as no RMS cut on the PD is performed. All these effects lead to a higher survival probability for the LD analysis.

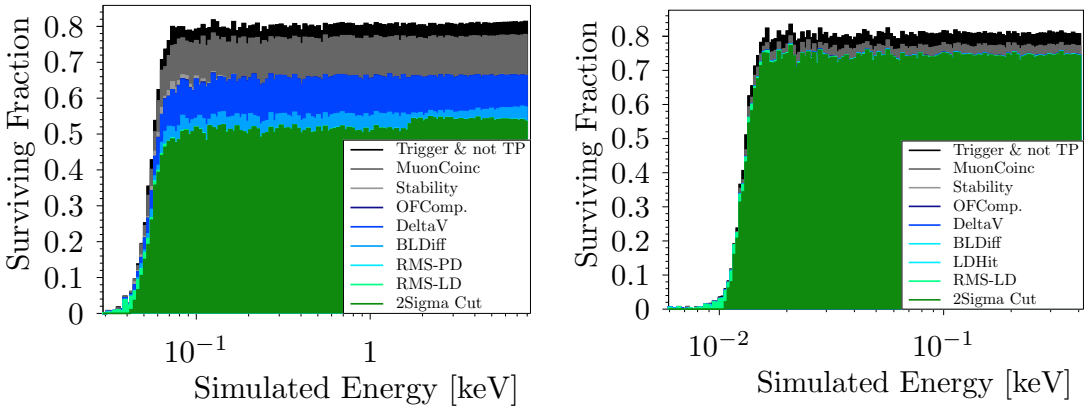

Figure 7.10: Comparison of the survival probabilities for each cut for the PD analysis (left) and the LD analysis (right)

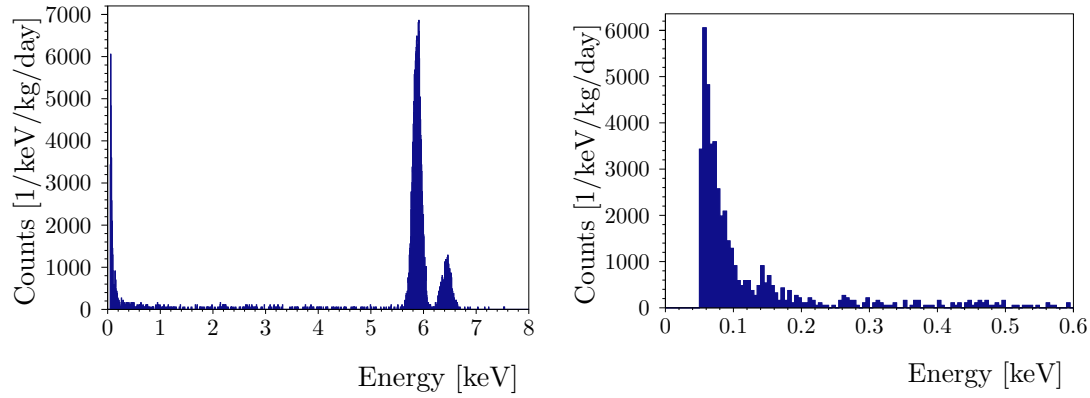

Figure 7.11: Resulting energy spectrum after application of all cuts corrected by the survival probability of the PD analysis. Left: Energy range until 8 keV. Right: Zoom to the lower energy range up to 0.6 keV. An exponentially rising excess below 200 eV is observed.

The resulting energy spectra after all cuts, corrected by the respective survival probability, are shown in figure 7.11 for the PD analysis and figure 7.12 for the LD analysis.
For the PD analysis, the two ^{55}Fe lines at 5.9 keV and 6.4 keV are resolved nicely and could be reconstructed by the OFilter. At energies below 200 eV, the spectrum rises exponentially towards the threshold. At 150 eV, a peak-like structure is observed, also present in other detectors of this run [127]. The origin is currently under investigation by the CRESST simulation group, and first results hint toward a feature induced by the ^{55}Fe source present in the module. The spectrum for the LD is shown until an energy of 400 eV as events above could not be reconstructed reliably with the OFilter due to the low truncation limit of this detector and also not by the truncated fit due to the detectors self-heating problems. Also, this detector observes an exponentially rising excess towards the threshold.

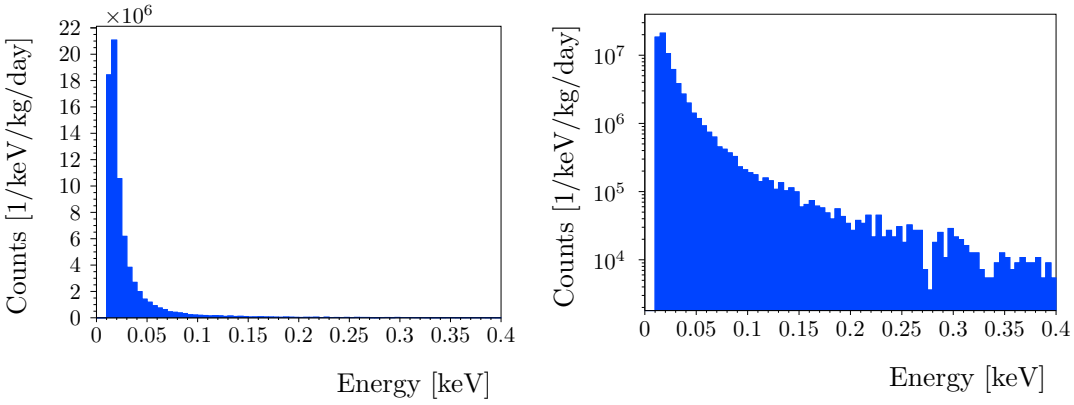

Figure 7.12: Resulting energy spectrum up to 400 eV for the LD analysis after all cuts have been applied to the data and after correction with the survival probability. Left: Spectrum with a linear y-axis. Right: Same spectrum with a logarithmic y-axis for better visibility of the events at energies above 100 eV.

7.3 Dark Matter Exclusion Limit for Detectors TUM93A and TUM93A-L

For the calculation of the Yellin DM exclusion limits [126], as described in section 7.2.4, a bandfit was performed for the PD analysis. No bandfit could be performed for the LD analysis as the analysis only uses a single channel. Hence, all events are included in the ROI for the Yellin limit determination.

For the bandfit of TUM93A-Ph, a time-dependent approach is used: The survival probability is determined for each data segment and background components in the spectra are allowed to vary with time. In this way, rate decreases of, e.g. the two ^{55}Fe X-ray lines and other parts of the energy spectra like the LEE component can be modelled correctly. Figure 7.13 shows the fit results to the *Bck* energy spectrum (top right), the *Ncal* energy spectrum (top left), the LY spectra (middle left and right) and the resulting description of the bands in the LY plot on the bottom as described in section 7.2.4. The histograms and the graphs show the absolute number of events not yet corrected by the survival probability and not normalised to exposure. The plots are shown in this way to allow for a comparison with the LY scatter plot, where each data point represents one event. In the *Bck* plot, a flat background (electron- and γ-events), two ^{55}Fe lines (γ-events) and the LEE are visible. To model the LEE, an additional component is used (see brown fit line). In the *Ncal* spectrum, again, a flat background, two ^{55}Fe lines and the LEE are present. In addition, the neutron calibration creates an exponential background starting from around 1 keV also rising exponentially towards the threshold. It also causes a higher flat background level. These additional features are fitted by three components for the three recoil bands.

For the calculation of the DM exclusion limit, the mean line of the Oxygen band is set as an upper limit of the region of interest and the lower 99.5% boundary of

the Tungsten band, which was done in this way for previous CRESST analyses. For the LD analysis, all events are used to calculate the DM exclusion limit. All events are weighted by their survival probabilities, and the spectra are normalised to the exposure. The resulting exclusion limits, calculated with the Yellin optimum interval approach, are shown in figure 7.14 for TUM93A in dark blue and TUM93A-L in light blue. For comparison, the CRESST-III 2019 limit is shown in red. The TUM93A limit is weaker than the DetA limit achieved with the CRESST-III data. This has several reasons. First, the threshold is higher than the DetA threshold of 30.1 eV. Second, the ^{55}Fe source causes a higher flat background in the ROI of TUM93A, weakening the limit. Third, the excess observed in DetA was decaying over time. As DetA was measured for roughly two years, the average excess was lower than the excess in the data set used for TUM93A.
The exclusion limit of TUM93A shows a little upward bump around a DM mass of 1.2 GeV/c^2 and a positive analysis was performed to understand the origin of this feature. In a positive analysis, the LEE is erroneously assumed to be a DM signal (which was excluded by several observations in the community [128]), and a DM "island" is derived from it. The positive analysis is described in detail in [124]. The best-fit value for the positive analysis shows that the LEE mimics a DM signal of $\sim$1.2-1.3 GeV/c^2. Hence, the Yellin limit is weaker at these energies as it interprets the LEE as a possible DM signal.
The LD analysis for TUM93A-L yields a limit down to as low as 0.12 GeV/c^2 due to the low threshold and, together with other LDs operated in the ongoing data-taking campaign, explores new parameter space in the field of low-mass DM search. The limit stops at an energy of $\sim$0.9GeV/c^2 due to the nonlinearity of the LD above 400 eV of recoil energy.
Also, in the case of TUM93A-L, the excess events significantly limit the sensitivity to lower cross sections. Hence, a better understanding of the origin of the LEE is crucial. The following section covers LEE observations based on the two detectors, TUM93A and TUM93A-L, in detail and compares them to other detectors of the ongoing and previous CRESST data-taking campaigns. The results are set into context with results from other experiments in the field of low-threshold DM search.

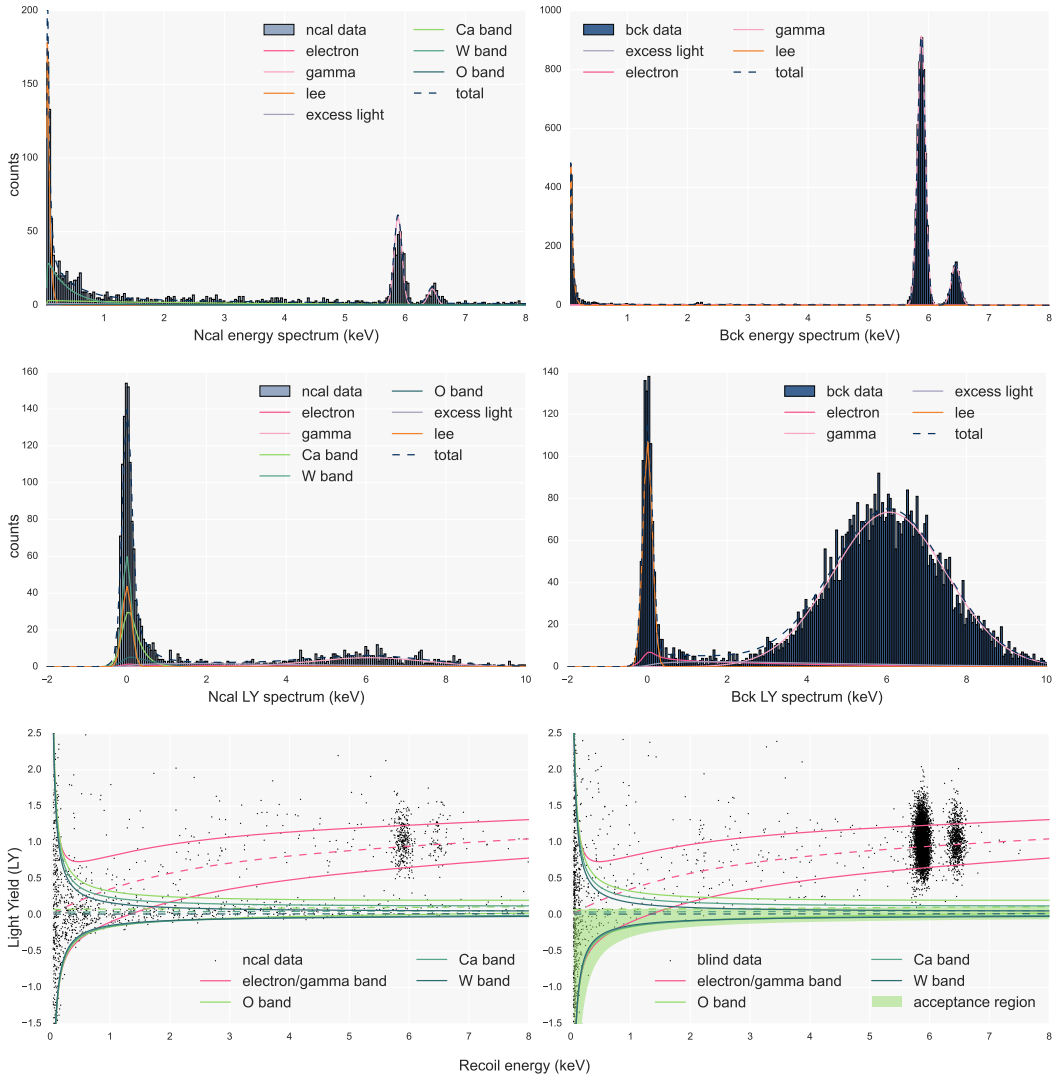

Figure 7.13: Results of the likelihood bandfit for TUM93A. Top: Fitted spectrum for the *Ncal* data set (left) and the *Bck* data set (right), including the description of the two ^{55}Fe calibration lines, the excess and in the case of the neutron calibration, the different recoil bands. Middle: Fit of the LY spectra for the *Ncal* data (left) and the *Bck* data set (right). The so-called excess-light events are those situated above the e^-/γ-band and modelled by an additional component. Bottom: Resulting LY spectrum showing the resulting bands fitted for TUM93A for the *Ncal* spectrum (left) and *Bck* spectrum (right). In the *Bck* spectrum, the green-shaded area indicates the acceptance region for the Yellin exclusion limit.

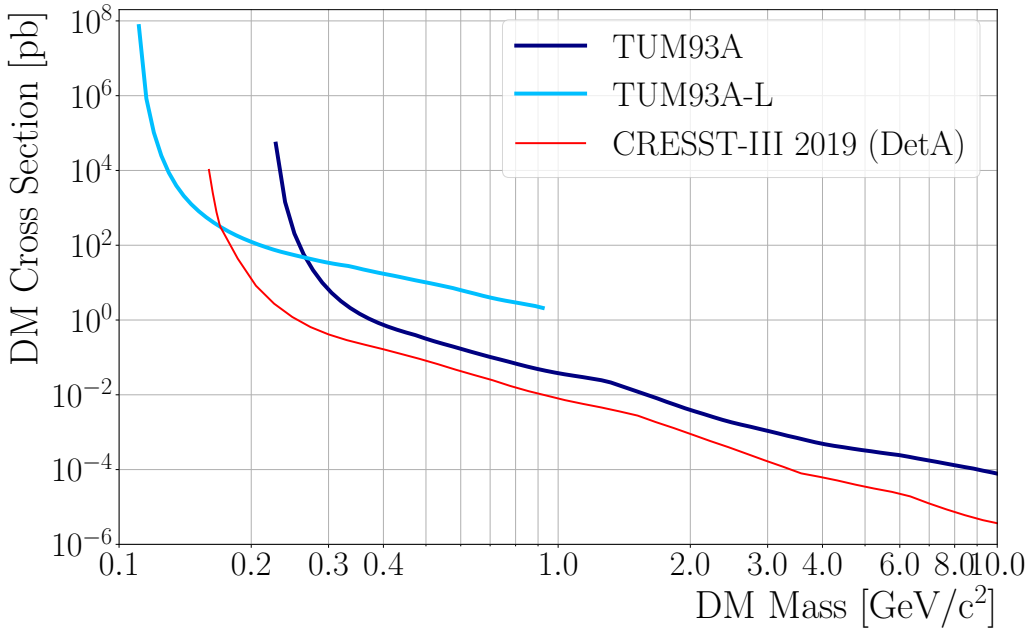

Figure 7.14: DM exclusion limits of TUM93A (dark blue) and TUM93A-L (light blue) in comparison to the CRESST-III 2019 DetA limit (red).

7.4 Investigation and Interpretation of the Low Energy Excess

This section covers the comparison of the observed LEE spectra in TUM93A and TUM93A-L, a pulse shape comparison between the LEE events and the analysis templates, as well as the temperature and time dependence of the LEE in both analyses. In addition, intrinsic stress as a possible source of the LEE is investigated by comparing the LEE in two $CaWO_4$ crystals with different intrinsic stress levels. The analysis tools used for this investigation are not part of CAT and were, as part of this dissertation, developed in collaboration with the CRESST analysis group.

7.4.1 Comparison of the Excess in Different Detectors

A sharp rise of events below ∼200 eV is observed for both detectors. Figure 7.15 shows the time-averaged spectra for a reduced blind data set corrected by time-dependent survival probabilities for both TUM93A and TUM93A-L. The reduced set was selected to compare different detector modules in a common time window. The spectra are compared in different configurations: normalised to their measurement time (left) and to measurement time and mass (right). The LEEs of TUM93A and TUM93A-L do not agree independently of how the spectra are scaled. The light detector with the smaller mass sees the highest LEE rate, even in absolute rate.
To understand and cross-check the difference in the rate between the two detectors

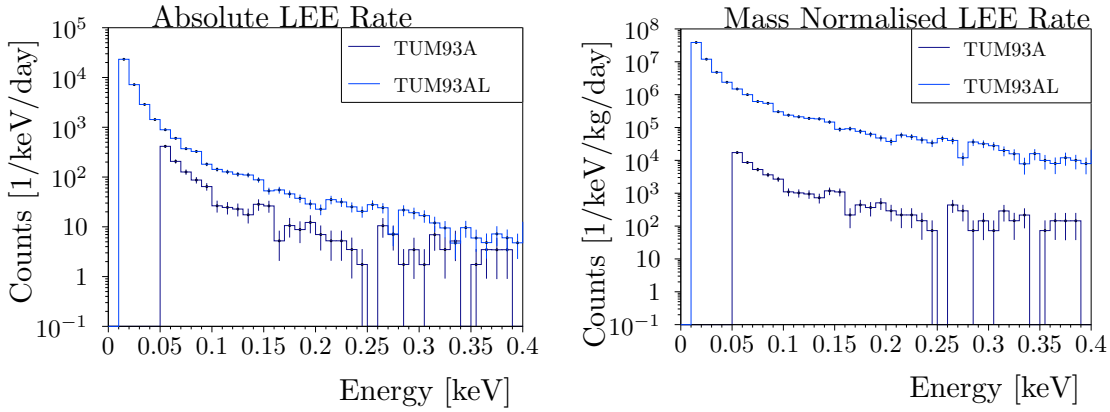

Figure 7.15: Comparison of the LEE spectra for TUM93A and TUM93A-L. Left: Absolute rate measured in both detectors normalised only to the measuring time and their respective survival probabilities. Right: The rate of both detectors normalised by their mass.

from the same module, the results are compared to similar detectors from the same data-taking campaign. Unfortunately, no second $CaWO_4$ module was analysed with an LD-only analysis. Hence, TUM93A is compared to the module Comm2, analysed in [129], which also consists of a $CaWO_4$ crystal (not produced at TUM), and TUM93A-L is compared to another SOS light detector, the Li1-L, analysed in [109]. All four detectors are plotted together in figure 7.16.
The rate among the $CaWO_4$ detectors agrees well. The result of the Li1-L detector confirms the trend of the higher rate in the light detector. This observation hints towards a dependency of the LEE on the detector material. More spectra from other detector materials were published in [128].

7.4.2 Pulse Shape of Excess Events

To investigate the event type causing the LEE, a template is created by averaging all pulses above the threshold up to an energy of two times the baseline resolution above this threshold. In this way, several hundred LEE pulses are used to create the LEE template. This procedure was applied to both TUM93A and TUM93A-L. In the case of TUM93A, this LEE template (light blue) was compared to the analysis template created from the ^{55}Fe X-ray events (red) shown in figure 7.17 (top). Both templates agree well with each other hinting towards a particle-like origin of the LEE, with particle-like meaning both electron and nuclear recoil events. For TUM93A-L, no comparison to the ^{55}Fe-template could be made, as the detector is already saturated at this energy. In addition, the pulses in the detector suffer from strong self-heating effects in the TES, as explained in section 5.4.2. Hence, the LEE template (red) is compared to templates created from several energy regions above the threshold (shown in rainbow colours) and to a template created from scintillation light events from the $CaWO_4$ scintillation (shown in grey) in figure 7.17 (bottom).

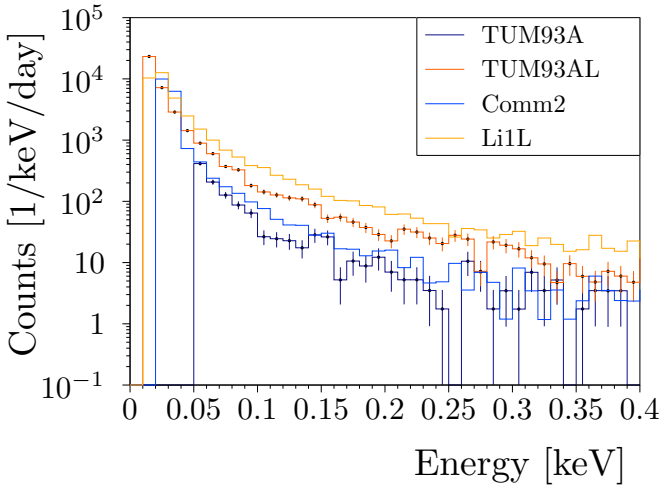

Figure 7.16: Comparison of the LEE of TUM93A (dark blue, $CaWO_4$) with Comm2 (light blue, also $CaWO_4$) [129] and TUM93A-L (red, SOS detector) with Li1-L (orange, also SOS) [109] in absolute rate. The rates in the $CaWO_4$ absorbers agree well. The rates in the LDs are higher than those in the main absorbers. However, they do not agree as well as for the main absorbers.

The comparison underlines the pulse-shape change due to the self-heating towards higher energies. The LEE template, however, shows a similar rise time compared to the higher energetic events. A comparison to the scintillation light template indicates that the rise time for scintillation light events is slower. This hints at a particle-like origin of the LEE events not originating from scintillation light in the module.

7.4.3 Time and Temperature Dependence

As already mentioned above, the LEE decayed over time for DetA. To investigate the time dependence of the LEE in TUM93A and TUM93A-L, an energy region of 60 eV to 120 eV was selected from the data and the number of events in this energy region was corrected by the file-by-file survival probability. The total rate of LEE events from this energy region is plotted in figure 7.18 for the *Bck* data set (blind and training set for better statistics) of TUM93A and TUM93A-L. Each data point represents roughly 150 h of measuring time. For both analyses, a decay of the LEE rate is observed, which is fitted by an exponential function plus a constant:

$$R(t) = A \cdot \exp\left(-\frac{t}{\tau}\right) + C \tag{7.14}$$

The fit results for both detectors are shown in table 7.6, and we published them together with the results for modules Comm2, Si2-L and Sapp2 in [128]. All CRESST-III detectors show a decay in the LEE rate with an average decay time of (149 ± 40) days [128].

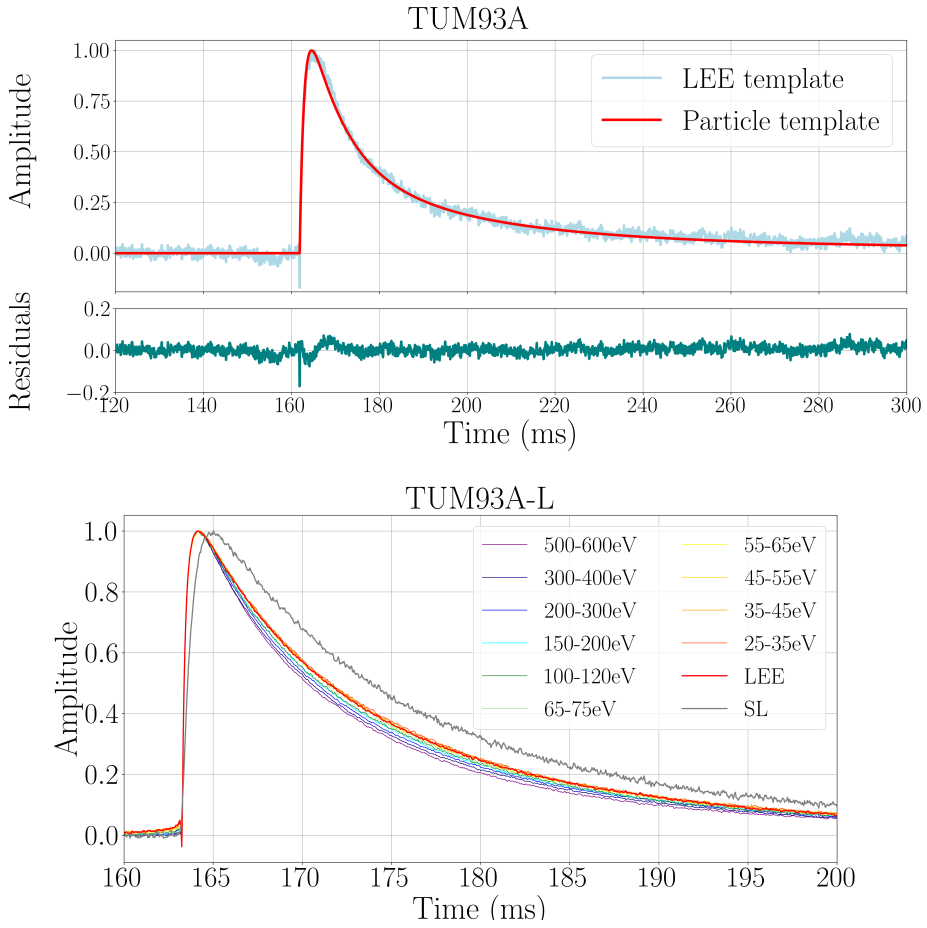

Figure 7.17: Top: Comparison of the TUM93A LEE template (light blue) with the analysis template (red) used to create the OFilter with residuals. Bottom: TUM93A-L LEE template (red) compared to templates built from events at higher energies. Due to the energy-dependent pulse shape change in TUM93A-L, the LEE template cannot be compared to a single high-energetic template. Hence, several templates from a broad energy region are plotted to underline the non-linearity. However, the rise time of these templates all agree with each other. In comparison, a template from $CaWO_4$ scintillation light is plotted in grey, and a slower rise time is visible.

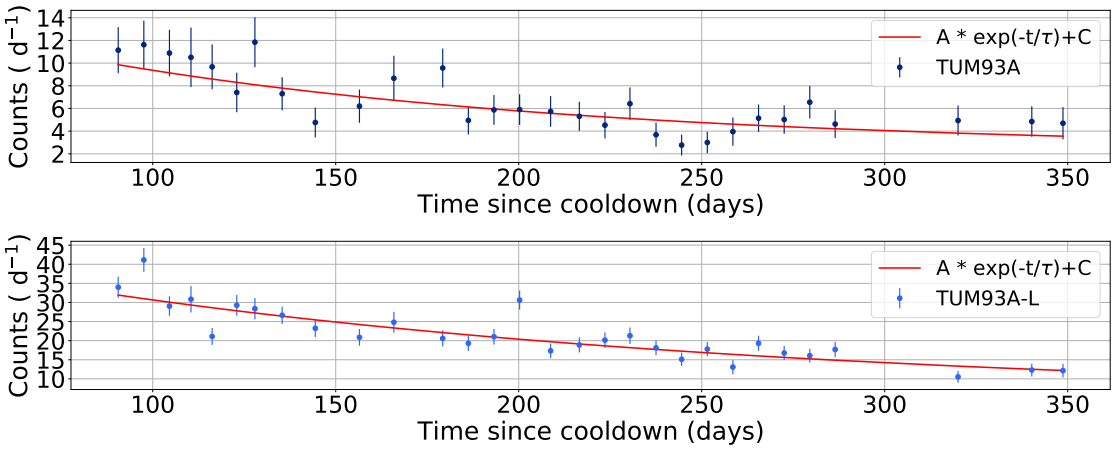

Figure 7.18: Time dependence of the LEE count rate in the energy region 60-120 eV for TUM93A (top) and TUM93A-L (bottom). Each data point represents roughly 150 h of measuring time. The data is fitted using equation 7.14.

Detector	Amplitude [1/d]	Decay Time [d]	Constant [1/d]
TUM93A	20.7 ± 6.4	101.2 ± 30.3	2.6 ± 0.7
TUM93A-L	42.9 ± 5.6	167.6 ± 53.7	7.2 ± 3.4

Table 7.6: Fit results for the LEE *Bck* data in the energy range from 60 to 120 eV fitted with the function of equation 7.14 for both TUM93A and TUM93A-L.

Neutron Calibration Influence on the LEE

The *PostCal* data set was recorded after the neutron calibration to study the impact of the neutron calibration on the LEE rate. This allows for assessing whether defects created by the neutron calibration can cause a rise in the LEE rate. The LEE rate continued to decay with the same decay time. Therefore, no influence was detected. This disfavours defects caused by, e.g. cosmic radiation as a source of the LEE.

Temperature Dependence of the LEE

The EDELWEISS experiment also observed a decay of their heat-only event rate in an energy range above 5 keV, which was reset to a higher value after an unintended warm-up of their cryostat [130]. To study whether a temperature cycle also influences the LEE in CRESST, a dedicated temperature study was performed following the *Bck* and *PostCal* data set. The detectors were warmed to 60 K and kept at this temperature for several weeks before the *Awu* data set was taken. Several smaller warm-ups to 600 mK, 200 mK and 3.5 K were performed during the *Awu* data set. Figure 7.19 shows the time-dependent LEE rate for TUM93A and TUM93A-L for the whole data-taking period, including the *Bck*, *PostCal* and *Awu* data sets. The coloured areas indicate the *Ncal* and the warm-ups. At the bottom of the plot, the decay rate of the ^{55}Fe source is shown as a reference, which agrees very well with

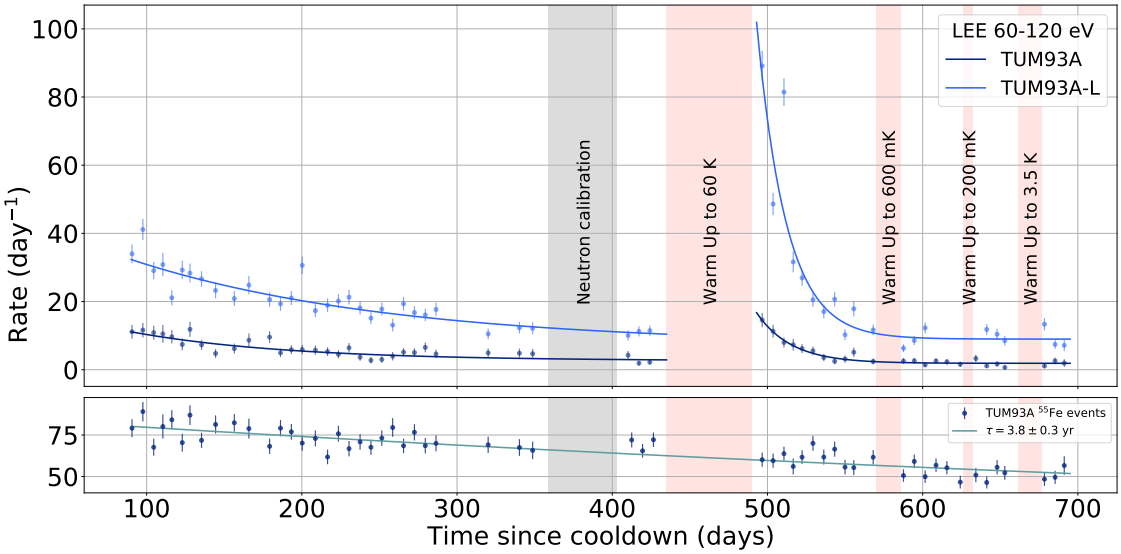

Figure 7.19: Top: Time-dependent evolution of the LEE rate in the energy region (60-120) eV for the detectors TUM93A and TUM93A-L in days since the first cooldown of the CRESST cryostat with this detector configuration. The shaded areas indicate the neutron calibration and four different warm-ups. Bottom: Time evolution of the ^{55}Fe events detected by TUM93A fitted by an exponential. The decay time of 3.8 ± 0.3 yr matches the literature value of 3.9 yr [122].

the decay rate found in literature [122]. This provides an important cross-check for the correct handling of the time-dependent survival probability of each detector. Between $\sim$ 610 and 630 days, several files have been excluded for TUM93A-L as the detector showed an unusually high trigger rate and worse noise conditions both in the low-energy and medium-energy regions in this time period.
A much higher LEE rate is observed after the warm-up to 60 K, whereas the smaller temperature cycles seem to have no impact on the LEE rate. The decay time of the LEE rate after the warm-up to 60 K is roughly an order of magnitude smaller than the decay time in the *Bck* data files. The decay times are summarised in table 7.7. At the time of writing, further temperature cycles are planned to investigate at which temperature the rate of the LEE starts to rise. These temperature cycles are not included in this work.

Detector	DataSet	Amplitude [1/d]	Decaytime [d]	Constant [1/d]
TUM93A	Bck+PostCal	20.7 ± 6.4	101.2 ± 30.3	2.6 ± 0.7
	Awu	15.5 ± 2.3	22.4 ± 3.7	7.2 ± 0.2
TUM93A-L	Bck+PostCal	42.9 ± 5.6	167.6 ± 53.7	7.2 ± 3.4
	Awu	97.9 ± 15.4	19.0 ± 3.2	9.0 ± 1.4

Table 7.7: Fit results for the TUM93A and TUM93A-L LEE rate for the *Bck+PostCal* time period and the *Awu* period

The observation of the temperature dependence of the LEE rate excludes radioactive sources as the primary origin of the LEE as these would not change their rate during a thermal cycle, as shown by the rate of the ^{55}Fe source. In addition, this observation excludes a DM origin for the LEE excess. A temperature dependence hints at stress-related origin like intrinsic crystal stress, external stress from the holding structures or contact stress between the TES and the crystal surface.

7.4.4 Investigation of Intrinsic Stress as Source of the Excess

The results presented above hint at a stress-related source of the LEE. A primary goal of this work is to test whether the LEE could originate from intrinsic stress in the crystal, which relaxes over time, causing low-energetic events. To investigate and minimise this possible effect, the $CaWO_4$ growth process was optimised by reducing thermal gradients during crystal growth by installing a heat radiation shield and an additional heating disk (see section 3.3.2). A birefringence measurement showed that the intrinsic stress could be reduced by this optimisation (see section 3.3.3).
To make any statement about the LEE present in the stress-reduced crystal TUM93, it has to be compared to another TUM-grown crystal for which a birefringence measurement is available so that the intrinsic stress can be compared together with the LEE. For this, the crystal TUM73, installed as the detector "E" in the data-taking campaign from Mai 2016 to February 2018, is selected as a birefringence measurement is available for this crystal.
As explained in section 3.3.3, intrinsic stress causes a phase shift of the polarised light sent through the crystal in the birefringence setup proportional to the stress. These form so-called fringes, and for isotropic material, the order of these fringes (e.g. the number) is directly proportional to the stress in the crystal lattice. As $CaWO_4$ is an anisotropic material, the stress cannot be easily calculated from the fringe order. However, a qualitative statement about the stress in the crystal can be made by comparing the different fringe orders between two crystals. For this, a 60 s exposure picture of the TUM73 crystal (produced in [46]) is compared with a 60 s exposure picture of TUM89, which was grown with the same settings as TUM93 (TUM93 was not measured in this setup to avoid contamination of the crystal surfaces before mounting the crystal in a CRESST detector). The resulting grey-scale pictures are shown in figure 7.20 colour coded to highlight the differences in the detected intensities. For TUM73, several fringes can be seen in the crystal's four corners and the middle of the crystal. For TUM89, only one fringe is visible in each corner of the crystal, and no fringes are visible in the middle of the crystal. As the number of fringes is proportional to the intrinsic stress, this observation shows that the crystal TUM73 has a higher intrinsic stress than TUM89 and, hence, to TUM93. Therefore, a higher LEE would be expected in TUM73 than in TUM93 if intrinsic stress were a source for the LEE.
To compare the LEE in both crystals, a re-analysis of the TUM73 data was performed in this work following all the analysis steps described for TUM93A, including

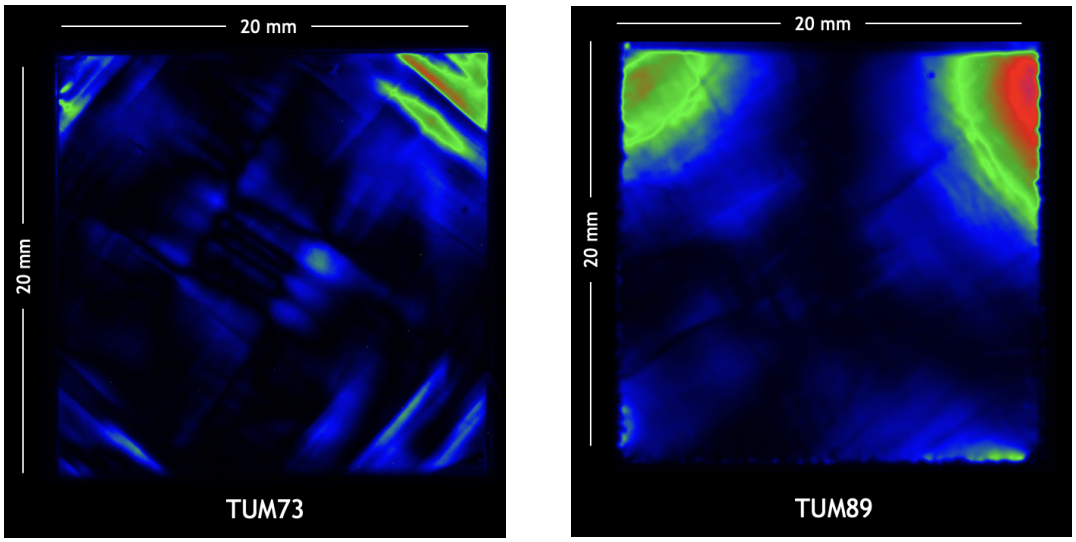

Figure 7.20: Colourcoded fringe patterns of the birefringence measurements of TUM73 and TUM89 (grown with the same settings as TUM93). The black and white pictures are colour-coded to highlight the pictures' differences.

a survival probability simulation. The analysis is based on the analyses published in [43, 48] and uses the threshold and CPE factors determined therein.

As mentioned above, the LEE decays exponentially once the detectors are cooled down to their operating temperature. Hence, this effect must be considered for comparison, and common time periods must be selected. For TUM93A, the periods of the warm-up tests cannot be used as the LEE is higher in these time periods. For TUM73, several time periods show step features appearing on the baseline, which have to be excluded. For the comparison, a time period of 10 days starting ∼150 days after the cooldown and another period of 10 days starting at ∼600 days after the cooldown were selected. Based on the time-dependent observations made in TUM93A and TUM93A-L, this allows the comparison of the LEE in a region where the LEE has not yet decayed and another region where the rate has significantly decayed. The results of the comparison are shown in figure 7.21 for the time period starting 150 days after the cooldown on the left and for the time period of 600 days after the cooldown on the right. In both cases, the LEE spectra of each detector are corrected by the respective survival probabilities.

Figure 7.21 shows that the LEE spectra from both detectors decayed between the 150 days spectra and the 600 days spectra, as is expected from the time-dependent rates observed in TUM93A and TUM93A-L. The LEE in TUM73 shows a similar shape but a lower rate than TUM93A 150 days after the cooldown. At 600 days after the cooldown, the LEE seems to have nearly fully decayed in TUM73, whereas it is still present in TUM93A.

The integrated LEE rate of both detectors in an energy region of 70 eV to 120 eV (explicitly selected in a way that the survival probability curve is flat for the energy region to avoid any correction uncertainties) is summarised in table 7.8.

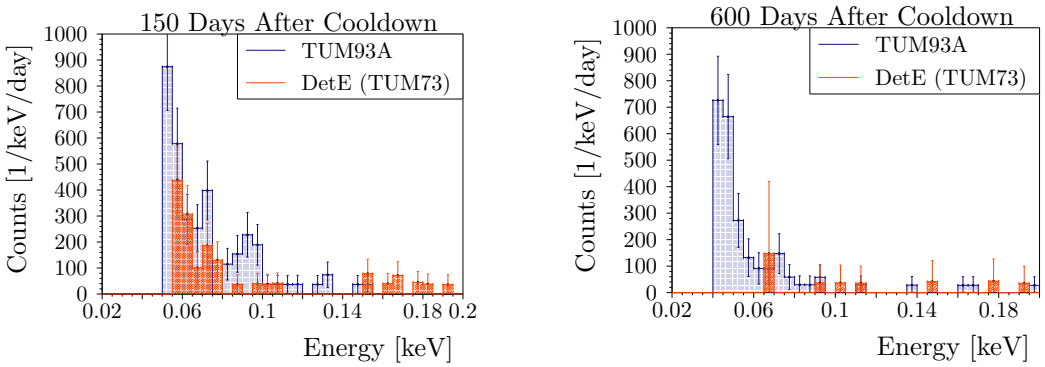

Figure 7.21: LEE spectra of TUM93A (blue) and TUM73 from DetE (red) normalised to counts per keV and day. Left: spectra from a 10 day measurement period 150 days after the cooldown. Right: spectra 600 days after the cooldown. All spectra are corrected by their respective time-dependent survival probabilities.

Detector	Counts/day (70-120 eV)	
	150 days	600 days
TUM93A	2.99 ± 0.53	1.97 ± 0.39
TUM73	0.98 ± 0.31	0.24 ± 0.14

Table 7.8: LEE rate in counts/day for TUM93A and TUM73 for a time period of ∼10 days evaluated 150 days and 600 days after the cooldown of the detectors.

It shows that the TUM73 LEE rate is overall lower compared to TUM93A. In the time period 150 days after the cooldown, it is ∼3 times lower, 600 days after the cooldown, even ∼8 times.
From the comparison of the birefringence patterns, the exact opposite behaviour of the LEE in the two detectors is expected if the LEE is caused by intrinsic stress, as TUM73 shows higher intrinsic stress than TUM93. As the LEE is, however, lower by a factor of 3 to 8, intrinsic stress is excluded as a primary source for the LEE by this comparison.

7.4.5 Conclusions from the Low Energy Excess Analysis

The LEE is present in all CRESST-III modules with a sufficiently low threshold currently operated and analysed by the CRESST collaboration. The results were summarised and published by D. Fuchs, M. Kaznacheeva, A. Nilima and myself in [128]. In the present work, the LEEs of TUM93A and TUM93A-L were studied and compared in terms of absolute rate and scaled by mass. The small 0.6 g LD, shows an overall higher rate than the 24 g $CaWO_4$ detector in all cases. The LEE rate agrees well among the two $CaWO_4$ detectors, TUM93A and Comm2, with TUM93A having a slightly lower rate, and overall a higher rate could be observed for SOS wafer detectors TUM93A-L and Li1-L. This might hint towards a material dependence of the LEE.
A comparison of the pulse shape of the LEE events with the pulse shape of more high-energetic events shows that the LEE events have a particle-like pulse shape which hints at a particle-like origin of the LEE events.
The LEE rate decays over time, resets after a warm-up to 60 K and decays faster afterwards, excluding radioactive origins (intrinsic and external) and DM as a possible source. In addition, the neutron calibration does not affect the LEE rate disfavouring defects in the crystal lattice as a source of the LEE. These observations hint at a stress-induced LEE.
The crystals TUM89 (grown with TUM93 settings) and TUM73 were compared in a birefringence setup to investigate intrinsic stress as an origin for the LEE. The resulting pictures show a higher order of fringes in TUM73, translating to higher stress in this crystal. Comparing the LEE in both crystals operated in different CRESST data-taking campaigns shows a higher LEE in TUM93A compared to TUM73 by a factor of $\sim$3 when comparing the LEE after 150 days and by a factor of $\sim$8 after 600 days. This observation excludes intrinsic stress as the primary source of the LEE and hints towards an external stress effect.
These observations also agree with the results of other experiments presented at the EXCESS workshops favouring externally induced stress as a source of the LEE. In the EXCESS workshop in February 2022, M. Pyle showed for SuperCDMS and the SPICE/HeRALD collaboration that measurements performed with their CDMS-2 and CPD detectors hint at external stress induced by a strong clamping of their CPD detectors, which show a higher background compared to CDMS-2, even though they feature a lower mass [131]. It was concluded that a substantial component of the LEE is caused by externally induced microfractures from the holding of their detectors. This observation also disfavours the intrinsic stress of the Si-wafers as a dominant origin of the LEE, as the smaller detector showed higher LEE rates [131]. At the last EXCESS workshop, which was held as a satellite workshop of IDM2022, the SPICE/HeRALD collaboration showed two measurements of the same detector mounted in two different ways to test the external stress hypothesis further. In one case, the detector was mounted "stress-free" by hanging the detector on three bond wires without another contact with the holder. The other measurement was done with the detector glued to the copper plate, providing a "high-stress" environment as glueing detectors induces stress. A significant increase in LEE in the detector

glued to the copper plate was observed, proving that external stress can cause the shape of the LEE, as observed by many experiments. The hanged detector, however, still showed a LEE below 200 eV. From this, they concluded that an additional stress component has to be present, naming the possibility of contact stress between the TES thin films and the crystal surface [132].
Summarising the various observations, stress induced by the detector holders or the interface between TES and crystal seems to be the dominating source of the LEE observed in the low-energy cryogenic detector community. The ongoing CRESST data-taking campaign and the analysis performed in this work contributed to identifying the source of the LEE by excluding several hypotheses and narrowing down the list of possible origins to the two mentioned above. This is a significant step in understanding the LEE and crucial for the search for low-mass DM and coherent elastic neutrino nucleon scattering. For an in-depth understanding of external stress and the TES-interface stress, CRESST is currently developing completely new detector module designs, including a stress-minimising holding system, fully vetoed detector holding and a double-TES module to test whether the characteristics of the LEE depend on the location of the interaction in the crystal or the surface between TES and crystal.

Chapter 8

^{17}O Enrichment of $CaWO_4$

Section 2.6 discusses how the low natural abundance of ^{17}O (0.038%) limits CRESST's sensitivity for spin-dependent DM searches. Enriching the crystal with ^{17}O has the potential to significantly improve the sensitivity of CRESST-III with the same crystal quality and performance as DetA. To study the impact of ^{17}O enrichment on the sensitivity of CRESST-III, several limit projections created in the scope of this thesis are shown in section 8.1. Since the simulations show promising results, a method similar to the annealing process was developed in cooperation with Prof. A. Erb and two $CaWO_4$ crystals were enriched in this way (see section 8.2). The amount of ^{17}O in the crystals was then determined by nuclear magnetic resonance spectroscopy in cooperation with Prof. Haase at Universität Leipzig (see section 8.3).

8.1 Sensitivity Studies for ^{17}O Enriched $CaWO_4$

In this work, two different simulations are performed to investigate the impact of a higher ^{17}O content in $CaWO_4$ on the sensitivity of CRESST. First, the module DetA with its published threshold, mass and exposure but with a 200 times higher ^{17}O abundance of 7.6%. Second, the same simulation with an additional background reduction by a factor of 100 for a prediction of an achievable limit if the background reduction goals of CRESST are reached.
For the sensitivity studies, the software Romeo, developed and documented in [123, 124] is used. The basic functionality of the software, which is used to fit the measured spectra with a band fit and to calculate a DM limit using the Yellin optimum interval method, is described in section 7.2.4. For the enrichment studies, an implemented simulation tool using the official DetA data set together with the official fit parameters is used. The results for the different simulations are presented in figure 8.1, along with the exclusion limits of other experiments as a reference.
Enriching a standard CRESST detector crystal to an abundance of 7.6% ^{17}O (dark green) improves the spin-dependent limit of DetA (shown in red) almost linearly with the enrichment factor. It would provide a leading limit in the low-mass parameter space. It is competitive with a limit derived with a $LiAlO_2$ crystal oper-

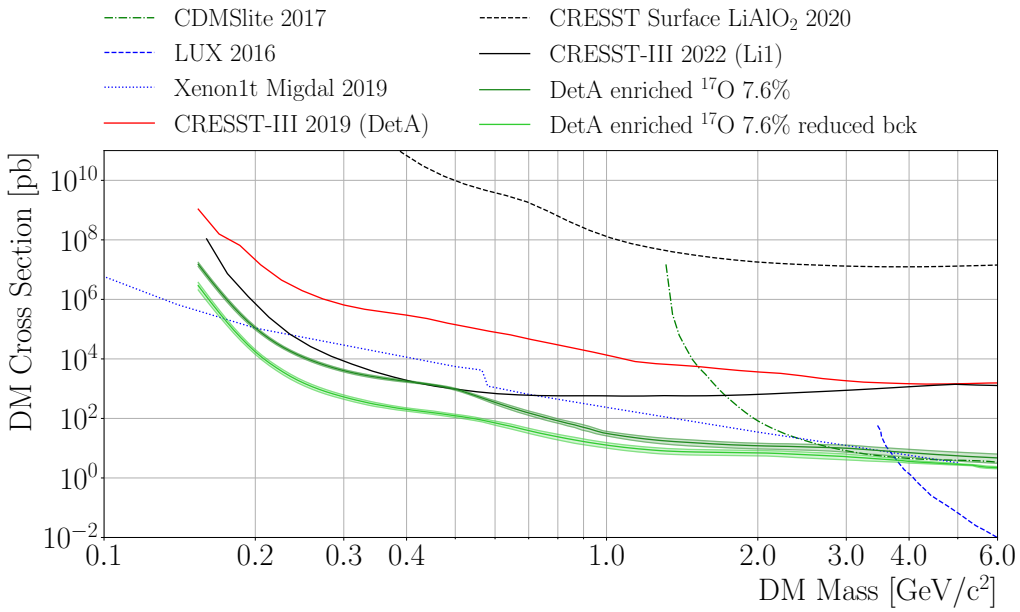

Figure 8.1: Exclusion limits for neutron-only spin-dependent DM-nucleus cross section versus DM particle mass by various experiments [65, 66, 68, 64, 133]. The DetA limit also published in [37] is shown in solid red. The limit projection obtained by the simulation for an enriched $CaWO_4$ crystal with 7.6% ^{17}O abundance is shown in dark green. In contrast, the projection for DetA with a 7.6% ^{17}O abundance and a reduced background in the region of interest is shown in light green. The recently published limit obtained from the blind data set of the ongoing run with a $LiAlO_2$ crystal is shown in solid black.

ated in the ongoing CRESST data-taking campaign. The projection with reduced background (light green) improves the $LiAlO_2$ limit by more than one order of magnitude, underlining the importance of reducing intrinsic impurities in the $CaWO_4$ crystals. Therefore, CRESST would benefit from enriching $CaWO_4$ with ^{17}O for spin-dependent DM searches.

8.2 Annealing of $CaWO_4$ in ^{17}O Enriched Gas

Following the promising results from the sensitivity projections, a method is developed to increase the ^{17}O fraction in $CaWO_4$ crystals. It uses oxygen diffusion into the crystal at temperatures close to the material's melting point. This process is used in the annealing process described in section 3.2.3, where oxygen vacancies in the $CaWO_4$ crystal are filled by diffusion of oxygen into the crystal lattice. In principle, post-growth annealing could be performed with an ^{17}O enriched atmosphere. However, this would not be cost-effective as the furnace is flushed with 10 l/h oxygen during the annealing process, meaning that most of the ^{17}O would be lost to the air. In addition, it is not necessary to enrich the whole crystal with ^{17}O as a large part of the crystal ingot (shoulder, tail and the outer areas of the cylindrical part) is not

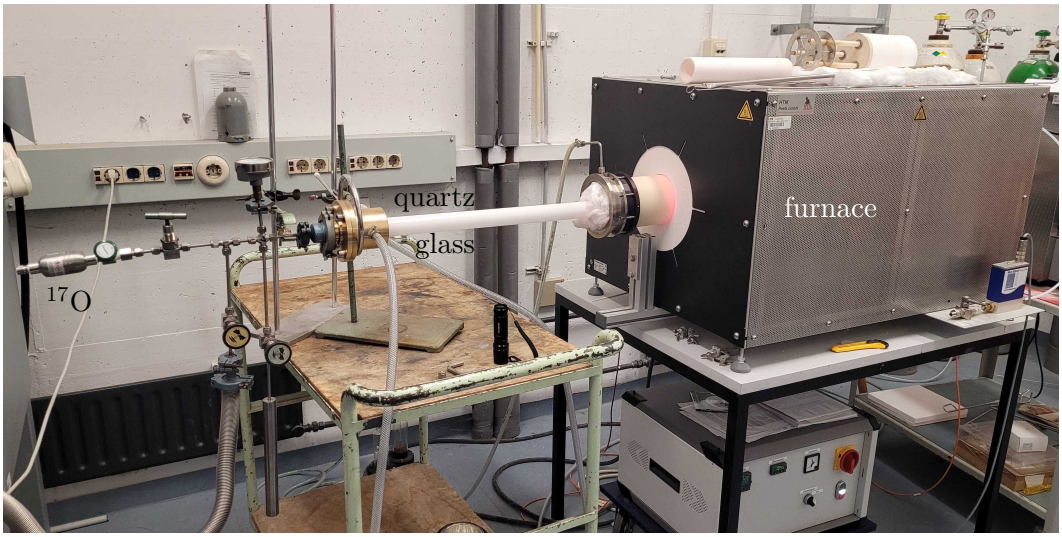

Figure 8.2: Setup for the annealing of a $CaWO_4$ crystal with ^{17}O enriched gas. The enriched gas is contained in the pressure bottle on the very left. With the gas handling, the quartz glass tube partially in the furnace can be evacuated and filled with oxygen gas. The connector between the quartz glass and the gas handling system is water-cooled.

used as a detector. Therefore, the diffusion of ^{17}O into an already cut CRESST-III detector crystal of 24 g in a closed vessel filled with ^{17}O enriched oxygen is favoured. The detector crystal has to be cut from an already annealed crystal to avoid cleavage during the cutting process. In this case, the diffusion is not driven by the chemical gradient of the vacancies but is reduced to the self-diffusion coefficient. These self-diffusion coefficients for minerals range over several orders of magnitudes from low values of e.g. $D^{1300°C}_{Almandine}=(6.06 \cdot 10^{-19})\,m^2/s$ up to $D^{1300°C}_{Biotite}=(1.75 \cdot 10^{-14})\,m^2/s$ [134]. For $CaWO_4$ this coefficient is not known and from the successful annealing, no direct statement about the order of magnitude can be made as the enrichment is driven by the vacancy gradient. To understand the order of magnitude of the diffusion coefficient of $CaWO_4$ and to determine the enrichment time needed to achieve the required enrichment level for CRESST, the diffusion coefficient has to be determined experimentally.

For this, the annealing furnace was modified by the installation of a quartz glass tube, closed at one side. The quartz glass is partially inserted into the furnace with the closed side, leaving one-third of the tube outside. A water-cooled brass connector is glued to this part of the tube, connecting the tube to the gas handling system. This allows the whole system to be evacuated and a 70 % ^{17}O enriched oxygen atmosphere to be filled into the tube. A picture of the setup is shown in figure 8.2.

In this setup, a CRESST-shaped ~20x20x10 mm^3 crystal cut from TUM68 was annealed at a temperature of 1300 °C for 20 h and another crystal cut from TUM56 was

annealed for 200 h together with a small 5x5x5 mm^3 $CaWO_4$ sample with unknown growth number.

8.3 Determination of ^{17}O content in $CaWO_4$

Nuclear magnetic resonance or relaxation (NMR) spectroscopy can be used to determine the ^{17}O enrichment of the $CaWO_4$ crystals, as it is sensitive to the nuclear spin of $\frac{5}{2}$ of ^{17}O [135]. Because of this, ^{17}O is also widely used as a tracer in chemistry and biology, and the method is well studied [135]. The basics of NMR are described in the following [89]: Atoms with a non-vanishing nuclear spin moment have an associated magnetic moment.

$$\mu = \gamma \hbar I \tag{8.1}$$

with I the nuclear spin, γ the gyromagnetic ratio and $\hbar$ the Planck constant. In a static magnetic field B_0 in z-direction μ performs a precession motion around the z-axis

$$\frac{d\mu}{dt} = \mu \otimes B_0 \tag{8.2}$$

The angular frequency of this precession is the so-called Larmor frequency ω_L

$$\omega_L = \gamma \cdot B_0 \tag{8.3}$$

and the energy levels of nuclear magnetic dipoles are quantised according to

$$U_m = -m\gamma\hbar B_0 \tag{8.4}$$

With m = -I, -I+1, ..., I-1, I, so for ^{17}O, six states are possible, and the spins occupy the states according to the Boltzmann distribution [136]. The spins of the nuclei are precessing out of phase in the B_0 field, i.e. randomly oriented around the z-axis. As a result, the net nuclear magnetisation M (the vector sum of all individual nuclear magnetic moments) is aligned parallel to B_0 and has no xy component.
For the NMR measurement, a B_1 field is introduced into the sample by sending an RF pulse at the isotope Larmor frequency through a coil perpendicular to B_0. This causes the spins to become phase coherent and the magnetisation M to flip in the xy plane. In the optimal case, the spins are flipped by 90° [136].

$$M_{x,y} = M \cdot sin(\alpha) \tag{8.5}$$

The precession of the magnetisation $M_{x,y}$ at the Larmor frequency induces a signal voltage in the RF receiver coil. The signal decays with time, driven by a de-phasing of the spins (via a process called spin-spin relaxation, T_2) and by a relaxation of the spins to their equilibrium state in the z-direction (called spin-lattice relaxation, T_1). The signal in the RF coil is therefore called the free induction decay (FID) signal [136]. In NMR, the signal is collected by several iterations of irradiation and

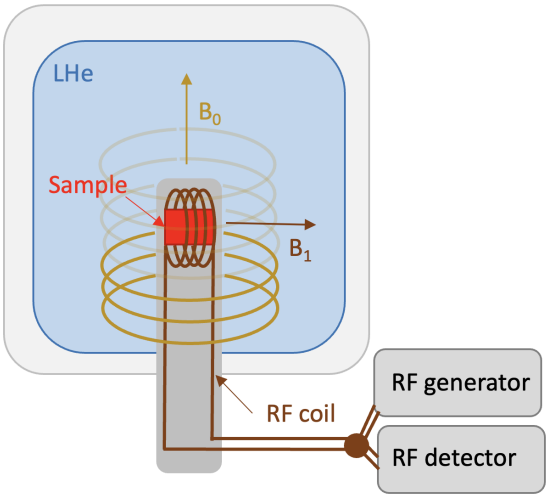

Figure 8.3: Schematic drawing of an NMR setup. Coils cooled with LHe induce a strong static magnetic field B_0 (light brown). The sample (red) is placed in a sample tube and surrounded by an RF coil, creating a magnetic field B_1 (dark brown) perpendicular to B_0. The coil applies the Larmor frequency, which excites the spin states and measures the relaxations of the spins in an alternating pattern.

detection of the FID signal. The spins must be fully decayed to their equilibrium state before a new pulse can be sent. The waiting time between pulses is usually set to five times T_1.

A schematic drawing of the NMR setup is shown in figure 8.3. The magnetic coils (shown in copper-brown) are immersed in liquid helium (LHe), creating a strong magnetic field B_0. The sample (red) is surrounded by the RF coil, which generates a magnetic field B_1 perpendicular to B_0 and is placed in the centre of the B_0 magnet. The coil generates and detects RF signals at the Larmor frequency of a specific isotope.

In the scope of this work, the 20x20x10 mm^3 $CaWO_4$ crystals were measured at the NMR setup of the University of Leipzig [1] and the 5x5x5 mm^3 cube will be measured in the scope of a Bachelor thesis there in the near future. The measurements are performed with a homogeneous magnetic field $B_0 = 11.74\,T$ and a coil tuned to the ^{17}O Larmor frequency of 67.8 MHz. A Bruker Ascend 500 setup is used as shown in figure 8.4 on the left. The coil specially prepared for the measurement of the CRESST-shaped crystal is shown in figure 8.4 on the right.

In solids, the detected frequency depends not only on the Larmor frequency of the isotope, but is also influenced by the crystal structure and surrounding isotopes with nuclear spins. The three main effects are described below:

[1] by the group of Prof. Haase at the Felix Bloch Institute for Solid State Physics

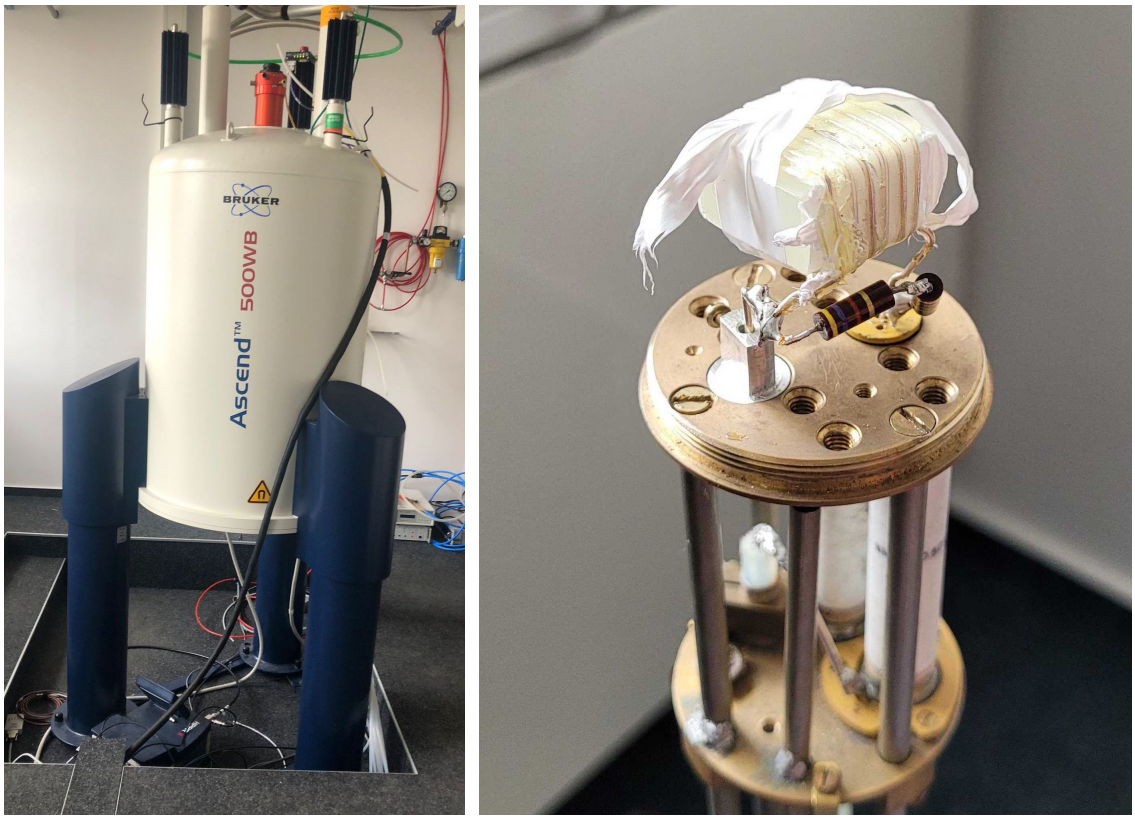

Figure 8.4: Left: Setup for the NMR measurement with the B_0 magnet of 11.74 T. The sample can be inserted into the magnet from the bottom. Right: Mounted B_1 coil surrounding the $CaWO_4$ crystal, wrapped in Teflon for better stability. This sample holder is inserted into the magnet shown on the left.

Quadrupole Coupling

In solid-state materials, the electric charge distribution of nuclei with $I > \frac{1}{2}$ is non-spherical. Therefore, there is an electrostatic field gradient in the material. This associates an electrostatic energy to each nuclear orientation, i.e. the spin states of the nuclei. The nuclei have an electric quadrupole moment q, which measures the deviation of the nuclear charge from spherical symmetry. The intensity of the electrostatic field gradient is described by Q. The electric quadrupole interaction is given by [136]

$$\Delta\nu = \frac{3e^2qQ}{4hI(2I-1)}(3\cos^2\theta - 1) \tag{8.6}$$

Where e is the electron charge, I the quantum number of the nucleus, $\Delta\nu$ the change in energy level between different spin states and Θ the orientation of the material with respect to the magnetic field. Thus the energy transitions usually described by the Larmor frequency are split into five different frequencies, with the frequency difference defined by the orientation of the crystal. This is shown in figure 8.5: For

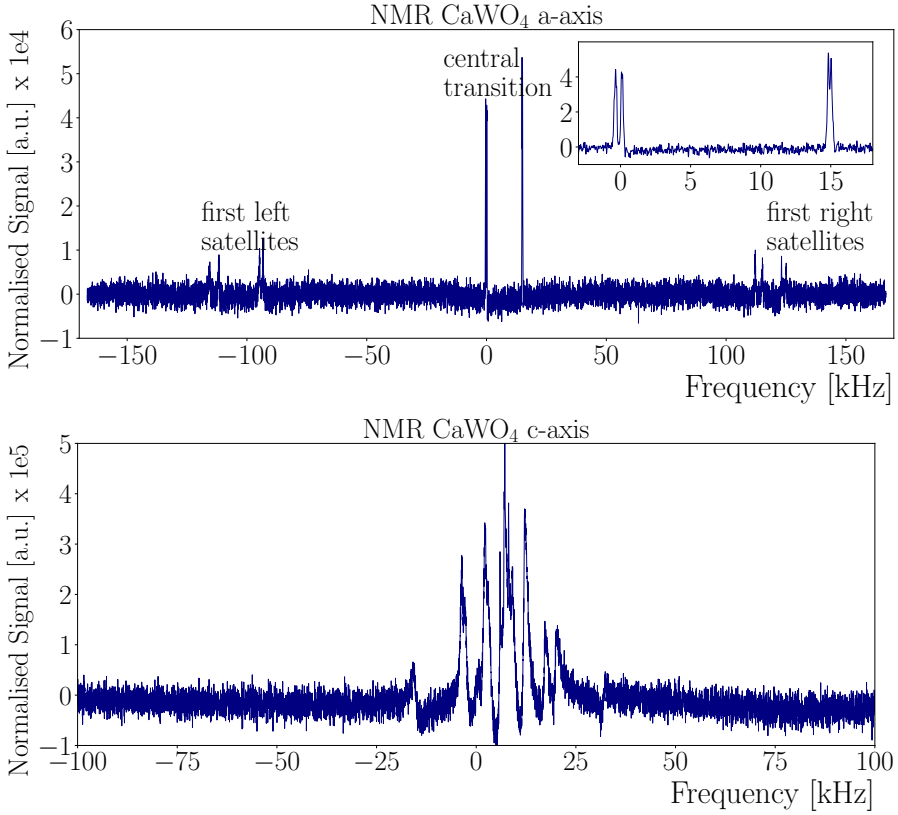

Figure 8.5: NMR scans over a broad frequency range of a non-enriched 20x20x10 mm $CaWO_4$ crystal. The frequency is given in kHz derivation from the 67.8 MHz excitation Larmor frequency of ^{17}O. top: NMR scan with the a-axis parallel to the B_0 field. The quadrupole splitting for the ^{17}O line into the central and the first satellites are visible. In total, ^{17}O splits into five different lines. Only three are visible in the plot, as the other two were out of the sensitivity range of the measurement. In addition, each quadrupole line splits into four lines (shown in the insert plot) due to the chemical shift effect due to the electron orbitals surrounding the ^{17}O nuclei. Overall 20 lines are present due to the two effects, and only 12 are visible in the spectrum. Bottom: Spectrum of the $CaWO_4$ crystal measured with the c-axis parallel to the B_0 axis. The 20 lines from the quadrupole splitting and chemical shift overlap in this orientation.

$CaWO_4$, the energy levels overlap when the c-axis is parallel to B_0 (bottom) and are separated for measurement along the a-axis (top).

The resulting Fourier-transformed spectra, normalised by the number of scans, are shown in kHz derivation from the Larmor excitation frequency of ^{17}O of 67.8 MHz. For the measurement along the a-axis (top), three quadrupolar levels are visible, the central one and the first left and right satellites. The other two satellites were too far out of the sensitivity range selected for this measurement and are therefore not visible in the plot. The splitting of both the central transition and the satellites into four additional lines is due to the so-called chemical shift and is explained in

the next section. The central transition has a higher intensity (i.e. the integral of the peak) because this energy level is closer to the excitation frequency and the sensitivity of the receiver coil is tuned to this frequency [136]. The relative proportion of intensity between the different quadrupolar levels is material dependent and remains fixed when comparing two samples with the same measurement settings. The intensity corresponds to the total amount of ^{17}O in the crystal lattice [137]. When measured along the c-axis, the quadrupolar levels overlap and no clear separation is visible. This underlines the importance of the angle Θ to the magnetic field B_0 as it strongly influences the position of the lines in the spectra. In the case of $CaWO_4$, measurements should be made with the a-axis parallel to B_0 to allow good discrimination between the quadrupolar levels.

Chemical Shift

Another effect causing the splitting of the resonance line is the so-called chemical shift. The quadrupolar splitting described above is due to the non-spherical charge distribution of the nuclei. The chemical shift is due to the different electron densities in the crystal lattice at the four different oxygen positions in the WO_4^{2-} ions. In the tetragonal structure of the WO_4^{2-} ions, two oxygens bind with a double bond and two with a single bond. Therefore the electron density at these two distinct oxygen positions is different. In addition, depending on the crystal orientation, each of the four oxygens has a different orientation with respect to B_0. The electron density therefore shields the oxygen nuclei differently from the magnetic field. This shielding or de-shielding, described by σ, can change the frequency by [136]

$$\Delta\nu = \frac{\gamma\sigma B_0}{2\pi} \tag{8.7}$$

where γ is the gyromagnetic ratio. This splits each quadrupolar line into four lines, with a more pronounced splitting between the single and double bond oxygens, as shown in figure 8.5 (top) in the insert plot, which zooms in on the central quadrupole transition. The actual splitting also depends on the angle of the crystal lattice in the magnetic field, similar to the quadrupolar splitting.

Dipolar Coupling

In addition to the quadrupolar effects and the chemical shift, the spins of other nearby atoms can influence the local magnetic field at each ^{17}O isotope. In the case of only two nuclei with the same magnetic moment μ, the influence on the resonance frequency is expressed as [136]

$$\Delta\nu = \frac{3\mu^2}{hr^3}(3\cos^2\Theta - 1) \tag{8.8}$$

with the distance r between the two nuclei. In the crystal lattice, the ^{17}O isotopes are randomly distributed at different oxygen positions, so that each ^{17}O sees its own

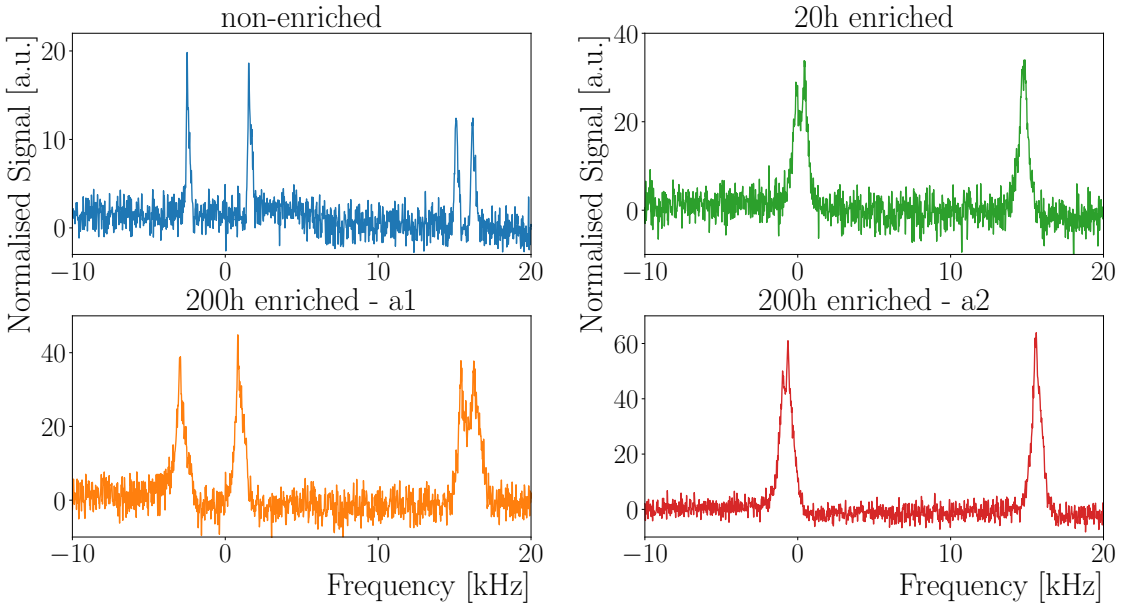

Figure 8.6: Comparison of the NMR spectra of the non-enriched $CaWO_4$ crystal (top-left, blue), the 20 h enriched crystal (top-right, green) and the 200 h enriched crystal (bottom, orange and red) measured along both a-axes. The spectra are normalised to the number of measurement cycles, and the peaks' intensities are proportional to the ^{17}O content in the sample. The positions of the peaks differ between the measurements as they depend on which of the a-axis was aligned parallel to B_0.

averaged local field caused by the others. This leads to a broadening of the detected line depending on the local density of the ^{17}O isotopes [137].

Analysis of ^{17}O Content

To determine the absolute ^{17}O content in a $CaWO_4$ crystal, an enriched sample is compared to a non-enriched sample. The non-enriched sample used in this work was also cut from crystal TUM68 and measured in the same NMR setup as the two enriched samples. All three crystals are of similar size and were oriented along their a-axis as determined by a Laue camera at TUM. Due to the long spin relaxation time T_1 in $CaWO_4$ crystals of $\sim$3 min, which is several orders of magnitude higher than the usual T_1 times of $\mathcal{O}$(ms), the FID signals are recorded for 15 min after each RF pulse.
In order to obtain an adequate signal-to-noise ratio, the unenriched crystal was measured for 495 cycles (123.75 h), the 20 h enriched crystal TUM68 for 99 cycles (24.75 h) and the 200 h enriched crystal TUM56 for 94 cycles (23.5 h) along one a-axis and 142 cycles (35.5 h) along the other a-axis. The resulting Fourier transformed spectra, normalised to the number of cycles, are shown in figure 8.6. The x-axis shows the frequency difference with respect to the excitation frequency and the y-

axis shows the recorded signal normalised to the number of measurement cycles in arbitrary units.

The position of the four peaks differs between the two measurements shown on the left and right. This is due to the orientation of the a-axis. Between the two measurements of the 200 h enriched crystal, the sample was rotated 90 degrees to measure along the other a-axis in the crystal (the axes are denoted a1 and a2). Although the lattice constants are the same for both a-axes, the NMR response is different. Nevertheless, the position of the peaks does not affect the integral of the peaks. Therefore, all the measurements can be compared to determine the enrichment factors.

This work uses two approaches to determine peak intensities: a Gaussian fit and a numerical integral. The Gaussian fit is motivated by the theoretical shape of the signal which, due to dipolar coupling, is expected to follow a random distribution if the crystal has a constant enrichment factor. This assumption is valid for the unenriched crystal as it should have the natural abundance of ^{17}O, but inhomogeneities in the magnetic field distort the signal shape. For the enriched crystals, the density of ^{17}O is not homogeneous, meaning that each isotope has a different local field, and the resulting peak is a sum of different Gaussian functions weighted by the density profile in the crystal. A sum of two Gaussians can empirically describe this behaviour but introduces uncertainties into the model.

Because of these effects, the signals are usually integrated numerically in NMR. This approach is more sensitive to the baseline noise of the measurement than the Gaussian fit approach and requires a good signal-to-noise ratio. A linear baseline correction is applied to the numerical integral to account for baseline shifts in the data. The numerical integrals are usually plotted as a cumulative integral curve with the data.

In this work, the numerical integration and the Gaussian fit are used to determine the intensity of the peaks and are compared. The results are shown in figure 8.7, and the resulting intensities are summarised in table 8.1.

The red fitted curve represents the Gaussian fit to the data. For the enriched crystals, two Gaussians were fitted to each peak to empirically describe the line broadening. The cumulative integral is shown in purple and scaled by a factor of 100 for better visibility. For the overlapping peaks, only a combined numerical integral could be calculated. The two different a-axes along which the 200 h enriched crystal was measured are labelled a1 and a2.

The resulting integrals for the two different orientations in which the 200 h enriched crystal was measured agree within their respective uncertainties, confirming that the results are independent of the choice of the a-axis aligned parallel to the B_0 field. From the integrals an enrichment factor is determined by comparison with the unenriched measurement. This factor must be corrected for the size of the individual crystals, which differ on a $\mathcal{O}(1\,\mathrm{mm})$ scale. The 200 h enriched crystal was damaged during the slow cooling of the furnace after enrichment and $\sim$4 % of the surface with a depth of $\sim$0.5 mm was destroyed.

The enrichment factors are summarised in table 8.2 again for the results of the

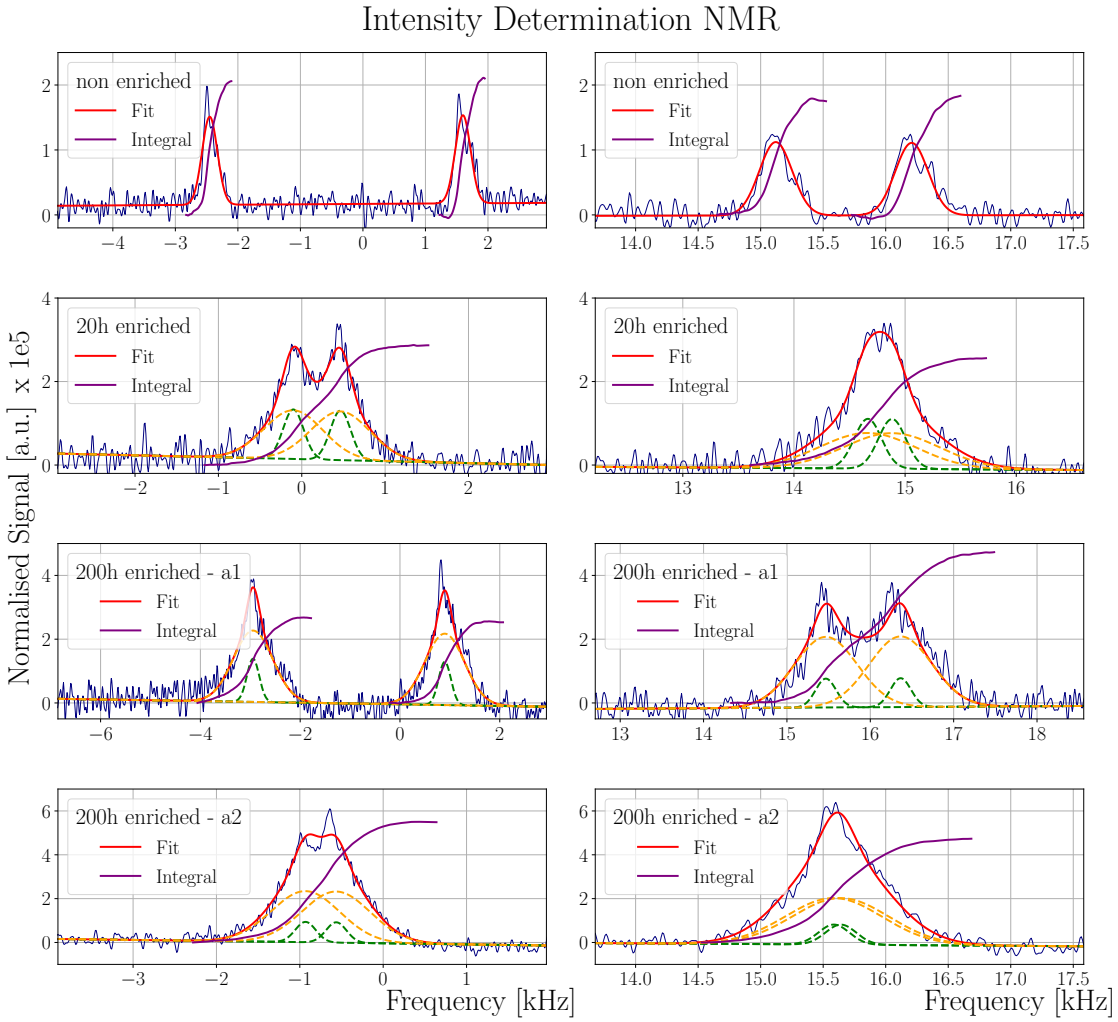

Figure 8.7: Intensity determination in all four measurements of the three $CaWO_4$ crystals. From top to bottom: Non-enriched crystal TUM68, 20 h enriched crystal TUM68, 200 h enriched crystal TUM56 along a-axis a1 and 200 h enriched crystal TUM56 along a-axis a2. The non-enriched peaks are fitted with a single Gaussian model and the enriched peaks with a double Gaussian each. The combined fit is shown in red, and the individual double-Gaussian components are shown in green and orange. The cumulative numeric integrals are shown in purple, scaled down by a factor of 100 for better comparability.

Gaussian fit, the numerical integral and an averaged factor from both approaches. The theoretically achievable limits with the enriched $CaWO_4$ detectors are shown in blue in figure 8.8. The enrichment factors are much smaller than the factor of 200, which was the goal of the enrichment campaign. Nevertheless, it would be possible to improve the exclusion limits with both crystals.
Comparing the enrichment factors for the 20 h and 200 h enrichments shows that increasing the enrichment time by a factor of 10 resulted in an increase in enrichment of $\sim$2.2. The expected increase would have been $\mathcal{O}(\sqrt{10})$ since diffusion at a constant

	Integrals	
	Gauss Fit	Numeric Integral
non-enriched	$(1.58 \pm 0.02) \cdot 10^8$	$(1.55 \pm 0.07) \cdot 10^8$
20 h enriched	$(5.38 \pm 0.08) \cdot 10^8$	$(5.43 \pm 0.01) \cdot 10^8$
200 h enriched - a1	$(1.001 \pm 0.010) \cdot 10^9$	$(9.92 \pm 0.13) \cdot 10^8$
200 h enriched - a2	$(1.002 \pm 0.010) \cdot 10^9$	$(1.022 \pm 0.033) \cdot 10^9$

Table 8.1: Resulting intensities for the non-enriched and enriched $CaWO_4$ crystals measured with NMR in Leipzig.

surface concentration C_s into a material is described by the Van-Ostrand-Dewey solution of the diffusion equation with a given initial concentration C_0 inside the sample, C_c the concentration at each point x, D the diffusion coefficient and t the time [138]:

$$\frac{C_c - C_s}{C_0 - C_s} = \text{erf}\left(\frac{x}{2\sqrt{Dt}}\right) \tag{8.9}$$

This discrepancy can be explained by a leak that occurred during the 200 h enrichment process. Air entered the vessel and diluted the ^{17}O with the normal oxygen present in the air. To quantify the amount of dilution, the recovered atmosphere after enrichment was measured with a mass spectrometer [1]. The resulting spectrum is shown in dark blue in figure 8.9, and a measured air sample is shown in red for comparison.
From the nitrogen peak a contamination of the total gas of $(22.78 \pm 0.14)\%$ can be calculated. Looking at the ratio of the oxygen isotopes, an enrichment of $(51.86 \pm 0.19)\%$ is calculated instead of the original $(70.99 \pm 0.001)\%$. Since the diffusion described by the equation 8.9 is dependent on C_s, this change in the enrichment level of the gas must be taken into account. With this additional information the diffusion coefficient D can be calculated by integrating the profile described by equation 8.9 over the whole crystal volume and inserting the measured ^{17}O abundance, the surface concentration and natural abundance and the enrichment time. For the

[1] operated by C. Vogl from the LEGEND group at E15

	Enrichment factors			^{17}O Abundance
	Gauss Fit	Numeric Integral	Combined	Combined
20 h	3.22 ± 0.08	3.31 ± 0.15	3.26 ± 0.10	$(0.124 \pm 0.004)\,\%$
200 h - a1	7.22 ± 0.20	7.1 ± 0.7	7.26 ± 0.23	$(0.276 \pm 0.009)\,\%$
200 h - a2	7.22 ± 0.20	7.5 ± 0.4		

Table 8.2: Resulting enrichment factor and resulting ^{17}O abundance from the NMR measurement of the 20 h and 200 h enriched crystal.

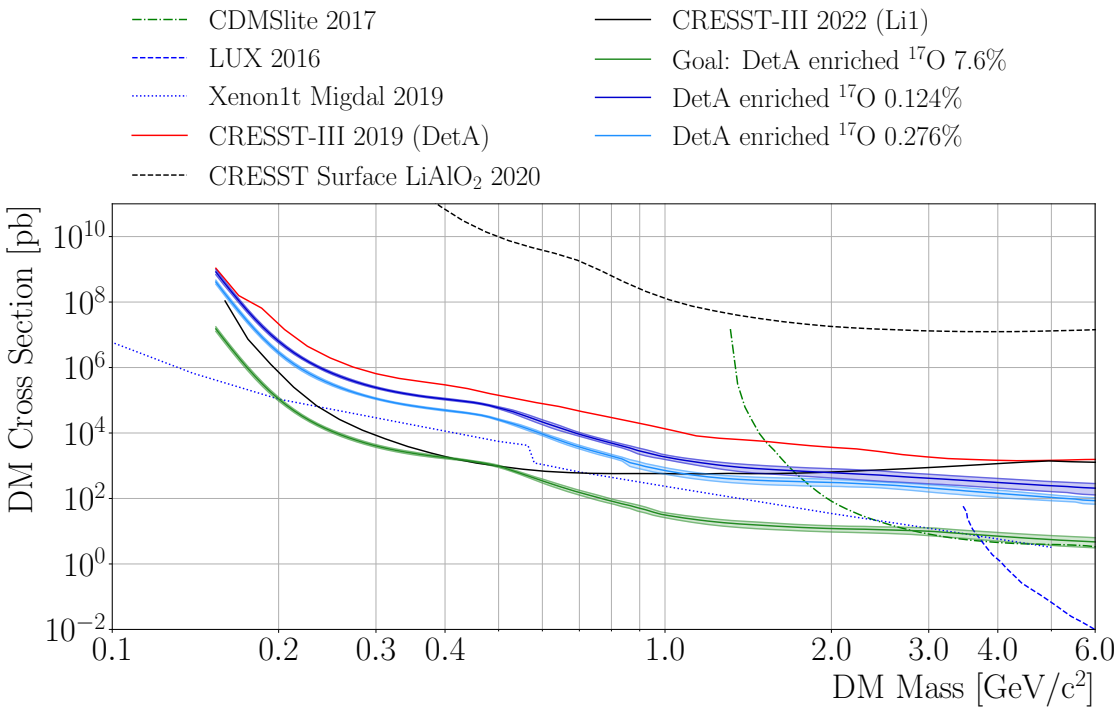

Figure 8.8: Limit projections of the two enriched $CaWO_4$ crystals in orange for the 20 h enrichment (solid orange) and the 200 h enrichment (dashed orange), in comparison to the limits already shown in figure 8.1. The original goal of the enrichment procedure is shown in green.

200 h enrichment, an average surface concentration of (60±10)% is assumed, since the exact ^{17}O concentration at any time during the enrichment cannot be determined from the recovered gas.

The resulting diffusion coefficients from the two different enrichment experiments are $D^{20\,h}_{1300\,^\circ C} = (1.10 \pm 0.\ 11)\cdot 10^{-16} m^2/s$ and $D^{200\,h}_{1300\,^\circ C} = (1.2 \pm 0.4)\cdot 10^{-16} m^2/s$ which are in good agreement within their respective uncertainties. The value also lies within the diffusion coefficient range of other minerals, which ranges from $10^{-14} m^2/s$ to $10^{-19} m^2/s$. The diffusion coefficient is lower than expected from the observations of the vacancy annealing performed on $CaWO_4$ in the past. In hindsight, this process might be driven mostly by a vacancy out-diffusion.

Knowing these diffusion coefficients, the concentration profile can be plotted in 1D as a function of depth from the surface for different enrichment times (see figure 8.10, top). The concentration profile for 20 h enrichment is plotted in dark blue, 200 h in medium blue and one year in turquoise. The diffusion coefficient used for this projection is $D^{20\,h}_{1300\,^\circ C}$. In addition, the time-dependent average enrichment for different crystal geometries can be calculated from the diffusion coefficients (see figure 8.10, bottom). This is the first time that it is possible to predict the achievable enrichment factors for $CaWO_4$. The curve for the standard CRESST size 20x20x10 mm^3 $CaWO_4$ crystals is shown in red. The curve for the next generation CRESST 10x10x10 mm^3

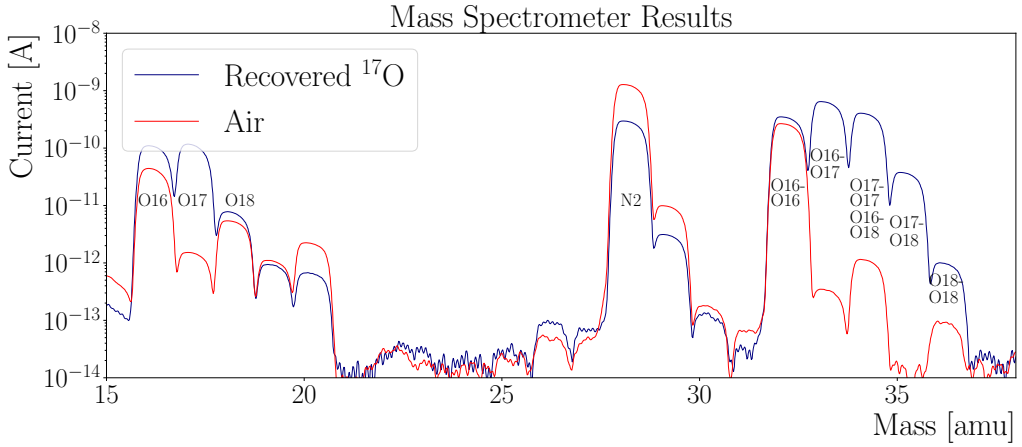

Figure 8.9: Results of a mass spectrometer measurement of the recovered oxygen after the 200 h enrichment procedure (blue) in comparison to a standard air sample (red). Shown is the measured current against the measured mass in amu. Oxygen is measured in two configurations: as a molecule and as ionised oxygen. At 28 amu, the nitrogen molecule is visible, which gives an insight into how much air entered the leak during the enrichment process.

detectors is shown in magenta and for the 5x5x5 mm^3 $CaWO_4$ crystals used in the NUCLEUS experiment in dark blue.

These results show that the desired enrichment factor of 200 is impractical with the current setup. Although a smaller crystal size increases the enrichment factor, miniaturisation of the crystals even below the 5x5x5 mm^3 crystal would not provide a better DM limit due to the small mass of the crystals. Therefore another approach is needed to increase the enrichment factor of the crystals.

One possibility is to increase the diffusion coefficient by increasing the temperature at which the exchange takes place. This is due to the temperature dependence of the diffusion coefficient according to the Arrhenius equation (see equation 3.3). As the activation energy of $CaWO_4$ is unknown, the temperature-dependent diffusion coefficient cannot be calculated. Nevertheless, it can be estimated from other minerals with similar properties. Figure 8.11 (top) shows a collection of several minerals from [134]. Most of the minerals show similar temperature-dependent behaviour. For them, the diffusion coefficient when the temperature is changed from 1300 °C to 1400 °C increases by a factor of ∼2.7±0.3. From this, the diffusion coefficient for $CaWO_4$ at 1400 °C can be estimated to be $(3.0\pm0.4)\cdot10^{-16}$ m^2/s. The $CaWO_4$ data points for both 1400 °C and 1300 °C are added to the plot in red. With this increased diffusion coefficient, the average enrichment over time is estimated for a 5x5x5 mm^3 $CaWO_4$ crystal (light blue) and compared to that at 1300 °C (dark blue) in figure 8.11 (bottom). The plot shows, that the higher temperature during enrichment does not allow for significantly higher enrichment factors to be achieved in a reasonably short time. Additionally, the quartz glass cannot withstand such high temperatures.

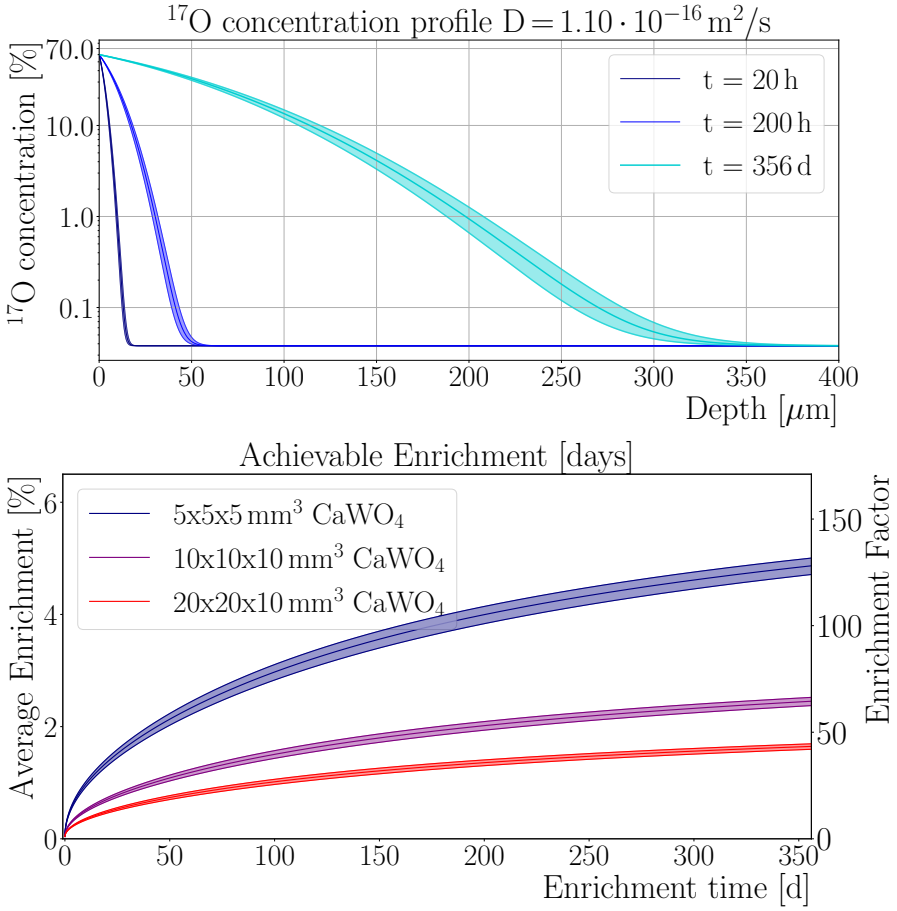

Figure 8.10: Top: One-dimensional ^{17}O concentration profile for different enrichment times in $CaWO_4$ for the $D^{20\,h}_{1300\,°C}$ diffusion coefficient in dependence of the depth from the surface. Bottom: Prediction for an average enrichment as a function of time for three different $CaWO_4$ detector crystals.

Another possibility to substantially increase the enrichment factor would be to enrich the $CaWO_4$ powder prior to the crystal growth process. Due to the fine grain size of the powder and a diffusion length of $\mathcal{O}(10\,\mu m)$, the oxygen can be completely exchanged with the surrounding 70 % enriched ^{17}O atmosphere until the concentrations are in equilibrium. For the growth process, the atmosphere would have to be changed from 99 % argon and 1 % oxygen to an oxygen-free atmosphere to avoid back-exchange of the melt with the oxygen in the atmosphere. Alternatively, enriched oxygen could be added to pure argon gas to create the 1 % oxygen and 99 % argon atmosphere that is recycled after growth.

Regardless of the atmosphere, the $CaWO_4$ crystal contains oxygen vacancies after growth, which must be filled by annealing. This has to be done in an enriched atmosphere to avoid back-exchange of ^{17}O from the crystal lattice. As the typical annealing temperature is 1400 °C, the system has to be modified using an Al_2O_3

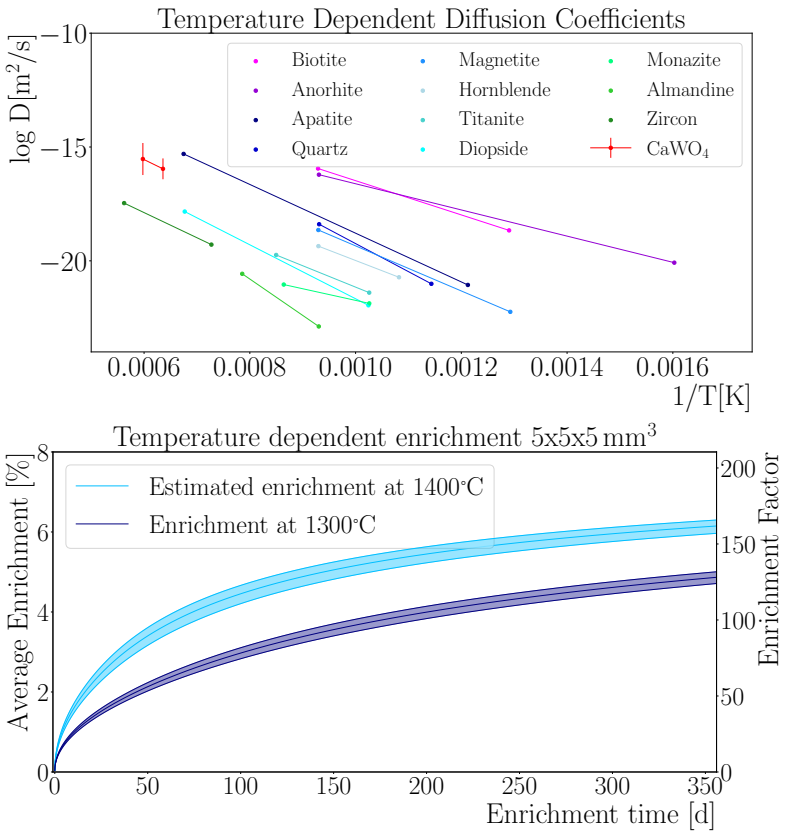

Figure 8.11: Top: Temperature-dependent diffusion coefficients for several minerals. The figure is adapted from [134], and the determined data points for oxygen diffusion in $CaWO_4$ at 1300 °C and 1400 °C are added in red, the error bars are scaled by 10 for better visibility. Overall, a similar temperature dependence is observed. Bottom: Expected enrichment on a 5x5x5 mm^3 $CaWO_4$ crystal at a temperature of 1400 °C.

ceramic. Due to the technical effort needed to implement these changes, these modifications could not be performed in the scope of this thesis anymore.

Chapter 9

Development of an α-Screening Station at TUM

The saturation time determination provides a strong tool to ascertain the radiopurity of TUM crystals from CRESST data. However, the feedback on the crystal growth is relatively slow as CRESST data-taking campaigns usually run over $\sim$2 years and at least half a year of preparation is needed before each run. Hence, a measurement in a facility at TUM would be beneficial in order to determine the crystals radiopurity before selecting the best crystal for detector production for CRESST. With such a measurement the impact of other purification processes like recrystallisation could also be investigated. The crystal TUM81, e.g., which was recrystallised from TUM61 and is, due to segregation effects, expected to have a higher radiopurity compared to standard CRESST detector crystals, has not been measured yet. For its measurement and other TUM-grown crystals, a module based on the i-stick method used in CRESST was developed in the framework of this thesis and in [139]. Section 9.1 gives an overview of the experimental site where the α-screening module is operated, section 9.2 describes the modification applied to this setup to make such a measurement feasible, followed by section 9.3, which describes the module development. The current status of the measurement is described in section 9.4. This module's main goals and working principle are also published in [140].

9.1 The ^{3}He/^{4}He Dilution Refrigerator Facility in the Shallow Underground Laboratory

The TUM owns a unique experimental site, the shallow underground laboratory (UGL), which houses several experiments, including a ^{3}He/^{4}He dilution refrigerator Kelvinox 100. The laboratory is shielded by $\sim$6 m of soil and gravel from cosmic rays, corresponding to $\sim$15 m.w.e. reducing the flux of atmospheric muons by a factor of $\sim$3 and nearly entirely shields the site from the hadronic components [141]. This shielding is crucial to operating large crystals as the rate in a non-shielded laboratory would cause a too-high count rate in the module. In the scope

of this work, it was taken part in the re-setup of the cryogenic system after the cryostat was moved to this experimental site.[1]

The ^{3}He/^{4}He dilution refrigerator works like the CRESST cryostat, reaching a base temperature of $\mathcal{O}(10\,\mathrm{mK})$. This is achieved in three cooling steps. First, the cryostat is placed in a liquid ^{4}He bath (temperature $\sim 4\,\mathrm{K}$). In a second step, the liquid helium is sucked into a so-called 1K-pot which is cooled down to 1.2 K by pumping on the ^{4}He. In the last step, the ^{3}He/^{4}He mixture is used to cool the cryostat down to the base temperature. At a temperature below $\sim$900 mK the mixture separates into two phases: a pure Fermi liquid ^{3}He phase and a Bose-Einstein suprafluid ^{4}He phase in which a certain amount of ^{3}He is diluted. This is due to the different zero-point energies of the two isotopes as ^{4}He is a boson following the Bose-Einstein statistics and ^{3}He the Fermi-Dirac statistics. Hence ^{3}He has a higher energy. As the two phases in equilibrium have to have the same chemical potential, ^{3}He diffuses into the ^{4}He phase, diluting this phase. Due to the different enthalpies of the phases, energy from the surrounding system is needed. Hence, this process effectively cools the surrounding materials down to several mK [142]. In a dilution refrigerator, this process is exploited. In the so-called mixing chamber, ^{3}He diffuses into the diluted ^{4}He phase, cooling the chamber until an equilibrium is reached. To avoid this equilibrium condition, some part of the diluted phase is sucked into the so-called still, heated to a temperature of $\sim 600\,\mathrm{mK}$. By pumping with a high vacuum turbo pump, the ^{3}He evaporates from the diluted phase, thereby reducing the concentration of ^{3}He in the diluted phase, which is, in turn, causing a diffusion from the ^{3}He phase into the diluted phase in the mixing chamber to restore the equilibrium condition. The extracted ^{3}He from the still is guided back through the 1K-pot, re-liquified and added to the pure ^{3}He phase. In this way, constant cooling is achieved. A schematic drawing of the setup is shown in figure 9.1, indicating the mixing circuit's central parts, including the 1K-pot, still and mixing chamber. The inner vacuum chamber encloses all these parts to avoid heat conductivity from the different temperature stages in the cryostat, which gets colder towards the lowest part, the mixing chamber. The cryostat is immersed in the liquid helium bath, enclosed by the dewer, also called the outer vacuum chamber. To shield the cryostat even further from radiation and to reduce the count rate, it is surrounded by a lead castle which can also be closed on the top if needed. In the scope of [23, 143], a muon veto system was installed to tag the remaining muons.

In addition to the shielding against hadronic components of the cosmic radiation and the reduction of muons by the soil provided by the experimental site, the additional shielding by the lead castle and the active tagging of the muons, the cryostat provides long measurement periods as the liquid helium has to be refilled every six days only (compared to the CRESST cryostat which has to be filled every second day). Combining these elements makes it a perfect location for long-term measurements on full crystal ingots.

[1] The main work on this re-setup was performed by A. Langenkämper and is described in detail in [23].

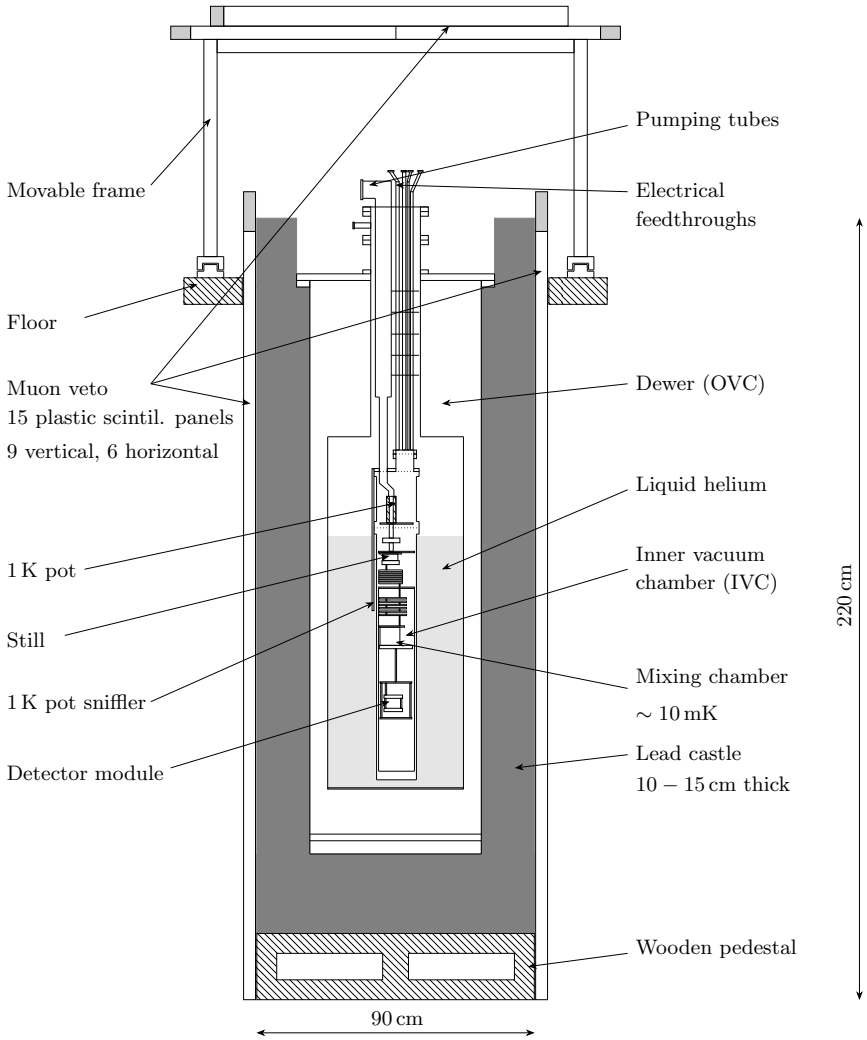

Figure 9.1: Schematic drawing of the cryogenic setup in the UGL. Several layers of active and passive shielding surround the cryostat. It is surrounded by a muon veto, lead shielding and liquid ^{4}He bath. The most important parts of the mixing circuit of the cryostat as well as the 1K pot are indicated in the drawing. The figure is taken from [23].

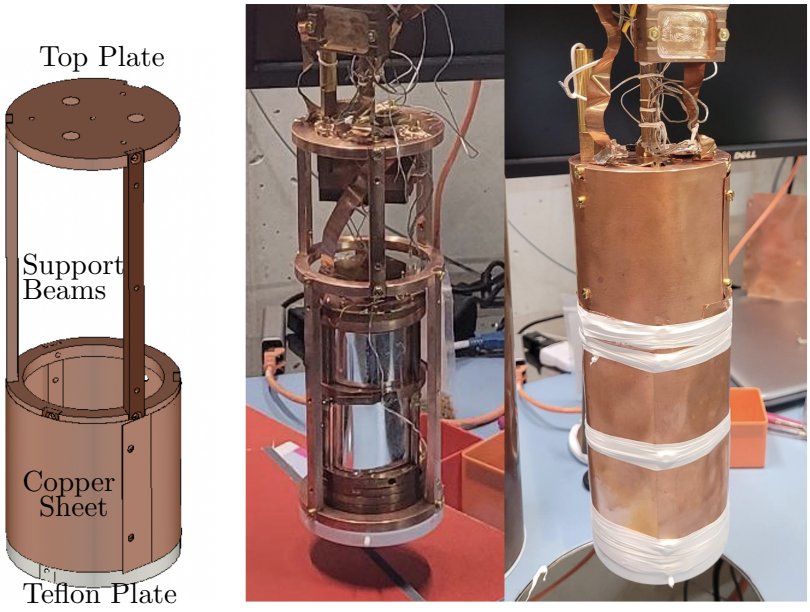

Figure 9.2: Mixing chamber shield for the dilution refrigerator in the UGL. Left: Technical drawing of the shield. It is modular and consists of a two-stage support structure which can be assembled together or individually. A copper sheet is wrapped around the structure to close the module. Middle: Mounted support structure below the mixing chamber. Two modules are installed in it, a small one in the top and a larger one in the bottom. Right: Fully closed shield with Teflon wrapped around the lower parts of it to avoid any thermal contact to the outer shield.

9.2 Installation of a Mixing Chamber Shield

One downside of this cryostat is that TES with transition temperatures below $\sim$30 mK do not go into transition even though the mixing chamber provides temperatures of $\sim$ 10 mK. To solve the transition temperature constraints of this cryostat, a mixing chamber temperature shield was designed in the context of this work to shield the detectors from the heat radiation of warmer parts of the cryostat. The shield consists of a support structure which is coupled to the mixing chamber of the cryostat in which the modules can be mounted and thermalised. Around this structure, a copper sheet is fixed with the focus of allowing no line of sight between the detectors and other parts of the cryostat. As the cryostat is a little tilted, a disk of thermally insulating Teflon with a slightly larger diameter is mounted to the bottom of the shield to avoid thermal connection to the outer shield. The shield is modular and can be operated either in a short, medium or long version. The technical drawing of this shielding and pictures from it mounted in the cryostat are shown in figure 9.2[1] .
To test the effect of the mixing chamber shield, a TES produced on a silicon wafer

[1]The technical drawings were created by A. Marangos and the copper parts were machined by the E15 workshop at TUM

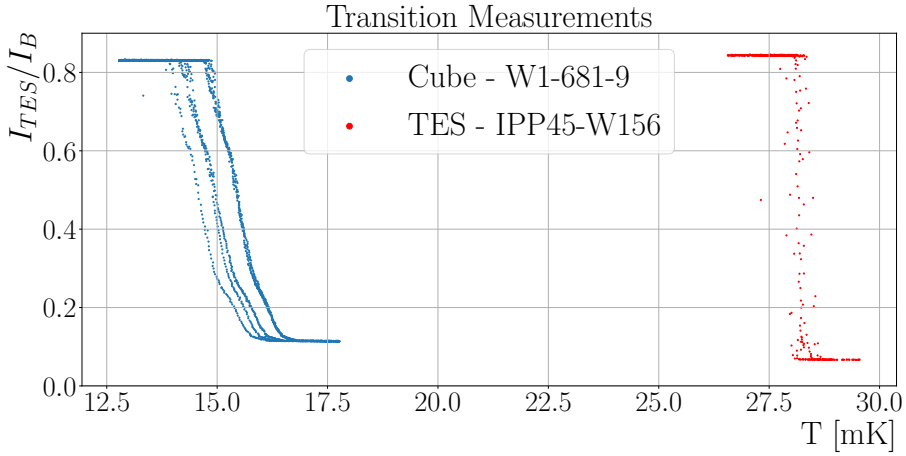

Figure 9.3: Results from TES transition measurements in the UGL cryostat inside the mixing chamber shield. The TES IPP45-W156 (red) shows a transition at ∼18 mK and the $CaWO_4$ detector W1-681-9 between 15 mK and 16 mK. The different transition curves of the detector W1-681-9 are due to hysteresis effects during the temperature sweeps. They are the first TES in this cryostat showing transition temperatures below 30 mK.

(production number IPP45-W154)[2] with a known transition temperature of 28 mK was measured. It showed a transition at ∼28 mK which is the first time a TES went into transition below 30 mK in this setup. The resulting transition curve from the normal to the superconducting phase is shown in figure 9.3 in red. The data points represent the share of the current going through the TES. When the TES is superconducting a higher fraction of the current passes the TES instead of the shunt resistor. Based on these results, a 5x5x5 mm^3 $CaWO_4$ cube with TES number W1-681-9 [3] with a nominal transition temperature of ∼18 mK was tested. It showed a transition at ∼15-16 mK, validating the positive effect of the mixing chamber shield on the reachable transition temperatures in this setup. The measured transition curve is shown in figure 9.3 in blue.
Additionally, the 5x5x5 mm^3 $CaWO_4$ cube was used to determine the reachable detector performance with the mixing chamber shield in this cryostat. For this, the detector was set up, following the procedure described in section 4.5. The detector was operated for ∼3 days with a continuous data acquisition and analysed with the same procedure as TUM93A in chapter 7 using the lines from the ^{55}Fe source for calibration. The threshold was chosen to allow for 1 noise trigger per gram day of exposure. The threshold and resolution in Volt and energy units are summarised in table 9.1.
The resulting spectrum and trigger and cut efficiencies are shown in figure 9.4 and 9.5. The spectrum shows the two peaks from the ^{55}Fe calibration source, as well

[2] The TES was produced by T. Ortmann at TUM
[3] The detector was originally produced for the NUCLEUS experiment by D. Hauff at the Max Planck Institute for Physics

Detector	[mV]	[eV]
Resolution	0.160 ± 0.002	6.91 ± 0.07
Threshold	0.973	39.8 ± 4.2

Table 9.1: Baseline resolution and threshold in [mV] and [eV] for the measurement of the 5x5x5 mm^3 $CaWO_4$ detector in the UGL cryostat. The threshold in Volts does not have an uncertainty as it corresponds to the value set in the trigger process.

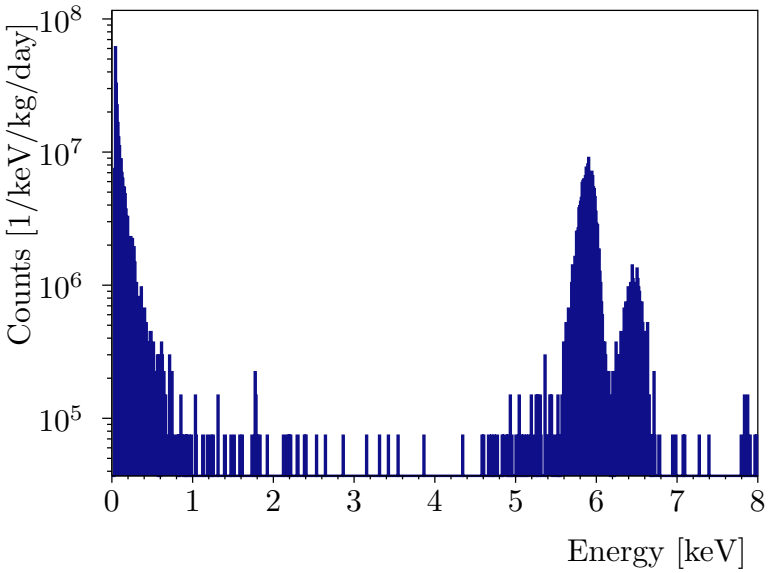

Figure 9.4: Resulting spectrum of the measurement of the 5x5x5 mm^3 $CaWO_4$ cube in the UGL wet cryostat normalised by time, mass and cut efficiency.

as the LEE present in the module. At the time of writing, the data-taking with this detector is continued by the NUCLEUS experiment combining the cryogenic measurement with a muon instrumentation to investigate the different backgrounds at UGL in preparation for the blank assembly of NUCLEUS in the same laboratory. These results show that the wet cryostat facility at UGL is now suited to run low-threshold detectors with low transition temperatures after the successful installation of the mixing chamber shield.

9.3 Alpha-Module Development

For the development of the alpha module, several requirements have to be fulfilled. The module has to fit into the experimental space of the UGL mixing chamber shield, which provides a cylindrical experimental volume of ~200 mm in height and 65 mm in diameter. As crystal ingots have different sizes and shapes the module should be modular so it can easily be adapted to each crystal ingot. Changing a crystal ingot should be fast and easy without introducing any glueing or bonding. To minimise

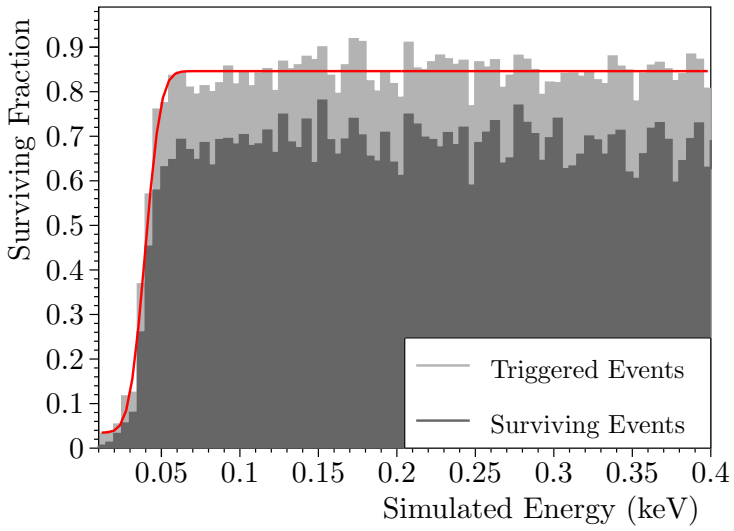

Figure 9.5: Trigger (light grey) and cut efficiency (dark grey) for the analysis performed on the 5x5x5 mm^3 $CaWO_4$ cube. The threshold is determined by fitting an error function to the trigger efficiency and shown in red.

the background from materials in the near vicinity to the crystal, the module should be produced from radiopure copper, also used to produce the CRESST modules. In addition, the resolution should be sufficient to separate α-lines from the natural decay chains.

To fulfil the requirements, the module is designed following the design of the CRESST-II modules with a diameter of 62 mm which just fits the experimental volume inside the mixing chamber shield. An easy adaption of the module to different crystal ingot sizes is possible since many detector parts of CRESST-II modules are still in stock. To allow for an accurate measurement of α-decays without the need to glue or sputter a TES on the crystal ingot, the module is based on the i-stick concept successfully used in CRESST. Meaning high energetic events in the main crystal, which produce many phonons, transmit a small percentage of their energy to the holding stick, and a light detector detects the corresponding scintillation light. Hence, the module is designed with one main i-stick on which the $CaWO_4$ crystals are placed. In CRESST, the resolution of the i-stick to events happening in the main crystal is $\mathcal{O}(100\,\mathrm{keV})$. To improve the resolution, a new i-stick is designed. The CRESST-i-sticks are made from $CaWO_4$ and designed to be small to fit the module design. They are flattened at the end, and a TES produced on a silicon wafer is glued to the stick. For the TUM α-screening module, a more solid i-stick is designed from silicon.

The i-stick is then mounted into the lower part of the module, a solid copper housing in which the i-stick is held by a copper clamp and connected via wire bonding to the readout electronics. On top of this copper housing, a framework of CRESST-II module parts is mounted. A CRESST-III Si-LD produced at MPP, which was not

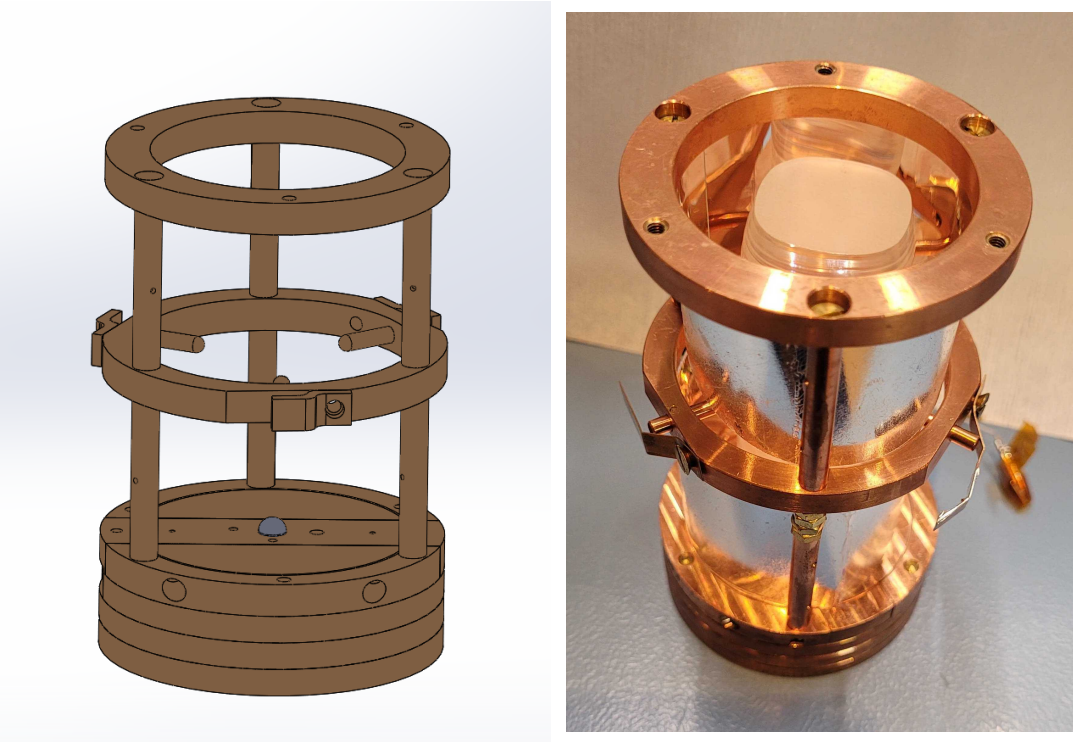

Figure 9.6: Left: CAD drawing of the α-screening module. Right: Fully mounted module containing the crystal TUM81.

mounted in CRESST due to its transition temperature above 30 mK is mounted on top of it. Figure 9.6 shows the technical drawings (left) and the mounted module containing the crystal TUM81 without the LD (right).

9.4 Status and Perspective

At the time of writing, the module is fully mounted, containing the recrystallised $CaWO_4$ crystal TUM81 and the i-stick is equipped with a TES produced at MPP [1]. In total, the module was installed in the cryostat three times and no measurement could be performed yet. This is due to thermalisation problems of the massive $CaWO_4$ crystal which were unexpected and are probably due to a missing dedicated thermal link to the crystal. The original idea was to thermalise the crystal via the i-stick to allow for maximum signal collection efficiency. In this configuration, the module did not cool down. In an attempt with a massive copper link glued to the crystal, the i-stick did go into transition, showing that the thermalisation is, indeed, the reason for the transition problems in the first attempt. The transition measurement of the i-stick is shown in figure 9.7. In this configuration, the i-stick was optimised and operated for several hours, however, due to the massive thermal link glued to the $CaWO_4$ crystal the energy resolution was in the order of several

[1] The TES was produced in the scope of a Masters Thesis by M. Zanirato and M. Mancuso

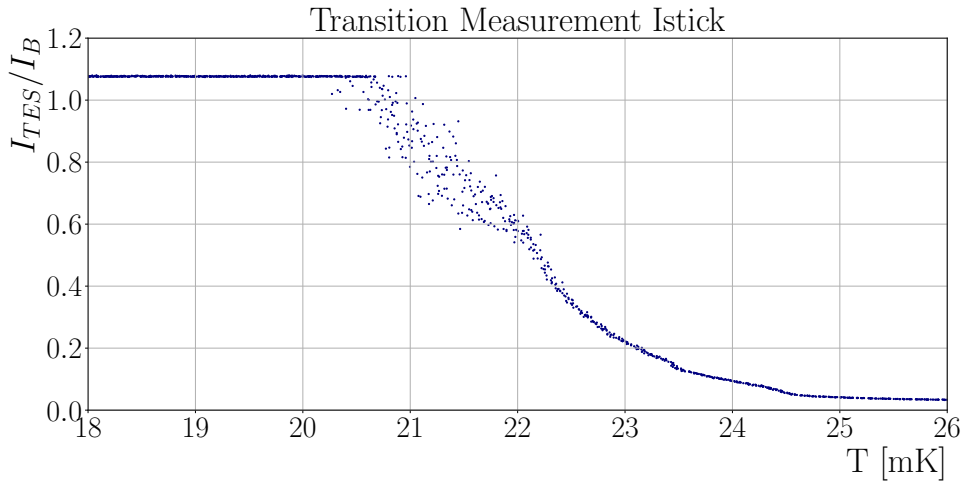

Figure 9.7: Transition measurement of the i-stick in the measurement campaign in which the $CaWO_4$ crystal was coupled strongly to the mixing chamber by a massive copper stripe. The broadness of the transition is probably due to a delay of the crystal adjusting to the changing temperature of the mixing chamber.

hundred keV and additionally the LD could not be operated due to an electronic failure of the SQUID.
In a third attempt, the copper link was removed, and three brass clamps were added to the module and a TES was glued to the crystal surface and connected by three gold bond wires to the copper holder for the thermalisation of the $CaWO_4$ crystal. This time, the LD showed a transition, the i-stick, however, did not.
The results from the three attempts show that a delicate balance between the thermal connection of the crystal to the i-stick and the module holder is needed for the successful operation of the module. This connection has to be determined experimentally in upcoming measurement campaigns. Due to time constraints and usage of the setup by others, this could not be achieved in the scope of this thesis. To already prepare the analysis and understanding of the data from this measurement, a simulation of the experimental site and the module was developed by V. Mokina from the CRESST simulation group to provide an understanding of the background environment in the shallow underground laboratory. Figure 9.8 shows the implementation of the α-module in ImpCRESST, a simulation tool based on Geant4. On the left, the module is shown enclosed by a reflective foil. On the right, the shoulder of TUM93 is mounted, which is also planned to be measured with this module. This shows the flexibility of the module to different crystal sizes and geometries.
In combination with the simulations, the module will allow to investigate the purity of TUM81 in the near future and provide feedback on recrystallisation as a purification tool for the $CaWO_4$ crystal production.

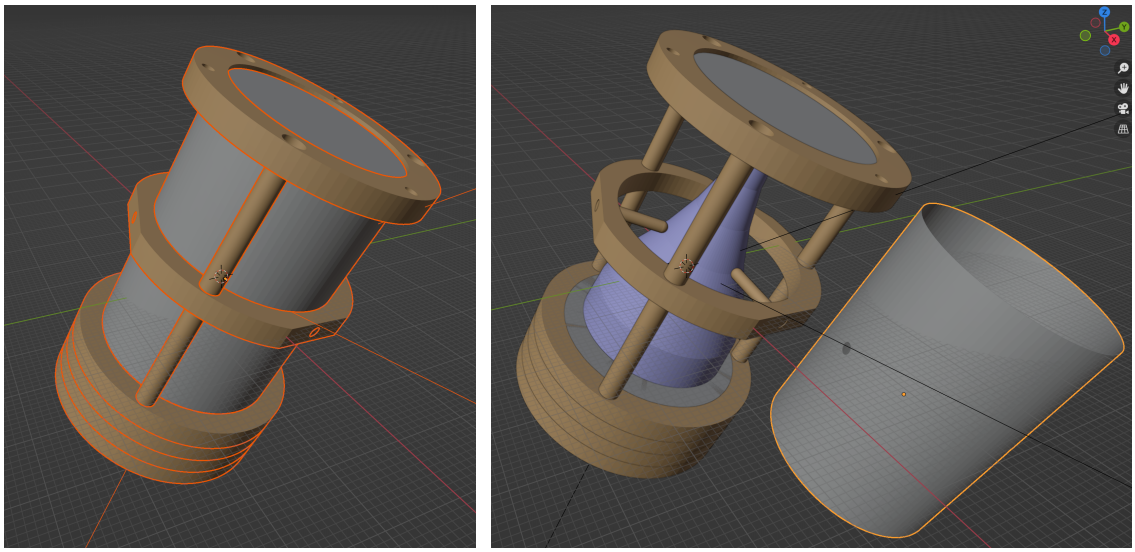

Figure 9.8: Left: Implementation of the full α-screening module, including a scintillating foil, in the collaboration internal software ImpCRESST. Right: Module without the scintillating foil. In this implementation, the shoulder of TUM93 is mounted in the module, which can be adapted to various sizes and shapes of $CaWO_4$ crystals. Simulations provided by V. Mokina.

Chapter 10

Summary

The work presented in this dissertation was performed in the framework of the CRESST experiment and aimed to increase CRESSTs sensitivity for DM searches. CRESST probes DM particles via their elastic scattering off target nuclei in scintillating $CaWO_4$ crystals operated at cryogenic temperatures $\mathcal{O}(10\,\mathrm{mK})$. The interaction of a particle with the target crystal produces mainly phonons (heat), which are detected by a highly sensitive transition edge sensor (TES), and scintillation light, which is detected by a second cryogenic detector, also equipped with a TES. The two-channel readout allows discrimination between different types of interaction, as the relative light output strongly depends on the type of interaction. Electromagnetic interactions are in the e^-/γ-band with the highest light output, α-decays are located in the α-band with a factor of 4-5 less light output, and nuclear recoils, which are potential DM recoils in the lowest band with almost no light produced. In this way, a large percentage of background can be vetoed from the region of interest (ROI) for DM search. To enhance the light output and reduce the rate in the e^-/γ-band, a method to grow high-purity $CaWO_4$ crystals has been developed by Technische Universität München (TUM). In the past, the crystal production included a fabrication of the $CaWO_4$ powder from the cleanest available raw materials $CaCO_3$ and WO_3. These state-of-the art crystals provide a higher radiopurity compared to commercially available $CaWO_4$ crystals.

The latest detectors developed for CRESST-III phase 1 are optimised to search for low-mass DM, reaching thresholds as low as 30.1 eV. In 2019, with this excellent detector performance and background reduction via the usage of TUM-$CaWO_4$ crystals, CRESST improved its sensitivity to low-mass DM by a factor of three down to $0.16\,\mathrm{GeV/c^2}$ and lowered existing exclusion limits at $0.5\,\mathrm{GeV/c^2}$ by CRESST-II by a factor of thirty. The sensitivity of CRESST is currently limited by radioactive backgrounds and excess events below 200 eV.

As the ultimate goal of CRESST is to probe the DM parameter space down to the neutrino floor by upgrading the facility, these backgrounds need to be reduced to allow an increase in sensitivity with exposure.

The sensitivity studies performed in this work compare the effects of background and low energy excess (LEE) reductions on the sensitivity of CRESST. For higher

DM masses, the sensitivity is mainly limited by the radiopurity and for lower masses by the LEE. Therefore, both components need to be reduced in order to achieve the sensitivity required for CRESST.

This dissertation focuses on reducing the intrinsic radioactive background of the $CaWO_4$ detector crystals by two orders of magnitude. To achieve this goal, a comprehensive chemical purification process was developed at TUM to reduce the impurities by a factor of 100. It consists of purifying the raw material $CaCO_3$ by liquid-liquid extraction using the extractant TOPO, which specifically removes the uranium and thorium contents of the powder. $CaCO_3$ and WO_3 are then purified by a coprecipitation reaction before being synthesised in a precipitation reaction to form $CaWO_4$. Afterwards, the $CaWO_4$ powder was washed and calcinated. Screenings of the $CaWO_4$ powder produced by the novel production method with chemical purification show promising results concerning the reduction of impurities. The powder's purity is higher than the detection limits of the screening methods. Hence, a more sensitive screening method is needed to evaluate its exact purity.

In 2019, the crystal TUM93 with a mass of 596.81 g and a length of 122 mm was grown from the chemically purified powder. Three CRESST-III detector crystals were cut from the crystal ingot and assembled into three CRESST modules named TUM93A, TUM93B and TUM93C, with the crystal TUM93A being cut from the upper part of the crystal ingot. Modules TUM93A and TUM93B were equipped with an instrumented stick to read out the energy transfer of high-energy α decays in the crystals. All modules were mounted in the CRESST setup.

To determine the radiopurity of the purified TUM93 crystal, a radiopurity analysis was performed for all three TUM93 modules. For this purpose, an α-decay analysis was performed and used as input to describe the contribution of intrinsic background sources to the background measured in the ROI for the DM search via secular equilibrium assumptions in the three natural decay chains.

For the TUM93A module, the α-decay rate was determined by both an analysis using the instrumented holding stick and a method developed in this thesis, the saturation time analysis. The overall α activity results are in very good agreement, and the saturation time determination provides a better energy resolution of $\sim$20 keV compared to the resolution of the instrumented holding stick of $\sim$260 keV. The saturation time method was also applied to the TUM93B and TUM93C modules, which do not have an instrumented stick or for which the stick was not working for cross-check analysis. A higher rate is observed for both modules, which can be attributed to segregation effects during crystal growth.

For TUM93A and TUM93C, the α decay rates of individual isotopes were determined and secular equilibrium groups were defined according to the results. Overall, the activity of all α-decaying isotopes, except ^{210}Po, was reduced compared to the TUM-grown crystals TUM40 and TUM56. For the decay chains of ^{235}U and ^{232}Th, only limits could be derived due to a low count rate. Overall, a significant reduction of the heavy elements uranium and thorium, one of the main targets of the chemical purification, was achieved. A high rate of ^{210}Po suggests the introduction of ^{210}Pb during purification or surface contamination of the crystal. Overall, an

intrinsic α decay rate of (369 $\pm$ 19)μBq/kg was measured for TUM93A and (487 $\pm$ 22)μBq/kg for TUM93C. This corresponds to an improvement of the detected α-activity compared to the crystal TUM40 by factors of 8.3 and 6.3, respectively.

These results were used as input to derive the expected count rate in the ROI for DM search in CRESST caused by radioactive impurities. For this purpose, the β-decays of the natural decay chains were simulated by Monta Carlo (MC) simulations and probability density functions (PDFs) describing the expected energy spectrum were generated from the resulting templates. The PDFs were scaled according to the α decay rates from the same secular equilibrium group, and the intrinsic background in the ROI was modelled accordingly. The expected background from intrinsic impurities is 0.13 counts/keV/kg/d in an energy range up to 40 keV and 0.15 counts/keV/kg/d up to 5 keV. The expected intrinsic background in TUM93A was compared with the expected background in TUM40, also modelled with this approach, and a reduction factor of $\sim$8.2 below an energy of 5 keV was found. The four isotopes, ^{234}Th, ^{227}Ac, ^{207}Tl and ^{211}Pb, contributing most to the intrinsic background in TUM40 were reduced by an order of magnitude, and only the activities of the isotope ^{210}Pb and its daughters were increased. Without the increase in these isotopes, a reduction by a factor of 30 instead of 8 would have been possible below 5 keV when comparing TUM93A and TUM40. This underlines the importance of understanding how the ^{210}Pb was introduced. Overall, the intrinsic background in TUM93A contributes only 2.1 % to the total background level in the 10-40 keV energy region, and for TUM93C the contribution is 4.7 %. The dominant contribution determined by MC simulations is radiation from the shielding and surroundings of the setup.

In order to investigate the ultimate sensitivity achievable with the intrinsic purity of TUM93A compared to the sensitivity achievable without purification, energy spectra, assuming the intrinsic contamination as the only contribution, were simulated in the absence of a DM signal. The simulations were performed for a threshold of 54 eV, the current threshold of TUM93A, and for a threshold of 10 eV, which has already been reached by several of the CRESST detectors operated in the ongoing data-taking campaign. As expected, the lower threshold provides a higher sensitivity in the low-mass DM region. With the quality of TUM93A up to an exposure of 50 kgd a background-free measurement and thus a linear improvement with increasing exposure would be possible. Above 50 kgd the sensitivity gain deviates from the background-free case. At the exposure goal of 1000 kgd the sensitivity for a DM mass of 0.3 GeV/c^2 would be $4.25 \cdot 10^{-6}$ pb, a factor of 1.8 worse compared to the background free case, and at a DM mass of 0.8 GeV/c^2 a sensitivity of $4.56 \cdot 10^{-7}$ pb could be achieved, a factor of 1.9 worse compared to the background free case. In the case of a DM mass of 0.8 GeV, the sensitivity is nearing the $CaWO_4$ neutrino floor at a cross-section of $6.74 \cdot 10^{-8}$ pb. For crystals with the TUM40-grade quality, a background-free measurement is only possible at exposures $\mathcal{O}$(1 kgd). Achievable sensitivities at an exposure of 1000 kgd would be $1.26 \cdot 10^{-5}$ pb for a DM mass of 0.3 GeV/c^2 and $1.26 \cdot 10^{-6}$ pb for a DM mass of 0.8 GeV/c^2, so factors 2.96 and 2.83

worse than with a TUM93-grade crystal. These simulations will guide the future data taking for a given background configuration.

The other focus of this thesis is the understanding and reduction of the source of the LEE observed below 200 eV. As the LEE is also present in other low-threshold experiments and is particle-like, i.e. not due to noise events, the whole community is extensively studying its origin and has compiled a list of possible hypotheses. One of these hypotheses is intrinsic stress in the target crystals, which could relax over time.

To investigate the intrinsic stress hypothesis, simulations of the temperature gradients during crystal growth were performed, and the Czochralski furnace at TUM was modified to reduce these gradients, which create the intrinsic stress. The amount of intrinsic stress in several crystals grown in different furnace configurations was compared, and a qualitative reduction of intrinsic stress by the modifications was found. The TUM93 crystal was grown from purified powder and in the stress-optimised growth furnace with optimised growth parameters.

In this thesis, the detector TUM93A with a threshold of 53.95 eV and its light detector TUM93A-L with a threshold of 13 eV were analysed. In all detectors the LEE is present and decays with time and a decay constant $\mathcal{O}(100\,\mathrm{d})$. To study this decay in more detail, the detectors were heated to 60 K and cooled down to their operating temperatures. An increase in LEE was observed in all modules, which decayed with a reduced decay time of $\mathcal{O}$(10-20 d), approaching a similar rate level as before the warm-up. Several smaller warm-ups to temperatures of 200 mK, 600 mK and 3.5 K were carried out and no effect on the LEE rate was found. At the time of writing, several warm-ups are planned to investigate the temperature at which a rate increase is visible. The observations have helped to rule out several hypotheses for the origin of the LEE. The temperature and time dependences rule out an external origin such as DM or intrinsic and external radioactive decay.

Possible explanations for the observed features could still be intrinsic or external stress, or the TES-crystal interface. To investigate intrinsic stress as a potential source of the LEE, the crystal TUM73 was measured in a birefringence setup and the stress pattern was compared with the TUM93 crystal grown in the stress-reduced setup. As expected, the TUM73 crystal has a higher intrinsic stress. A re-analysis of the data recorded up to 2018 with the TUM73 crystal in module E shows a lower LEE rate than TUM93, despite the higher intrinsic stress measured in this crystal, excluding intrinsic stress as a primary source of LEE.

Further, a DM analysis was performed on the TUM93A light detector due to its low threshold. It shows a leading sensitivity for DM masses down to $0.12\,\mathrm{GeV/c^2}$.

In 2019, CRESST-III phase one also set leading exclusion limits on the sensitivity to spin-dependent DM interactions using the isotope ^{17}O in $CaWO_4$ with a natural abundance of only 0.038 %. In the framework of this work, simulations have been carried out to investigate how an enrichment of the $CaWO_4$ crystals with ^{17}O would improve the sensitivity for spin-dependent DM searches. The increase in sensitivity is linear with the amount of ^{17}O. Therefore, an idea for the enrichment of $CaWO_4$ by oxygen diffusion at temperatures of ∼80-90 % of the melting point was developed

and a setup for the enrichment was assembled. This idea was based on the annealing process applied to $CaWO_4$ after the growth, in which oxygen diffuses into the crystal and fills vacancies in the whole bulk of the crystal. As the annealing diffusion is driven by a gradient caused by the vacancies, the self-diffusion of ^{17}O is expected to be lower. In the case of other minerals, self-diffusion coefficients typically span the range from $10^{-14}m^2/s$ to $10^{-19}m^2/s$. Enrichment of $CaWO_4$ crystals through self-diffusion becomes feasible with higher coefficients and infeasible with lower values. An experimental diffusion coefficient determination was carried out to assess the potential for self-diffusion-based enrichment in $CaWO_4$.
Two CRESST detector crystals were enriched at 1300 °C for 20 h and 200 h respectively, resulting in ^{17}O contents of 0.124 % and 0.276 %. A diffusion coefficient of $(1.10 \pm 0.11) \cdot 10^{-16} m^2/s$ was calculated from these values. This is the first time a diffusion coefficient was measured for $CaWO_4$. As the diffusion length is of the order of several tens of micrometers, so much smaller than the crystal's dimension, only the outer parts of the $CaWO_4$ crystals are enriched. Hence, the enrichment of powder with a grain size similar to the diffusion length is proposed.
Additionally, a method to improve the radiopurity of $CaWO_4$ crystals via recrystallisation is investigated. Due to segregation effects during crystal growth, impurities are less likely to be incorporated into the crystal lattice. Therefore, the growth process itself is a purification method. In order to study the segregation factors in $CaWO_4$, the crystal TUM81 was grown from the remelted crystal TUM61. In this work, a module was developed which allows to measure the intrinsic contamination of this crystal via an i-stick measurement in the cryogenic facility at the shallow underground laboratory (UGL) in Garching. For this, the UGL wet dilution refrigerator was successfully equipped with a mixing chamber shield, which lowers the achievable transition temperatures measurable in this cryostat down to at least 15 mK and achievable detector resolutions down to ~ 6 eV. Parts of the module have been tested individually in this cryostat. However, due to thermal problems, the whole module has yet to be operated. In the future, the different thermal connections have to be optimised. Another possibility to measure TUM81 is the addition of a carrier-TES glued onto the $CaWO_4$ crystal and an energy reconstruction via the saturation time method developed in this work.

Chapter 11

Conclusion and Outlook

With the intrinsic purity of TUM93, developed in the scope of this thesis, a background-free measurement up to 50 kgd and a steady increase in sensitivity with exposure up to CRESST's design target of 1000 kgd would be possible. This shows that CRESST is no longer limited by crystal quality and that the purification campaign has been successful in achieving this goal.

There are several other constraints that need to be considered for the mass production of $CaWO_4$ crystals for the CRESST upgrade. Firstly, purification requires a lot of workforces, as only 50 g of powder can be purified in one turn. Since it takes ∼1500 g of powder to grow one crystal, 30 purification processes are required, each taking a week. Therefore, the purification cannot easily be scaled up for mass production of the purified crystals, so TUM93 may be the crystal with the ultimate purity achievable for CRESST. Secondly, the comparison of the achievable exclusion limit with the different intrinsic purity of TUM40 and TUM93 shows that in the current state, where the background is dominated by external radiation, the difference in crystal purity has only a small effect on the achievable CRESST sensitivity. Consequently, the other background components have to be eliminated first.

Meanwhile, other purification processes, such as recrystallisation, are being investigated. If similar purification factors could be achieved with this process, it would provide a method that requires less workforce. The achievable cleaning factor will be determined in the near future by measuring the TUM81 crystal in the TUM shallow underground facility. In addition, detector crystals cut from TUM82, also made from re-melted crystal material, are currently being prepared for installation in the next CRESST data acquisition campaign. The saturation time analysis can be used to investigate the purity of these crystals. Depending on the results, a combination of both chemical purification and recrystallisation may be used to produce the $CaWO_4$ crystals for the CRESST upgrade.

The low-energy excess (LEE) studies performed in this thesis show that intrinsic stress, external and intrinsic radiation as well as DM can be excluded as primary sources for the LEE. This is in good agreement with results published in [128] concerning other CRESST detectors and from the community [47, 131, 132, 144]. All the results point to an external source of stress caused by the holders of the detectors

or the surface between the sensor and the crystal. To gain more information on the energies required to reset the LEE, the CRESST data-taking campaign is still ongoing and several warm-ups to different temperatures are planned to investigate the dependence on these energies. In addition, new detector modules are being designed to address the external and TES stress hypotheses. These new modules are expected to be installed later this year.
The ^{17}O enriched $CaWO_4$ crystals could also be installed in the next CRESST data-taking campaign to increase the sensitivity for spin-dependent DM searches as they have a factor of 3.26 and 7.26 higher ^{17}O content. The enrichment facility is currently being upgraded to allow an even higher enrichment of the $CaWO_4$ crystals. This will involve replacing the quartz glass with an Al_2O_3 ceramic vessel with a larger diameter, which can withstand higher temperatures and allow the enrichment of several hundred grams of $CaWO_4$ powder. Due to the increased diffusion coefficient at higher temperatures and the small grain size of the powder, the oxygen can be fully exchanged in this way. The addition of ^{17}O to the growth atmosphere or even a different atmosphere are investigated for crystal growth. In total, enrichments up to $\mathcal{O}(10\%)$ with the isotope ^{17}O will be possible with this setup.

Appendix A

Sensitivity Simulations

In the scope of this work, several sensitivity simulations were performed for various scenarios of LEE and background levels. In this section, the resulting limits are shown in more detail.

DetA

The simulated exclusion limits are shown for selected exposures for different cases of the LEE in figure A.1. As a comparison, the published DetA limit is always shown in red. The case with the full LEE present as measured in DetA is shown on the top left, the case for the absolute LEE contribution reduced by a factor of 10 on the top right, by a factor of 100 on the bottom left and the case for no LEE present on the bottom right. For the simulations, the DetA data was fitted and parametrised, and the LEE's corresponding parametrisation was reduced.
These simulations were additionally performed in the same way for different levels of the flat background above the LEE to see the impact of an overall background reduction. For this, the background was reduced by a factor of 10 and by a factor of 100. For both cases, the simulated exclusion limits are shown for selected exposures in figure A.2 for the reduction by a factor of 10 and in figure A.3 for the reduction by a factor of 100.
Figure A.4 shows sensitivity projections for different LEE and background combinations for a DM mass of 4.8 GeV.

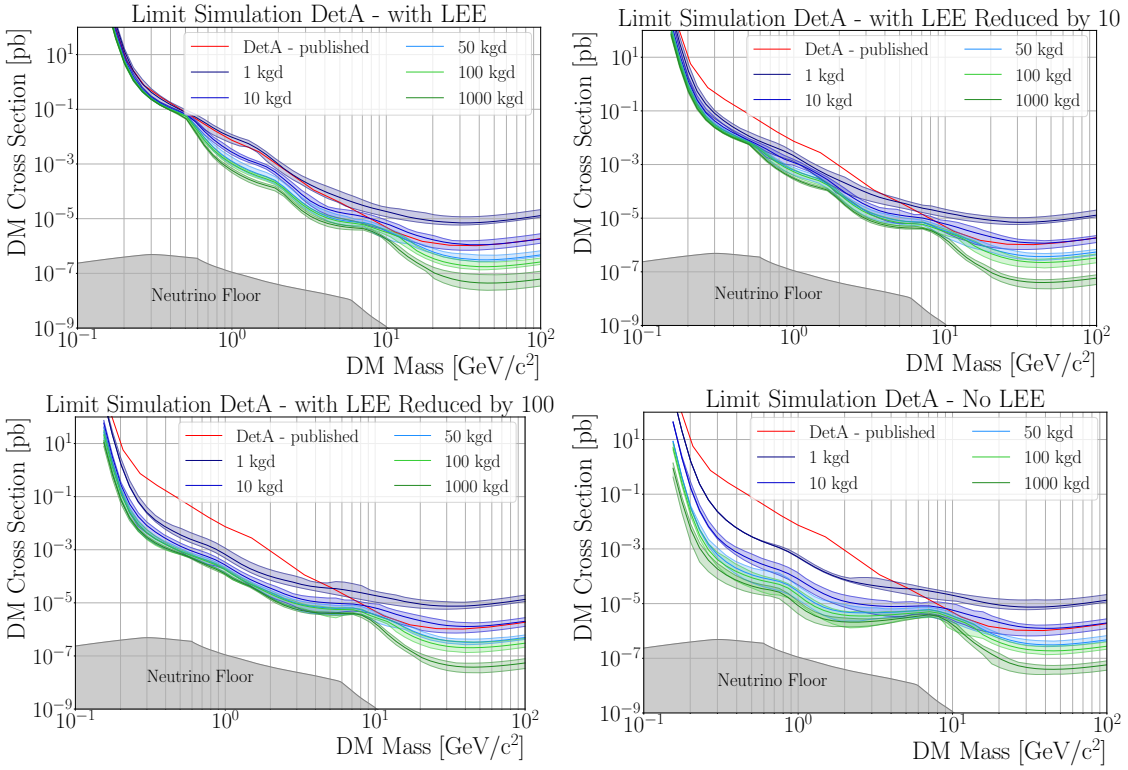

Figure A.1: Limit simulations for the module DetA operated in CRESST-III. Each subplot shows simulated limits for different exposures, ranging from 1 kgd to 1000 kgd. The simulations were performed for the case of the full LEE present in the data (top left) as well as for reduced fractions of the LEE. A reduction of the LEE by a factor of 10 is shown in the top right plot, by a factor of 100 in the bottom left and fully without a LEE component in the bottom right.

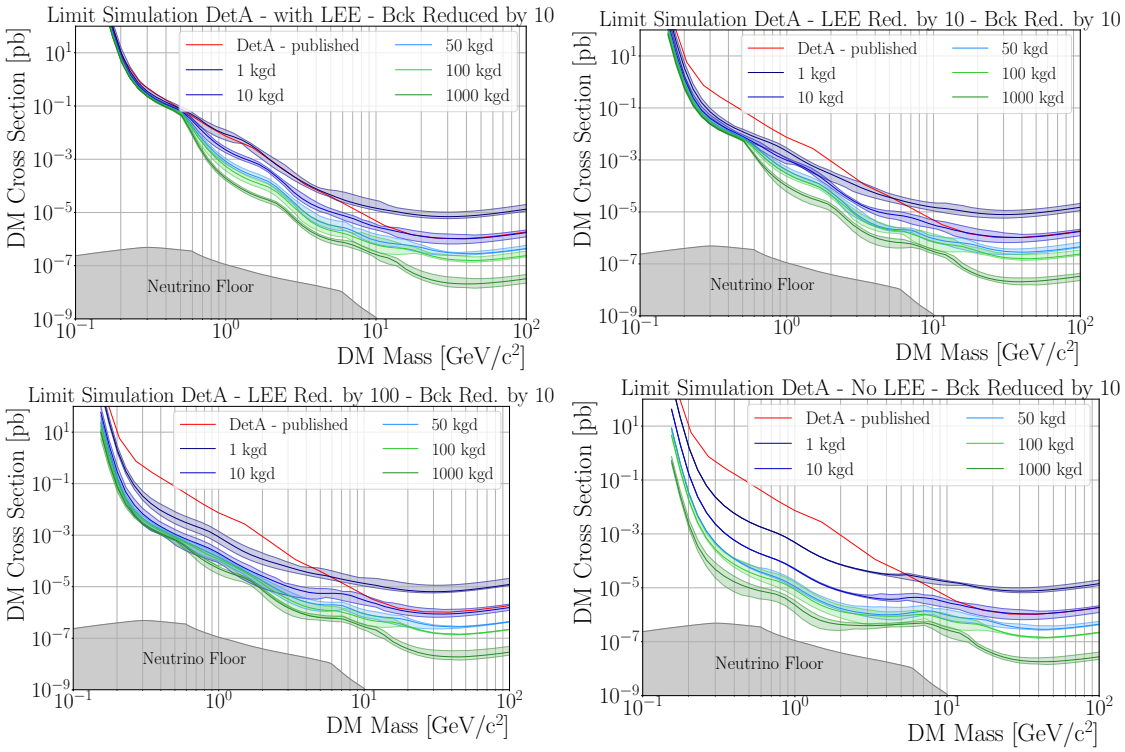

Figure A.2: Limit simulations for the module DetA operated in CRESST-III. Each subplot shows simulated limits for a reduced flat background level by a factor of 10 for different exposures, ranging from 1 kgd to 1000 kgd. The simulations were performed for the case of the full LEE present in the data (top left) as well as for reduced fractions of the LEE. A reduction of the LEE by a factor of 10 is shown in the top right plot, by a factor of 100 in the bottom left and fully without a LEE component in the bottom right.

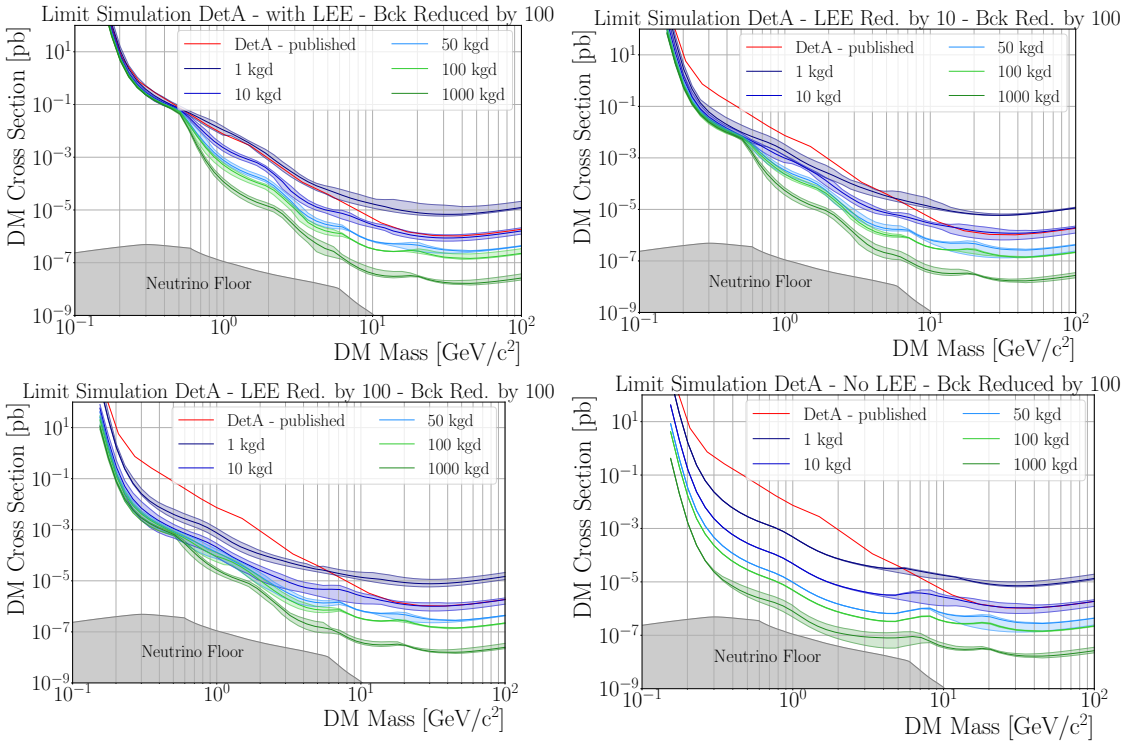

Figure A.3: Limit simulations for the module DetA operated in CRESST-III. Each subplot shows simulated limits for a reduced flat background level by a factor of 100 for different exposures, ranging from 1 kgd to 1000 kgd. The simulations were performed for the case of the full LEE present in the data (top left) as well as for reduced fractions of the LEE. A reduction of the LEE by a factor of 10 is shown in the top right plot, by a factor of 100 in the bottom left and fully without a LEE component in the bottom right.

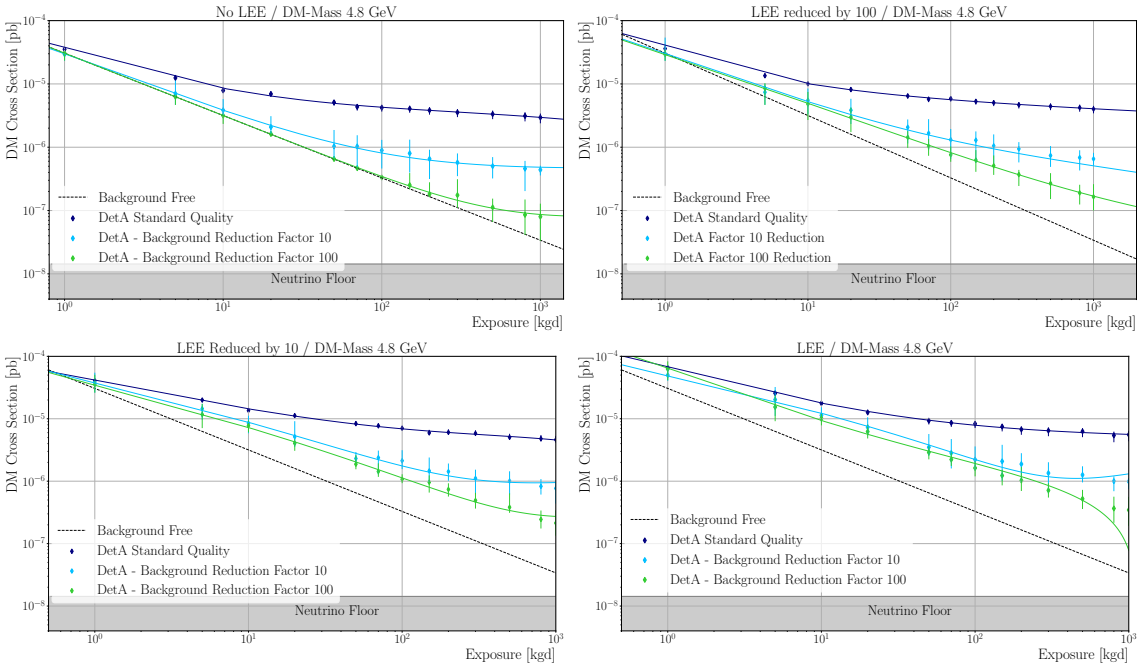

Figure A.4: Sensitivity projections for a DM mass of 4.8 GeV as a function of exposure and background level for different LEE fractions. The simulated sensitivity for the standard background level is shown in dark blue, reduced by a factor of 10 in light blue and by a factor of 100 in green. On the top left, the case for no LEE is shown, top right with 1% of the DetA LEE level, bottom left with 10% and bottom right with the full LEE. The black dashed line represents the sensitivity improvement in the case of a background-free measurement and is the same in all four plots.

TUM93A and TUM40

In section 6.5.4, the ultimately reachable sensitivity with the crystals TUM93A and TUM40 is studied by simulating the limits based on only their intrinsic contamination. This is done for different thresholds for TUM93A, namely the current threshold of 54 eV and for a 10 eV threshold, which will probably be reached with the next generation $CaWO_4$ detector modules. For the TUM40 intrinsic background, a simulation with a 10 eV threshold is performed. The resulting limit projections for selected exposures are shown for each case in figure A.5.

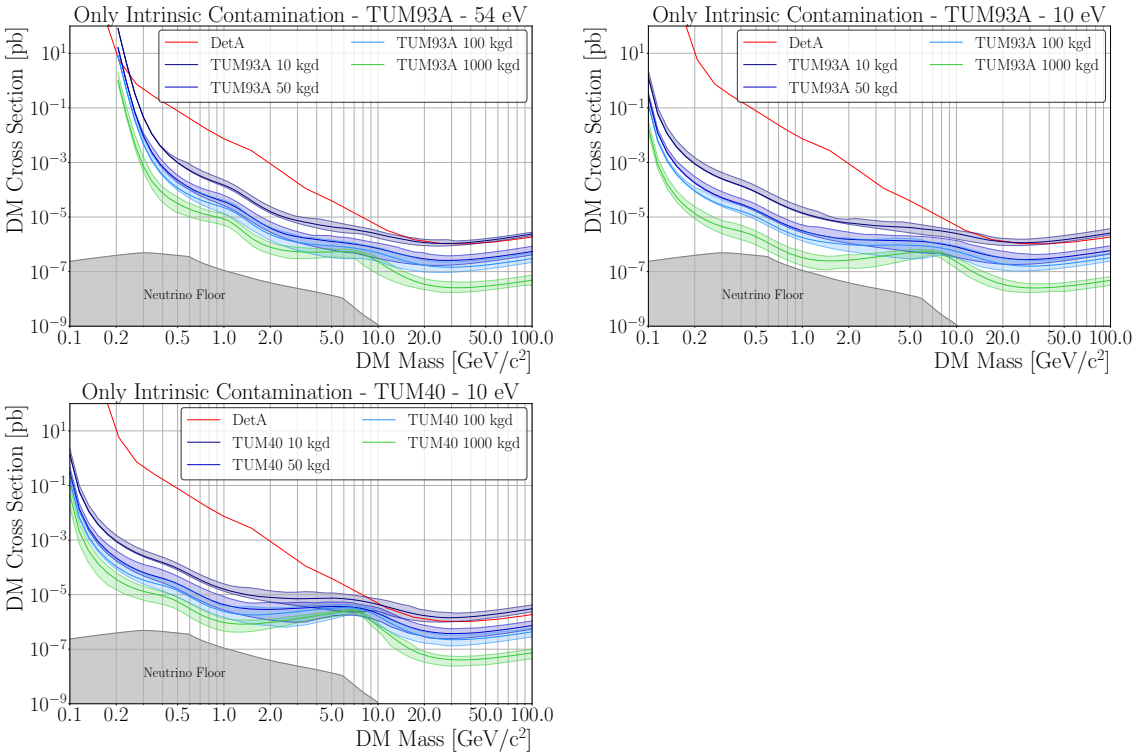

Figure A.5: Limit simulations for the ultimately reachable sensitivity with the intrinsic purity of TUM93A and TUM40. The reachable limits for different exposures are shown for TUM93A with a threshold of 54 eV (top), for TUM93A with a threshold of 10 eV (middle) and TM40 with a 10 eV threshold (bottom).

Appendix B

Analysed Files and Cut Parameters

In the scope of this work, different sets of data have been analysed for both the low energy analysis of TUM93A and TUM93A-L and the high energy analysis of TUM93A, TUM93B and TUM93C.
In the following, the file lists used for each analysis are summarised in B.1 for the low energy analysis and in B.2 for the radiopurity analysis. Afterwards, the cuts for the different analyses are summarised in B.3.
Each file is ∼50 h long as the cryostat has to be refilled with LHe every 2-3 days, for which the data taking has to be interrupted. Data files with problems in the data taking or an unusually high percentage of instability of detectors are excluded from the analysis.

B.1 File List Low Energy Analysis

For the low energy analysis, the data set is split into the training data set and the blind data set to ensure a blind analysis for calculating DM limits with the detectors. For the training set, the first six files and roughly every tenth file afterwards were selected.

bck_003	bck_004	bck_005	bck_006	bck_007	bck_008	bck_018
bck_028	bck_039	bck_048	bck_058	bck_069	bck_078	bck_089

Table B.1: Training data set used to train the cuts applied blindly to the DM analysis data set.

The blind data set consists of all collected files passing the data quality criteria minus the files from the training data set.
A neutron calibration of the ROI in the nuclear recoil bands was performed. This was followed by another background data set, the Postcal set, taken to ensure that

bck_009	bck_010	bck_011	bck_012	bck_013	bck_014	bck_016
bck_017	bck_019	bck_020	bck_021	bck_022	bck_024	bck_025
bck_026	bck_027	bck_030	bck_031	bck_032	bck_034	bck_036
bck_037	bck_038	bck_045	bck_046	bck_047	bck_049	bck_050
bck_051	bck_052	bck_053	bck_054	bck_055	bck_056	bck_057
bck_060	bck_061	bck_062	bck_066	bck_067	bck_070	bck_071
bck_072	bck_073	bck_074	bck_077	bck_079	bck_080	bck_081
bck_082	bck_083	bck_084	bck_085	bck_086	bck_087	bck_088
bck_090	bck_091	bck_092	bck_093	bck_094	bck_095	bck_096
bck_097	bck_098	bck_099	bck_100	bck_101	bck_120	bck_121
bck_122	bck_123	bck_124	bck_125	bck_127	bck_128	bck_129
bck_130						

Table B.2: Blind data set used to calculate the DM limits.

the neutron calibration had no impact on the overall background levels, specifically the LEE.

bck_postcal_008	bck_postcal_009	bck_postcal_010	bck_postcal_011
bck_postcal_012	bck_postcal_013	bck_postcal_014	bck_postcal_015
bck_postcal_016	bck_postcal_017	bck_postcal_018	

Table B.3: Postcal data set taken after the neutron calibration with the AmBe source.

To investigate the time and temperature dependence of the LEE, the detectors were warmed up to 60 K, and after being cooled back down, a new data set was taken, the After WarmUp (AWU) data set. Several smaller warmups were performed during this data set.

awu_bck_002	awu_bck_003	awu_bck_005	awu_bck_007	awu_bck_008
awu_bck_009	awu_bck_010	awu_bck_011	awu_bck_012	awu_bck_013
awu_bck_014	awu_bck_015	awu_bck_016	awu_bck_017	awu_bck_018
awu_bck_019	awu_bck_020	awu_bck_021	awu_bck_022	awu_bck_023
awu_bck_024	awu_bck_025	awu_bck_026	awu_bck_027	awu_bck_028
awu_bck_029	awu_bck_030	awu_bck_031	awu_bck_032	awu_bck_033
awu_bck_034	awu_bck_035	awu_bck_037	awu_bck_038	awu_bck_039
awu_bck_040	awu_bck_041	awu_bck_042	awu_bck_043	awu_bck_044
awu_bck_045	awu_bck_046	awu_bck_047	awu_bck_048	awu_bck_049
awu_bck_050	awu_bck_051	awu_bck_052	awu_bck_053	awu_bck_054
awu_bck_055	awu_bck_056	awu_bck_063	awu_bck_064	awu_bck_065
awu_bck_066	awu_bck_067	awu_bck_068	awu_bck_069	awu_bck_070
awu_bck_072	awu_bck_073	awu_bck_074	awu_bck_078	awu_bck_079
awu_bck_080	awu_bck_082	awu_bck_083	awu_bck_085	awu_bck_088
awu_bck_090	awu_bck_091			

Table B.4: After WarmUp (AWU) data set collected since the first controlled warmup to investigate the LEE rate dependency on the thermal cycle. Files in grey not used for TUM93A-L analysis.

B.2 Radiopurity Analysis

The whole background data set was used to analyse the e^-/γ-background in TUM93A and TUM93C. For TUM93A, some files were excluded and greyed out. For the radiopurity analysis using the saturation time and i-stick analysis, no discrimination between the blind and training data set is needed as the analysis is not performed blindly. In addition, the warmups do not impact the radioactive background. Hence, all files can be combined into one data set. For the i-stick analysis, several files had to be excluded due to stability and noise issues in the i-stick, they are greyed out in the table B.5. Three files could not be used for the saturation time analysis but in the i-stick analysis. They are highlighted in yellow.

bck_003	bck_004	bck_005	bck_006	bck_007	bck_008	bck_009
bck_010	bck_011	bck_012	bck_013	bck_014	bck_016	bck_017
bck_018	bck_019	bck_020	bck_021	bck_022	bck_024	bck_025
bck_026	bck_027	bck_028	bck_030	bck_031	bck_032	bck_034
bck_036	bck_037	bck_038	bck_039	bck_045	bck_046	bck_047
bck_048	bck_049	bck_050	bck_051	bck_052	bck_053	bck_054
bck_055	bck_056	bck_057	bck_058	bck_060	bck_061	bck_062
bck_066	bck_067	bck_069	bck_070	bck_071	bck_072	bck_073
bck_074	bck_077	bck_078	bck_079	bck_080	bck_081	bck_082
bck_083	bck_084	bck_085	bck_086	bck_087	bck_088	bck_089
bck_090	bck_091	bck_092	bck_093	bck_094	bck_095	bck_096
bck_097	bck_098	bck_099	bck_100	bck_101	bck_102	bck_107
bck_108	bck_109	bck_110	bck_111	bck_112	bck_113	bck_114
bck_119	bck_120	bck_121	bck_122	bck_123	bck_124	bck_125
bck_127	bck_128	bck_129	bck_130			

Table B.5: File list for the e^-/γ-background analysis of TUM93A and TUM93C. Files not used for the Analysis of TUM93A are greyed out

bck_003	bck_004	bck_005	bck_006	bck_007
bck_008	bck_009	bck_010	bck_011	bck_012
bck_013	bck_014	bck_016	bck_017	bck_018
bck_019	bck_020	bck_021	bck_022	bck_024
bck_025	bck_026	bck_027	bck_028	bck_030
bck_031	bck_032	bck_034	bck_036	bck_037
bck_038	bck_039	bck_041	bck_043	bck_044
bck_045	bck_046	bck_047	bck_048	bck_049
bck_050	bck_051	bck_052	bck_053	bck_054
bck_055	bck_056	bck_057	bck_058	bck_060
bck_061	bck_062	bck_066	bck_067	bck_069
bck_070	bck_071	bck_072	bck_073	bck_074
bck_077	bck_078	bck_079	bck_080	bck_081
bck_082	bck_083	bck_084	bck_085	bck_086
bck_087	bck_088	bck_089	bck_090	bck_091
bck_092	bck_093	bck_094	bck_095	bck_096
bck_097	bck_098	bck_099	bck_100	bck_101
bck_102	bck_107	bck_108	bck_109	bck_110
bck_111	bck_112	bck_113	bck_114	bck_119
bck_120	bck_121	bck_122	bck_123	bck_124
bck_125	bck_127	bck_128	bck_129	bck_130
awu_bck_002	awu_bck_003	awu_bck_005	awu_bck_007	awu_bck_008
awu_bck_009	awu_bck_010	awu_bck_011	awu_bck_012	awu_bck_013
awu_bck_014	awu_bck_015	awu_bck_016	awu_bck_017	awu_bck_018
awu_bck_019	awu_bck_020	awu_bck_021	awu_bck_022	awu_bck_023
awu_bck_024	awu_bck_025	awu_bck_026	awu_bck_027	awu_bck_028
awu_bck_029	awu_bck_030	awu_bck_031	awu_bck_032	awu_bck_033
awu_bck_034	awu_bck_035	awu_bck_037	awu_bck_038	awu_bck_039
awu_bck_040	awu_bck_041	awu_bck_042	awu_bck_043	awu_bck_044
awu_bck_045	awu_bck_046	awu_bck_047	awu_bck_048	awu_bck_049
awu_bck_050	awu_bck_051	awu_bck_052	awu_bck_053	awu_bck_054
awu_bck_055	awu_bck_056	awu_bck_063	awu_bck_064	awu_bck_065
awu_bck_066	awu_bck_067	awu_bck_068	awu_bck_069	awu_bck_070
awu_bck_072	awu_bck_073	awu_bck_074	awu_bck_078	awu_bck_079
awu_bck_080	awu_bck_082	awu_bck_083	awu_bck_085	awu_bck_088
awu_bck_090	awu_bck_091			

Table B.6: File list for the α-background analysis of TUM93A, TUM93B and TUM93C. Files which were not used for the i-stick analysis of TUM93A are shown in grey, files only used for the i-stick analysis and not for the saturation time analysis in yellow.

B.3 Analysis Cuts Low Energy Analysis

The cuts applied to the data set of TUM93A for the low energy analysis are summarised in table B.7. The index 0 corresponds to the PD, and the index 1 to the LD. The upper and lower limits for the stability cuts are given in square brackets. Only periods with control pulses in this PulseHeight region are labelled as stable. The parameter TFA (Trigger Filter Amplitude) describes the amplitude determined by the OFilter trigger, the OFAmplitude derived by the window OFilter. In the OFilter comparison cut, the determined amplitudes of the window OFilter and the OFilter trigger are compared to remove pulses which were reconstructed wrongly due to boundary effects of the window OFilter. The DeltaV cut removes voltage spikes, and the BLDiff cut removes decaying baselines and pulses with flux quantum losses. The two RMS cuts remove wrongly reconstructed events in the PD and LD. The LY cut is a physical cut and removes events with a too-high light yield and acts on the test pulse equivalent amplitude of the events multiplied by the CPE factors.

Cut	**CutValue**
Stability	PD: [3.32,3.40], LD: [1.63,1.73]
MuonVeto	± 5 ms
OF Comp	(abs(OFAmplitude[0]-TFA[0])/OFAmplitude[0])<0.02
DeltaV	MinimumDerivative[0]/BaseLineRMS[0]>-600
BLDiff	BaseLineDiff[0]<0.02 & BaseLineDiff[0]>-0.015
RMS-PD	(OFAmplitude[0]>0.25 & OFRMS[0]<0.0013) $\vee$ (OFAmplitude[0]<0.25 & OFRMS[0]<0.00115)
RMS-LD	(OFAmplitude[1]>0.4 & OFRMS[1]<0.02) $\vee$ (OFAmplitude[1]<0.4 & OFRMS[1]<0.002)
LYCut	(TPEAmp.TPEAmp[1]$\cdot$12.6283/(TPEAmp.TPEAmp[0]$\cdot$3.07382)<6

Table B.7: Cuts applied to the particle event pulses of TUM93A for the low energy analysis. The index 0 corresponds to the PD, and the index 1 to the LD.

The cuts applied to the data set of TUM93AL for the low energy analysis are summarised in table B.8. The index 0 corresponds to the PD, and the index 1 to the LD. Similar to the TUM93A analysis, in the first cut, the determined amplitudes of the window OFilter and the OFilter trigger are compared to remove pulses which were reconstructed wrongly due to boundary effects of the window OFilter. The DeltaV cut removes voltage spikes, and the BLDiff cut removes decaying baselines and pulses with flux quantum losses. The LDHits cut removes events with too-high PD amplitude, which could hint at a scintillation light event similar to the LY cut. The LD-RMS removes poorly reconstructed amplitudes.

Cut	CutValue
Stability	PD: [3.32,3.40], LD: [1.63,1.73]
MuonVeto	±5 ms
OF Comp	abs(OFAmplitude[1]-TFA[1])/OFAmplitude[1])<0.02
DeltaV	MinimumDerivative[1]/BaseLineRMS[1]>-600
BLDiff	BaseLineDiff[1]<0.02 & BaseLineDiff[1]>-0.02
LDHits	OFAmplitude[0]<0.004 ∨ (OFAmplitude[1]>3.5 & OFAmplitude[0]<0.012)
RMS-LD	(OFAmplitude[1]>1 & OFRMS[1]<0.1) ∨ (OFAmplitude[1]<0.6 & OFRMS[1]<0.0027) ∨ (OFAmplitude[1]>0.6 & OFAmplitude[1]<1 & OFRMS[1]<0.0035)

Table B.8: Cuts applied to the pulses of TUM93AL for the low energy analysis. The index 0 corresponds to the PD, and the index 1 to the LD.

B.4 Analysis Cuts Radiopurity Analysis

B.4.1 e^-/γ-background analysis

The cuts applied to the e^-/γ-background analysis of TUM93A and TUM93C are summarised in table B.9 and B.10 respectively. The amplitude determined by the standard event or template fit is labelled with SEFitResults. The upper and lower limits for the stability cuts are given in square brackets. Only periods with control pulses in this region are labelled as stable.

Cut	CutValue
Stability	PD: [3.32,3.40], LD: [1.63,1.73]
MuonVeto	±5 ms
DeltaV	MinimumDerivative[0]/BaseLineRMS[0]>-600
BLDiff	BaseLineDiff[0]<1 & BaseLineDiff[0]>-0.4
RMS-PD	SEFitResultsRMS[0]<0.014
LYCut	SEFitResultsAmplitude[1]/SEFitResultsAmplitude[0]<1

Table B.9: Cuts applied for the e^-/γ-background analysis of TUM93A. The index 0 corresponds to the PD, and the index 1 to the LD.

Cut	CutValue
Stability	PD: [2.27, 2.34], LD: [1.83,1.85]
MuonVeto	±5 ms
DeltaV	MinimumDerivative[0]/BaseLineRMS[0]>-700
BLDiff	BaseLineDiff[0]<1 & BaseLineDiff[0]>-0.2
RMS-PD	SEFitResultsRMS[0]<0.02
LYCut	SEFitResultsAmplitude[1]/SEFitResultsAmplitude[0]<2

Table B.10: Cuts applied for the e^-/γ-background analysis of TUM93C. The index 0 corresponds to the PD, and the index 1 to the LD.

B.4.2 α-background analysis

For the α-background analysis, no stability cut was applied to the PD as the large energies of α-events cause the detector to be unstable. For the i-stick analysis, a stability cut was applied as only a tiny signal is transmitted to the i-stick, and no instabilities are caused in it.
For the saturation time, different parameters were used. Times labelled with SatTimePD_{90} denote saturation times which were determined by the point when the pulses reach 90 % of their PulseHeight, SatTimePD_{75} for the time when the pulses reach 75 % of their pulse height. For the LD saturation time, the area below the pulse from the onset to the saturation time point is integrated, denoted by SatTimeLD_{90Int}.

Cut	CutValue
Stability	LD: [1.63,1.73], istick: [0.78,0.96]
MuonVeto	±2 ms
BLDiff	BaseLineDiff[0]<5 & BaseLineDiff[2]>-0.2
Istick PulseHeight	SEFitResults[2]<0.35
RiseTime	RiseTime[0]<0.3
DecayTime	DecayTime[0]<0
AlphaEvents	(SEFitResultsAmplitude[2]>0.05 & SatTimeLD_{90Int} <1900) ∨ SEFitResultsAmplitude[2]>0.1

Table B.11: Cuts applied to the α-background analysis of TUM93Ai. The index 0 corresponds to the PD, the index 1 to the LD and the index 2 to the i-stick.

Cut	**CutValue**
MuonVeto	± 2 ms
Squid Reset	PulseHeight[0]<5
RiseTime	RiseTime[0]<0.3
AlphaEvents	(SatTimePD$_{90}$ >500 & SatTimeLD$_{90Int}$ <2000) $\vee$ SatTimePD>600

Table B.12: Cuts applied to the saturation time α-background analysis of TUM93A. The index 0 corresponds to the PD, and the index 1 to the LD.

Cut	**CutValue**
MuonVeto	± 2 ms
RiseTime	RiseTime[0]<0.4
DecayTime	DecayTime[0]<0
AlphaEvents	(SatTimePD$_{75}$ >500 & SatTimeLD$_{90Int}$ <400) $\vee$ SatTimePD$_{75}$ >765

Table B.13: Cuts applied to the saturation time α-background analysis of TUM93B. The index 0 corresponds to the PD, and the index 1 to the LD.

Cut	**CutValue**
MuonVeto	± 2 ms
DeltaV	MinimumDerivative[0]/BaseLineRMS[0]>-1000
RiseTime	RiseTime[0]<0.9
DecayTime	DecayTime[0]<0
BLDiff	BaseLineDiff[0]>0.1
AlphaEvents	(SatTimePD$_{90}$ >300 & SatTimeLD$_{90Int}$ <1000) $\vee$ SatTimePD$_{90}$ >370

Table B.14: Cuts applied to the saturation time α-background analysis of TUM93C. The index 0 corresponds to the PD, and the index 1 to the LD.

Appendix C

α-Line Analysis TUM93A and TUM93C

Table C.1 shows the results of the α-line fits to the data sets of TUM93A and TUM93C. The values are given with the combined statistical uncertainties of the fit and Poissonian counting statistics. For isotopes with small counting statistics, the numbers are given as 90 % C.L. Poisson upper limits, derived from the statistical table 40.3 in [116]. For ^{231}Pa and ^{228}Th, no values can be stated due to an overlap of these two isotopes with the neighbouring ^{210}Po events which have a relatively high rate. All numbers or limits are compared to the detected activity in the crystal TUM40. Improvement factors of 10 or higher are indicated by green colour, and isotopes for which a higher rate is detected than TUM40 are indicated in red. Overall a reduction of the activity of all isotopes but ^{210}Po is detected.
Table C.2 compares these values with the crystal TUM56. For TUM56, the resolution in the α-region was not sufficient to distinguish single isotopes from each other. Hence, only groups of isotopes are compared. Improvement factors of 10 or higher are again highlighted in green. Comparing TUM93 to TUM56 also shows a significant reduction of intrinsic impurities in TUM93.

Isotope	Activity [μBq/kg]			Improvement	
	TUM93A	TUM93C	TUM40	TUM93A	TUM93C
^{238}U	13.6 ± 5.5	16.6 ± 5.3	1010 ± 20	74.5	60.9
^{234}U	21.1 ± 6.0	28.6 ± 10.1	1080 ± 30	53.4	39.3
^{226}Ra			43.0 ± 9.9		
^{230}Th	13.3 ± 5.1	29.9 ± 10.1	55.8 ± 5.4	4.2	1.86
^{222}Rn*	35.3 ± 6.2	38.9 ± 7.9	38.1 ± 4.9	1.1	1.0
^{218}Po* (+ ^{227}Th)	$<18.9 \pm 6.9$	$<17.2 \pm 6.3$	34.1 ± 9.9	>1.8	>2.0
^{214}Bi/Po*	19.5 ± 5.9	25.3 ± 6.5	47.4 ± 4.9	2.4	1.9
^{210}Po ext.	147.4 ± 12.2	274.4 ± 19.4	~ 5 (**)	-	-
^{210}Po int.	149.7 ± 12.5	248.4 ± 18.6	17.8 ± 4.0	0.12	0.07
^{235}U	<6.9	<11.3	39.5 ± 4.4	>5.7	>3.5
^{231}Pa	-	<9.0	23.2 ± 4.4	-	>2.6
^{227}Ac	<4.1	<3.9	98 ± 20	>23.9	>22.8
^{227}Th* (+ ^{218}Po)	$<18.9 \pm 6.9$	$<17.2 \pm 6.3$	105 ± 19	>5.6	>6.1
^{223}Ra*	<6.9	<13.4	104 ± 7	>15.1	>7.7
^{219}Rn/^{215}Po*	<4.1	<3.9	107 ± 7	>26.3	>27.6
^{211}Bi*	<4.1	<11.3	105 ± 7	>25.8	>9.3
^{232}Th	<9.4	<11.3	9.2 ± 2.3	>1.0	>0.8
^{228}Th	-	-	15.2 ± 4.1	-	-
^{224}Ra	<9.0	11.9 ± 5.2	19.8 ± 8.1	>2.2	1.7
^{220}Rn*	<4.1	<3.9	8.4 ± 3.4	>2.1	>2.2
^{216}Po*	<4.1	<3.9	0 ± 0	-	-
^{212}Bi*	<6.9	<11.3	7.7 ± 8.9	>1.1	>0.7
^{211}Bi/Po*	<4.1	< 11.3	15.8 ± 2.8	> 3.9	>1.4

Table C.1: Detected α-decays in TUM93A and TUM93C in comparison to the crystal TUM40 analysed in [45]. The isotopes are sorted by their decay chains indicated by the first isotope in each block. Purification factors >10 are highlighted in green. A red factor corresponds to an increase in the rate. The (**) indicates that the value was estimated from the histogram in the paper, as it was not stated explicitly. The peaks of ^{234}U and ^{226}Ra, as well as the peaks for ^{218}Po and ^{227}Th, could not be resolved due to their close energies. Hence a total activity is given for both and a minimal purification factor conservatively assuming that all the activity belongs to the isotope compared to the respective TUM40 isotope. The uncertainties are a combination of fit and bin-wise Poissonian errors given to the fit for the isotopes, which could be fitted by a Gaussian distribution. For the other isotopes with a small number a 90 % C.L. Poisson upper limit was derived according to table 40.3 in [116]. Isotopes that should be in secular equilibrium due to their short decay times are denoted with * for the three decay chains. For isotopes with half-life times larger than the scope of the data-taking period, secular equilibrium can be broken due to chemical purification and crystal growth.

Isotope	Activity [μBq/kg]			Improvement	
	TUM93A	TUM93C	TUM56	TUM93A	TUM93C
^{232}Th	<9.4	<11.3	52 ± 23	>5.5	>4.6
^{238}U	13.6 ± 5.5	16.6 ± 5.3	293 ± 54	27.2	17.7
^{235}U ^{230}Th ^{234}U ^{226}Ra	36.1 ± 8.1	63.6 ± 26.4	409 ± 68	11.3	6.4
^{211}Bi	< 4.1	<11.3	77 ± 30	>18.9	>6.8

Table C.2: Detected α-decays in TUM93A and TUM93C compared to the crystal TUM56 from [46]. As the resolution of TUM56 was insufficient to identify single lines over the whole energy range, the activity is given as a common value. For a better comparison, a common value for these elements is calculated for TUM93A and TUM93C. Improvement factors >10 are highlighted in green. The values are the same as shown in table C.1 but were combined to compare the detectors and TUM56.

Appendix D

e^-/γ-Background TUM93C

The e^-/γ-background simulation performed for TUM93A in section 6.5.2 was also performed for TUM93C. Also, for this module, the α-decay activities were used to scale PDFs of the β-decaying isotopes accordingly to describe the expected background in the e^-/γ-band from intrinsic impurities. The resulting contributions from the three natural decay chains ^{238}U (green), ^{235}U (yellow), and ^{232}Th (red) are shown in figure D.1 in comparison to the detected spectra (black) for the energy spectrum up to 500 keV (top) and up to 40 keV (bottom).
The preliminary results for a full background simulation of TUM93C by the CRESST simulation group are shown in figure D.2 (top) for a fit to the α-region and bottom for the e^-/γ-background up to 740 keV.

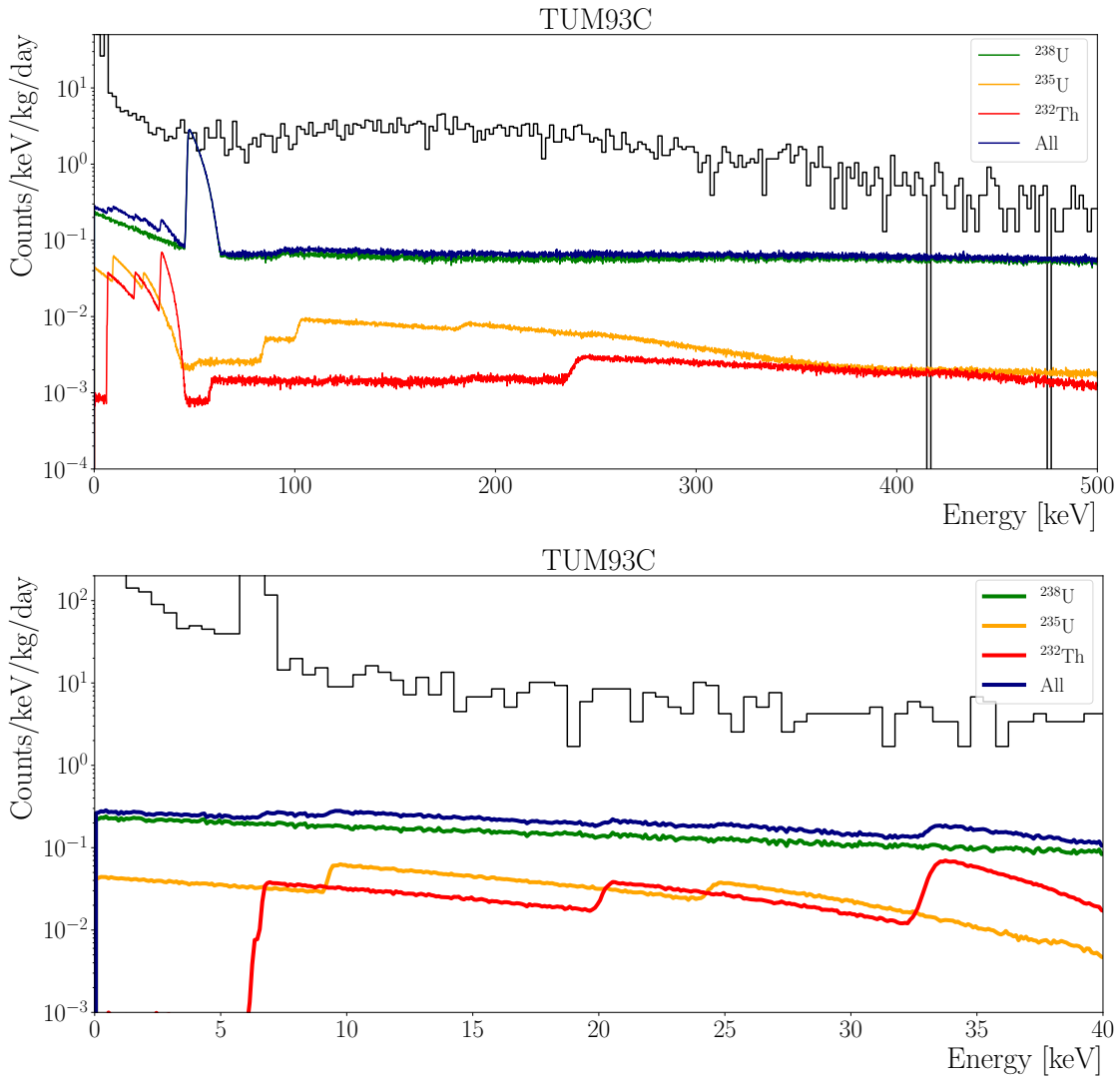

Figure D.1: Histograms of the efficiency corrected events in the e^-/γ-band recorded by TUM93C. The blue line indicates the sum of all background sources originating from the three natural decay chains ^{238}U (green), ^{235}U (yellow) and ^{232}Th (red) as derived from the secular equilibrium assumption with α-decaying isotopes in the decay chains (see text). Top: Energy region from 0 to 500 keV. The high ^{210}Pb contamination present in the crystals is visible at ∼60 keV. Bottom: Zoomed energy region up to 40 keV.

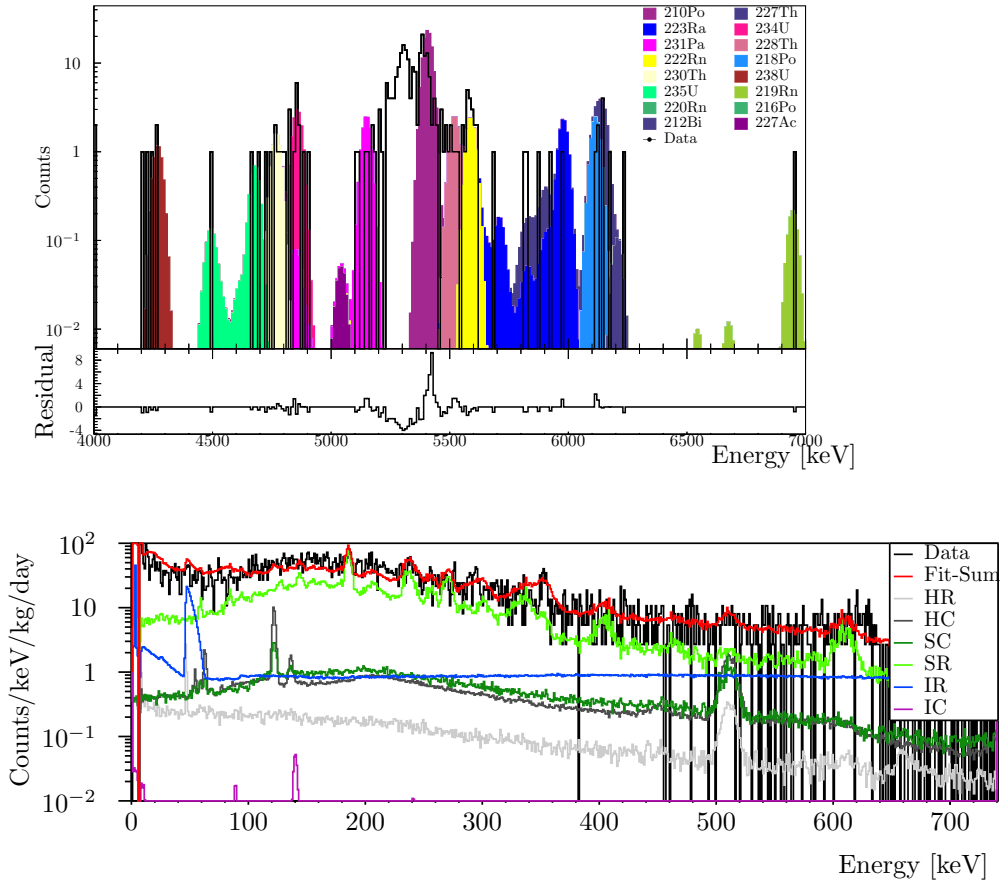

Figure D.2: Results of the combined likelihood fit to both the α-region and the e^-/γ-band of TUM93A. Top: Template fit to the α-region of TUM93A with the different isotopes. Bottom: Likelihood fit of the various background components to the TUM93A e^-/γ-band spectrum. The intrinsic contaminations which are fitted correlated with the α-activities are shown as a blue curve. Other background components from the holder in grey, the shielding in green and the cosmogenic activation of the crystal in magenta. Fit performed by J. Burkhart.

Appendix E

Intrinsic Contamination Sources TUM40 and TUM93A

In this section, the scaled templates of the three natural decay chains in TUM93A and TUM40 are compared to show which contribution of these isotopes in the e^-/γ-band could be reduced. A comparison for the ^{238}U chain is shown in figure E.1 for TUM40 (top) and TUM93A (bottom). The combined contribution from the ^{238}U chain isotopes was reduced in TUM93A compared to TUM40. In addition, the contributions of ^{234}Th and ^{234}Pa could be reduced significantly. On the other hand, the ^{210}Pb and contribution of its daughter nuclei were increased in TUM93A compared to TUM40.
In the ^{235}U chain, the combined contribution, including all the individual contributions, could be reduced in TUM93A compared to TUM40. A similar effect is observed in the ^{232}Th chain, where the overall level and the individual level of all isotopes besides ^{227}Ac were reduced.

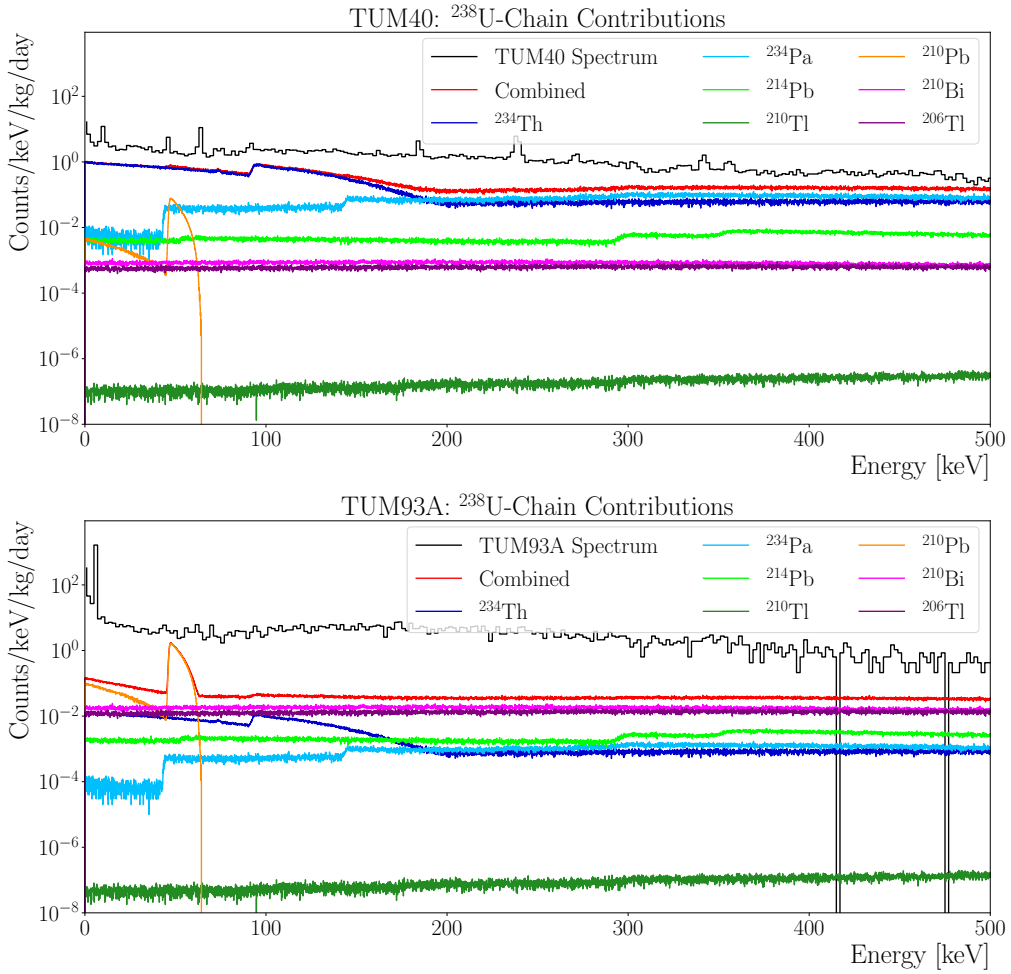

Figure E.1: Comparison of the scaled e^-/γ-templates of the^{238}U decay chain. The TUM40 contributions are shown on the top, and the TUM93A contributions on the bottom. Summed-up contributions for the whole chain are shown in red.

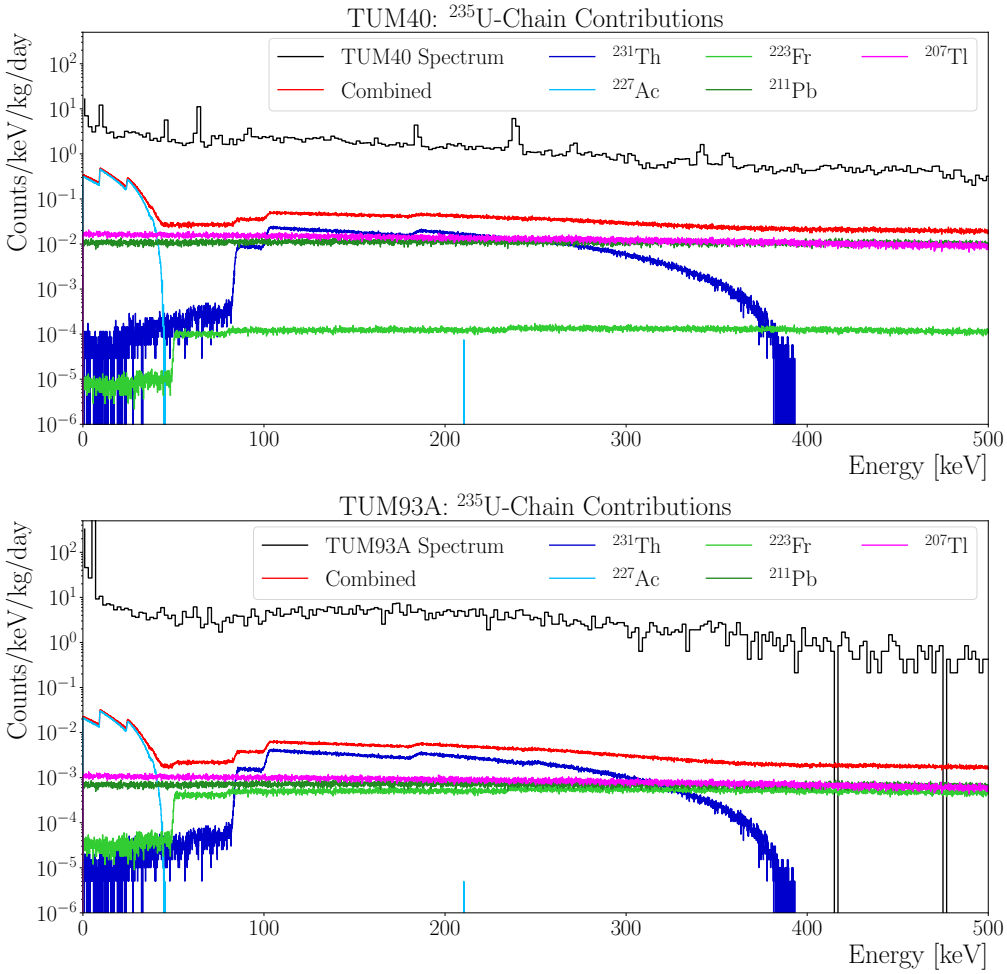

Figure E.2: Comparison of the scaled e^-/γ-templates of the^{235}U decay chain. The TUM40 contributions are shown on the top, and the TUM93A contributions on the bottom. Summed-up contributions for the whole chain are shown in red.

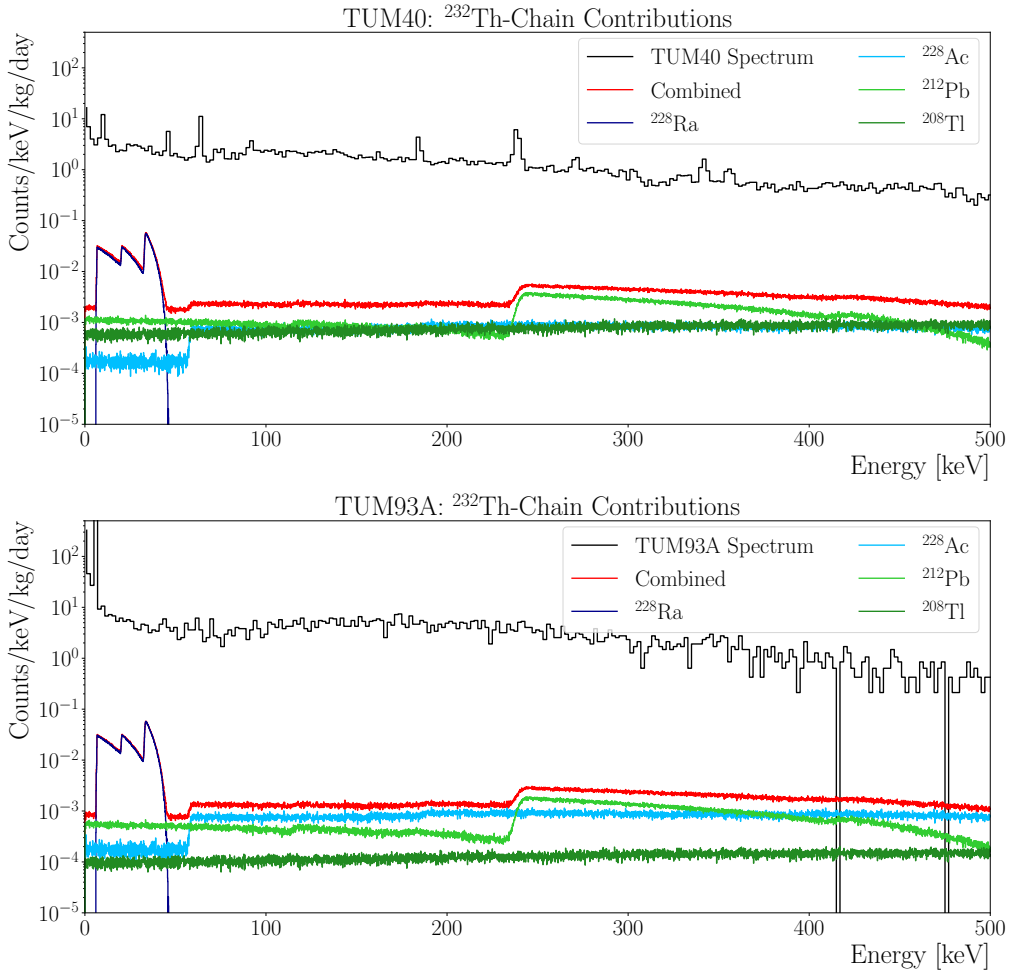

Figure E.3: Comparison of the scaled e^-/γ-templates of the^{232}Th decay chain. The TUM40 contributions are shown on the top, and the TUM93A contributions on the bottom. Summed-up contributions for the whole chain are shown in red.

Bibliography

[1] F. Zwicky, "Die Rotverschiebung von Extragalaktischen Nebeln," *Helvetica Physica Acta*, vol. 6, pp. 110–127, 1933.

[2] V. C. Rubin, W. K. Ford Jr, and N. Thonnard, "Rotational properties of 21 sc galaxies with a large range of luminosities and radii, from ngc 4605/r= 4kpc/to ugc 2885/r= 122 kpc," *The Astrophysical Journal*, vol. 238, pp. 471–487, 1980.

[3] K. Begeman, A. Broeils, and R. Sanders, "Extended rotation curves of spiral galaxies: Dark haloes and modified dynamics," *Monthly Notices of the Royal Astronomical Society*, vol. 249, no. 3, pp. 523–537, 1991.

[4] A. Einstein, "Lens-like action of a star by the deviation of light in the gravitational field," *Science*, vol. 84, no. 2188, pp. 506–507, 1936.

[5] M. Markevitch, A. Gonzalez, D. Clowe, A. Vikhlinin, W. Forman, C. Jones, S. Murray, and W. Tucker, "Direct constraints on the dark matter self-interaction cross section from the merging galaxy cluster 1e 0657–56," *The Astrophysical Journal*, vol. 606, no. 2, p. 819, 2004.

[6] R. Adam, P. A. Ade, N. Aghanim, Y. Akrami, M. Alves, F. Argüeso, M. Arnaud, F. Arroja, M. Ashdown, J. Aumont, *et al.*, "Planck 2015 results-i. overview of products and scientific results," *Astronomy & Astrophysics*, vol. 594, p. A1, 2016.

[7] N. Aghanim, Y. Akrami, M. Ashdown, J. Aumont, C. Baccigalupi, M. Ballardini, A. Banday, R. Barreiro, N. Bartolo, S. Basak, *et al.*, "Planck 2018 results-vi. cosmological parameters," *Astronomy & Astrophysics*, vol. 641, p. A6, 2020.

[8] E. Gawiser and J. Silk, "The cosmic microwave background radiation," *Physics Reports*, vol. 333, pp. 245–267, 2000.

[9] D. Fixsen, "The temperature of the cosmic microwave background," *The Astrophysical Journal*, vol. 707, no. 2, p. 916, 2009.

[10] P. Collaboration, P. Ade, N. Aghanim, C. Armitage-Caplan, M. Arnaud, *et al.*, "Planck 2015 results," *XIII. Cosmological parameters*, 2015.

[11] M. P. Hertzberg, "Structure formation in the very early universe," *Physics*, vol. 13, p. 16, 2020.

[12] C. S. Frenk and S. D. White, "Dark matter and cosmic structure," *Annalen der Physik*, vol. 524, no. 9-10, pp. 507–534, 2012.

[13] D. G. York, J. Adelman, J. E. Anderson Jr, S. F. Anderson, J. Annis, N. A. Bahcall, J. Bakken, R. Barkhouser, S. Bastian, E. Berman, *et al.*, "The sloan digital sky survey: Technical summary," *The Astronomical Journal*, vol. 120, no. 3, p. 1579, 2000.

[14] V. Springel, S. D. White, A. Jenkins, C. S. Frenk, N. Yoshida, L. Gao, J. Navarro, R. Thacker, D. Croton, J. Helly, *et al.*, "Simulations of the formation, evolution and clustering of galaxies and quasars," *nature*, vol. 435, no. 7042, pp. 629–636, 2005.

[15] J. Billard, M. Boulay, S. Cebrián, L. Covi, G. Fiorillo, A. M. Green, J. Kopp, B. Majorovits, K. Palladino, F. Petricca, *et al.*, "Direct detection of dark matter–appec committee report," *Reports on Progress in Physics*, 2022.

[16] A. Alavi-Harati, I. Albuquerque, T. Alexopoulos, M. Arenton, K. Arisaka, S. Averitte, A. Barker, L. Bellantoni, A. Bellavance, J. Belz, *et al.*, "Observation of direct cp violation in k s, l→ π π decays," *Physical Review Letters*, vol. 83, no. 1, p. 22, 1999.

[17] K. Abe, R. Abe, I. Adachi, B. S. Ahn, H. Aihara, M. Akatsu, G. Alimonti, K. Asai, M. Asai, Y. Asano, *et al.*, "Observation of large cp violation in the neutral b meson system," *Physical review letters*, vol. 87, no. 9, p. 091802, 2001.

[18] G. Servant and T. M. Tait, "Elastic scattering and direct detection of kaluza-klein dark matter," *New Journal of Physics*, vol. 4, no. 1, p. 99, 2002.

[19] H.-C. Cheng, J. L. Feng, and K. T. Matchev, "Kaluza-klein dark matter," *Physical review letters*, vol. 89, no. 21, p. 211301, 2002.

[20] G. Jungman, M. Kamionkowski, and K. Griest, "Supersymmetric dark matter," *Physics Reports*, vol. 267, no. 5-6, pp. 195–373, 1996.

[21] J. L. Feng, "Dark matter candidates from particle physics and methods of detection," *Annual Review of Astronomy and Astrophysics*, vol. 48, pp. 495–545, 2010.

[22] K. Petraki and R. R. Volkas, "Review of asymmetric dark matter," *International Journal of Modern Physics A*, vol. 28, no. 19, p. 1330028, 2013.

[23] A. Langenkämper, *Characterisation of the Muon Induced Neutron Background in a Shallow Laboratory with a LiF Cryogenic Detector*. Dissertation, Technische Universität München, 2023.

[24] G. Aad, B. Abbott, D. C. Abbott, A. Abed Abud, K. Abeling, D. K. Abhayasinghe, S. H. Abidi, O. AbouZeid, N. L. Abraham, H. Abramowicz, *et al.*, "Search for dark matter in events with missing transverse momentum and a higgs boson decaying into two photons in pp collisions at s =*sqrt*13 tev with the atlas detector," *Journal of High Energy Physics*, vol. 2021, no. 10, pp. 1–50, 2021.

[25] C. collaboration *et al.*, "Search for dark matter produced in association with a leptonically decaying z boson in proton-proton collisions at s =*sqrt*13 tev," *arXiv preprint arXiv:2008.04735*, 2020.

[26] J. M. Gaskins, "A review of indirect searches for particle dark matter," *Contemporary Physics*, vol. 57, no. 4, pp. 496–525, 2016.

[27] M. R. Buckley, E. Charles, J. M. Gaskins, A. M. Brooks, A. Drlica-Wagner, P. Martin, and G. Zhao, "Search for gamma-ray emission from dark matter annihilation in the large magellanic cloud with the fermi large area telescope," *Physical Review D*, vol. 91, no. 10, p. 102001, 2015.

[28] C. M. Karwin, S. Murgia, I. V. Moskalenko, S. P. Fillingham, A.-K. Burns, and M. Fieg, "Dark matter interpretation of the fermi-lat observations toward the outer halo of m31," *Physical Review D*, vol. 103, no. 2, p. 023027, 2021.

[29] N. Iovine, I. Collaboration, *et al.*, "Indirect search for dark matter in the galactic centre with icecube," *Journal of Instrumentation*, vol. 16, no. 09, p. C09009, 2021.

[30] J. M. Schmaler, *The CRESST Dark Matter Search - New Analysis Methods and Recent Results*. Dissertation, Technische Universität München, 2010.

[31] D. Akerib *et al.*, "Results from a search for dark matter in the complete LUX exposure," *Physical review letters*, vol. 118, no. 2, p. 021303, 2017.

[32] X. Cui *et al.*, "Dark matter results from 54-ton-day exposure of PandaX-II experiment," *Physical review letters*, vol. 119, no. 18, p. 181302, 2017.

[33] E. Aprile *et al.*, "Low-mass dark matter search using ionization signals in XENON100," *Physical Review D*, vol. 94, no. 9, p. 092001, 2016.

[34] X. Collaboration, E. Aprile, *et al.*, "Dark matter search results from a one ton-year exposure of xenon1t," *Physical review letters*, vol. 121, no. 11, p. 111302, 2018.

[35] L. Hehn *et al.*, "Improved EDELWEISS-III sensitivity for low-mass WIMPs using a profile likelihood approach," *The European Physical Journal C*, vol. 76, no. 10, pp. 1–10, 2016.

[36] R. Agnese *et al.*, "First Dark Matter Constraints from a SuperCDMS Single-Charge Sensitive Detector," *Phys. Rev. Lett.*, vol. 121, p. 051301, 2018.

[37] A. Abdelhameed *et al.*, "First results from the CRESST-III low-mass dark matter program," *Physical Review D*, vol. 100, no. 10, p. 102002, 2019.

[38] G. Angloher, P. Carniti, I. Dafinei, N. Di Marco, A. Fuss, C. Gotti, M. Mancuso, P. Martella, L. Pagnanini, G. Pessina, *et al.*, "Cosinus: Cryogenic calorimeters for the direct dark matter search with nai crystals," *Journal of Low Temperature Physics*, vol. 200, no. 5, pp. 428–436, 2020.

[39] G. Angloher *et al.*, "Commissioning run of the CRESST-II dark matter search," *Astroparticle Physics*, vol. 31, no. 4, pp. 270–276, 2009.

[40] G. Bellini *et al.*, "Cosmic-muon flux and annual modulation in Borexino at 3800 m water-equivalent depth," *Journal of Cosmology and Astroparticle Physics*, vol. 2012, no. 05, p. 015, 2012.

[41] P. Belli, R. Bernabei, S. d'Angelo, M. De Pascale, L. Paoluzi, R. Santonico, N. Taborgna, N. Iucci, and G. Villoresi, "Deep underground neutron flux measurement with large BF3 counters," *Il Nuovo Cimento A (1965-1970)*, vol. 101, no. 6, pp. 959–966, 1989.

[42] F. Pröbst, M. Frank, S. Cooper, P. Colling, D. Dummer, P. Ferger, G. Forster, A. Nucciotti, W. Seidel, and L. Stodolsky, "Model for cryogenic particle detectors with superconducting phase transition thermometers," *Journal of low temperature physics*, vol. 100, no. 1, pp. 69–104, 1995.

[43] M. Stahlberg, *Probing Low-Mass Dark Matter with CRESST-III*. Dissertation, Technische Universität Wien, 2020.

[44] N. I. Ferreiro, *Increasing the sensitivity to low mass dark matter in CRESST-III with a new DAQ and signal processing*. Dissertation, Technische Universität München, 2018.

[45] R. Strauss *et al.*, "Beta/gamma and alpha backgrounds in CRESST-II Phase 2," *Journal of Cosmology and Astroparticle Physics*, vol. 2015, no. 06, p. 030, 2015.

[46] A. Münster, *High-Purity $CaWO_4$ Single Crystals for Direct Dark Matter Search with the CRESST Experiment*. Dissertation, Technische Universität München, 2017.

[47] P. Adari *et al.*, "Excess workshop: Descriptions of rising low-energy spectra," 2022.

[48] P. Bauer, *Data Analysis for the CRESST Experiment: New Methods, improved Alpha Analysis, and Results on Light Data Matter and Backgrounds*. Dissertation, Technische Universität München, 2020.

[49] G. Angloher *et al.*, "Results on low mass WIMPs using an upgraded CRESST-II detector," *The European Physical Journal C*, vol. 74, no. 12, pp. 1–6, 2014.

[50] G. Angloher *et al.*, "Results on light dark matter particles with a low-threshold CRESST-II detector," *The European Physical Journal C*, vol. 76, no. 1, pp. 1–8, 2016.

[51] G. Angloher *et al.*, "Results on MeV-scale dark matter from a gram-scale cryogenic calorimeter operated above ground," *Eur. Phys. J. C*, vol. 77, p. 637, Sept. 2017.

[52] Q. Yue *et al.*, "Limits on light weakly interacting massive particles from the CDEX-1 experiment with a p-type point-contact germanium detector at the China Jinping Underground Laboratory," *Physical Review D*, vol. 90, no. 9, p. 091701, 2014.

[53] R. Agnese *et al.*, "New results from the search for low-mass weakly interacting massive particles with the CDMS low ionization threshold experiment," *Physical review letters*, vol. 116, no. 7, p. 071301, 2016.

[54] A. Aguilar-Arevalo *et al.*, "Search for low-mass WIMPs in a 0.6 kg day exposure of the DAMIC experiment at SNOLAB," *Physical Review D*, vol. 94, no. 8, p. 082006, 2016.

[55] E. Armengaud *et al.*, "Searching for low-mass dark matter particles with a massive Ge bolometer operated above ground," *Physical Review D*, vol. 99, no. 8, p. 082003, 2019.

[56] R. Agnese *et al.*, "Search for low-mass weakly interacting massive particles with SuperCDMS," *Physical review letters*, vol. 112, no. 24, p. 241302, 2014.

[57] C. E. Aalseth *et al.*, "CoGeNT: A search for low-mass dark matter using p-type point contact germanium detectors," *Physical Review D*, vol. 88, no. 1, p. 012002, 2013.

[58] P. Agnes *et al.*, "Low-mass dark matter search with the DarkSide-50 experiment," *Physical review letters*, vol. 121, no. 8, p. 081307, 2018.

[59] D. Akerib *et al.*, "Results of a search for sub-GeV dark matter using 2013 LUX data," *Physical review letters*, vol. 122, no. 13, p. 131301, 2019.

[60] "An experiment to search for dark-matter interactions using sodium iodide detectors," *Nature*, vol. 564, no. 7734, pp. 83–86, 2018.

[61] J. Collar, "Search for a nonrelativistic component in the spectrum of cosmic rays at Earth," *Physical Review D*, vol. 98, no. 2, p. 023005, 2018.

[62] Q. Arnaud *et al.*, "First results from the NEWS-G direct dark matter search experiment at the LSM," *Astroparticle Physics*, vol. 97, pp. 54–62, 2018.

[63] C. Amole *et al.*, "Dark matter search results from the PICO-60 CF 3 I bubble chamber," *Physical Review D*, vol. 93, no. 5, p. 052014, 2016.

[64] A. Abdelhameed *et al.*, "First results on sub-GeV spin-dependent dark matter interactions with ^{7}Li," *The European Physical Journal C*, vol. 79, no. 7, pp. 1–7, 2019.

[65] R. Agnese *et al.*, "Low-mass dark matter search with CDMSlite," *Physical Review D*, vol. 97, no. 2, p. 022002, 2018.

[66] D. Akerib *et al.*, "Results on the spin-dependent scattering of weakly interacting massive particles on nucleons from the run 3 data of the LUX experiment," *Physical review letters*, vol. 116, no. 16, p. 161302, 2016.

[67] C. Fu, P.-I. Collaboration, *et al.*, "Spin-Dependent Weakly-Interacting-Massive-Particle–Nucleon Cross Section Limits from First Data of PandaX-II Experiment," *Physical Review Letters*, vol. 120, no. 4, p. 049902, 2018.

[68] X. Collaboration, E. Aprile, *et al.*, "Constraining the spin-dependent WIMP-nucleon cross sections with XENON1T," *Physical review letters*, vol. 122, no. 14, p. 141301, 2019.

[69] L. Einfalt, *PhD Thesis in preparation.* Dissertation, Technische Universität Wien.

[70] A. Aguilar-Arevalo, X. Bertou, C. Bonifazi, M. Butner, G. Cancelo, A. C. Vazquez, B. C. Vergara, C. Chavez, H. Da Motta, J. D'Olivo, *et al.*, "The connie experiment," in *Journal of Physics: Conference Series*, vol. 761, p. 012057, IOP Publishing, 2016.

[71] A. Aguilar-Arevalo *et al.*, "Results on low-mass weakly interacting massive particles from an 11 kg d target exposure of damic at snolab," *Phys. Rev. Lett.*, vol. 125, p. 241803, Dec 2020.

[72] E. Armengaud *et al.*, "Searching for low-mass dark matter particles with a massive Ge bolometer operated above ground," *Phys. Rev. D*, vol. 99, p. 082003, 2019.

[73] Q. Arnaud *et al.*, "First Germanium-Based Constraints on Sub-MeV Dark Matter with the EDELWEISS Experiment," *Phys. Rev. Lett.*, vol. 125, p. 141301, 2020.

[74] G. Agnolet, W. Baker, D. Barker, R. Beck, T. Carroll, J. Cesar, P. Cushman, J. Dent, S. De Rijck, B. Dutta, *et al.*, "Background studies for the miner coherent neutrino scattering reactor experiment," *Nuclear Instruments and Methods in Physics Research Section A: Accelerators, Spectrometers, Detectors and Associated Equipment*, vol. 853, pp. 53–60, 2017.

[75] R. Strauss *et al.*, "Gram-scale cryogenic calorimeters for rare-event searches," *Phys. Rev. D*, vol. 96, p. 022009, 2017.

[76] T. Salagnac *et al.*, "Optimization and performance of the CryoCube detector for the future RICOCHET low-energy neutrino experiment," 2021.

[77] L. Barak *et al.*, "SENSEI: Direct-Detection Results on sub-GeV Dark Matter from a New Skipper CCD," *Phys. Rev. Lett.*, vol. 125, p. 171802, 2020.

[78] D. W. Amaral *et al.*, "Constraints on low-mass, relic dark matter candidates from a surface-operated SuperCDMS single-charge sensitive detector," *Phys. Rev. D*, vol. 102, p. 091101, 2020.

[79] M. Wüstrich, *Improving Particle Discrimination and Achieving a 4π-Veto Detector Concept for the CRESST experiment*. Dissertation, Technische Universität München, 2019.

[80] F. Hamilton, *Development and Design of a Low Threshold Beaker Module for CRESST*. Master's thesis, Technische Universität München, 2022.

[81] W. M. Haynes, D. Lide, and T. Bruno, "Handbook of chemistry and physics: a ready-reference book of chemical and physical data," 2015.

[82] A. Senyshyn, H. Kraus, V. Mikhailik, and V. Yakovyna, "Lattice dynamics and thermal properties of $CaWO_4$," *Physical Review B*, vol. 70, no. 21, p. 214306, 2004.

[83] S. mindat database of minerals, "Scheelite," 2022.

[84] A. Erb and J.-C. Lanfranchi, "Growth of high-purity scintillating $CaWO_4$ single crystals for the low-temperature direct dark matter search experiments CRESST-II and EURECA," *CrystEngComm*, vol. 15, no. 12, pp. 2301–2304, 2013.

[85] A. Muenster, M. v. Sivers, *et al.*, "Radiopurity of $CaWO_4$ crystals for direct dark matter search with CRESST and EURECA," *Journal of Cosmology and Astroparticle Physics*, vol. 2014, no. 05, p. 018, 2014.

[86] M. v. Sivers *et al.*, "Low-temperature scintillation properties of $CaWO_4$ crystals for rare-event searches," *Journal of Applied Physics*, vol. 118, no. 16, p. 164505, 2015.

[87] J. Molenda *et al.*, "Status report on high temperature fuel cells in Poland – Recent advances and achievements," *International Journal of Hydrogen Energy*, vol. 42, pp. 4366–4403, 02 2017.

[88] A. Erb. personal communication.

[89] H. Mehrer, "Dependence of diffusion on temperature and pressure," *Diffusion in solids: Fundamentals, methods, materials, diffusion-controlled processes*, pp. 127–149, 2007.

[90] A. Erb, B. Greb, and G. Müller-Vogt, "In-situ resistivity measurements during the oxygenation of YBa2Cu3O7- δ and Gd0. 8Y0. 2Ba2Cu3O7- δ single crystals," *Physica C: Superconductivity and its applications*, vol. 259, no. 1-2, pp. 83–91, 1996.

[91] C. Stelian, J. Muzy, S. Labor, M. Fivel, H. Cabane, and T. Duffar, "Numerical Analysis of Thermal Stress in Semi-Transparent Oxide Crystals Grown by Czochralski and EFG Methods," *Crystal Research and Technology*, vol. 54, no. 1, p. 1800219, 2019.

[92] F. Hamilton, *Simulation der Temperaturverteilung während der Züchtung von $CaWO_4$ Kristallen für CRESST an der Czochralski Anlage der TUM*. Bachelor's thesis, Technische Universität München, 2019.

[93] K. Böttcher, W. Miller, and S. Ganschow, "Numerical Modeling of Heat Transfer and Thermal Stress at the Czochralski Growth of Neodymium Scandate Single Crystals," *Crystal Research and Technology*, vol. 56, no. 1, p. 2000106, 2021.

[94] COMSOL Inc., "COMSOL Multiphysics."

[95] W. Demtröder, *Mechanics and Thermodynamics*. Springer, 2017.

[96] H. Göldner and F. Holzweißig, *Leitfaden der Technischen Mechanik: Statik· Festigkeitslehre· Kinematik· Dynamik*. Springer-Verlag, 2019.

[97] C. Schmitz-Sinn, *Investigation of mechanical Stress in $CaWO_4$ Crystals for the CRESST Direct Dark Matter Search*. Bachelor's thesis, Technische Universität München, 2019.

[98] J. F. Doyle, J. W. Phillips, and D. Post, "Manual on Experimental Stress Analysis . Society for Experimental Mechanics," 1989.

[99] J. Schindelin *et al.*, "Fiji: an open-source platform for biological-image analysis," *Nature methods*, vol. 9, no. 7, pp. 676–682, 2012.

[100] K. H. Lieser, *Nuclear and radiochemistry: fundamentals and applications*. John Wiley & Sons, 2008.

[101] Z. B. Alfassi, *Determination of trace elements*. John Wiley & Sons, 2008.

[102] I. Kolthoff, "Theory of coprecipitation. The formation and properties of crystalline precipitates," *The Journal of Physical Chemistry*, vol. 36, no. 3, pp. 860–881, 2002.

[103] J. Rothe, *Achieving Low Threshold: Cryogenic Detectors for Low-Mass Dark Matter Searches*. Master's thesis, Max-Planck-Institut für Physik München, 2019.

[104] H. Kluck *et al.*, "Cosmic activation of Cresst's $CaWO_4$ crystals," in *Journal of Physics: Conference Series*, vol. 2156, p. 012227, IOP Publishing, 2021.

[105] I. Antcheva *et al.*, "Root—a c++ framework for petabyte data storage, statistical analysis and visualization," *Computer Physics Communications*, vol. 180, no. 12, pp. 2499–2512, 2009.

[106] F. Wagner, *Machine Learning Methods of the Raw Data Analysis of Cryogenic Data Matter Experiments*. Master's thesis, Technische Universität Wien, 2020.

[107] E. Gatti and P. F. Manfredi, "Processing the signals from solid-state detectors in elementary-particle physics," *La Rivista del Nuovo Cimento (1978-1999)*, vol. 9, no. 1, pp. 1–146, 1986.

[108] M. Mancuso *et al.*, "A method to define the energy threshold depending on noise level for rare event searches," *Nuclear Instruments and Methods in Physics Research Section A: Accelerators, Spectrometers, Detectors and Associated Equipment*, vol. 940, pp. 492–496, 2019.

[109] F. Wagner, *PhD Thesis in preparation.* Dissertation, Technische Universität Wien.

[110] A. Abdelhameed *et al.*, "Geant4-based electromagnetic background model for the CRESST dark matter experiment," *The European Physical Journal C*, vol. 79, no. 10, pp. 1–18, 2019.

[111] G. Angloher *et al.*, "Secular Equilibrium Assessment in a $CaWO_4$ Target Crystal from the Dark Matter Experiment CRESST using Bayesian Likelihood Normalisation," *arXiv preprint arXiv:2209.00461*, 2022.

[112] Lund/LBNL Nuclear Data Search, "Table of Radioactive Isotopes ," 2022.

[113] A. Kinast *et al.*, "Improving the Quality of $CaWO_4$ Target Crystals for CRESST," *Journal of Low Temperature Physics*, pp. 1–7, 2022.

[114] F. Petricca. personal communication.

[115] C. Cozzini, G. Angloher, C. Bucci, F. von Feilitzsch, D. Hauff, S. Henry, T. Jagemann, J. Jochum, H. Kraus, B. Majorovits, *et al.*, "Detection of the natural α decay of tungsten," *Physical Review C*, vol. 70, no. 6, p. 064606, 2004.

[116] P. D. Group, P. Zyla, R. Barnett, J. Beringer, O. Dahl, D. Dwyer, D. Groom, C.-J. Lin, K. Lugovsky, E. Pianori, *et al.*, "Review of particle physics," *Progress of Theoretical and Experimental Physics*, vol. 2020, no. 8, p. 083C01, 2020.

[117] A. Karl, *Simulation based Background comparison of future detector modules of the CRESST experiment*. Master's thesis, Atominstitut Technische Universität Wien, 2022.

[118] A. Anokhina, S. Aoki, A. Ariga, L. Arrabito, D. Autiero, A. Badertscher, F. Bay, A. Bergnoli, F. B. Greggio, M. Besnier, *et al.*, "Study of the effects induced by lead on the emulsion films of the opera experiment," *Journal of instrumentation*, vol. 3, no. 07, p. P07002, 2008.

[119] V. Radchenko, J. W. Engle, J. J. Wilson, J. R. Maassen, F. M. Nortier, W. A. Taylor, E. R. Birnbaum, L. A. Hudston, K. D. John, and M. E. Fassbender, "Application of ion exchange and extraction chromatography to the separation of actinium from proton-irradiated thorium metal for analytical purposes," *Journal of Chromatography A*, vol. 1380, pp. 55–63, 2015.

[120] F. Reindl, *Exploring Light Dark Matter With CRESST-II Low-Threshold Detectors*. Dissertation, Technische Universität München, 2016.

[121] J. Burkhart, *Enhancing the Electromagnetic Background Model of CRESST-II*. Master's thesis, Atominstitut, Technische Universität Wien, 2022.

[122] *Update of X Ray and Gamma Ray Decay Data Standards for Detector Calibration and Other Applications*. Non-serial Publications, Vienna: INTERNATIONAL ATOMIC ENERGY AGENCY, 2007.

[123] D. Schmiedmayer, *Calculation of Dark-Matter Exclusion-Limits using a Maximum Likelihood Approach*. Master's thesis, Technische Universität Wien, 2016.

[124] D. Schmiedmayer, *PhD Thesis in preparation*. Dissertation, Technische Universität Wien.

[125] R. J. Strauß, *Energy-Dependent Quenching Factor Measurements of $CaWO_4$ Crystals at mK Temperatures and Detector Prototypes for Direct Dark Matter Search with CRESST*. Dissertation, Technische Universität München, 2013.

[126] S. Yellin, "Finding an upper limit in the presence of an unknown background," *Physical Review D*, vol. 66, no. 3, p. 032005, 2002.

[127] D. Fuchs, *PhD Thesis in preparation*. Dissertation, Technische Universität München.

[128] G. Angloher *et al.*, "Latest observations on the low energy excess in CRESST-III," *arXiv preprint arXiv:2207.09375*, 2022.

[129] G. Shubham, *PhD Thesis in preparation*. Dissertation, Technische Universität Wien.

[130] E. Queguiner, *Analysis of the data of the EDELWEISS-LT experiment searching for low-mass WIMP*. Dissertation, 10 2018.

[131] M. Pyle, "Low-Energy Phonon and Heat-Only Events in Solid-State Detectors." EXCESS Workshop, 2022.

[132] D. Mckinsey, "Stress Induced Background in Cryogenic Crystal Calorimeters." EXCESS Workshop IDM, 2022.

[133] G. Angloher, S. Banik, G. Benato, A. Bento, A. Bertolini, R. Breier, C. Bucci, J. Burkhart, L. Canonica, A. D'Addabbo, *et al.*, "Testing spin-dependent dark matter interactions with lithium aluminate targets in cresst-iii," *arXiv preprint arXiv:2207.07640*, 2022.

[134] J. R. Farver, "Oxygen and hydrogen diffusion in minerals," *Reviews in Mineralogy and Geochemistry*, vol. 72, no. 1, pp. 447–507, 2010.

[135] G. Wu, "Solid-state 17O NMR spectroscopy of organic and biological molecules," *Modern Magnetic Resonance*, pp. 1–20, 2017.

[136] R. S. Macomber, *A complete introduction to modern NMR spectroscopy*. John Wiley & Sons, 1997.

[137] R. Gühne, "Electronic properties of the topological insulators bi_2se_3 and bi_2te_3," 2020.

[138] J. Goldstein and A. Moren, "Diffusion modeling of the carburization process," *Metallurgical Transactions A*, vol. 9, pp. 1515–1525, 1978.

[139] K. von Mirbach, *Background studies of $CaWO_4$ crystals for the CRESST Direct Dark Matter Search*. Bachelor's thesis, Technische Universität München, 2019.

[140] A. Kinast, E. Mondragon, A. Erb, A. Langenkämper, M. Kaznacheeva, T. Ortmann, L. Pattavina, W. Potzel, S. Schönert, and R. Strauss, "Development of a cryogenic alpha-screening facility at the shallow underground laboratory at tum," in *Journal of Physics: Conference Series*, vol. 1468, p. 012248, IOP Publishing, 2020.

[141] R. Burkhardt, *Abschätzung der Abschirmwirkung des Garchinger Untergrundlabors (UGL) durch die Messung des Myomen-Flusses inner- und ausserhalb des UGLs.* . Bachelor's thesis, Technische Universität München, 2012.

[142] C. Enss and S. Hunklinger, *Low-temperature physics*. Springer Science & Business Media, 2005.

[143] L. Klinkenberg, *Commissioning of an Active Muon-Veto to Study Muon-Induced Background at Sub-keV Energies* . Master's thesis, Technische Universität München, 2021.

[144] C. Strandhagen, "Stress Induced Background in Cryogenic Crystal Calorimeters." EXCESS Workshop, 2021.

Acknowledgements

Abschließend möchte ich mich bei allen bedanken, die diese Arbeit ermöglicht haben. Ein großer Dank geht an Prof. Stefan Schönert für die Möglichkeit meine Arbeit am Lehrstuhl zu machen. Danke für die vielen Erfahrungen die ich hier machen konnte und die Unterstützung während der Arbeit. Ein weiterer Dank geht an unseren Gruppenleiter Dr. Raimund Strauß, der unsere Gruppe im Laufe meiner Arbeit übernommen hat. Danke für die engagierte Betreuung und die vielen hilfreichen Diskussionen.

Bei Prof. Andreas Erb will ich mich für die gute Zusammenarbeit bei der Herstellung der $CaWO_4$ Kristalle bedanken. Die gesamten Optimierungen die in dieser Arbeit gelistet sind, wären ohne deine Hilfe nicht möglich gewesen. Danke auch an das gesamte Kristalllabor für die Hilfe beim Bearbeiten der Kristalle. An dieser Stelle möchte ich mich auch bei meiner Bachelorstudentin Fiona Hamilton für die Temperatursimulationen und beim Institut für Kristallzüchtung und speziell bei Dr. Wolfram Miller für die Hilfe bei diesen Simulationen bedanken. Sie waren ein Grundstein für die Optimierungen der Züchtung. Danke auch an meine Bachelorstudentin Cordula Schmitz-Sinn für die Stress Messungen der Kristalle. Bei Prof. Jürgen Haase will ich mich für die herzliche Aufnahme in seiner Arbeitsgruppe während der NMR Messungen in Leipzig bedanken. Ohne deine Erfahrung und dein Engagement wären diese Messungen in dem Zeitrahmen der Arbeit nicht möglich gewesen. Thanks to Menna, Jamie and Crina for helping with the measurements. Ich möchte an dieser Stelle auch Christop Vogl für die Hilfe bei der Massenspektrometer Messung des Sauerstoffes danken. Außerdem möchte ich mich bei Dr. Hong Hanh Trinh Thi für die Entwicklung der $CaWO_4$ Pulver Reinigung bedanken und für das angenehme Arbeitsklima während der Reinigung. A big thank you also goes to Dr. Luca Pattavina, Dr. Valentyna Mokina and Dr. Holger Kluck. Your knowledge on radioactive backgrounds, especially the $CaWO_4$ crystals, including intrinsic radiopurity and cosmic activations, was of huge value for this work. Thanks, Jens Burkhart and Robert Breier, for the help with the radiopurity simulations. Special thanks to Luca for being a great office colleague, always having an open ear for any questions and the input on all radiopurity and crystal growth-related chapters of this work! I would like to thank all my proofreaders: Dr. Alexander Langenkämper, Dr. Martin Stahlberg, Dr. Victoria Wagner, Dr. Luca Pattavina, Margarita Kaznacheeva, Dr. Raimund Strauß and Dr. Walter Potzel.

I also want to thank the whole team at Max Planck for the great atmosphere during the detector mounting for CRESST, especially Dr. Lucia Canonica for the pleasant working atmosphere in the clean room for many weeks. Thanks also to Dr. Michele

Mancuso and Dieter Hauff for interesting insights into TES production for these detectors.
Furthermore, I want to thank the CRESST analysis group for the great working atmosphere, especially during the pandemic via zoom and Mattermost. Though, initially, the thesis was designed to lean more into the hardware side, these few months of being stuck in home office changed that a little, Christian even counts be as a full-time analysis group member in his analysis team summaries now xD. So thanks to all fellow PhD students Rita, Felix, Dominik, Shubham, Leonie, Anna, Sarah, Lena and Daniel. It was so great to finally meet you all in person at our post-pandemic collaboration meeting in Ringberg. Thank you, Daniel, Martin, Felix and Leonie, for your patience in solving any issues I had using your analysis programs. I also want to thank Dr. Federica Petricca for the feedback on my radiopurity analysis and the help concerning the energy calibration. Ein großer Dank geht auch an Dr. Franz Pröbst für die stete Unterstützung in allen Tages- und Nachtzeiten, sei es bei der Analyse oder während einer Schicht oder eines Cooldowns am Gran Sasso. In unseren zahlreichen Gesprächen hab ich unglaublich viel gelernt. Bei Prof. Florian Reindl möchte ich mich für die Hilfe in Analysefragen und beim Detektorenaufsetzen in CRESST bedanken. Unser Mattermost Chatverlauf ist nach wie vor mein Lexikon für den Umgang mit ccs und dem HeaterBiasClient. Danke Dr. Martin Stahlberg für die vielen Diskussionen über Analyse, das Debuggen von Code, Einfügen von neuen Methoden in CAT usw.
Furthermore, I would like to thank the whole chair for a great working atmosphere. Danke an unsere Teamassistentinnen Sabine und Paola für die Unterstützung in organisatorischen Angelegenheiten. Ein großer Dank geht auch an unsere Werkstatt die alle Teile auch manchmal ohne exakte technische Zeichnung für diese Arbeit hergestellt haben. Thanks to the cryo group, for all the help and support for the cryostat measurements performed in this work. Ein ganz besonderer Dank geht an Dr. Alexander Langenkämper. Ich glaube fast alles was ich über Kryostaten weiß, hab ich von dir gelernt. Danke für die tolle Zusammenarbeit während meiner Master und Doktorarbeit sei es beim Detektorzusammenbau, Kryostatenbetrieb oder bei der Analyse! Außerdem möchte ich Dr. Victoria Wagner für die viele Hilfe am Kryostaten danken, ohne deine Hilfe wären die Messungen für Alex und meine Arbeit zeitlich nicht schaffbar gewesen. Außerdem möchte ich mich bei Dr. Johannes Rothe für die vielen Diskussionen über Detektoren, Kryostaten, SQUIDS usw. bedanken . Ein großer Dank geht auch an meine Bachelorstudentin Katharina von Mirbach mit der ich das Alpha-Modul zusammen entwickelt habe. Danke an Tobias Ortmann für die Zusammenarbeit seit der Bachelorarbeit und für dein oft kurzfristiges Einspringen beim Kühlfalle füllen.
Zu guter Letzt will ich meiner Familie und meinen Freunden hier danken. Danke für die Unterstützung v.a. in der Endphase der Arbeit und dass ihr euch mit Fragen wie "wann gibst du denn jetzt endlich ab" ein wenig zurück gehalten habt ;) Der größte Dank geht an die Person, die den meisten Frust während der Endphase abbekommen hat. Danke für deine Hilfe und Unterstützung in so vielen Dingen, ich weiß garnicht wo ich anfangen soll :)